

RESOLVING JET-DRIVEN FEEDBACK ON SUB-KPC SCALES

By

Henry Rooney Morgan Zovaro

A THESIS SUBMITTED FOR THE DEGREE OF DOCTOR OF PHILOSOPHY
OF THE AUSTRALIAN NATIONAL UNIVERSITY
RESEARCH SCHOOL OF ASTRONOMY AND ASTROPHYSICS
JULY 2020



© Henry Rooney Morgan Zovaro, 2020.

All Rights Reserved

Declaration

I hereby declare that the work in this thesis is that of the candidate alone, except where indicated below or in the text of the thesis. The work was undertaken between the 15th of February, 2016 and the 9th of July, 2020 at the Australian National University (ANU), Canberra. It has not been submitted in whole or in part for any other degree at this or any other university.

Statement of Contribution

This thesis has been submitted as a Thesis by Compilation in accordance with the relevant ANU policies. Each of the three main chapters is therefore a completely self-contained article, which has been published in, or submitted to, a peer-reviewed journal, or is in preparation for doing so. The status of each article and extent of the contribution of the candidate to the research and authorship is indicated below:

- **Chapter 2: Zovaro, H. R. M.**, Sharp, R., Nesvadba, N. P. H., Bicknell, G. V., Mukherjee, D., Wagner, A. Y., Groves, B., Krishna, S. *Jets blowing bubbles in the young radio galaxy 4C 31.04*, 2019, MNRAS, 484, 3393–3409. R. Sharp led the NIFS proposal, and carried out the observations. H. R. M. Zovaro carried out the reduction, analysis and interpretation of the observations with guidance from co-authors, and wrote all text and created all figures.
- **Chapter 3: Zovaro, H. R. M.**, Nesvadba, N. P. H., Sharp, R., Bicknell, G. V., Groves, B., Mukherjee, D., Wagner, A. Y. *Searching for signs of jet-driven negative feedback in the nearby radio galaxy UGC 05771*, 2019, MNRAS, 489, 4944–4961. H. R. M. Zovaro led the OSIRIS proposal, and carried out the observations, data reduction, analysis and interpretation with guidance from co-authors. H. R. M. Zovaro wrote all text and created all figures with the exception of Section 3.5 and parts of Section 3.4.3, both provided by N. P. H. Nesvadba.
- **Chapter 4: Zovaro, H. R. M.**, Sharp, R., Nesvadba, N. P. H., Kewley, L. J., Sutherland, R. S., Taylor, P., Groves, B., Wagner, A. Y., Mukherjee, D., Bicknell, G. V., *Unravelling the enigmatic ISM conditions in Minkowski’s Object*, in preparation. H. R. M. Zovaro assisted with the WiFeS observations, which were led by R. Sharp. H. R. M. Zovaro carried out the data reduction, analysis and interpretation with guidance from co-authors. H. R. M. Zovaro wrote all text and created all figures with the exception of Fig. 4.16 and a paragraph in Section 4.7, both provided by P. Taylor, and Appendix D, provided by G. V. Bicknell.

The candidate also made contributions to the following articles during the course of the candidature:

- Riseley, C. J., Galvin, T. J., Keel, S., Duchesne, S. W., Intema, H. T., Anderson, C. S., Heald, G., Hunstead, R. W., Hurley-Walker, N., O’Brien, A., Koribalski, B. S., Whiting M., **Zovaro, H. R. M.**, *Revisiting the Giant Radio Galaxy ESO 422–G028 I: Spectropolarimetric Properties of the Core/Jet System*, in preparation.

-
- Andreoni, I., Ackley, K., Cooke, J., [and 122 others, including **Zovaro, H. R. M.**], *Follow Up of GW170817 and Its Electromagnetic Counterpart by Australian-Led Observing Programmes*, 2017, PASA, 34, id.e069 21 pp.
 - **Zovaro, A. M.***, Bennet, F., Copeland, M., Rigaut, F., D’Orgeville, C., Grosse, D., *Harnessing Adaptive Optics for Space Debris Collision Mitigation*, Proceedings of the Advanced Maui Optical and Space Surveillance Technologies Conference, held in Wailea, Maui, Hawai‘i, September 20-23, 2016, Ed.: S. Ryan, The Maui Economic Development Board, id.127
 - Copeland, M., Bennet, F., **Zovaro, A. M.***, Rigaut, F., Piatrou, P., Korhikoski, V., Smith, C., *Adaptive Optics for Satellite and Debris Imaging in LEO and GEO*, Proceedings of the Advanced Maui Optical and Space Surveillance Technologies Conference, held in Wailea, Maui, Hawai‘i, September 20-23, 2016, Ed.: S. Ryan, The Maui Economic Development Board, id.67
 - Vaccarella, A., Sharp, R., Ellis, M., Singh, S., Bloxham, G., Bouchez, A., Conan, R., Boz, R., Bundy, D., Davies, J., Espeland, B., Hart, J., Herrald, N., Ireland, M., Jacoby, G., Nielsen, J., Vest, C., Young, P., Fordham, B., **Zovaro, A. M.***, *Avalanche photo diodes in the observatory environment: lucky imaging at 1-2.5 microns*, Proceedings of the SPIE, Volume 9908, id. 99082X 8 pp. (2016)
 - **Zovaro, A. M.***, Bennet, F., Rye, D., D’Orgeville, C., Rigaut, F., Price, I., Ritchie, I., Smith, C., *Simpler Adaptive Optics using a Single Device for Processing and Control*, Proceedings of the Advanced Maui Optical and Space Surveillance Technologies Conference, held in Wailea, Maui, Hawai‘i, September 15-18, 2015, Ed.: S. Ryan, The Maui Economic Development Board, id.104

Henry Rooney Morgan Zovaro

*denotes publication under previous name.

Acknowledgements

Doing a PhD is *hard*. Learning how to become an independent researcher is difficult enough, let alone moving to a new city, away from your friends and family. In spite of all this, however, I am fortunate enough to look back on these years of my life with fondness, in no small part due to the people around me. Many thanks are due, more than can fit on one page.

First and foremost, I want to thank the many people who've helped me transform what essentially began as data sitting on a hard drive into the hundred or so pages of work presented in this thesis. I am incredibly thankful to my supervisors, Rob, Geoff, Nicole, Dipanjan, Alex and Brent, for the countless hours spent reading my (often incoherent) paper drafts, responding to my (even less coherent) emails, and attending conference calls at weird hours of the day to discuss my work. I'd also like to thank everyone in GEARS3D for their insightful comments during group meetings, and for encouraging me to look at my research from new perspectives.

I especially want to thank Rob, for teaching me how to become a good scientist, for reminding me that my research matters, and for helping me navigate more than one difficult transition during my time at RSAA. I could not have asked for a better supervisor.

I also thank my past mentors, in particular Francis for taking me on as a summer research student back in 2014 (and perhaps most importantly, for convincing me to come back to Stromlo for a PhD), and to Céline and François for their support during the first year of my PhD. I'd like to also thank Joss Bland-Hawthorn for taking me on as a research student as an undergrad at the University of Sydney in 2012, which was my first introduction to research in astronomy. Joss's contagious enthusiasm for everything weird and wonderful in the Universe has stuck with me ever since, and played no small part in motivating me to pursue a PhD in astrophysics.

I owe a great deal to my mum and dad, for encouraging me to pursue my interests in science from a young age (even if they couldn't help me with my maths homework). I am extremely grateful for their financial support whilst I was studying as an undergrad, which enabled me to take on research projects during semester breaks. Without their support, I would never have had the opportunity to pursue a PhD.

I'd like to thank the many friends I've made in Canberra, and everyone in the Stromlo community, for making my time in Canberra so unforgettable. I'd especially like to thank Alec and Fiona for the countless enjoyable conversations we've shared during coffee breaks. I am also indebted to May, for dragging me out of the house when I first moved to Canberra, and didn't have many friends. And to everyone in Impossible Discrepancy, for the many enjoyable hours we've spent playing Destiny together: who knew that blasting aliens with shotguns would be such an excellent distraction?

Last but not least, I want to thank my partner Josh, for reminding me that

there's more to life than work, and for making Canberra feel like home. Meeting you was one of the best things that's ever happened to me.

To Dennis Morgan.

Abstract

Relativistic jets from active galactic nuclei are known to have a profound impact on their environment, both enhancing (‘positive feedback’) and inhibiting (‘negative feedback’) star formation under certain conditions. However, the role that these feedback processes play in shaping the properties of their host galaxies and environment remains elusive. In particular, efforts to catch feedback ‘in the act’ have been hampered by the spatial resolution required to resolve the jets’ environment.

In this thesis, I advance our understanding of jet-driven feedback by comparing hydrodynamical simulations to high angular resolution optical and near-infrared integral field spectroscopy (IFS) observations, which allow us to probe the critical sub-kpc scales necessary to bridge the gap between theory and observations.

To investigate feedback processes driven by young jets, I led observational programs focusing on the local radio galaxies 4C 31.04 and UGC 05771. Both galaxies harbour young jets confined to the interstellar medium (ISM), with very long baseline interferometry (VLBI) revealing jets ~ 100 pc and ~ 10 pc in size in 4C 31.04 and UGC 05771 respectively. Using adaptive optics-assisted near-infrared IFS from Gemini/NIFS and Keck/OSIRIS, I found signatures of jet-ISM interactions at radii up to 100 times larger than the size of the jets in both galaxies, a surprising result which indicated the existence of low surface-brightness jet plasma not visible in the VLBI observations. This is consistent with contemporary hydrodynamical simulations which show that the main jet streams may become temporarily halted by dense clumps in the ISM, whilst secondary plasma streams—which have a much lower surface brightness—can percolate through channels in the ISM, reaching much larger radii. The fact that this phenomenon was observed in both galaxies suggests it may be common in young radio galaxies, and may regulate star formation by driving shocks into the ISM.

To investigate jet-induced star formation, I led a study of Minkowski’s Object, a peculiar star-forming dwarf galaxy located in the path of the radio jet from the galaxy NGC 541 in the nearby cluster Abell 194. I carried out an IFS study of this enigmatic object using WiFeS on the ANU 2.3 m telescope, and determined that the observed emission line ratios are consistent with star formation, with a minor contribution from non-stellar ionisation sources, and an unusually large metallicity variation within the object, the origin of which remains unclear.

Contents

Acknowledgements	v
Abstract	ix
1 Introduction	1
1.1 Radio galaxies	2
1.2 The evolution of young radio galaxies: predictions from hydrodynamical simulations	5
1.3 Jet-induced feedback	9
1.3.1 Negative feedback	9
1.3.2 Positive feedback	11
1.4 Observing jet-induced feedback	12
1.4.1 Integral field spectroscopy	12
1.4.2 Optical diagnostic diagrams	16
1.4.3 Metallicity diagnostics	17
1.4.4 Measuring the star formation rate	19
1.4.5 The Kennicutt-Schmidt relation	19
1.5 Thesis overview	20
2 Jets blowing bubbles in the young radio galaxy 4C 31.04	23
2.1 Introduction	24
2.2 Previous observations of 4C 31.04	26
2.2.1 Host galaxy properties	26
2.2.2 Radio properties	27
2.2.3 Previous observations of the circumnuclear medium	27
2.3 Observations and data reduction	28
2.3.1 Observations	28
2.3.2 NIFS data reduction in IRAF	29
2.3.3 MAD smoothing	29
2.3.4 Emission line fitting	30
2.4 Results	32
2.4.1 Nuclear [Fe II] emission	32
2.4.2 H ₂ emission	32
2.5 Discussion	40
2.5.1 Updated jet flux estimate	44
2.5.2 The origin of the [Fe II] emission	45
2.5.3 The origin of the H ₂ emission	46
2.5.4 Age of the radio source	50
2.5.5 Density distribution of the clumpy ISM	50

2.6	Conclusion	52
3	Searching for signs of jet-driven feedback in the radio galaxy UGC 05771	55
3.1	Introduction	56
3.2	Host galaxy and radio source properties	58
3.3	OSIRIS observations	59
3.3.1	Observations	59
3.3.2	Data reduction	60
3.3.3	Emission line fitting	61
3.3.4	Results	61
3.4	CALIFA observations	66
3.4.1	Observations and data reduction using PIPE3D	66
3.4.2	Stellar properties	67
3.4.3	Emission line analysis	68
3.5	IRAM observations	74
3.5.1	Observations	74
3.5.2	Data reduction	75
3.5.3	Results	75
3.6	Discussion	77
3.6.1	Evidence for jet-ISM interaction in UGC 05771	77
3.6.2	How extended is the radio source?	78
3.6.3	Are the jets inducing negative feedback in UGC 05771?	79
3.6.4	Constraining the parameters of the ISM density distribution	80
3.7	Conclusion	81
4	Unravelling the enigmatic ISM conditions in Minkowski's Object	85
4.1	Introduction	86
4.2	Minkowski's Object	87
4.3	Abell 194 and NGC 541	87
4.3.1	Properties of the radio jet	88
4.4	Observations and data reduction	90
4.4.1	Data reduction	91
4.5	Stellar population analysis	94
4.6	Emission line gas	98
4.6.1	Emission line fitting	98
4.6.2	Kinematics and morphology	98
4.6.3	Reddening	98
4.6.4	Electron density	100
4.6.5	Excitation mechanism	100
4.6.6	Star formation rate	109
4.6.7	Metallicity and ionisation parameter	109
4.7	Possible explanations for the metallicity variation	110
4.7.1	Enrichment from star formation	110
4.7.2	An enriched jet-driven outflow from NGC 541	112
4.7.3	Pre-existing enriched gas in the stellar bridge	112
4.8	On the formation of Minkowski's Object	113
4.9	Conclusion	115

5	Conclusions and summary	117
5.1	Jets blowing bubbles in the young radio galaxy 4C 31.04	117
5.2	Searching for signs of jet-driven feedback in the radio galaxy UGC 05771	118
5.3	Unravelling the enigmatic ISM conditions in Minkowski's Object . . .	118
5.4	Future work	119
5.4.1	Jet-ISM interactions in large samples of compact radio galaxies	119
5.4.2	Sub-kpc scale jet-driven feedback at high redshift	120
5.4.3	Further investigation of the ISM conditions in Minkowski's Object	121
5.5	Summary and final remarks	121
6	Appendix	123
A	UGC 05771: the morphology of the radio source	123
B	UGC 05771: ruling out beam smearing	126
C	Minkowski's Object: additional PPXF fits	128
D	Minkowski's Object: estimation of shock velocities	132
E	Minkowski's Object: additional metallicity diagnostics	134
	Bibliography	137

1

Introduction

When the Traveler left Harmony, it made a monument out of the black hole's polar jet. In the jet there is a hollow mast which sings in radiance... It towers above this star system like a monument to treason. It beams with silver light. It sings a radio lullaby, made of soothing lies.

Oryx, the Taken King, *Destiny*

The properties of galaxies in our Universe are shaped by complex processes occurring across cosmic time. Some of the most important processes are believed to be driven by the supermassive black hole that resides in the centre of each galaxy.

Most galaxies are predicted to have experienced a phase in which the supermassive black hole was accreting dust and gas from its surroundings, like water swirling around a plughole, feeding and growing. During this period, the nucleus of such a galaxy is known as an active galactic nucleus (AGN).

The extreme conditions arising from the immense gravitational pull of the black hole give rise to a plethora of high-energy phenomena. The disc of accreting material can emit enormous amounts of electromagnetic radiation at all wavelengths, outshining the combined light of every star in the galaxy. Many AGN also exhibit collimated structures that emit very strongly at radio wavelengths. These structures, known as *jets*, are thought to be streams of charged particles from the accretion disc that have been accelerated to relativistic speeds by the intense magnetic fields in the vicinity of the black hole.

Through these mechanisms, the supermassive black hole can have a tremendous impact upon the stars and gas in the host galaxy at distances far greater than the scale of its gravitational influence. However, although AGN have been an alluring topic of study for astrophysicists for many decades, the impact that a period of AGN activity has upon the properties of its host galaxy is still poorly understood. In

particular, the role that jets play in the context of galaxy evolution remains shrouded in mystery. In this thesis, I use spatially resolved spectroscopic observations of local galaxies to shed light on feedback processes taking place in and around the host galaxies of AGN with jets.

Here, I provide key background information relevant to the work presented in this thesis. I introduce radio galaxies, before discussing our current understanding of jet-driven feedback processes gleaned from both theoretical and observational studies. Finally, I give an overview of integral field spectroscopy and other techniques used to analyse the observational data presented in this thesis, before giving a roadmap of the thesis.

1.1 Radio galaxies

The first confirmed extragalactic source of radio-frequency radiation was discovered by Walter Baade and Rudolph Minkowski, when the pair used the Hale 200 inch telescope to find an optical counterpart for the bright radio emission observed in the Cygnus constellation (Baade & Minkowski 1954). This led to the identification of the archetypal radio galaxy Cygnus A (Fig. 1.1), a massive structure, hundreds of kpc in length, that glows at radio wavelengths.

The astronomers of the era struggled to explain the source of the radio emission. The initial explanation put forth by Baade and Minkowski was that the radio-frequency radiation was converted from kinetic energy generated by a collision between two galaxies. Other theories for the energy source included the collapse of a supergiant star, matter-antimatter annihilations and chain reactions of supernova explosions occurring near the centres of these radio-loud galaxies (Robinson et al. 1965).

Today, it is accepted that the radio emission is emitted by *relativistic jets*. Jets are streams of plasma launched from the vicinity of an accreting supermassive black hole, which is known as an active galactic nucleus (AGN). Although the launching

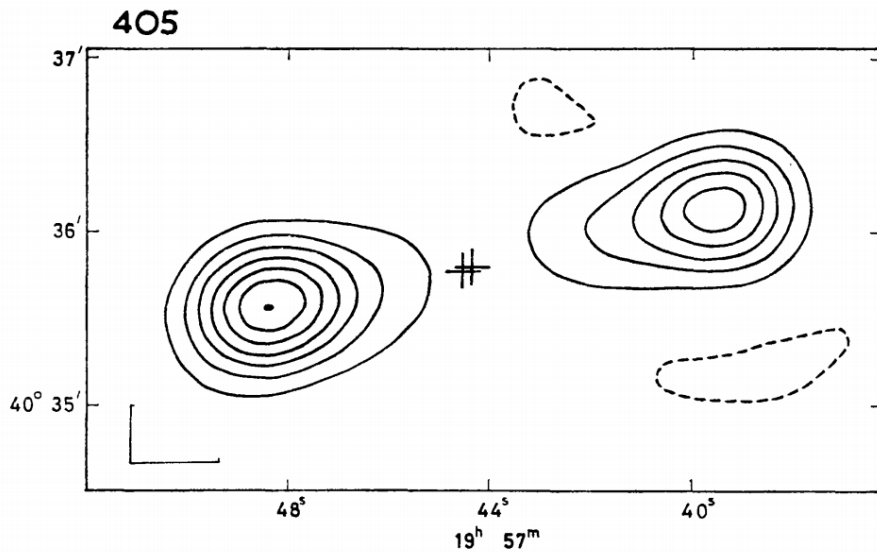


Figure 1.1: An early interferometric radio observation at 1407 MHz of the radio galaxy Cygnus A (MacDonald et al. 1968), one of the first radio sources to be associated with an extragalactic object.

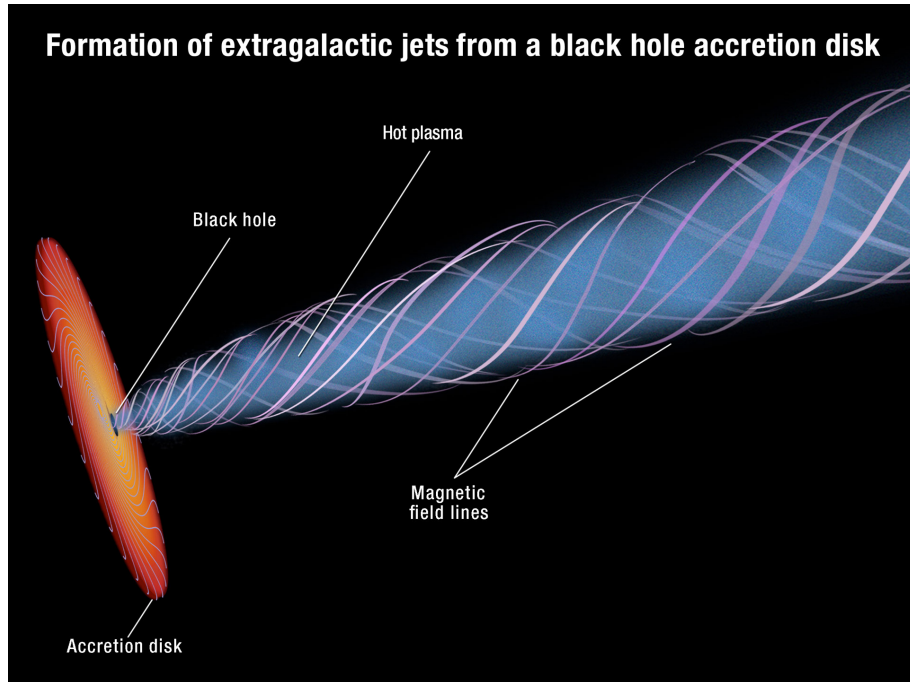
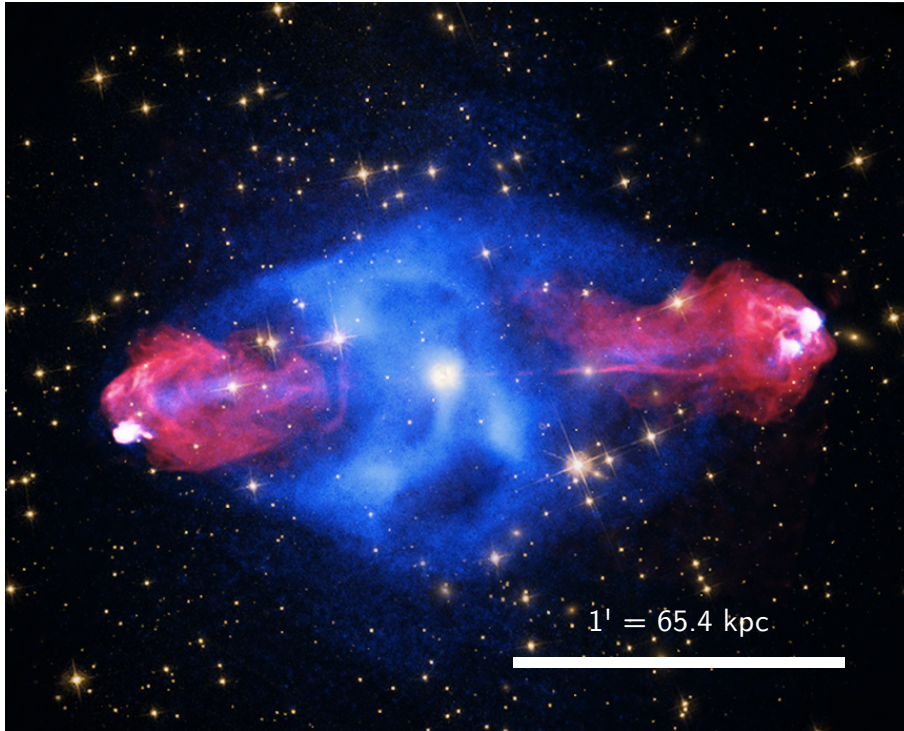


Figure 1.2: A diagram showing the formation of a jet from an accretion disc. Note that only one jet is shown in the diagram; in reality jets are thought to form as bipolar pairs. *Credit: NASA, ESA, and A. Feild (STScI). Available: <https://www.spacetelescope.org/images/opo1332b/>*

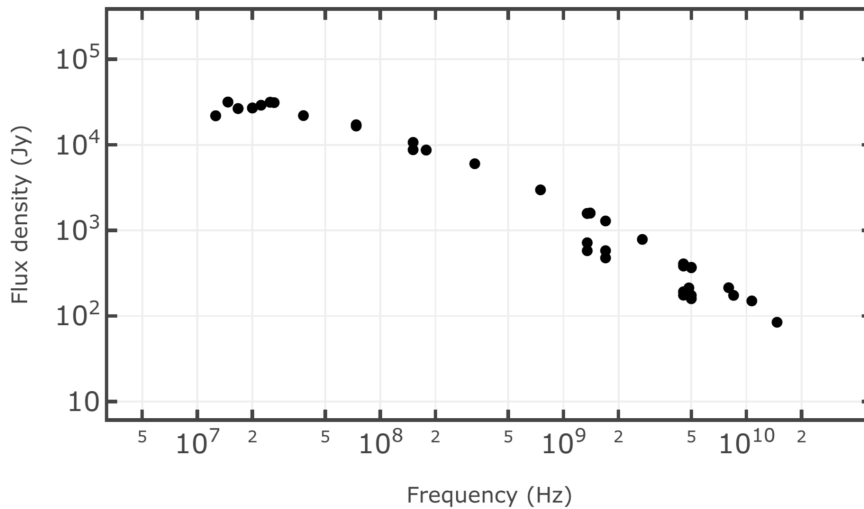
mechanism of jets is still debated (as detailed in the review by Blandford et al. 2019), it is currently thought that the rapid orbital velocities of charged particles in the accretion disc cause magnetic field lines to become tangled and warped, accelerating hot plasma to relativistic speeds and forming bipolar, collimated jets, as illustrated in Fig. 1.2.

The charged particles in the jet plasma interact with the ambient magnetic field and emit synchrotron radiation that is detectable at radio wavelengths. The intrinsic spectrum of the radio plasma is determined by the energy distribution of electrons in the plasma, $P(E)$, which typically follows a steep power law due to Fermi acceleration (Rybicki & Lightman 1979). Electrons lose energy as they emit synchrotron radiation at a rate proportional to E^2 , meaning that the highest-energy electrons—which also emit at the highest frequencies—decay the fastest. This leads to a characteristic steepening of the radio spectrum at high frequencies, which can in turn be used to estimate the age of the radio source. Extended radio sources such as Cygnus A (Fig. 1.3a) tend to have steep spectra due to their advanced ages (Fig. 1.3b).

Jets vary widely in their morphological and spectral properties. Devised by Fanaroff & Riley (1974), FR I- and FR II-type radio galaxies are the two main classes of radio galaxy with extended jets, and differ by the morphology of the radio emission. FR II sources are characterised by jets that end in well-defined lobes, with relatively little emission along the jet axis; Cygnus A is an example of an FR II source. The jets of FR I sources, on the other hand, have ribbon-like morphologies that decrease in brightness as they propagate further away from the host galaxy, forming meandering structures with poorly-defined end points. The jets in FR I and FR II sources have typically propagated far beyond the confines of their host galaxy, an indication that they have been ‘switched on’ for hundreds of Myr (Shulevski et al. 2019). In some



(a)



(b)

Figure 1.3: A modern view of the radio galaxy Cygnus A. In (a) the radio emission is indicated in pink, the X-ray emission in blue and the optical emission in yellow (*Credit: X-ray: NASA/CXC/SAO; Optical: NASA/STScI; Radio: NSF/NRAO/AUI/VLA; available: <https://apod.nasa.gov/apod/ap150124.html>*). The radio spectrum (b) follows a power law, as is typical for extended radio galaxies (*Credit: The NASA/IPAC Extragalactic Database**).

cases, these sources can grow as large as several Mpc, spanning several degrees in the sky (Willis et al. 1974; Banfield et al. 2016; Dabhade et al. 2017). It is common for the jets in these sources to be asymmetric or bent, which is believed to be due to interactions with their environment (e.g., Sakelliou et al. 2008; Rodman et al. 2019; Moravec et al. 2019).

*The NASA/IPAC Extragalactic Database (NED) is funded by the National Aeronautics and

Extended jets may also appear to be compact due to orientation effects. If the jets are oriented within a few degrees of the line of sight, the radio source will appear to be compact, and only one jet will be visible due to relativistic effects. These sources also display high flux variability and may appear to have superluminal expansion speeds. These *beamed* sources are not to be confused with intrinsically compact radio sources, which are discussed below.

Although not as photogenic as FRI- or FRII-type sources, at the other end of the size scale are *compact radio galaxies*. With radio morphologies less than ~ 10 kpc in extent, these are galaxies with jets that are still confined to the interstellar medium (ISM) of their host galaxy and are possibly very young. In Chapters 2 and 3, I focus on two types of compact radio galaxies: Gigahertz Peak Spectrum (GPS) and Compact Steep Spectrum (CSS) sources. GPS and CSS sources are characterised by their peaked radio spectra, where the spectral turnover occurs at frequencies from 1 – 10 GHz in GPS sources and $\lesssim 500$ MHz in CSS sources (see O’Dea 1998, for an in-depth review).

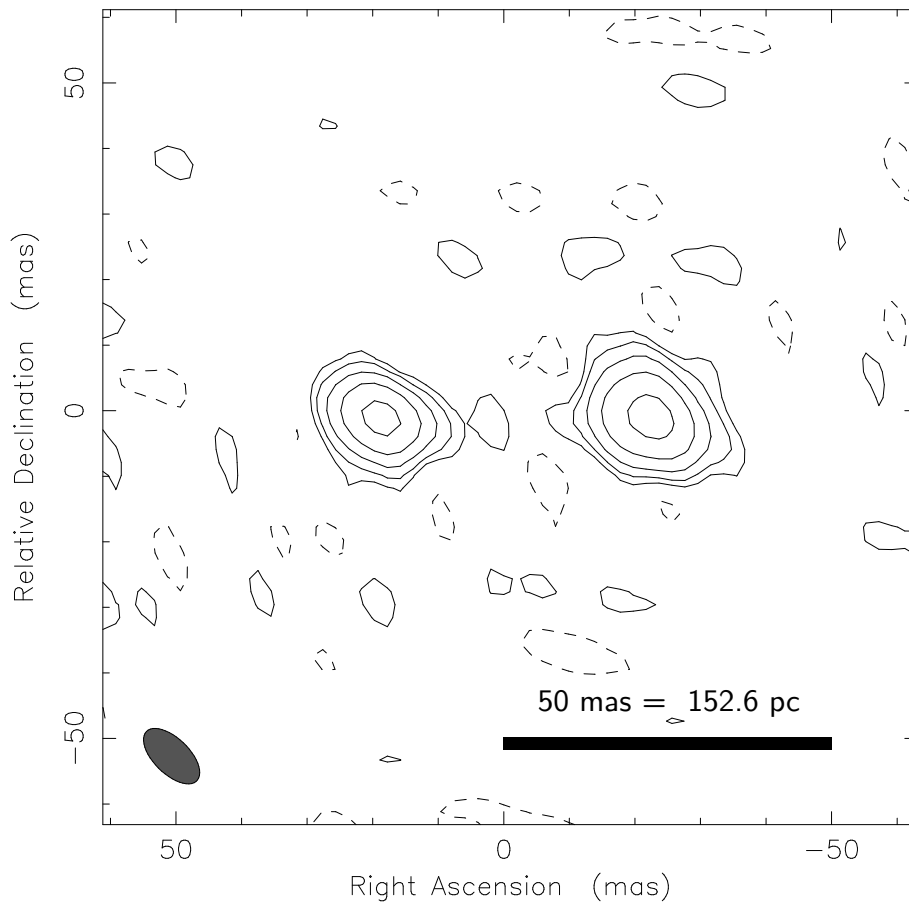
Fig. 1.4a shows the morphology of the archetypal GPS source PKS 1934–638 at $z = 0.18$. The termination points of the jets—separated by approximately 130 pc—are the two ‘hot spots’ visible in the radio image, and are a result of strong interactions between the jet plasma and the ISM. Other common morphological features of GPS and CSS sources include bright radio emission along the jet axis, and unresolved emission located at the core of the host galaxy. It is also common for compact radio galaxies to have asymmetric radio morphologies due to inhomogeneities in the ISM.

There are two absorption mechanisms that may contribute to the spectral turnover in GPS and CSS sources: free-free absorption (FFA) and synchrotron self-absorption (SSA). Both FFA and SSA alone can cause a spectral turnover, and it is most likely that both FFA and SSA contribute in some way. However, recent observations (e.g., Callingham et al. 2017; Keim et al. 2019) and theoretical studies (Bicknell et al. 2018) indicate that FFA may be the dominant absorption mechanism in GPS and CSS sources, although this is still debated (e.g., Collier et al. 2018).

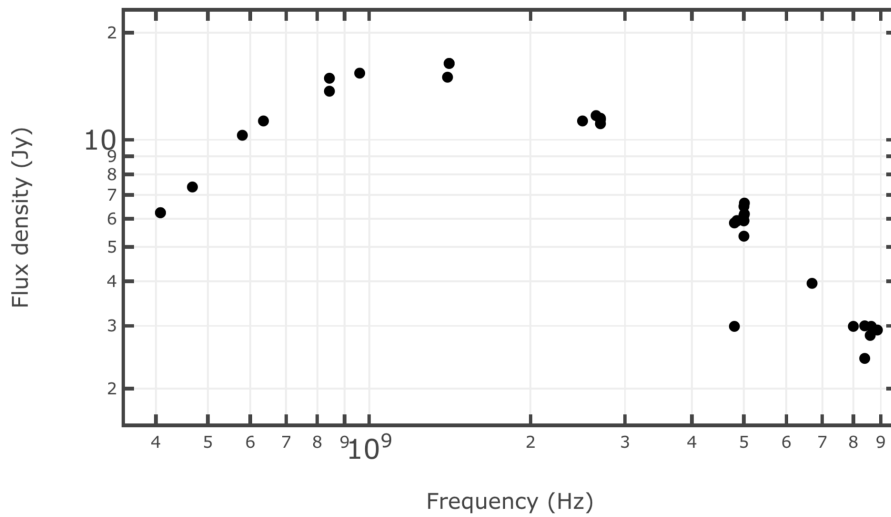
There are two hypotheses for the compactness of GPS and CSS sources: the ‘frustration’ and the ‘youth’ hypotheses. Age estimates of GPS and CSS sources inferred from lobe expansion velocities and synchrotron spectral decay yield ages ranging from $10^2 - 10^5$ yr (Murgia 2003), suggesting many are compact simply because they are young, thereby representing an early evolutionary stage of extended radio galaxies. However, the relatively small number counts of extended radio galaxies in comparison to the number of GPS and CSS sources suggests that not all will evolve into FRI- and FRII-type radio galaxies (An & Baan 2012). Perpetually compact GPS and CSS sources are thought to be ‘frustrated’, with jets insufficiently powerful to escape the host galaxy’s dense ISM, thus permanently remaining ‘trapped’.

1.2 The evolution of young radio galaxies: predictions from hydrodynamical simulations

Hydrodynamical simulations are a valuable tool for enhancing our understanding of the evolution of radio galaxies, as they enable us to explore the ways in which



(a)



(b)

Figure 1.4: The GPS source PKS 1934–638, which harbours extremely compact jets only several milliarcseconds in extent, corresponding to a size of approximately 130 pc. The morphology of the radio source, adapted from Tzioumis et al. (2010), is shown in (a). The radio spectrum (b) follows a power law at high frequencies, but has a distinct turnover at approximately 1 GHz, which is characteristic of compact radio sources (*Credit: The NASA/IPAC Extragalactic Database*).

the properties of the jets and their environment affect both the host galaxy and the morphology of the radio source. They also provide a detailed view into jet-ISM interactions on scales far smaller than can be probed at any wavelength, even with the world's largest telescopes. At the most basic level, these simulations involve a jet consisting of low-density, high-temperature fluid propagating through an ambient medium that is designed to replicate ISM conditions in radio galaxies.

Realistically modelling the environment is key: whilst many of the first simulations of jet evolution modelled the ISM as having a uniform (e.g., Krause 2003) or a smooth, radially-varying density profile (e.g., Carvalho & O'Dea 2002), the asymmetric morphologies of many compact radio sources indicate that the ISM in real galaxies is in fact inhomogeneous and turbulent. Contemporary simulations adopt more realistic ISM density distributions, one of which is the *log-normal density distribution*. The log-normal distribution has a probability distribution function (PDF) (e.g., Sutherland & Bicknell 2007)

$$P(n) = \frac{1}{\sqrt{2\pi}s} \exp \left[-\frac{(\ln n - m)^2}{2s^2} \right] \quad (1.1)$$

where n is the density, m is the natural logarithm of the mean density and s is the standard deviation in $\ln n$. In contrast to simple power-law density profiles, the log-normal distribution gives rise to a clumpy and inhomogeneous medium. Another advantage of the log-normal distribution is that it is physically motivated. In an isothermal medium, turbulence creates cascading eddies which drive hydrodynamical shocks into the ISM. The turbulent cascade locally enhances n in a multiplicative fashion, corresponding to an additive process in $\ln n$, resulting in a Gaussian PDF in $\ln n$ via the central limit theorem (e.g., Nordlund & Padoan 1999).

Three-dimensional simulations by Sutherland & Bicknell (2007) of a jet propagating through a turbulent, inhomogeneous medium demonstrated that the distribution of the ISM has a profound impact on the way that the radio source evolves, which can be divided into four distinct stages:

1. **The flood-and-channel phase (Fig. 1.5a).** As the jet begins to emerge from the vicinity of the nucleus, it is deflected by dense clumps in the ISM. The plasma splits, dividing into many different streams that propagate over a large solid angle. The streams follow paths of least resistance through the ISM, accelerating clouds outwards in the process.
2. **The energy-driven bubble phase (Fig. 1.5b).** The plasma streams combine and form a quasi-spherical bubble, which drives a shock into the ISM, accelerating material outwards. In this phase, the main stream of plasma emerging directly from the nucleus may become temporarily 'stuck' behind particularly dense clouds, and emits very brightly at radio wavelengths due to strong interactions with the surrounding medium. Meanwhile, the bubble inflated by the secondary streams can continue to expand relatively quickly. As a result, the brightest regions of the jet plasma, corresponding to the main stream, are embedded in a much larger region of low-surface brightness plasma filling the bubble.
3. **The jet breakout phase (Fig. 1.5c).** Eventually, the jet clears a path through the ISM, enabling it to accelerate towards the edge of the bubble.

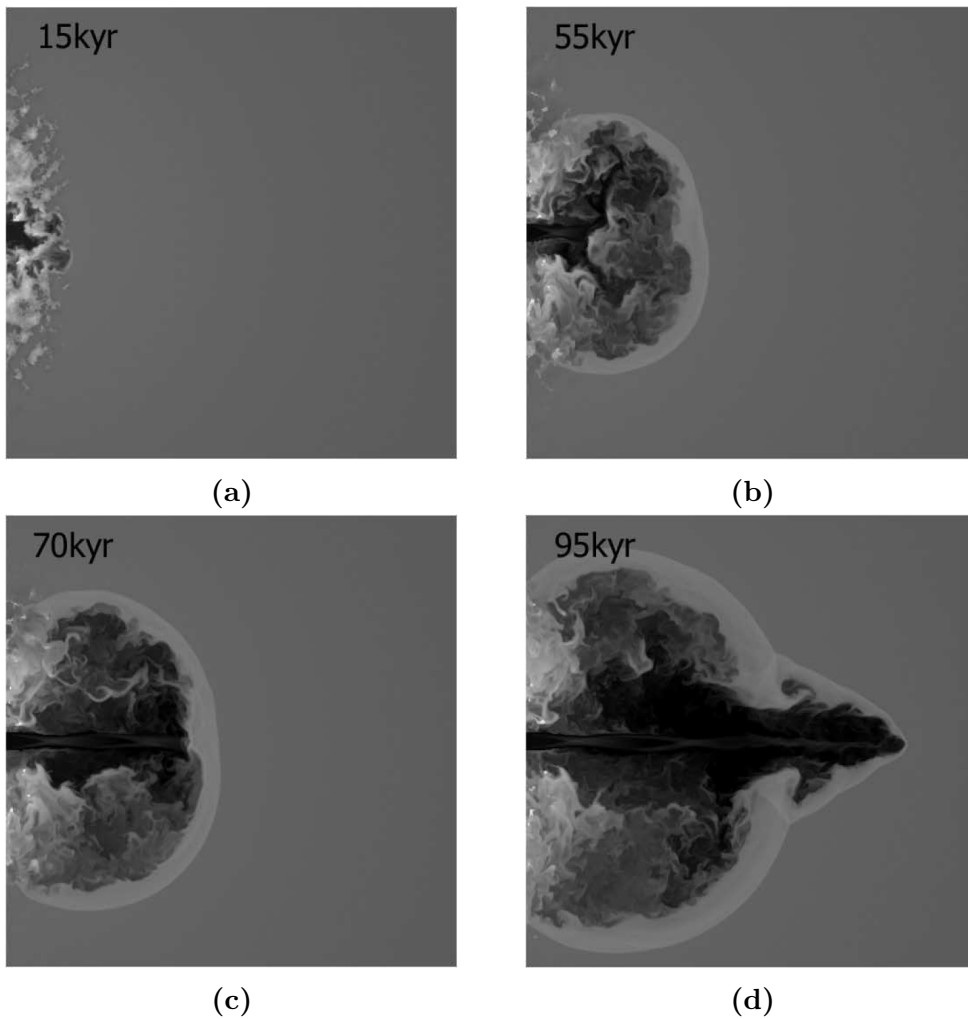


Figure 1.5: Mid-plane slices of a hydrodynamical simulation from Sutherland & Bicknell (2007) taken at different time steps showing (a) the flood-and-channel phase, (b) the energy-driven bubble phase, (c) the jet breakout phase and (d) the ‘classical’ phase. The greyscale indicates density, ranging from $\log(n) = -3.0$ (black) to $\log(n) = 4.0$ (white).

Once the main jet stream reaches the edge of the bubble, it breaks out, and overtakes the bubble, drilling more rapidly through the ISM as the density decreases further away from the nucleus.

4. **The ‘classical’ phase (Fig. 1.5d).** Eventually, the tip of jet escapes the confines of the ISM altogether and can expand freely into space, forming an extended FR I- or FR II-type source.

The jets of compact radio galaxies generally interact much more strongly with the ISM than those in more extended sources, in which the jets have already cleared a path through the ISM, enabling the jet plasma to escape with minimal interference. By contrast, in compact radio galaxies, the jets are still trapped by the ISM, meaning that a much higher percentage of the jet’s momentum is imparted into the surrounding gas, manifesting as hydrodynamical shocks and turbulence over a wide solid angle (Mukherjee et al. 2016; Wagner et al. 2016). These strong interactions between the jets and the ISM in these early stages of evolution mean that compact radio galaxies represent a transitory, yet important, phase, in which the jets influence the evolution of their host galaxy via important *feedback processes*.

1.3 Jet-induced feedback

In the context of galaxy evolution, feedback processes from AGN or star formation are processes that regulate star formation. Through many decades of theoretical and observational studies, it is now known that feedback induced by both jets and radiation-driven winds from AGN accretion discs have played a pivotal role in shaping the observed properties of galaxies across cosmic time, such as *scaling relations* (i.e., widely-observed correlations between galaxy properties such as the $M_{\text{BH}} - \sigma_*$ relation (Ferrarese & Merritt 2000; Gebhardt et al. 2000) and the fundamental plane (Djorgovski & Davis 1987)) and *luminosity functions* (i.e., the comoving number density of galaxies in the Universe as a function of luminosity).

Sub-grid models that accurately account for the effects of AGN feedback are essential ingredients of cosmological simulations if they are to reproduce the observed properties of the Universe. Indeed, simulations that do not include AGN feedback processes over-predict the number of extremely massive star forming galaxies in comparison with observations, suggesting these mechanisms may be responsible for inhibiting star formation in high-mass galaxies, causing the observed break in the galaxy luminosity function (e.g., Croton et al. 2006).

Before feedback can be properly understood, it is important to understand how stars form. In the simplest picture, clouds of gas in the ISM are subject to two forces: (1) internal pressure, arising from random thermal motions of the gas particles, causing the cloud to expand; and (2) the cloud’s self-gravity, which causes the cloud to contract. Under ideal conditions, these two forces are in equilibrium: when the gravitational force overcomes the internal pressure, the cloud will contract, thus increasing the density of the cloud. This in turn increases the temperature and pressure within the cloud, which prevents further collapse. However, interactions between gas particles accelerate the cooling rate of the gas, which in turn decreases the internal pressure, causing the cloud to contract further. If this ‘runaway cooling’ process continues unimpeded, eventually the cloud will become dense enough to ignite hydrogen fusion, and a star is formed.

Observations and theoretical simulations suggest that star formation is far more complex than this simple picture. For example, turbulence and magnetic fields in the ISM are thought to play an important role (Federrath 2015). Moreover, in many astrophysical scenarios these star forming clouds are subject to feedback processes which prevent or enhance star formation. Stellar winds, supernova explosions, winds from luminous accretion discs and jets are all known to drive these feedback processes; in the following, I focus on jet-induced feedback processes.

1.3.1 Negative feedback

Negative feedback occurs when star formation is inhibited. As discussed in Section 1.2, hydrodynamical simulations show that as young jets interact with the dense and inhomogeneous ISM, gas clouds become shredded and ablated, forming into filaments that are accelerated outwards (Mukherjee et al. 2016; Wagner et al. 2016). The jet plasma, propagating at speeds exceeding the sound speed in the ambient medium, creates *hydrodynamical shocks*. These shocks drive heat and turbulence into their surroundings, preventing the gas from cooling and collapsing to form stars. As shown in Fig. 1.6, although jets are inherently directional, they create

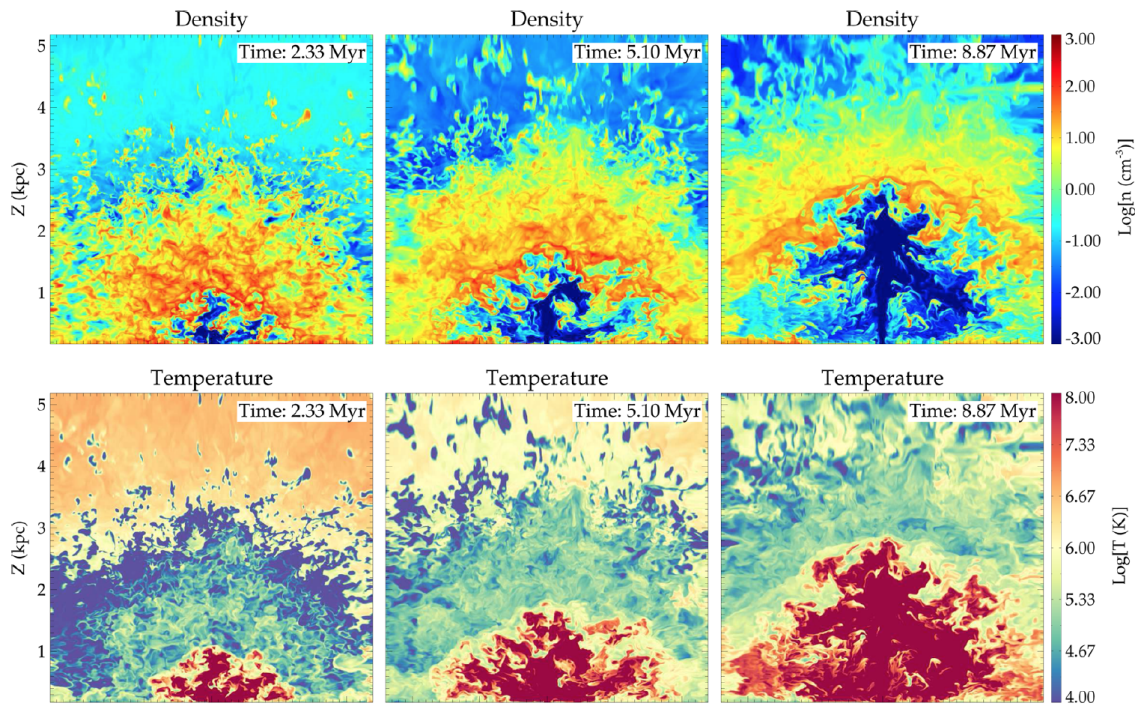


Figure 1.6: Mid-plane density (top) and temperature (bottom) slices from a hydrodynamical simulation from Mukherjee et al. (2016) in which a relatively low-power jet ($P_{\text{jet}} = 10^{43} \text{ erg s}^{-1}$) drives shocks and turbulence into the inhomogeneous ISM, heating the gas and accelerating it outwards.

a quasi-spherical region of influence in the ISM.

Shock signatures are regularly observed in radio galaxies; reservoirs of warm, shock-heated molecular gas are relatively common in low-redshift elliptical galaxies hosting low-luminosity radio AGN (Ogle et al. 2010). In some galaxies, jet-driven shocks have been shown to prevent star formation. For example, despite harbouring a massive reservoir of molecular gas, the nearby radio galaxy 3C 326 N has an extremely low star formation rate due to the continual injection of turbulence from the jets, keeping the gas warm and therefore unable to form stars (Nesvadba et al. 2010, 2011).

Jets may also prevent star formation by regulating the gas content of their host galaxy. Extended jets from radio galaxies in clusters prevent cooling of the intra-cluster medium, in doing so preventing galaxies from accreting additional gas (e.g., McNamara & Nulsen 2012). AGN jets and winds are the only mechanisms that can remove significant amounts of gas from most galaxies (Nesvadba et al. 2006); whilst episodes of intense star formation can generate winds and launch outflows, only in very low-mass galaxies are these outflows able to escape the host galaxy’s potential. In particular, at high redshift, where the relatively gas-rich conditions are believed to have given rise to more powerful AGN, jets may have had the potential to remove up to 50% of the gas from their hosts (Nesvadba et al. 2006). In the local Universe, outflows in ionised, molecular and atomic gas have been observed in both compact (Holt et al. 2008) and extended (Morganti et al. 2005) powerful radio galaxies. Even relatively low-power jets ($\lesssim 10^{44} \text{ erg s}^{-1}$) have been observed to drive multi-phase outflows in the local Universe, e.g., in the nearby galaxies ESO 428–G14 (May et al. 2018) and in HE 1353–1917 (Husemann et al. 2019).

However, in many cases, the majority of material in these outflows has speeds below the escape velocity of the host galaxy’s gravitational potential. This means that most of the gas will eventually rain back down into the system, forming a ‘fountain’ (Nesvadba et al. 2010; Alatalo et al. 2015). Although the gas is not permanently lost from the galaxy, there may be a temporary reduction in the star formation rate due to the loss of gas, and turbulence that arises when the gas ‘rains’ back down into the galaxy (Mukherjee et al. 2016).

1.3.2 Positive feedback

Positive feedback occurs when star formation is triggered by the passage of a jet through a cloud of gas. Fragile et al. (2004) summarise the basic workings of jet-induced star formation as follows. Shocks induced by the jets compress overdense clumps within the cloud, increasing their density, and enhancing the rate of collisional excitation between gas particles. This in turn increases the efficiency with which the gas loses energy via line emission, thus decreasing the temperature, which in turn causes the clump to compress further in order to remain in pressure equilibrium with its surroundings. This leads to the formation of dense filaments of gas, as seen in the bottom panel of Fig. 1.7. Provided that the filaments are able to cool sufficiently rapidly that they are not destroyed by hydrodynamical instabilities, the gas undergoes ‘runaway cooling’: its density increases until it undergoes gravitational collapse, and stars are formed.

There are many variables that influence the likelihood of jet-induced star formation. Whether or not runaway cooling will occur is highly sensitive to both the density of the pre-shocked gas and the speed of the shock (Fragile et al. 2004). Additionally, different configurations of magnetic fields within and outside the cloud can either enhance or prevent cloud collapse (Fragile et al. 2005). The jet properties are also important: jets that are too powerful are more likely to heat and disperse the gas before it has time to cool, instead causing negative feedback. For this reason, FRI jets are thought to be more effective at inducing star formation than FRII jets, which tend to be more energetic: FRI jets tend to have lower Mach numbers and are less likely to induce turbulent heating in the surrounding gas (Fragile et al. 2017). In any given scenario, however, jet-induced shocks are likely to have a distribution of velocities due to inhomogeneities in the ambient medium, resulting in both collapsing and dispersing regions.

Star forming regions embedded within ionised gas filaments along the path of a jet have been observed in both Centaurus A and Minkowski’s Object; this latter object forms the focus of Chapter 4. The origin of the star-forming gas is believed to differ in each source, however. The gas in the jet-induced star forming region of Centaurus A most likely originated from an existing ring of HI orbiting the host galaxy (Crockett et al. 2012; Santoro et al. 2016) (Fig. 1.8a), most likely a remnant of a previous merger between Centaurus A and a neighbouring galaxy. In contrast, all of the neutral gas associated with Minkowski’s Object is located along the path of the jet (Fig. 1.8b), which may be evidence that the jet triggered the condensation of this gas from the intracluster medium (Croft et al. 2006; Lacy et al. 2017). The variations in properties between these two objects demonstrates that positive feedback is a complex process of which our understanding is incomplete.

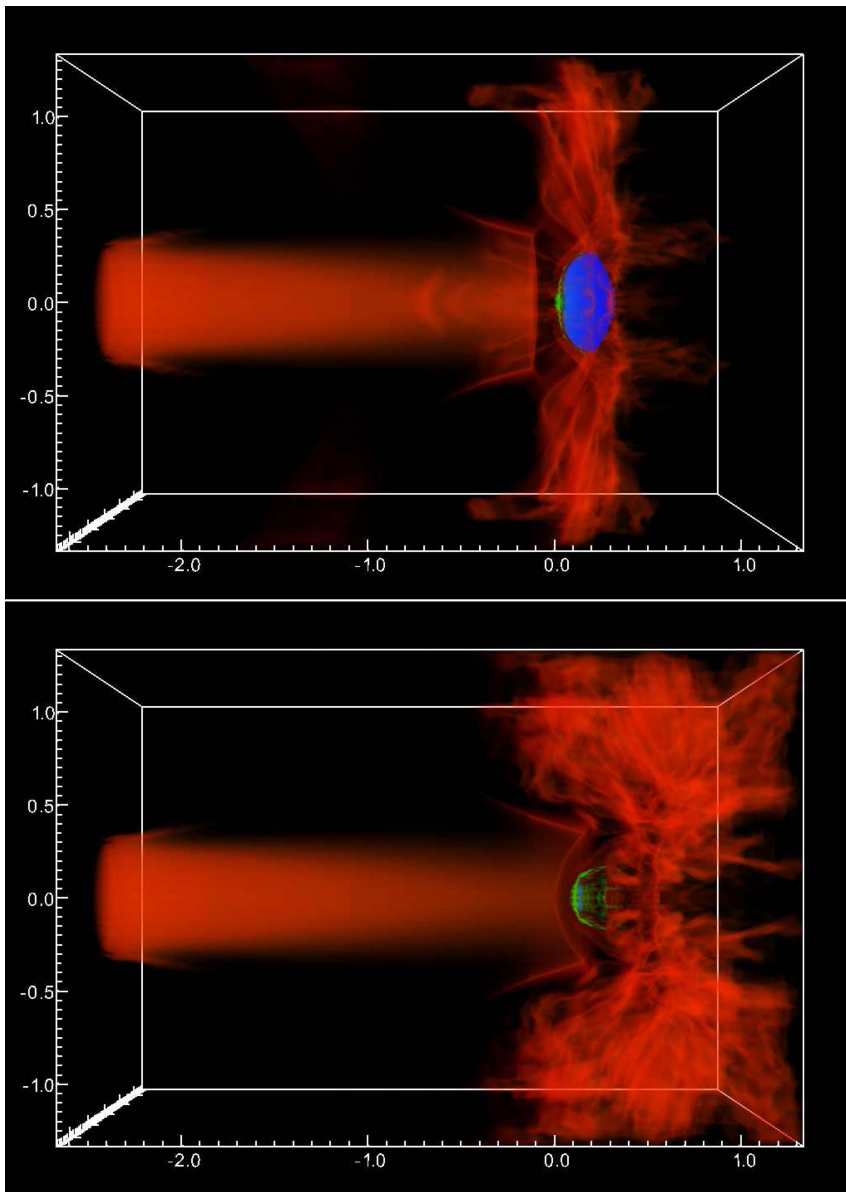


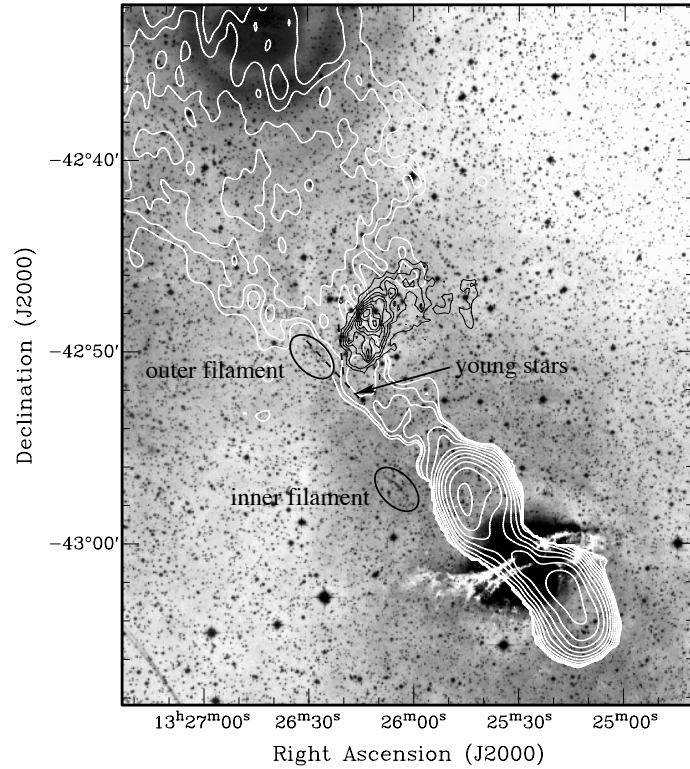
Figure 1.7: Intermediate (top) and final (bottom) snapshots of a hydrodynamical simulation carried out by Fragile et al. (2017) of jet-induced star formation. The jet (red) interacts with the initially atomic gas cloud (blue) which condenses, forming filaments of dense, molecular gas (green). Axes are marked in units of the initial cloud radius.

1.4 Observing jet-induced feedback

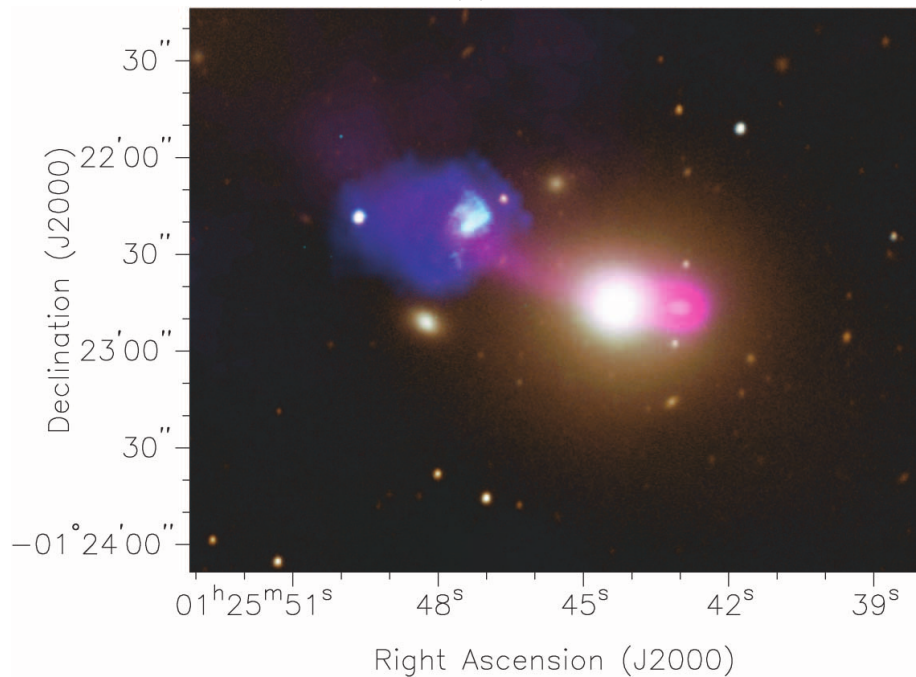
1.4.1 Integral field spectroscopy

The electromagnetic spectrum of a galaxy contains a wealth of information. Absorption features in the continuum can be used to infer the properties of the galaxy's stars, including their chemical composition and the star formation history. Emission lines probe the gas in the interstellar medium, and can be used to estimate properties such as density and temperature, or to determine the excitation mechanism causing the line emission. Meanwhile, the widths and relative shifts of different spectral features reveal the kinematics of the gas and stars.

Although a great deal of information about a galaxy can be obtained from a



(a)



(b)

Figure 1.8: The two best-studied examples of jet-induced star formation in the local Universe. The multi-wavelength image of Centaurus A from Oosterloo & Morganti (2005) is shown in (a), in which the optical image is overlaid by the radio continuum from the jet (white contours) and the H I cloud (black contours). The filaments associated with star formation are also indicated. The multi-wavelength image of Minkowski's Object from Croft et al. (2006) is shown in (b); the optical image (RGB) is overlaid by the radio continuum from the jets of NGC 541 (pink) and the H I (blue). Minkowski's Object is the bright, filamentary structure embedded in the right-hand side of the H I cloud.

single spectrum, multiple spectra extracted from different regions of the galaxy can provide valuable information about its evolutionary history. Emission and absorption features can be used to investigate the dynamics of the gas and stars in the galaxy, and can reveal disrupted kinematics such as inflowing or outflowing gas. Spatially resolved emission line fluxes can reveal variations in the ISM properties across the galaxy, including chemical abundances. Meanwhile, spatially resolved stellar continua enable the star formation history in different regions of the galaxy to be investigated, which may reveal sites of new, or recently quenched, star formation. Crucially, spatially resolved spectroscopy facilitates direct comparison of observations with high-resolution hydrodynamical simulations, enabling these theoretical models to be validated. For these reasons, *integral field spectroscopy* (IFS) is an invaluable tool for studying jet-driven feedback processes.

Integral field spectrographs are instruments that capture spectra simultaneously along multiple lines of sight across the field of view, producing a *data cube*, in which each spatial pixel (*spaxel*) of the image contains a spectrum, as shown in Fig. 1.9. They generally operate in the optical or near-infrared (IR) wavelength ranges, both of which contain key spectral features that can be used to study jet-driven feedback.

Integral field spectrographs comprise an *integral field unit* (IFU), which re-formats the light entering the telescope to enable spectra to be simultaneously captured over a two-dimensional area of the sky. The IFU feeds a spectrograph, which disperses the light to create spectra. There are several different IFU designs used in

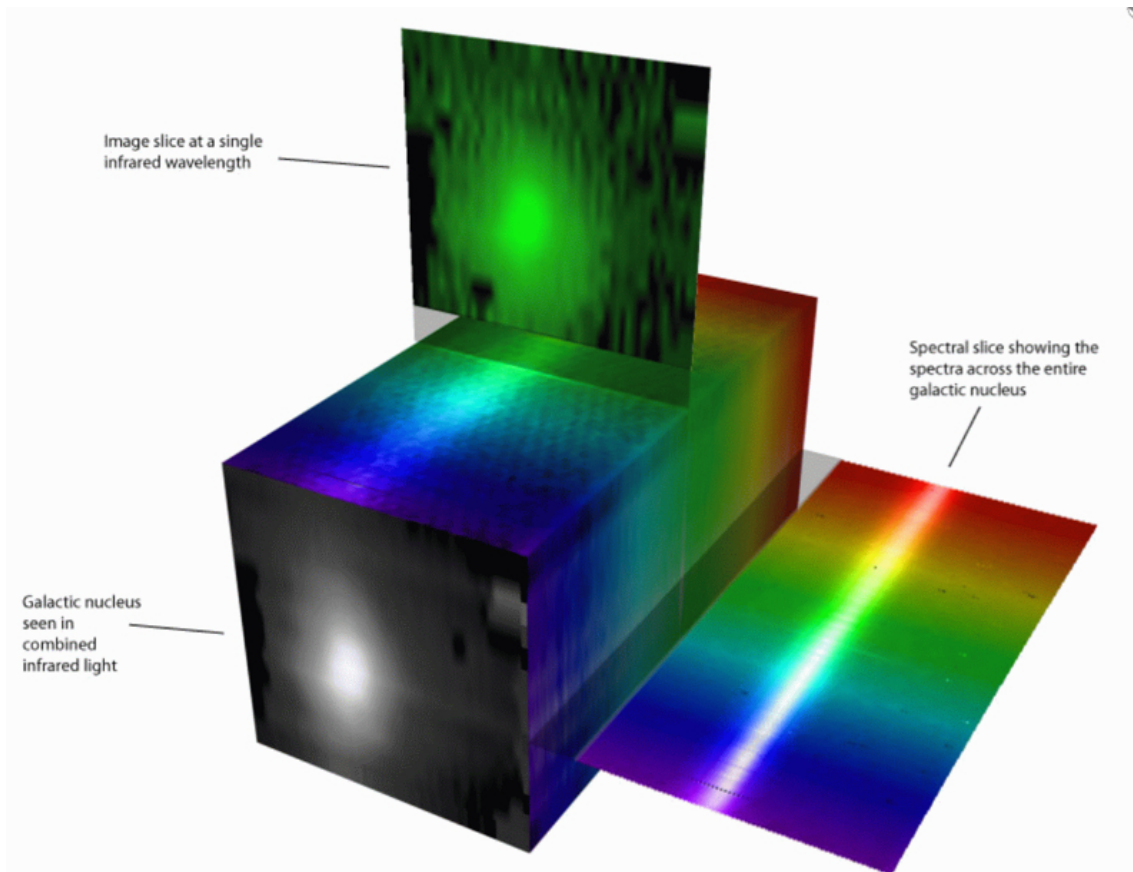


Figure 1.9: A schematic of a data cube. Each slice in the data cube represents an image at a given wavelength. Credit: Stephen Todd (ROE) and Douglas Pierce-Price (JAC); available: <http://ifs.wikidot.com/what-is-ifs>

modern integral field spectrographs. Here I will discuss image slicer, lenslet array and fibre bundle IFUs, all of which were used to obtain the observations presented in this thesis.

In an image slicer IFU, light from the telescope is reflected off an image slicer, a series of tilted mirror segments located at the telescope’s focal plane, which ‘fan out’ slices of the image in different directions. A second set of mirrors reflects the light from each slice such that the slices are arranged end-to-end, as illustrated in Fig. 1.10. The column of slices forms a slit which is directed into a spectrograph, thus forming a spectrum of the object in each slice. As a result of the dispersion, spatial resolution across the slice width is lost. The spatial resolution of the resulting data cube is therefore determined by the number of slices and by the sampling of each slice on the detector along the slice length. WiFeS on the ANU 2.3 m telescope (Dopita et al. 2007, 2010) and NIFS on the Gemini North 8 m telescope (Hart et al. 2003; McGregor et al. 2003) are both image slicer IFUs.

In a lenslet array IFU, the telescope focal plane is re-imaged onto a two-dimensional array of microlenses or lenslets. As shown in Fig. 1.10, each lenslet forms a pupil image at its focus, thus forming a grid of pupil images corresponding to each lenslet in the array. The grid is then passed into the spectrograph, where the pupil images are dispersed and directed onto a detector. To avoid spectra from neighbouring lenslets overlapping one another on the detector, the dispersion axis of the spectrograph must be rotated with respect to the lenslet array. Additionally, because the light is passed into the spectrograph in a grid format, the wavelength coverage must be restricted to avoid spectra from different lenslets overlapping one another. The Spectroscopic Areal Unit for Research on Optical Nebulae (SAURON, Bacon et al. 2001), one of the very first IFUs, is a lenslet array IFU, as is OSIRIS on the Keck 10 m telescope (Larkin et al. 2006).

Fibre-bundle IFUs consist of multiple optical fibres tightly packed together to form a bundle that is placed at the focal plane of the telescope, enabling each fibre to collect light from a different region of the sky. At the other end of the unit, the fibres are rearranged into a line, as illustrated in Fig. 1.10, and the light is directed into a spectrograph, thereby creating spectra from the light collected in each fibre. The relative simplicity of fibre-bundle IFUs compared to lenslet array or image slicer IFUs has enabled the development of instruments with many IFUs. Large galaxy surveys such as SAMI (Bryant et al. 2015; Scott et al. 2018) and MANGA (Bundy et al. 2015) have taken advantage of such instruments to observe multiple galaxies simultaneously. However, both the thickness of the fibre cladding, and the circular cross-section of the fibres, means that a single pointing does not provide spatially contiguous coverage of an object, unlike image slicer or lenslet array IFUs. Spatially contiguous coverage of an object therefore requires multiple dithered exposures, which may be non-trivial to recombine (e.g., Sharp et al. 2015). Alternatively, a lenslet array can be placed in front of the fibre bundle, where the contiguous packing of square or hexagonal lenslets compensates for the gaps between fibres. The PMAS instrument on the Calar Alto Observatory 3.5 m telescope, used to carry out the CALIFA galaxy survey (Sánchez et al. 2012, 2016b), is a lens array-fibre bundle IFU (Roth et al. 2005).

In recent years, integral field spectrographs have become workhorse instruments for studying galaxy evolution, with the advent of large IFU surveys including MANGA, SAMI and CALIFA enabling statistical studies of spatially resolved properties of

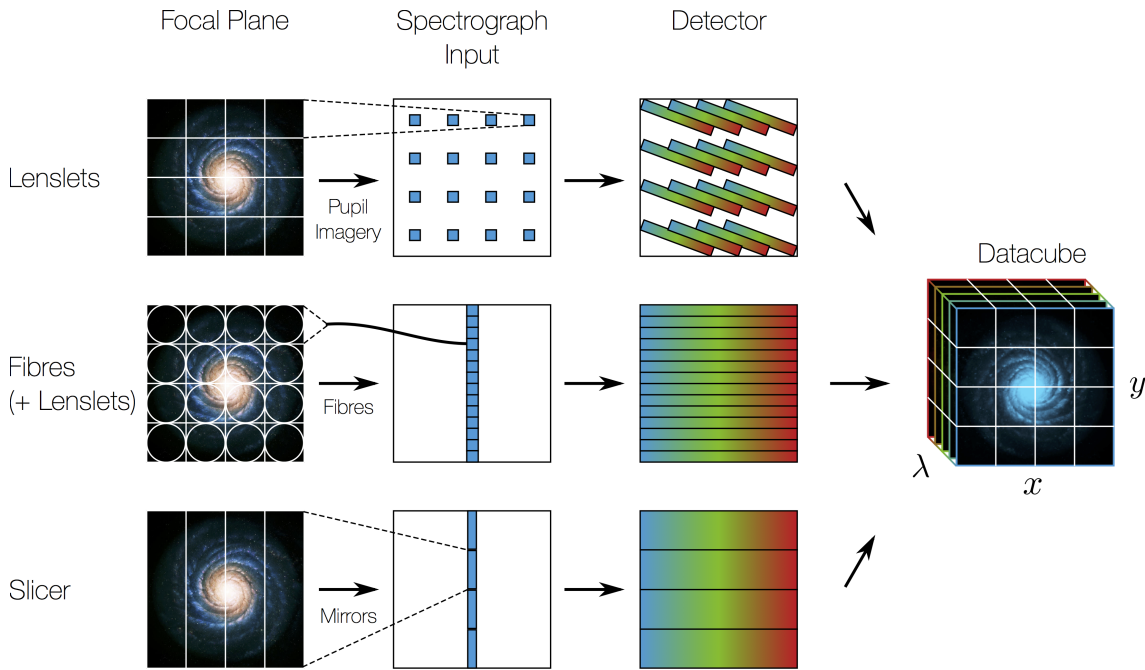


Figure 1.10: A diagram showing the operational principles of lenslet array, fibre-bundle and image slicer IFUs (JWST User Documentation 2016–).

galaxies in the local Universe.

Today, integral field spectrographs on the world’s largest telescopes can achieve sub-arcsecond angular resolution using *adaptive optics*, which are complex optical systems that compensate for the blurring effects of the Earth’s turbulent atmosphere. Through the exquisite angular resolution provided by these instruments, integral field spectrographs enable us to study sub-kpc scale jet-ISM interactions in the local Universe for the first time. IFS thus represents a valuable tool in investigating the importance of jet-driven feedback in galaxy evolution across cosmic time.

In the next few sections, I discuss various parameters that can be inferred by analysing IFS data.

1.4.2 Optical diagnostic diagrams

The flux ratios of various combinations of emission lines can be used to infer the dominant sources of radiation contributing to the line emission in a galaxy, such as young stars, AGN accretion discs and shocks. Because shocks are a key signature of jet-ISM interactions, reliably distinguishing shocks from other forms of excitation is particularly relevant to the work in this thesis.

First proposed by Baldwin et al. (1981) and expanded upon by Veilleux & Osterbrock (1987), the basic idea of an *optical diagnostic diagram* (ODD) is that the process causing the line emission (the *excitation mechanism*) can be inferred from the ratios of different pairs of emission line fluxes.

Examples of commonly-used ODDs are shown in Fig. 1.11. Each axis represents the a ratio of the fluxes of two emission lines, and the resulting parameter space is partitioned into different regions depending on the excitation mechanism. Kewley et al. (2001) and Kauffmann et al. (2003) developed relations that give the maximum $[\text{O III}]\lambda 5007/\text{H}\beta$ ratio for a given $[\text{N II}]\lambda 6583/\text{H}\alpha$, $[\text{S II}]\lambda\lambda 6716, 6731/\text{H}\alpha$

and $[\text{O I}]\lambda 6300/\text{H}\alpha$ ratio that can arise from star formation. $[\text{O III}]\lambda 5007/\text{H}\beta$ ratios in excess of these relations indicate some contribution from a harder radiation field. Seyfert-like and so-called Low Ionisation Nuclear Emission Region (LINER)-like emission both lie beyond the line of maximal star formation, and are separated by the empirical relation of Kewley et al. (2006). Seyfert-like emission arises from a power-law ionising radiation field emitted by a luminous AGN accretion disc, whilst the origin of LINER-like emission remains unclear, although it has been proposed that it is caused by harder ionising radiation fields from low-luminosity AGN, shocks and post-AGB stars. Post-AGB stars are main-sequence stars that have evolved through the asymptotic giant branch, and emit a hard ionising spectrum due to their hot ($\sim 30,000$ K) atmospheres. They exist in any stellar population older than ~ 1 Gyr, and become the dominant ionisation source in regions where star formation has ceased. Although ODDs alone are insufficient to determine the excitation mechanism of gas with LINER-like emission line ratios, the kinematics and spatial distribution of the line emission can be used to break this degeneracy. LINER emission caused by an AGN will be localised to the centre of a galaxy, unlike that from post-AGB stars.

Theoretical shock models can yield line ratios lying in all three regions of the ODDs presented in Fig. 1.11 (e.g., Alatalo et al. 2016; Allen et al. 2008; Rich et al. 2013), meaning that this form of excitation can be impossible to distinguish with these ODDs alone. However, shock excitation generally results in a high velocity dispersion due to the supersonic velocities of the gas. In particular, a clear signature of shock excitation is a localised increase in the velocity dispersion of the gas compared to that of the stars (Belfiore et al. 2016).

1.4.3 Metallicity diagnostics

The gas-phase abundance of elements more massive than helium, also known as the *metallicity*, contains valuable information about the dynamical and star formation history of a galaxy. Stars expel metals into their surroundings via winds and supernova explosions, whilst interactions with other galaxies can drive flows of metal-rich or metal-poor gas into a galaxy. Jets are also able to drive outflows of enriched gas over large distances (Kirkpatrick et al. 2009, 2011), which may be visible as a local enhancement in the metallicity.

Because oxygen is the most abundant element other than hydrogen and helium in the Universe by mass, metallicity is usually expressed as the relative abundance of oxygen to hydrogen, $\log(\text{O}/\text{H}) + 12^\dagger$.

Metals are important coolants in the ISM. Collisionally excited atoms radiate energy away via line emission, in doing so lowering the electron temperature, which can therefore be used to estimate the metallicity (the ‘direct method’). However, temperature-sensitive lines such as $[\text{O III}]\lambda 4363$ are very faint and difficult to observe in most objects (Kewley et al. 2019a). Alternatively, the metallicity can be estimated using ratios of strong emission lines that are sensitive to gas-phase abundances. These *metallicity diagnostics* are derived using stellar population synthesis models

[†]The added value of 12 is simply a convention, and was chosen because even the least abundant elements in the sun (which have abundances $\log(\text{X}/\text{H}) = -12$) will have an abundance greater than zero using this definition, thus making it easier to compute abundances in computers with limited memory (David Nicholls, *priv. comm.*).

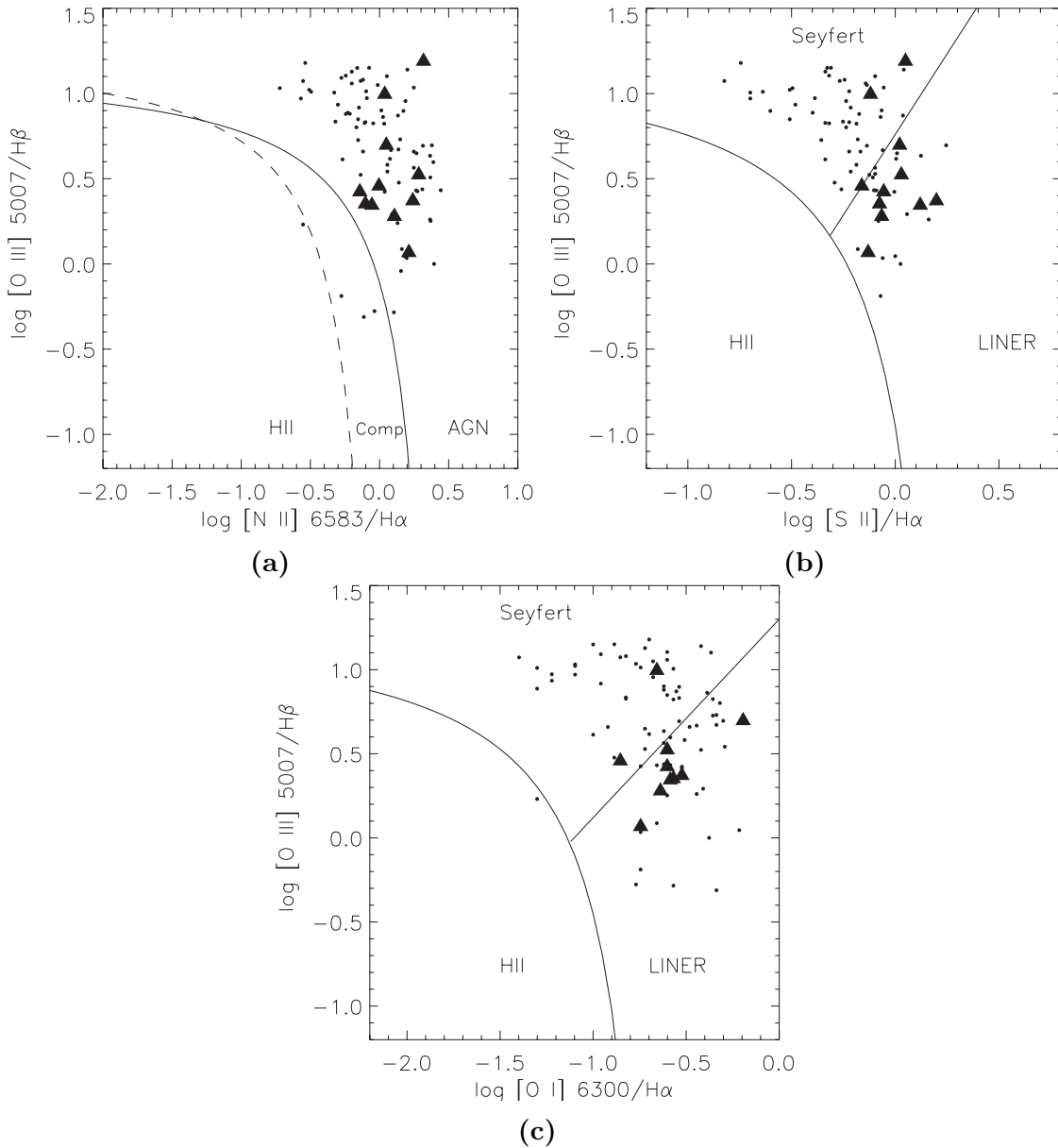


Figure 1.11: ODDs from Ogle et al. (2010). The curved dashed and solid lines of Kauffmann et al. (2003) and Kewley et al. (2001) respectively separate excitation from star-formation (below) and more energetic radiation fields (above). The solid diagonal line is that of Kewley et al. (2006), which separates Seyfert- and LINER-like emission line ratios. Each point represents a radio galaxy. Many lie in the LINER region, implying either low-luminosity AGN, evolved stars or shocks are the dominant excitation mechanism.

to calculate the ionising spectrum, in conjunction with theoretical photoionisation models produced using programs such as MAPPINGS (Sutherland et al. 2018), to generate synthetic emission-line spectra. Commonly used diagnostics include N2O2 ($[N II]\lambda 6583/[O II]\lambda\lambda 3726, 3729$) and R23 ($([O II]\lambda 3726 + [O III]\lambda\lambda 4959, 5007)/H\beta$).

Care must be taken when interpreting metallicities estimated using these diagnostics, for a number of reasons:

- Applied to the same object, different diagnostics can yield metallicities with systematic offsets of up to 0.7 dex (Kewley & Ellison 2008).
- Most are only valid over certain metallicity ranges, and some line ratios are

two-valued as a function of $\log(\text{O}/\text{H}) + 12$.

- The models used to produce metallicity diagnostics generally only include stellar radiation fields, and therefore may not yield accurate results when other sources of ionisation are present, such as the harder radiation fields produced by AGN or shocks (e.g., Kewley & Ellison 2008).
- Many diagnostics are highly sensitive to the *ionisation parameter* q , which is the ionising photon flux per unit density of hydrogen atoms (also expressed as the *dimensionless ionisation parameter* $\mathcal{U} = q/c$). For a diagnostic to yield an accurate result, $\log(\mathcal{U})$ must be known; in this case, the metallicity and ionisation parameter should be solved for in an iterative fashion to ensure they are consistent with one another (Kewley & Dopita 2002).

1.4.4 Measuring the star formation rate

Accurately estimating the star formation rate (SFR) in a galaxy is central to any study of feedback. It is therefore essential to understand the caveats and limitations of the various ways in which SFRs can be estimated.

Stars emit ultraviolet (UV) radiation that ionises neutral hydrogen. Hydrogen ions recombine with free electrons before radiatively de-exciting, emitting an $\text{H}\alpha$ photon in roughly 50% of recombinations. Only stars more massive than $\sim 20 M_{\odot}$ (i.e., O- and some B-type stars) emit enough ionising radiation to produce measurable $\text{H}\alpha$ emission (Calzetti 2013); these are also the most short-lived stars, enabling $\text{H}\alpha$ to be used as a tracer of the instantaneous SFR. For a star of fixed luminosity, the total $\text{H}\alpha$ flux is the same regardless of the ISM density (Dopita & Sutherland 2003). Therefore, assuming a stellar mass distribution, i.e. an *initial mass function* (IMF), the total number of stars can be inferred from the measured $\text{H}\alpha$ luminosity. Other hydrogen recombination lines such as $\text{Br}\gamma$ can also be used.

There are several caveats associated with using H I recombination lines as SFR indicators. The assumption of a particular IMF introduces a systematic uncertainty. Additionally, absorption and scattering of photons by interstellar dust lowers the line flux; correcting for this extinction is model-dependent and has its own systematic uncertainties. In galaxies hosting jets, perhaps the biggest caveat of using these lines as a SFR indicators is that emission can also arise from shocks and by photoionisation from the AGxN, in which case the SFR represents a strict upper limit.

The SFR can also be estimated by directly measuring the ionising photon flux of hot, massive stars. Like $\text{H}\alpha$ -based SFR estimates, UV SFRs are subject to a number of systematic uncertainties. Dust absorbs and scatters UV light much more strongly than $\text{H}\alpha$; moreover, both post-AGB stars (Singh et al. 2013; Belfiore et al. 2016), found in old stellar populations, and AGN accretion discs can emit strongly in the UV, contaminating the SFR estimate.

1.4.5 The Kennicutt-Schmidt relation

A typical method of determining whether positive or negative feedback is taking place is to compare the observed SFR to that expected given the amount of gas available using the Kennicutt-Schmidt (KS) relation. The KS relation is an empirical relation between the projected molecular gas mass surface density Σ_{gas} in $M_{\odot} \text{pc}^{-2}$

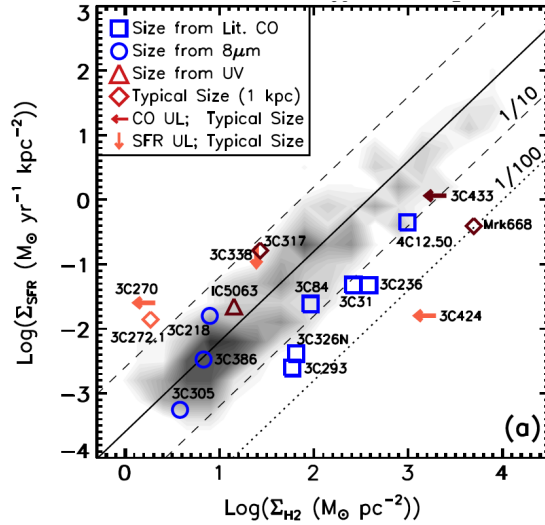


Figure 1.12: Kennicutt-Schmidt relation diagram of Lanz et al. (2016) which shows the original KS relation (solid black line). The coloured points indicate radio galaxies, most of which sit below the KS relation, suggesting that the jets may be inhibiting star formation. The grey contours indicate galaxies that do not host radio sources.

and the star formation rate surface density Σ_* in $M_\odot \text{ yr}^{-1} \text{ kpc}^{-2}$. The relation has the form of a power law, $\Sigma_* = A \Sigma_{\text{gas}}^N$ (Schmidt 1959; Kennicutt 1998).

The original KS law together with the sample of galaxies of Kennicutt (1998) is shown in Fig. 1.12. Whilst this simple relation holds for many galaxies, the large amount of scatter in the relation implies that the star formation rate is influenced by factors other than the surface density of molecular gas. Indeed, more sophisticated star formation relations have been developed in recent years, which account for variables such as the free-fall time, magnetic fields and turbulence which reduce the scatter present in the original KS relation (e.g., Krumholz et al. 2012; Salim et al. 2015). None the less, the original KS relation is still frequently used as a basic test of whether feedback is occurring (e.g., Lanz et al. 2016).

Whilst SFR surface density is generally easily measured using a calibrator as discussed in 1.4.4, accurately estimating Σ_{gas} is more difficult. H_2 is essentially impossible to observe at low temperatures due to its lack of a dipole moment. Instead, the gas mass surface density is usually estimated using an emission line from a tracer of dense gas with a dipole moment, such as $^{12}\text{CO}(1-0)$. The line intensity is then converted to a total molecular gas mass using a conversion factor α_{CO} , which depends on the gas-phase metallicity. α_{CO} is generally very difficult to estimate in galaxies other than our own; hence in most cases, the Milky Way value is assumed, which may introduce significant systematic uncertainties in Σ_{gas} .

1.5 Thesis overview

Chapters 2, 3 and 4 of this thesis comprise journal articles, each of which represent a major portion of the work carried out as part of the candidature, as follows:

- Chapter 2 comprises my first refereed study (Zovaro et al. 2019a) as it appeared in The Monthly Notices of the Royal Astronomical Society (MNRAS), in which

I present Gemini/NIFS observations of the CSS source 4C 31.04 which reveal strong jet-ISM interactions on sub-kpc scales in the host galaxy.

- Chapter 3 comprises my second refereed study (Zovaro et al. 2019b), also published in MNRAS, in which I used Keck/OSIRIS to observe the CSS source UGC 05771 to investigate jet-ISM interactions. I also used additional multi-wavelength data including IFS from the CALIFA survey and CO observations to search for signatures of jet-induced negative feedback in the host galaxy.
- Chapter 4 comprises my third and final study, in the late stages of preparation for submission to a peer-reviewed journal. In this paper, I present IFS observations of Minkowski’s Object from the WiFeS instrument on the ANU 2.3 m telescope, revealing ISM conditions that reflect the object’s unusual origin.

Finally, in Chapter 5, I provide a summary of each paper, and discuss potential avenues for future research.

2

Jets blowing bubbles in the young radio galaxy 4C 31.04

Every day, she saw planets and comets and stellar nurseries right up close, plain as weather. Yet, there was something about being planetside that made it feel different. Perhaps stars were supposed to be viewed from the ground.

Becky Chambers

This chapter presents the content of the article *Jets blowing bubbles in the young radio galaxy 4C 31.04* (Zovaro et al. 2019a) as published in The Monthly Notices of the Royal Astronomical Society. The paper is reproduced here in full with minor formatting changes to make it consistent with the rest of the work in this thesis.

Abstract

We report the discovery of shocked molecular and ionised gas resulting from jet-driven feedback in the low redshift ($z = 0.0602$) compact radio galaxy 4C 31.04 using near-IR imaging spectroscopy. 4C 31.04 is a ~ 100 pc double-lobed Compact Steep Spectrum source believed to be a very young AGN. It is hosted by a giant elliptical with a $\sim 10^9 M_{\odot}$ multi-phase gaseous circumnuclear disc. We used high spatial resolution, adaptive optics-assisted H and K band integral field Gemini/NIFS observations to probe (1) the warm ($\sim 10^3$ K) molecular gas phase, traced by ro-vibrational transitions of H_2 , and (2), the warm ionized medium, traced by the $[\text{Fe II}]_{1.644 \mu\text{m}}$ line. The $[\text{Fe II}]$ emission traces shocked gas ejected from the disc plane by a jet-blown bubble 300 – 400 pc in diameter, whilst the H_2 emission traces

shock-excited molecular gas in the interior ~ 1 kpc of the circumnuclear disc. Hydrodynamical modelling shows that the apparent discrepancy between the extent of the shocked gas and the radio emission can occur when the brightest regions of the synchrotron-emitting plasma are temporarily halted by dense clumps, whilst less bright plasma can percolate through the porous ISM and form an energy-driven bubble that expands freely out of the disc plane. Simulations suggest that this bubble is filled with low surface-brightness plasma not visible in existing VLBI observations of 4C 31.04 due to insufficient sensitivity. Additional radial flows of jet plasma may percolate to \sim kpc radii in the circumnuclear disc, driving shocks and accelerating clouds of gas, giving rise to the H₂ emission.

2.1 Introduction

Feedback processes involving active galactic nuclei (AGN) have long been known to be important drivers of galaxy evolution. Quasar winds and jets from powerful AGN are believed to be important in shaping the galaxy luminosity function and in establishing the observed correlations between the properties of the bulge and the supermassive black hole (Silk & Rees 1998; Tremaine et al. 2002; Croton et al. 2006; King & Pounds 2015, and references therein). On much smaller scales, AGN feedback processes are likely to be equally important: in particular, interactions between radio jets and the interstellar medium (ISM) on sub-kpc scales may have a significant impact upon the evolution of the host galaxy, particularly in the earliest stages of jet evolution.

Hydrodynamical simulations of jets propagating through an inhomogeneous ISM (Mukherjee et al. 2016; Wagner et al. 2016) have shown that star formation in the host galaxy can both be enhanced and inhibited by interactions between the jets and the ISM on sub-kpc scales. Sutherland & Bicknell (2007, henceforth SB07) demonstrated that the evolution of young radio galaxies can be separated into distinct stages: a ‘flood-and-channel’ phase, followed by the formation of an energy-driven bubble that creates a bow shock as it expands, after which the jet breaks free of the bubble, finally forming extended FR II-like lobes. The expanding bubble driven by the jet plasma can ablate clouds and accelerate them to high velocities, preventing star formation and driving powerful outflows (e.g., in 3C 326 N; Nesvadba et al. 2010). Mukherjee et al. (2016) found that the energy-driven bubble can remain confined to the galaxy’s potential for a long time due to interactions with the inhomogeneous ISM. The bubble drives shocks and turbulence into the ISM, potentially leading to quenching of star formation. Conversely, the over-pressured plasma in the hot bubble can trigger gravitational instabilities and perhaps cloud collapse, enhancing star formation (Gaibler et al. 2012; Fragile et al. 2017). Despite mounting evidence from simulations of such ‘positive feedback’, jet-induced star formation has only been observed in a handful of sources, e.g., the $z = 3.8$ radio galaxy 4C 41.17 (Bicknell et al. 2000), 3C 285 (Salomé et al. 2015), Centaurus A (Salomé et al. 2017) and in Minkowski’s Object (Salomé et al. 2015; Lacy et al. 2017). Simulations show these feedback mechanisms are sensitive to both the ISM structure and jet power, making it difficult to predict whether star formation will be enhanced or inhibited, and in turn the impact on the evolution of host galaxy (Wagner et al. 2016; Zubovas & Bourne 2017; Mukherjee et al. 2018b). High-resolution observations of the ISM in young radio galaxies are therefore key to exposing the relationship between the

properties of the radio jets and the host galaxy.

Gigahertz Peak Spectrum (GPS) and Compact Steep Spectrum (CSS) sources are extragalactic radio sources characterised by a peak in their radio spectrum occurring in the GHz and ~ 100 MHz range for GPS and CSS sources respectively and compact (< 1 kpc) radio emission with resolved lobes and/or jets (for a comprehensive review see O’Dea 1998). Recent observations (e.g., Tingay et al. 2015; Callingham et al. 2017) indicate that the spectral peak is most likely caused by free-free absorption (FFA) of synchrotron emission by an ionized ISM with a varying optical depth, as proposed by Bicknell et al. (1997). More recently, hydrodynamical simulations by Bicknell et al. (2018) have indeed demonstrated that jets percolating through an ionized, inhomogeneous ISM can reproduce the observed spectra of GPS/CSS sources via FFA. The peaked spectrum and compact size of GPS and CSS sources suggests that they harbour young jets, temporarily confined by a dense ISM, and that the more powerful GPS and CSS sources are the progenitors of classical double-lobed radio sources. This ‘youth hypothesis’ is supported by age estimates based on breaks in the synchrotron spectrum and on hotspot advance velocities (O’Dea 1998). The compact nature of the jets in GPS and CSS sources therefore enables us to study jet-ISM interactions within the host galaxy in the earliest stages of evolution, and therefore represent an important class of sources in the context of AGN feedback.

4C 31.04 is a low-redshift ($z = 0.0602$) CSS source with highly compact (~ 100 pc across) lobes believed to be $\sim 10^3$ yr old (Giroletti et al. 2003, henceforth referred to as Gi03). The mottled and asymmetric radio morphology suggests strong interactions between the jets and a dense ISM. The proximity of 4C 31.04 enables us to probe jet-ISM interactions at the necessary sub-kpc scales with adaptive optics (AO)-assisted observations on an 8-metre telescope; none the less, no previous optical or near-infrared (IR) observations have resolved the host galaxy down to scales comparable to the size of the radio lobes.

With the aim of observing jet-induced AGN feedback in action, we observed 4C 31.04 with the Near-infrared Integral Field Spectrograph (NIFS) and the ALTAIR AO system on the Gemini North telescope in September 2016. In our NIFS observations, we probe both the warm molecular and ionized gas phases, both of which are important tracers of jet-ISM interactions. Many groups have carried out similar studies of young radio galaxies in the past (e.g., 3C 326 N (Nesvadba et al. 2010, 2011), 4C 12.50 (Morganti et al. 2013), IC 5063 (Tadhunter et al. 2014; Morganti et al. 2015), NGC 1052 (Morganti et al. 2005), NGC 1068 (Riffel et al. 2014), NGC 1275 (Scharwächter et al. 2013), NGC 4151 (Storchi-Bergmann et al. 2012) and PKS B1718-649 (Maccagni et al. 2016)). However, the 100 pc-scale jets of 4C 31.04 provide a rare opportunity to observe jet-ISM interactions in the very earliest stages of evolution. Moreover, 4C 31.04 has a wealth of auxiliary data at multiple wavelengths, including milliarcsecond-resolution very long baseline interferometry (VLBI) imaging, that enable us to better constrain the properties of the jets and of the host galaxy.

In Section 2.2 we summarise the properties of 4C 31.04 and its host galaxy gleaned from previous multi-wavelength studies. Section 2.3 details our NIFS observations and data reduction methods. In Section 2.4 we discuss the two distinct phases of the ISM we detect in our observations. We discuss the interpretation of our observations in the context of AGN feedback in Section 2.5 and summarise our findings

in Section 2.6.

For the remainder of this paper, we assume a cosmology with $H_0 = 69.6 \text{ km s}^{-1} \text{ Mpc}^{-1}$, $\Omega_M = 0.286$ and $\Omega_{\text{vac}} = 0.714$, implying a luminosity distance $D_L = 271.3 \text{ Mpc}$ and spatial scale of $1.17 \text{ kpc arcsec}^{-1}$ at the redshift $z = 0.0602$ of 4C 31.04 (Wright 2006).

2.2 Previous observations of 4C 31.04

2.2.1 Host galaxy properties

The host galaxy of 4C 31.04 is MCG 5-4-18, a giant elliptical approximately 2 H band magnitudes brighter than L_* at a redshift $z = 0.0602 \pm 0.0002$ (García-Burillo et al. 2007, henceforth Ga07). Willett et al. (2010) provide an upper limit of $M_{\text{BH}} \leq 10^{8.16} M_\odot$ on the mass of the central black hole using the width of the $[\text{O IV}]_{25.4 \mu\text{m}}$ line. We estimate the stellar mass M_* from the 2MASS K_s band magnitude using a simple stellar population model of Bruzual & Charlot (2003) with a single instantaneous burst of star formation, assuming solar metallicity, a Chabrier IMF and an age of a few Gyr. This yields $\log M_* \approx 11.4$.

This host galaxy has a Seyfert 2-like optical spectrum consistent with a predominantly old, metal-rich stellar population (Serote Roos & Gonçalves 2004; Gonçalves & Serote Roos 2004). Despite this, there is evidence for moderate levels of star formation (SF): Willett et al. (2010) detect polycyclic aromatic hydrocarbon (PAH) emission and weak silicate absorption features in spatially unresolved *Spitzer* mid-IR spectroscopy, indicating gas and dust heating by both ongoing SF and AGN. Despite the presence of silicate absorption features, which are generally associated with AGN tori (Li et al. 2008), 4C 31.04 has a *Wide-Field Infrared Explorer (WISE)* colour of $W1 - W2 \approx 0$, indicating minimal contribution to the mid-IR emission from a hot torus (Cluver et al. 2017). Using *Infrared Astronomical Satellite (IRAS)* $60 \mu\text{m}$ and $100 \mu\text{m}$ fluxes Ocaña Flaquer et al. (2010) estimate a star formation rate $\text{SFR}_{\text{FIR}} \approx 4.9 M_\odot \text{ yr}^{-1}$, comparable to that calculated by Willett et al. (2010) using PAH emission features ($\text{SFR}_{\text{PAH}} = 6.4 M_\odot \text{ yr}^{-1}$).

Perlman et al. (2001, henceforth Pe01) observed 4C 31.04 with the *Hubble Space Telescope (HST)* using the Wide Field Planetary Cam 2 (WFPC2) and NICMOS, revealing several obscuring dust features, including an edge-on circumnuclear disc with a pronounced warp. Mid-IR silicate absorption features indicate that the dust has a clumpy distribution (Willett et al. 2010). These and other multi-wavelength studies indicate that for a low- z radio host galaxy, 4C 31.04 harbours an unusually massive ($10^9 M_\odot$) multi-phase circumnuclear disc. This is discussed further in Section 2.2.3.

4C 31.04 is a projected distance of $\sim 20 \text{ kpc}$ from a spiral galaxy with redshift $z = 0.0548$ (van den Bergh 1970), corresponding to a cosmological distance separation greater than 20 Mpc and a velocity offset of approximately 1560 km s^{-1} . While it is possible that both galaxies are members of the same group, and that the apparent difference in redshift is due to their peculiar velocities, the velocity offset far exceeds the expected velocity dispersion for a small group ($\sim 200 - 400 \text{ km s}^{-1}$). We therefore conclude that the companion is not a group member, and that a past interaction between the two is highly unlikely. Indeed, 4C 31.04 does not show any sign of recent interaction such as tidal tails. On this basis, Pe01 conclude that any interaction must

have taken place $\gtrsim 10^8$ yr ago.

2.2.2 Radio properties

4C 31.04 is a Compact Steep Spectrum (CSS) source, with $P_{1.4 \text{ GHz}} = 10^{26.3} \text{ W Hz}^{-1}$ (van Breugel et al. 1984) and a spectral peak at ~ 400 MHz (estimated from the spectrum provided in the NASA/IPAC Extragalactic Database (NED)). The source has two edge-brightened radio lobes separated by ~ 100 pc with a weak inverted-spectrum core (Cotton et al. (1995), Gi03, Struve & Conway (2012)). The axis of the jets is approximately East-West, with a position angle (PA) $\approx 100^\circ$. The lobes are highly asymmetric, suggesting strong jet-ISM interaction (Giovannini et al. 2001). The Western lobe is relatively faint and diffuse, suggesting the jet is interacting with many small clouds (Bicknell 2002), whilst the Eastern lobe is brighter and more compact, and has a peculiar ‘hole’ that may be caused by an overdensity in the ISM that is impenetrable to radio plasma (Gi03).

Radio observations indicate 4C 31.04 is a truly young radio source. Low flux variability ($\lesssim 2$ per cent at 5 GHz) and polarization ($\lesssim 1$ per cent at 5 GHz) in the lobes suggest beamed emission is improbable (Gi03), and that the compactness of the source is unlikely an orientation effect. Giovannini et al. (2001) estimated that the jets are nearly coplanar with the sky, with an orientation angle $\theta \gtrsim 75^\circ$. Differential VLBI imaging of 4C 31.04 has revealed the radio emission to be rapidly expanding, with hotspot velocities of $\sim 0.3c$, yielding a dynamic age of ~ 550 yr; synchrotron decay modelling yields much older radiative ages of 3300 yr and 4500 – 4900 yr in the Eastern and Western lobes respectively (Gi03). The difference in these estimates may be the result of the jet termini moving from point to point as the source evolves (Sutherland & Bicknell 2007).

2.2.3 Previous observations of the circumnuclear medium

A number of multi-wavelength studies have shown that 4C 31.04 has a multiphase and dynamically unrelaxed circumnuclear disc that contains dust, molecular gas and atomic gas.

The $R-H$ colour map of Pe01 constructed from *HST* WFPC2/F702W and NICMOS/F160W images (our Fig. 2.1b and their fig. 2, bottom right) reveals several obscuring structures surrounding the nucleus, including a reddened circumnuclear disc, loops streaming from the Northernmost point of the disc, and a large S-shaped structure extending to the North and South. The circumnuclear disc is approximately perpendicular to the axis of the radio jets, and extends roughly 500 pc to the North and 1000 pc to the South. The disc is highly inclined, and is viewed almost edge-on.

Using the Institut de Radioastronomie Millimétrique (IRAM) 30 m telescope, Ocaña Flaquer et al. (2010) found double-horned $^{12}\text{CO}(2-1)$ and $^{12}\text{CO}(1-0)$ profiles with superimposed absorption, suggesting a massive inclined disc of molecular gas and a total H_2 mass of $(60.63 \pm 16.92) \times 10^8 M_\odot$. Ga07 also detected a disc-like structure in the 1 mm continuum with the IRAM Plateau de Bure interferometer (PdBI) ~ 1.4 kpc in size which is consistent with the dusty disc in the *HST* $R-H$ image. They also found $\text{HCO}^+(1-0)$ emission to the North and South of the nucleus, with kinematics consistent with a disc (their fig. 1b). Struve & Conway

(2012) detected H I absorption using VLBI observations, and estimated a column density $N_{\text{HI}} = 1.2 - 2.4 \times 10^{21} \text{ cm}^{-2}$. The velocity structure of the absorption is consistent with a large rotating disc of atomic gas coinciding with the kpc scale molecular disc. The H I optical depth is much higher in the Eastern lobe, indicating that the disc is inclined such that the Eastern lobe is viewed through a dense column of gas. This is consistent with earlier H I VLBI observations by Conway (1996), which also revealed a sharp ‘edge’ in the H I opacity in the Western lobe (their fig. 1). Conway (1996) also detected high-velocity H I clouds and FFA features in front of both lobes, which they attributed to the jets evaporating material off the inner edge of the circumnuclear disc.

Irregularities in the kinematics and morphology of gas and dust in the circumnuclear regions of the galaxy suggest unrelaxed dynamics. Pe01 fitted isophotes to the *HST* NICMOS F160W (*H* band) image and found significant anisotropies in the ellipticity and a PA that twists by tens of degrees in the innermost 2–4 kpc. Struve & Conway (2012) detected a narrow, redshifted H I absorption component consistent with a cloud at a radius $\gg 100$ pc falling into the nucleus, which may be a remnant of a merger or accretion event. Ga07 detected blueshifted ($\sim 150 \text{ km s}^{-1}$) HCO^+ (1 – 0) absorption over the centre of the galaxy, although we note that the uncertainty in the redshift of the source corresponds to an uncertainty in the galaxy’s systemic velocity of $\sim 100 \text{ km s}^{-1}$.

These observations show that the host of 4C 31.04 contains a dense, massive, circumnuclear disc, consisting of cold dust, both cold and warm molecular gas, and atomic gas. Twisted central isophotes and non-circular motions indicate that the disc is dynamically unrelaxed, perhaps due to a previous a merger or interaction, accretion of new material, or by jet-ISM interactions.

2.3 Observations and data reduction

2.3.1 Observations

We observed 4C 31.04 using the Near-infrared Integral Field Spectrograph (NIFS) (McGregor et al. 2003) on the 8.1-m Gemini North telescope on Mauna Kea in Hawai‘i. NIFS provides $R \sim 3500$ *J*, *H* and *K* band spectroscopy over a $3'' \times 3''$ field of view with $0.1'' \times 0.04''$ spaxels. NIFS is fed by the ALTAIR AO system which can be used in laser guide star (LGS) or natural guide star mode to provide near-diffraction limited resolution.

We obtained *H* and *K* band observations of 4C 31.04 using NIFS and the ALTAIR AO system used in LGS mode, using an off-axis guide star for tip/tilt correction, with a PA of 0° on 2016 September 22 during program GN-2016B-C-1. We used 600 s exposure times for both source and sky frames, integrating on-source for a total of 80 and 60 minutes in the *H* and *K* bands respectively. The HIPPARCOS stars HIP12218, HIP117774 and HIP12719, observed before and after 4C 31.04, were used as telluric and flux standards. The angular resolution (Full Width at Half Maximum (FWHM)) of our observations was approximately $0.20''$ and $0.17''$ in the *H* and *K* bands respectively, which we estimated by fitting Gaussian profiles to our standard star exposures.

2.3.2 NIFS data reduction in IRAF

We reduced the data using the GEMINI IRAF package, reducing science frames for both object and standard star exposures as follows.

We subtract individual sky frames from the science frames, pairing the sky frames taken closest in time to the science frame. We divide by a master flat field, then extract the slices from the science frames to form 3D data cubes. All data cubes are spatially interpolated to yield $0.05'' \times 0.05''$ square pixels. We then interpolate over bad pixels, apply the wavelength calibration and correct for spatial distortion. The wavelength solution was found using argon and xenon arc lamp exposures taken during the night, and spatial distortions were calibrated using an exposure of a Ronchi grating through a flat field.

To correct for telluric absorption lines, we generate a 1D spectrum of the telluric standard by co-adding the spectra within a $0.5''$ -diameter aperture centred on the star. We flatten the resulting 1D spectrum by dividing it by a normalised blackbody corresponding to the temperature of the star, estimated from its spectral class, and then fit and remove stellar absorption lines using a Voigt profile. We remove telluric absorption lines by dividing the object data cubes by the resulting 1D spectrum.

To flux calibrate the object data cubes, we use exposures of a standard star with given 2MASS H band and Ks band magnitudes to convert counts to units of monochromatic flux density. We generate a 1D spectrum of the flux standard in the same fashion as for the telluric standard, and multiply it by the normalised blackbody to restore its original spectral shape. We remove telluric absorption lines by dividing the spectrum by the 1D spectrum of the telluric standard. We then divide it by a blackbody spectrum in units of $\text{erg s}^{-1} \text{cm}^{-2} \text{\AA}^{-1}$ corresponding to the temperature of the flux calibration standard star. We fit a polynomial to the resulting spectrum to give the transfer function. To flux calibrate the object data cubes, we divide the individual object data cubes by the transfer function, the exposure time and the spaxel area to give units of $\text{erg s}^{-1} \text{cm}^{-2} \text{\AA}^{-1} \text{arcsec}^{-2}$. Finally, we shift and median-combine each object data cube to yield a single data cube.

2.3.3 MAD smoothing

We use a Median Absolute Deviation (MAD) smoothing algorithm with a radius of 2 pixels to smooth the reduced data cubes and to remove artefacts. In each wavelength slice, for each pixel, we compute the median and standard deviation σ of the surrounding pixels out to the specified radius, and reject those pixels with absolute value greater than 3σ from the median. We iterate until no more pixels are rejected. The value of the central pixel is then replaced by the mean of the remaining pixels, and the variance of the central pixel is replaced by the mean of the variance of the remaining pixels.

Before smoothing, the angular resolution of our observations corresponds to a FWHM of approximately 230 pc and 200 pc in the H and K bands respectively. After smoothing with a radius of 2 pixels, the resolution is decreased to approximately 300 pc and 280 pc in the H and K bands respectively.

2.3.4 Emission line fitting

We use MPFIT (Markwardt 2009), a PYTHON implementation of the Levenberg-Marquardt algorithm (Moré 1978) developed by M. Rivers* to fit single-component Gaussian profiles to the emission lines in each spaxel. We keep fits with reduced- $\chi^2 < 2$ and signal-to-noise ratio (S/N) > 1 . In all reported linewidths, we have accounted for instrumental resolution by subtracting the width of the line spread function (LSF) in quadrature from the width of the fitted Gaussian. We estimate the width of the LSF by fitting a Gaussian to sky lines close in wavelength to the relevant emission line.

Integrated line fluxes and upper limits for emission lines in 4C 31.04 are shown in Table 2.1. To calculate integrated line fluxes, we simply sum the fluxes found in each spaxel.

To calculate upper limits for line fluxes which are not detected using our χ^2 and S/N criteria, we use the following method. In each spaxel, we calculate the standard deviation σ in the continuum in a window centred on the emission line. We assume the non-detected emission line in that spaxel is a Gaussian with amplitude 3σ . The width we use depends on the emission line. For non-detected ro-vibrational H_2 lines, we use the measured width of the H_2 1–0S(1) emission line in that spaxel. For hydrogen recombination lines, we use the Gaussian sigma of 24.9 \AA we calculate from the measured equivalent width of 18 \AA for the combined $H\alpha$ and [N II] lines in a single-slit optical spectrum of 4C 31.04 reported by Marcha et al. (1996). When quoting integrated upper limits, we assume the lines are detected in every spaxel in which we detect the H_2 1–0S(1) emission line.

*Available <http://cars9.uchicago.edu/software/python/mpfit.html>.

Table 2.1: Emission line fluxes and their uncertainties. The integrated flux is measured by adding together the emission line fluxes in each individually fitted spaxel. Upper limits are computed using the method described in Section 2.3. All quantities are given in units of $\text{erg s}^{-1} \text{cm}^{-2}$.

Emission line	Total Integrated flux (erg s cm^{-2})	Integrated flux within $r \leq 0.2''$	Integrated flux outside $r > 0.2''$
H ₂ 1-0S(1)	$2.60 \pm 0.06 \times 10^{-15}$	$5.2 \pm 0.2 \times 10^{-16}$	$2.08 \pm 0.04 \times 10^{-15}$
H ₂ 1-0S(2)	$4.4 \pm 0.5 \times 10^{-16}$	$2.0 \pm 0.2 \times 10^{-16}$	$2.3 \pm 0.2 \times 10^{-16}$
H ₂ 1-0S(3)	$2.52 \pm 0.11 \times 10^{-15}$	$6.3 \pm 0.3 \times 10^{-16}$	$1.90 \pm 0.05 \times 10^{-15}$
H ₂ 2-1S(1)	$\leq 3.077 \times 10^{-15}$	$\leq 2.009 \times 10^{-16}$	$\leq 2.876 \times 10^{-15}$
H ₂ 2-1S(2)	$\leq 2.172 \times 10^{-15}$	$\leq 1.667 \times 10^{-16}$	$\leq 2.005 \times 10^{-15}$
H ₂ 2-1S(3)	$\leq 3.222 \times 10^{-15}$	$\leq 1.972 \times 10^{-16}$	$\leq 3.025 \times 10^{-15}$
H I Br γ	$\leq 4.500 \times 10^{-15}$	$\leq 3.411 \times 10^{-16}$	$\leq 4.159 \times 10^{-15}$
[Fe II] _{1.644} μm	$1.35 \pm 0.05 \times 10^{-15}$	—	—

Table 2.2: Ratios of the integrated fluxes of emission lines evaluated over the entire field of view (left column), within the central 0.2'' (middle column) and outside the central 0.2'' (right column). The integrated flux is measured by adding together the emission line fluxes in each individually fitted spaxel. Upper limits are computed using the method described in Section 2.3.

Emission line ratio	Total	Within $r \leq 0.2''$	Outside $r > 0.2''$
H ₂ 1–0 S(1)/H I Br γ	0.5774	1.5212	0.5000
H ₂ 1–0/2–1 S(1)	0.8443	2.5826	0.7229

2.4 Results

Diffraction-limited *HST* WFPC2 imaging has similar angular resolution to our NIFS observations (0.05''), enabling us to directly compare the two sets of observations. Fig. 2.1a shows the *K* band continuum (red) from our NIFS observations overlaid on to the *HST* *B* band image. Fig. 2.1b overlays the fluxes of the ro-vibrational H₂ emission (blue), which we detect in the *K* band, and the [Fe II]_{1.644 μ m} emission (green), which we detect in the *H* band, on to the *HST* *R* – *H* image, placing both emission lines in context. The H₂ emission traces the dusty disc, and shows hints of a warp to the North and South, suggesting the H₂ is part of the large S-shaped dust feature. Meanwhile, the [Fe II] emission is localised to the nucleus.

2.4.1 Nuclear [Fe II] emission

In our *H* band observations we detect [Fe II] $a^4D_{7/2} - a^4F_{9/2}$ (rest-frame wavelength 1.644 μ m) emission in the inner few 100 pc of 4C 31.04. Fig. 2.2 shows the *H* band continuum and the [Fe II] line flux, radial velocity and velocity dispersion.

We measure the spatial extent of the [Fe II] emission by fitting a 2D Gaussian to the integrated flux map. The emitting region is marginally resolved in our observations and is elongated, extending over ≈ 380 pc E-W and ≈ 320 pc N-S. The line profile is flat, asymmetric and broad, with a velocity dispersion of approximately 350 km s⁻¹ across the emitting region. We argue that the [Fe II] emission traces gas being accelerated out of the plane of the circumnuclear disc by the jet-driven bubble, which we discuss further in Section 2.5.

2.4.2 H₂ emission

We detect the H₂ 1–0 S(1), S(2) and S(3) emission lines in our *K* band spectra, corresponding to transitions involving changes in the rotational quantum number with $\Delta J = +2$ and the vibrational level transition $\nu = 1$ to $\nu = 0$. These ro-vibrational emission lines trace warm H₂ in the temperature range $\sim 10^3 - 10^4$ K. In Fig. 2.3, we show the flux distribution, radial velocity and velocity dispersion of the H₂ 1–0 S(1) line we detect in our NIFS observations. The flux extends over ≈ 2 kpc from North to South, and the radial velocity shows large-scale rotation, indicating that the warm H₂ is a part of the kpc-scale circumnuclear disc observed in CO, HCO⁺ and H I. The flux peaks sharply at the nucleus (Fig. 2.3b): indeed, we find that ≈ 20 per cent of the total flux is contained within the central 0.4''. In this section, we analyse the inner 0.4'' separately to the remaining H₂ emission in order

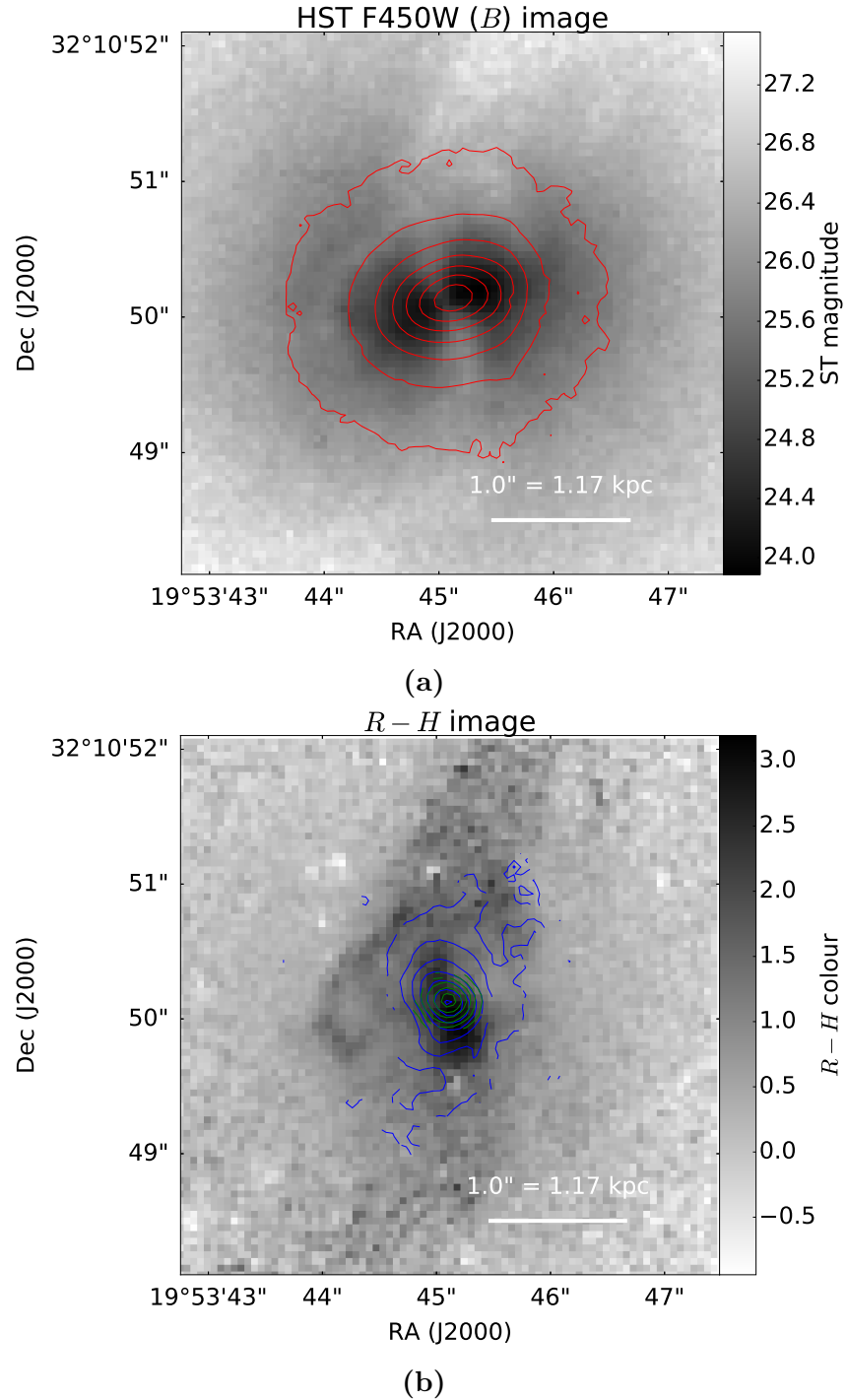


Figure 2.1: Our *K* band NIFS observations overlaid on to *HST* images. (a) shows the NIFS *K* band continuum (red contours) overlaid on to the *HST* WFPC2 *B* band (F450W) image. The *K* band contours represent the underlying stellar mass distribution, showing that the ‘cones’ to the East and West of the nucleus are not physical features, but a result of dust obscuration. The contours in (b) show the flux of the H_2 1–0S(1) (blue) and $[\text{Fe II}]_{1.644 \mu\text{m}}$ (green) emission lines overlaid on to the *R* – *H* image constructed using the *HST* WFPC2/F702W and NICMOS/F160W images. Whilst the $[\text{Fe II}]$ emission is concentrated to the central few 100 pc, the H_2 emission extends to ~ 1 kpc North and South of the nucleus, suggesting it is part of the massive circumnuclear disc.

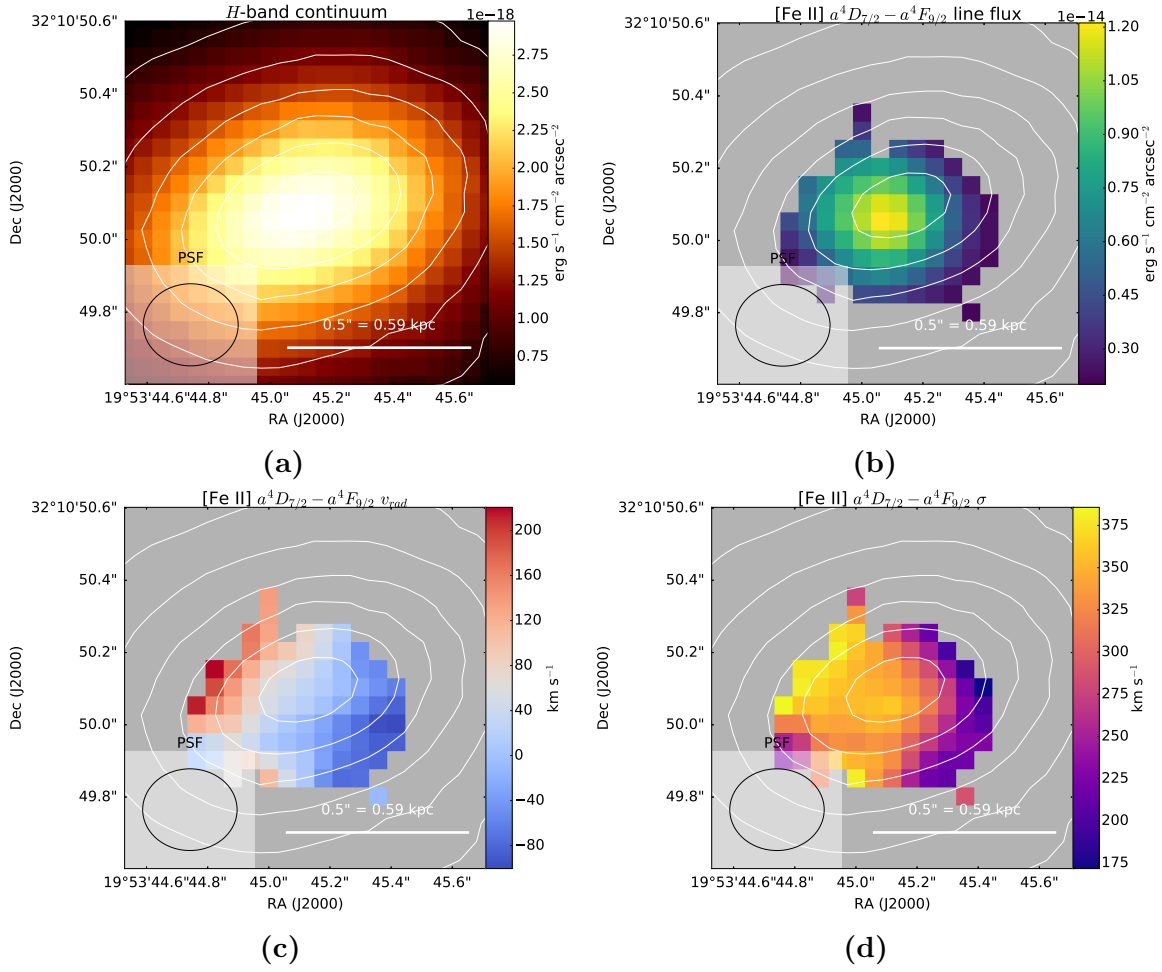


Figure 2.2: (a): the H band continuum; (b): [Fe II] $_{1.644 \mu\text{m}}$ integrated flux; (c): [Fe II] $_{1.644 \mu\text{m}}$ radial velocity (minus the systemic velocity of the galaxy obtained from the redshift of $z = 0.0602$); and (d): [Fe II] $_{1.644 \mu\text{m}}$ velocity dispersion (Gaussian σ). The H band continuum is indicated in contours and the FWHM of the PSF (taking into account the effects of MAD smoothing) is indicated in all figures.

to determine any differences in the excitation mechanism and temperature between the central and extended components.

Kinematics

To determine whether the H_2 belongs to the circumnuclear disc, we fit a simple disc model to our data using MPFIT. Our model has solid-body rotation out to a break radius r_b , and a flat rotation curve for $r > r_b$, and we fit the systemic velocity as a free parameter. We do not account for beam smearing in the fit. Fig. 2.4 shows the model fit and residuals, and Fig. 2.5 shows a cross-section of the radial velocities taken along the dashed black line shown in Fig. 2.4. The disc fit has a PA approximately perpendicular to the jet axis, indeed consistent with that of the circumnuclear disc detected in previous studies. The fitted inclination of the disc is consistent with the Easternmost edge being closest to us, which is also consistent with the greater H I opacity of the Eastern radio lobe (Conway 1996; Struve & Conway 2012). At the edge of the disc ($r \approx 0.8 \text{ kpc}$), the rotational velocity $v_c \approx 425 \text{ km s}^{-1}$ with respect to the systemic velocity is comparable to that

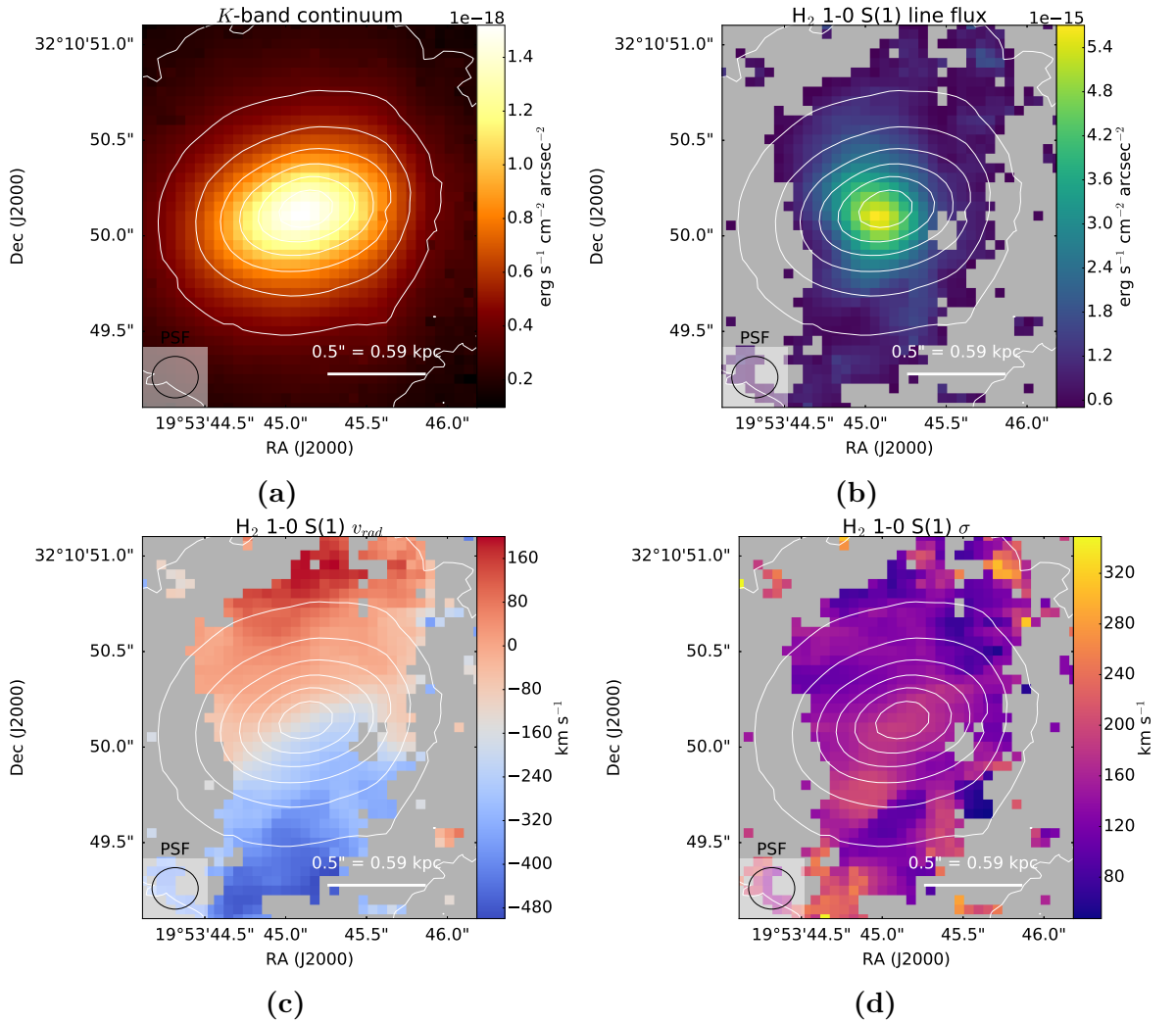


Figure 2.3: (a) the K band continuum; (b): H_2 1–0S(1) integrated flux; (c): H_2 1–0S(1) radial velocity (minus the systemic velocity of the galaxy obtained from the redshift of $z = 0.0602$); and (d): H_2 1–0S(1) velocity dispersion (Gaussian σ). The K band continuum is indicated in contours and the FWHM of the PSF (taking into account the effects of MAD smoothing) is indicated in all figures.

of the HCO^+ emission (Ga07). Therefore, our disc fit shows the warm H_2 probes the interior $\sim \text{kpc}$ of the circumnuclear disc of 4C 31.04, where the apparent solid-body rotation is a result of the warm H_2 not extending far enough into the disc to reach the turnover in the rotation curve.

Interestingly, the H_2 emission has a net blueshifted velocity of $\approx 150 \text{ km s}^{-1}$ relative to the systemic velocity derived using the redshift ($z = 0.0602$), which is markedly similar to that of HCO^+ (Ga07) and H I (Struve & Conway 2012) viewed in absorption over the nucleus.

A uniform distribution of dust in the disc could cause the flux-weighted mean velocity to have a significant blueshift; however this scenario would require an unrealistically large A_K . We instead speculate that the warm H_2 traces clouds of gas being radially accelerated by jet plasma percolating through the disc, and that the net blueshift is because redshifted gas on the far side of the disc is obscured by extinction.

We note that the $\sim 100 \text{ km s}^{-1}$ uncertainty in the redshift could be the cause

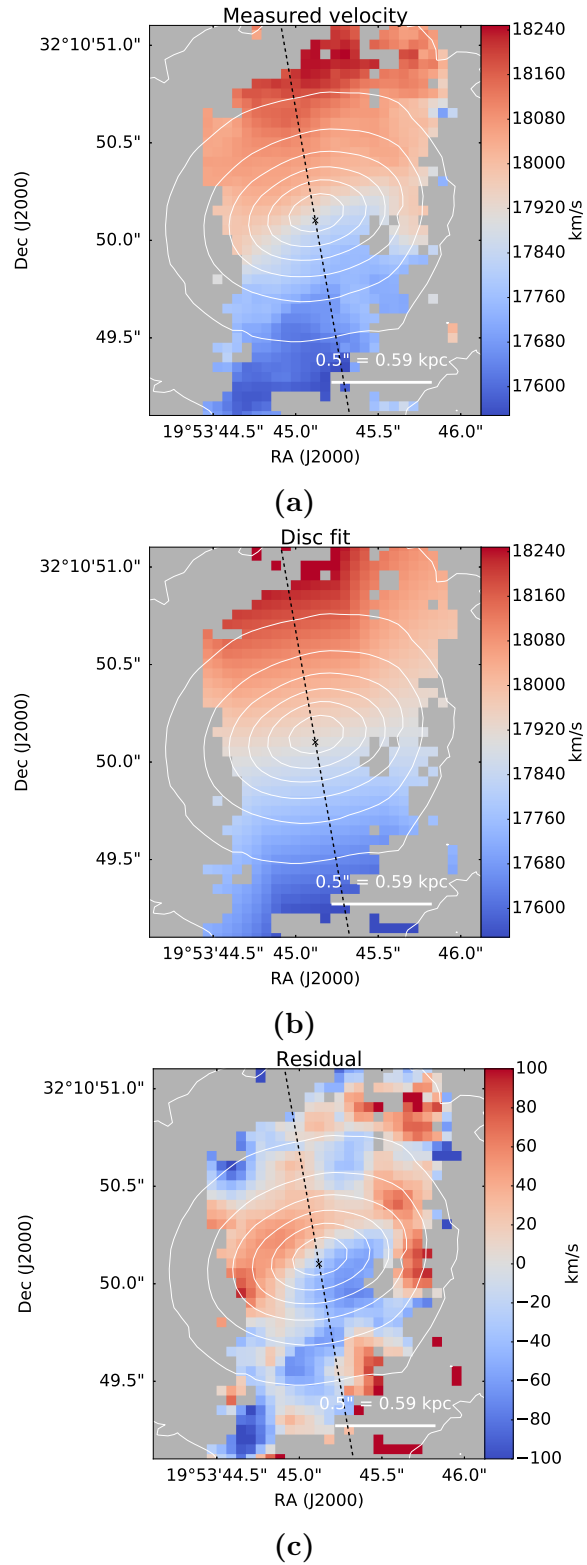


Figure 2.4: Kinematics of the H₂ 1–0S(1) emission line; (a): measured radial velocity, (b) radial velocity of the model fit, and (c) the residual. With the exception of the residual plot, all velocities are given with respect to the local standard of rest. The cross represents the location of the nucleus (i.e., the peak in the *K* band continuum). Fig. 2.5 shows a cross-section of the radial velocities taken along the dashed black line.

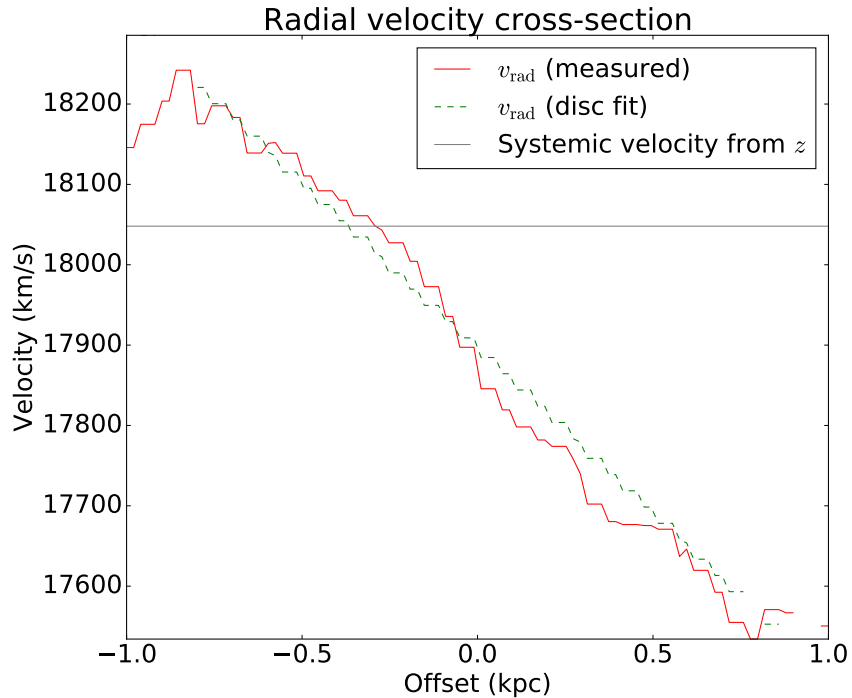


Figure 2.5: A cross-section of the measured (red solid line) and model fit (green dashed line) radial velocity taken along the black dashed lines indicated in Fig. 2.4. The systemic velocity of the galaxy, as estimated from the redshift, is indicated by the horizontal line, showing that the H_2 emission has a systemic blueshift of $\approx 150 \text{ km s}^{-1}$.

this apparent blueshift. However, adopting a lower redshift to force the HCO^+ , H I and H_2 components to coincide with the galaxy’s systemic velocity would result in the $[\text{Fe II}]$ emission in the nucleus being significantly redshifted. This would be difficult to explain under our interpretation that the $[\text{Fe II}]$ emission arises from the jet accelerating material out of the nucleus. We discuss this further in Section 2.5.3.

The velocity residuals of the disc fit (Fig. 2.4) reveal redshifted and blueshifted velocity residuals to the NE and SW of the nucleus respectively which are similar to the radial velocity of the $[\text{Fe II}]$ emission (Fig. 2.2c), suggesting the kinematics of the molecular disc could be disrupted by the same processes causing the $[\text{Fe II}]$ emission. However, referring to the *HST* $R - H$ image (Fig. 2.1) and to the flux distribution of the warm H_2 (Fig. 2.3b), the circumnuclear disc is clearly warped. The residuals in Fig. 2.4 could simply arise from our disc fit not accounting for this warp, and so this alone cannot be interpreted as evidence of kinematically disturbed molecular gas in the inner regions of the disc.

Gas temperature

If H_2 is in thermal equilibrium, the Boltzmann equation describes the level populations of the vibrational states. To determine whether or not the molecular gas is in thermal equilibrium, we use an excitation diagram, where we plot the level populations estimated from emission line fluxes as a function of the level energy (see Fig. 2.6). This also enables us to constrain the temperature of the warm H_2 . If the gas is in thermal equilibrium, the points will lie along a straight line in log space of level population versus transition energy with slope $-1/T_{\text{kin}}$ where T_{kin} is the kinetic temperature of the gas. To convert emission line fluxes to level populations we use

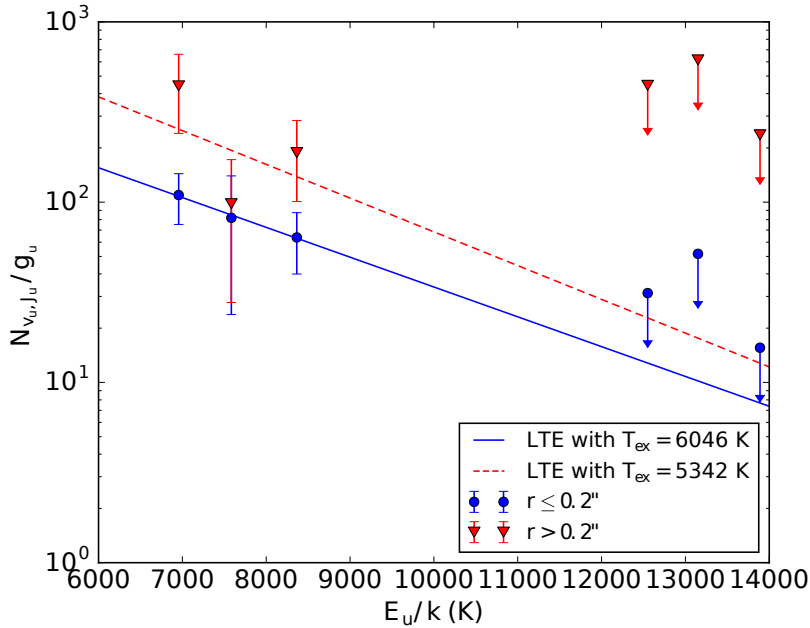


Figure 2.6: H₂ excitation diagram of 4C 31.04. Red triangles and blue circles indicate estimates of $N_{\text{obs}}(\nu_u, J_u)/g_u$ for the extended ($r > 0.2''$) and central ($r \leq 0.2''$) regions respectively. Arrows indicate emission lines for which we can only estimate upper limits.

the method described in Rosenberg et al. (2013):

$$\frac{N_{\text{obs}}(\nu_u, J_u)}{g_u} = \frac{4\pi\lambda_{u,l}}{hc} \frac{I_{\text{obs}}(u, l)}{A(u, l)}, \quad (2.1)$$

where $N_{\text{obs}}(\nu_u, J_u)$ is the observed column density of H₂ molecules in the upper level u , g_u is the statistical weight of the upper level, $\lambda_{u,l}$ is the rest-frame wavelength corresponding to the transition, $I_{\text{obs}}(u, l)$ is the measured flux of the transition and $A_{u,l}$ is the spontaneous emission coefficients, here obtained from Wolniewicz et al. (1998).

The excitation diagram for the H₂ 1–0S(1), S(2) and S(3) transitions in both the central and extended components of the H₂ is shown in Fig. 2.6, where we plot $N_{\text{obs}}(\nu_u, J_u)/g_u$ as a function of the temperature corresponding to the transition energy of each line. For non-detected emission lines we use the upper limits in these regions (Table 2.1). Unfortunately due to the close spacing in temperature of the H₂ 1–0S(1,2,3) transitions, and because we only have upper limits for the H₂ 2–1S(1,2,3) lines, we cannot place a very restrictive constraint on the temperature in the extended component of the H₂; however, the emission line fluxes in the central 0.4'' are consistent with a temperature 5000 – 6000 K, indicating that the H₂ in the central regions is much hotter than the ~ 300 K H₂ probed by *Spitzer* observations (Willett et al. 2010).

Excitation mechanism

Ro-vibrational H₂ emission can trace collisionally excited gas processed by shocks that are not fast enough to dissociate H₂ molecules. These emission lines can also be emitted by H₂ molecules excited by fluorescence from UV photons from O and

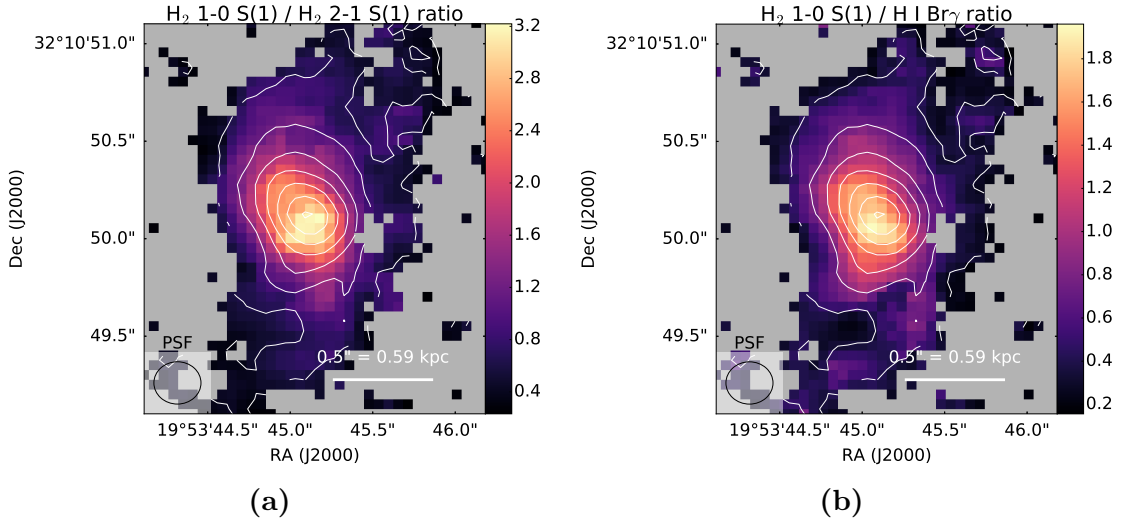


Figure 2.7: Emission line ratio maps that we use to determine the excitation mechanism for the warm H_2 in different regions. (a) shows the H_2 1–0 S(1)/ H_2 2–1 S(1) ratio and (b) shows the H_2 1–0 S(1)/Br γ ratio, and the white contours show the H_2 1–0 S(1) flux. The values of ~ 3 and ~ 2 in the inner $0.4''$ in (a) and (b) respectively suggest shocks, and not star formation, are the likely excitation mechanism.

B-type stars. We use two key emission line ratios (Table 2.2) to demonstrate that shock excitation is the most likely scenario.

Shock-excited H_2 can be distinguished from H_2 excited by a UV stellar radiation field by the relative level populations: fluorescent excitation tends to populate higher-level ν states more than shock excitation. Therefore line ratios of ro-vibrational emission lines involving the same J state transition with different upper ν levels can be used as indicators of the excitation mechanism. In shock-heated gas, the ratio of the H_2 1–0/2–1 S(1) lines tends to be much larger than in fluorescently-excited gas (e.g., Nesvadba et al. 2011). Fig. 2.7a shows this ratio in each spaxel. We have used upper limits to estimate the 2–1 S(1) flux; therefore these values should be interpreted as lower limits for the true line ratio. In the inner $0.4''$, the ratio of the integrated fluxes of the two lines exceeds ~ 2 , indicating shock excitation.

At high enough densities ($n \gtrsim 10^3 \text{ cm}^{-3}$), where H_2 is in LTE, level populations will be similar in both shock- and fluorescent-excited H_2 , in which case the line ratios are misleading. Here, we can eliminate fluorescent excitation by young stars because we do not detect Br γ , leaving shocks as the most likely mechanism. Fig. 2.7b shows the ratio H_2 1–0 S(1)/Br γ in each spaxel, where we have used upper limits to estimate the Br γ flux. In the inner $0.4''$, the ratio of the integrated fluxes of the two lines exceeds the 0.1–1.5 expected when the excitation source is UV heating in star-forming galaxies (Puxley et al. 1990). Additionally, our Br γ upper limits are pessimistic, because we assume a Gaussian sigma determined from the combined $\text{H}\alpha + [\text{N II}]$ equivalent width of Marcha et al. (1996) from an unresolved spectrum. Therefore, combining this result with the high H_2 1–0/2–1 S(1) ratio, we conclude that the ro-vibrational H_2 emission is excited by shocks in the central region.

In the extended component, we cannot rule out star formation as the source of excitation, although we note these results are not inconsistent with shock excitation, because both line ratios involve upper limits.

Table 2.3: Mass estimates of different gas phases in 4C 31.04.

Phase	Mass (M_{\odot})	Reference
M_{BH}	$\leq 10^{8.16}$	Willett et al. (2010)
$M_{\text{dyn}} (r < 0.8 \text{ kpc})$	3.4×10^{10}	This work
$M_{\text{H}_2, \text{warm}} (T = 2000 \text{ K})$	9.7×10^3	This work
$M_{\text{H}_2, \text{warm}} (T = 338 \pm 100 \text{ K})$	$(4.7 \pm 1.3) \times 10^6$	Willett et al. (2010)
$M_{\text{H}_2, \text{cold}}$	$(60.63 \pm 16.92) \times 10^8$	Ocaña Flaquer et al. (2010)
$M_{\text{H I}}$	4.8×10^7	Perlman et al. (2001)
$N_{\text{H I}}$	$(1.2 - 2.4) \times 10^{21} \text{ cm}^{-2}$	Struve & Conway (2012)

Mass estimates

We now estimate the dynamical mass and warm gas mass and compare our results with those from previous studies presented in Section 2.2.3.

Solid-body rotation in the H_2 radial velocity implies the mass distribution interior to the disc can be approximated as a uniform-density sphere. We estimate the enclosed dynamical mass using $M_{\text{dyn}} = v_c(r)^2 r / G$ where $v_c(r) \propto r$ is the rotational velocity at radius r and G is the gravitational constant. From our best-fitting thin-disc model, the rotational speed of the disc at its edge is $v_c(r = 0.8 \text{ kpc}) \approx 425 \text{ km s}^{-1}$ and a dynamical mass $M_{\text{dyn}} \approx 3.4 \times 10^{10} M_{\odot}$.

Dale et al. (2005) derived an expression for the mass of warm H_2 using the $\text{H}_2 1-0\text{S}(1)$ flux $F_{1-0\text{S}(1)}$ assuming LTE conditions and a temperature of 2000 K:

$$M_{\text{H}_2, \text{warm}} \approx 5.08 M_{\odot} \left(\frac{F_{1-0\text{S}(1)}}{10^{-16} \text{ W m}^{-2}} \right) \left(\frac{\text{d}}{\text{Mpc}} \right)^2. \quad (2.2)$$

Using this method we obtain $M_{\text{H}_2, \text{warm}} (T = 2000 \text{ K}) = 9.7 \times 10^3 M_{\odot}$. We note that we are only able to place an upper limit of $\approx 6 \times 10^4 \text{ K}$ on the H_2 temperature using our excitation diagram (Fig. 2.6), hence this mass is an approximate estimate.

Willett et al. (2010) also estimate the mass of warm H_2 using mid-IR pure rotational (0-0) H_2 emission lines from *Spitzer* observations. For 4C 31.04 they find $M_{\text{H}_2, \text{warm}} = (4.7 \pm 1.3) \times 10^6 M_{\odot}$ at a temperature $T = 338 \pm 100 \text{ K}$, a mass $\sim 10^2$ greater than the mass of much warmer H_2 we find. Combined with the temperature constraints provided by our excitation diagram (Fig. 2.6), we conclude that the ro-vibrational emission we detect in our NIFS observations traces a small, and relatively hot, fraction of the total warm H_2 in the nucleus of 4C 31.04.

In Table 2.3 we compare the mass estimates of different ISM phases of 4C 31.04 from this work and the literature. We assume that the most reliable estimate of the cold H_2 gas mass is that of Ocaña Flaquer et al. (2010) derived from CO measurements, which gives a warm H_2 -to-total molecular gas mass fraction of $\sim 10^{-3}$.

2.5 Discussion

In this section, we analyse the energetics, kinematics and morphology of the [Fe II] and H_2 emission and argue that they indicate strong jet-ISM interactions are occurring in 4C 31.04.

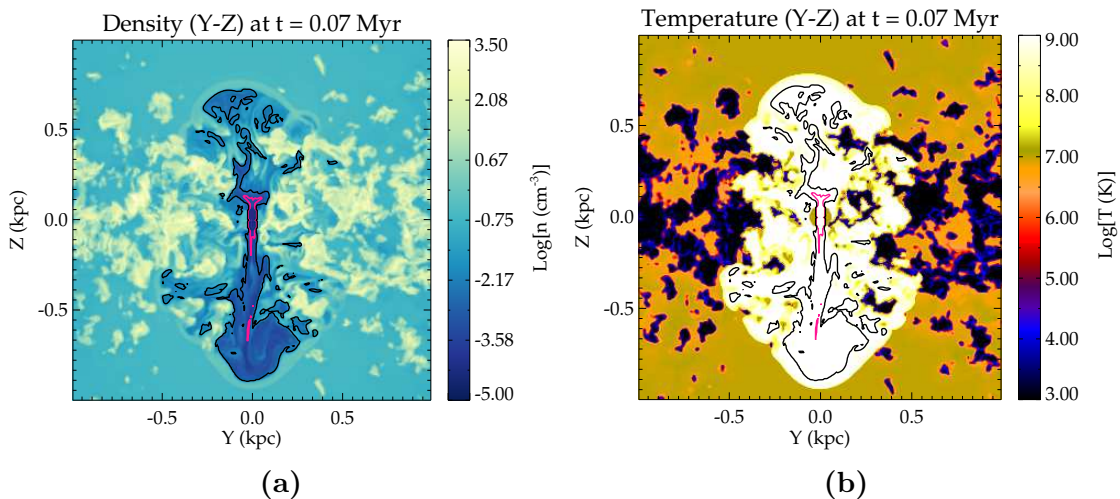


Figure 2.8: Mid-plane slices from a hydrodynamical simulation of a jet with $F_{\text{jet}} = 10^{45} \text{ erg s}^{-1}$ propagating in the Z -direction through a clumpy disc at an angle of 20° (model C of Mukherjee et al. (2018b); see their table 2 for simulation parameters); (a) shows the density and (b) shows the temperature. The magenta contours represent jet plasma that will emit brightly in the radio (jet tracer value $\phi = 0.5$) and the black contours trace much fainter plasma ($\phi = 0.005$) which fills the jet-driven bubble and drives shocks into the surrounding ISM.

Hydrodynamical simulations have shown that young, compact jets such as those in 4C 31.04 are capable of influencing the evolution of their host galaxies by injecting turbulence and driving shocks into the ISM (e.g., Sutherland & Bicknell 2007; Wagner & Bicknell 2011; Mukherjee et al. 2016, 2018a,b). Importantly, the coupling efficiency of the kinetic energy and momentum from the jet into the ISM peaks in these early stages of jet evolution (Wagner & Bicknell 2011; Mukherjee et al. 2016), emphasising the importance of this epoch in the context of jet-driven feedback.

In an early phase of jet evolution described as the ‘energy-driven bubble’ stage by SB07, the jets become deflected and split as they encounter dense clumps in the ISM, forming streams of plasma that percolate through the ISM over a broad solid angle. Midplane density and temperature slices of a hydrodynamical simulation showing this phenomenon are shown in Fig. 2.8, with corresponding synthetic radio images shown in Fig. 2.9. The jet plasma inflates a high pressure, pseudo-spherical, energy-driven bubble that drives a forward shock into the ISM, dispersing clouds and accelerating them outwards. The low-density synchrotron-emitting plasma in the bubble cavity manifests as extended, low surface brightness radio emission (e.g., fig. 5 in Wagner & Bicknell 2011). Simulations of jets propagating into dense, clumpy discs (Mukherjee et al. 2018b) have shown that jets may also drive subrelativistic flows of plasma into the disc plane, inducing shocks and turbulence. The jet plasma ablates clouds, and triggers hydrodynamical instabilities that form filaments. Ram pressure and thermal pressure gradients from shocks accelerates these clouds and filaments in a radial direction, introducing significant non-circular motions into the disc.

Our observations, together with its young age and small size, strongly suggest that the radio jets of 4C 31.04 are in the ‘energy-driven bubble’ stage, where the jets are interacting strongly with the dense and clumpy circumnuclear disc. By comparing our observations with hydrodynamical simulations, we formulate the model

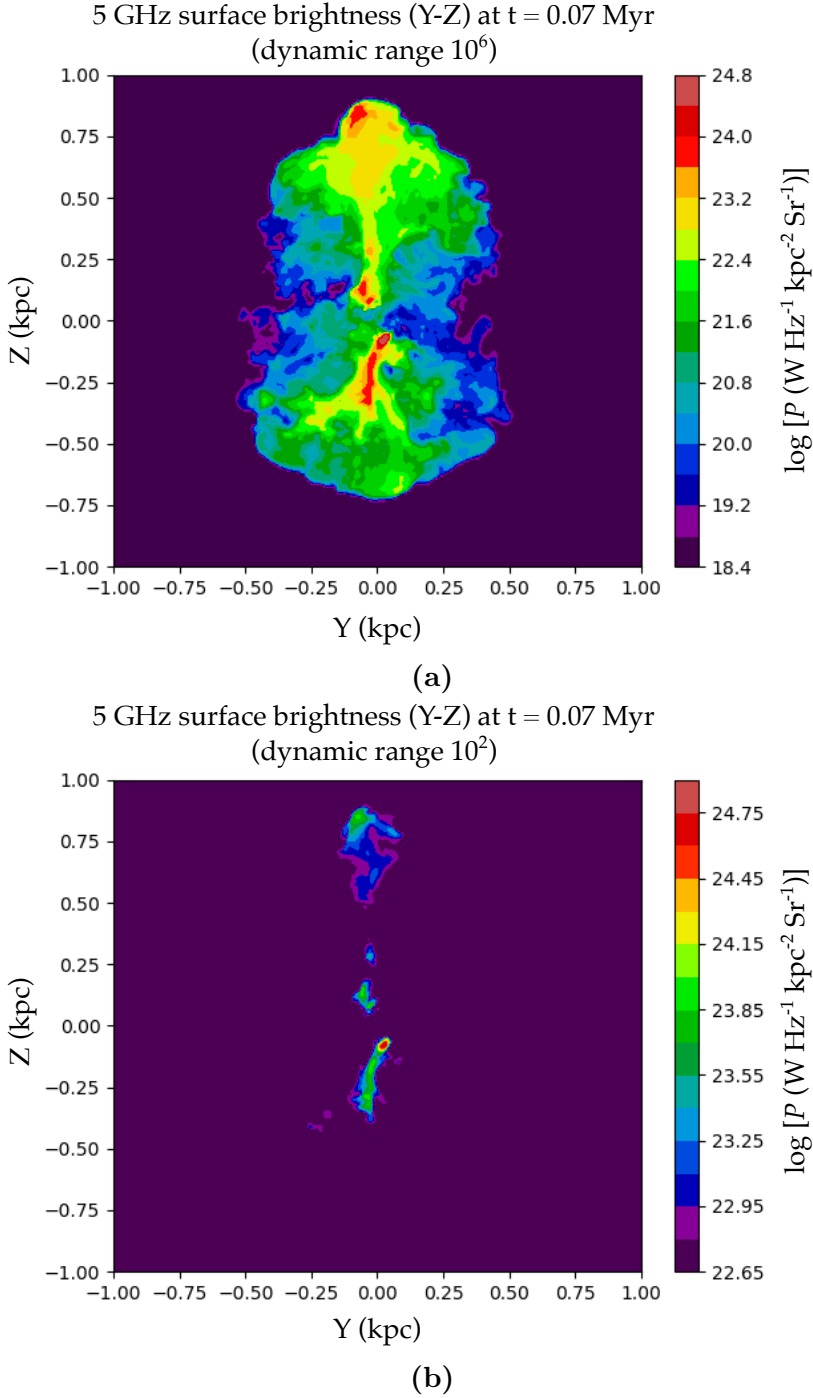


Figure 2.9: Synthetic radio surface brightness maps corresponding to the simulated mid-plane density and temperature slices shown in Fig. 2.8 at rest-frame 5 GHz with dynamic ranges of 10^6 and 10^2 respectively. The axis labels are in kpc and the intensity is given in $\log [P(\text{W Hz}^{-1} \text{kpc}^{-2} \text{Sr}^{-1})]$. Comparing (a) and (b) demonstrates that a high dynamic range may be necessary to observe low surface brightness plasma extending beyond the radio lobes into the jet-driven bubble. We note that the dynamic range of (b) is comparable to that of the 5 GHz VLBI observations of 4C 31.04 by Gi03, suggesting that higher dynamic range observations could reveal jet plasma out to the extent of the [Fe II] emission we observe in 4C 31.04.

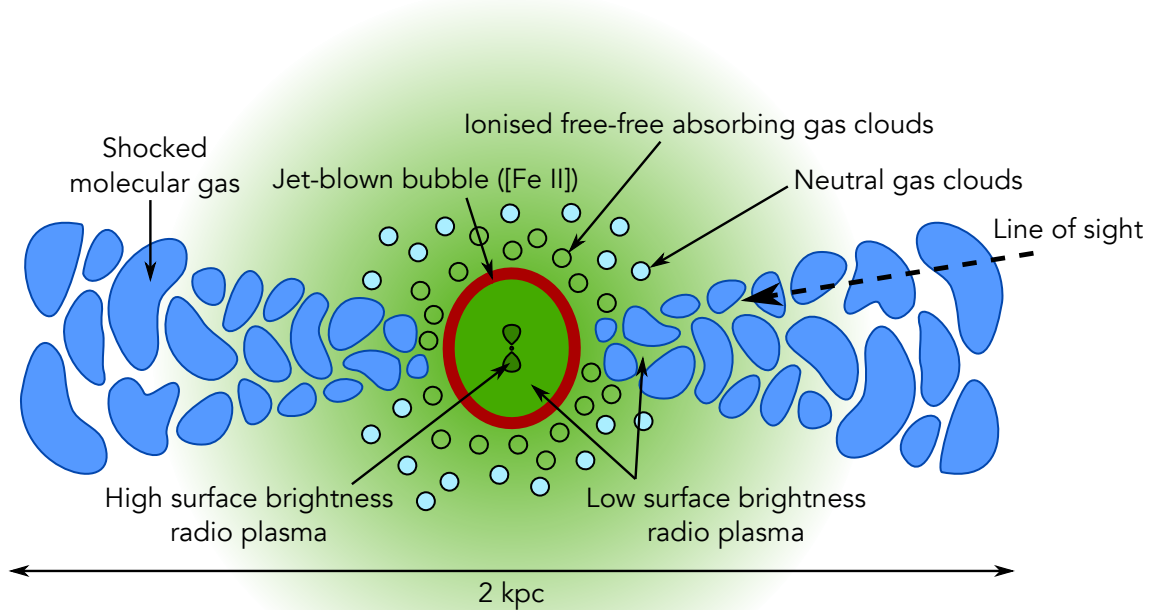


Figure 2.10: A top-down cross-section view of 4C 31.04 showing different components of the shocked gas in context, approximately to scale. Indicated in dark green are the 100 pc-scale radio lobes visible in VLBI observations Giovannini et al. (2001); Giroletti et al. (2003). The paler green region represents low surface-brightness jet plasma filling the jet-driven bubble, which drives a shock into the surrounding gas and causes [Fe II] emission (dark red). Jet plasma also percolates radially through channels in the clumpy circumnuclear disc (blue), driving shocks into neutral gas and causing H₂ emission. Clouds of ionized gas that free-free absorb synchrotron radiation from the jet plasma cause the spectral turnover at 400 MHz are indicated in transparent circles. The pale blue circles represent clouds of neutral gas. The line of sight is indicated by the dashed line; the disc is inclined such that the Western lobe is partially obscured by the disc, whereas the Eastern lobe is completely obscured by the disc, which is consistent with the H I absorption map (Conway 1996; Struve & Conway 2012).

described by Fig. 2.10, which shows a top-down cross-sectional view of the circumnuclear disc of dust and atomic and molecular gas orbiting the nucleus. The inclination of the disc is such that the Eastern radio lobe is obscured; this is consistent with the greater H I opacity on that side (Conway 1996; Struve & Conway 2012). The 100 pc-scale radio lobes (dark green) are shown to scale. The jet plasma inflates an expanding bubble which drives fast shocks into the surrounding ISM, destroying dust grains and launching material out of the disc plane, which is traced by [Fe II] (dark red) and high-velocity H I clouds (pale blue circles) detected in absorption by Conway (1996). Shocked ionized gas (transparent circles) free-free absorbs synchrotron emission from the jet plasma, causing the spectral turnover at 400 MHz. The jet plasma also drives radial flows into the disc, decelerating as it shocks molecular gas (blue), causing ro-vibrational H₂ emission. The plasma may also radially accelerate this gas to speeds $\sim 100 \text{ km s}^{-1}$, giving rise to non-circular motions including blueshifted H₂ emission and HCO⁺ and H I absorption.

2.5.1 Updated jet flux estimate

Comparing the jet flux with observed emission line luminosities is important in determining whether it is plausible for the jets to be causing the line emission. Hence, before we discuss the excitation mechanisms for the [Fe II] and H₂ emission in Sections 2.5.2 and 2.5.3 respectively, we provide an updated estimate of the jet flux of 4C 31.04.

SB07 estimate the jet flux in 4C 31.04 by calculating the minimum energy density in the radio lobes to produce the observed synchrotron flux in 1.7 GHz VLBI observations, and find $4.4 \times 10^{43} \text{ erg s}^{-1}$ and $1.5 \times 10^{43} \text{ erg s}^{-1}$ in the Western and Eastern lobes respectively. We follow the same minimum energy method to calculate the jet flux, this time using higher resolution VLBI observations of Gi03 to achieve an improved estimate. Our input and output parameters are shown in Table 2.4. Using their 5 GHz VLBA image, we divide both East and West lobes up into sections of approximately constant flux density. We model each section as volume with depth L along the line of sight, which we assume to be equal to its width. We assume the volumes contain a randomly oriented magnetic field of strength B and a relativistic electron population with distribution $N(\gamma) = K\gamma^{-a}$ for $\gamma \in [\gamma_1, \gamma_2]$. In this simple model, the minimum energy density required to produce a given specific intensity of synchrotron emission I_ν is

$$\varepsilon_{\text{min,tot}} = (1 + c_E)\varepsilon_{e,\text{min}} + \frac{B_{\text{min}}^2}{2\mu_0} \quad (2.3)$$

where $\varepsilon_{e,\text{min}}$ is the minimum energy density in relativistic electrons and c_E represents the energy fraction in other species, which we assume to be 0. The minimum energy magnetic field and energy density in particles are given by

$$B_{\text{min}} = \frac{m_e}{e} \left[\frac{a+1}{2} (1 + c_E) C_2(a)^{-1} \frac{c}{m_e} \left(\frac{I_\nu \nu^\alpha}{L} f(a, \gamma_1, \gamma_2) \right) \right]^{\frac{2}{a+3}} \quad (2.4)$$

$$\varepsilon_{p,\text{min}} = \frac{4}{a+1} \frac{B_{\text{min}}^2}{2\mu_0}$$

respectively, where $\alpha = (a - 1)/2$ is the spectral index of the synchrotron emission and $C_2(a)$ and $f(a, \gamma_1, \gamma_2)$ are constants. We find $\varepsilon_{p,\text{min}} \sim 10^{-5} \text{ erg cm}^{-3}$ and $B_{\text{min}} \sim 10^{-2} \text{ G}$ in all parts of the radio lobes.

We assume that that half of the energy injected by the jets goes into pdV work on the surrounding ISM and the other half into the energy density in both particles and magnetic field, which is typical of jet-driven bubble models (Bicknell et al. 1997). Under this assumption, the total energy in the lobes is given by

$$E_{\text{lobe}} = \frac{1}{2} \sum_{\text{min},i} \varepsilon_i V_i \quad (2.5)$$

and the corresponding jet flux, assuming a constant rate of energy injection over a time t_{lobe} , is given by

$$F_{\text{jet}} = \frac{1}{t_{\text{lobe}}} \frac{1}{2} \sum_{\text{min},i} \varepsilon_i V_i \quad (2.6)$$

Table 2.4: Parameters used in determining the jet flux. Output parameters are denoted with daggers (\dagger).

Parameter	Symbol	Value
Min. electron Lorentz factor	γ_1	10^2
Max. electron Lorentz factor	γ_2	10^5
Age of radio lobes (Gi03)	t_{lobe}	5000 yr
Temperature of ambient ISM	T_a	10^7 K
Density of ambient ISM	n_a	0.1 cm^{-3}
Radius of jet-blown bubble	$R_{[\text{Fe II}]}$	175 pc
Eastern jet flux \dagger	$F_{\text{jet, Eastern lobe}}$	$1.50 \times 10^{44} \text{ erg s}^{-1}$
Western jet flux \dagger	$F_{\text{jet, Western lobe}}$	$1.44 \times 10^{44} \text{ erg s}^{-1}$
Total jet flux	F_{jet}	$2.94 \times 10^{44} \text{ erg s}^{-1}$

where V_i is the volume and ε_i is the minimum energy computed using Eqn. 2.3. Assuming an upper limit for the age of the lobes $t_{\text{lobe}} = 5000 \text{ yr}$ from Gi03 based on synchrotron spectral decay, we find $F_{\text{jet, Western lobe}} = 1.44 \times 10^{44} \text{ erg s}^{-1}$ and $F_{\text{jet, Eastern lobe}} = 1.50 \times 10^{44} \text{ erg s}^{-1}$.

2.5.2 The origin of the [Fe II] emission

Fast shocks destroy dust grains, releasing Fe I into the gas phase, which then becomes singly ionized by the interstellar radiation field. In the post-shock region, Fe II becomes collisionally excited and emits emission lines in the near-IR, including [Fe II], which can therefore be used as a shock tracer.

Fig. 2.2 shows that the [Fe II] emission is localised to the innermost few 100 pc of the nucleus, and that the radial velocity field is consistent with material being ejected from the disc plane on either side. The kinematics and location of the [Fe II] emission suggest that it arises from shocks driven by the expanding bubble inflated by the radio jets.

However, SNe explosions can also give rise to strong [Fe II] emission; we now determine whether this is a plausible mechanism in 4C 31.04. To calculate the required SNe rate to produce the observed [Fe II] emission, we use the empirical relationship between SN rate and $[\text{Fe II}]_{1.26 \mu\text{m}}$ luminosity for starburst galaxies derived by Rosenberg et al. (2012):

$$\log \frac{\nu_{\text{SN rate}}}{\text{yr}^{-1}} = (1.01 \pm 0.2) \log \frac{L([\text{Fe II}]_{1.26 \mu\text{m}})}{\text{erg s}^{-1}} - (41.17 \pm 0.9) \quad (2.7)$$

Because $[\text{Fe II}]_{1.26 \mu\text{m}}$ lies outside the wavelength range of our observations, we assume any reddening is negligible and use the intrinsic ratio $[\text{Fe II}]_{1.26/1.64 \mu\text{m}} = 1.36$. The integrated luminosity is given by $L([\text{Fe II}]_{1.644 \mu\text{m}}) = 4\pi D_L^2 F([\text{Fe II}]_{1.644 \mu\text{m}}) = 1.19 \times 10^{40} \text{ erg s}^{-1}$ where $F([\text{Fe II}]_{1.644 \mu\text{m}})$ is the integrated flux (Table 2.1) and the luminosity distance $D_L = 271.3 \text{ Mpc}$. Using Eqn. 3.6 yields an integrated SN rate $\nu_{\text{SN rate, [Fe II]}} = 0.2761 \text{ yr}^{-1}$.

We now use the measured SFR to estimate $\nu_{\text{SN rate}}$ using a solar metallicity Starburst99 (Leitherer et al. 1999) model with a continuous $1 M_{\odot} \text{ yr}^{-1}$ SF law and a Salpeter IMF at an age of 1 Gyr. After multiplying to match the SFR of 4C 31.04

($4.9 M_{\odot} \text{ yr}^{-1}$, Ocaña Flaquer et al. 2010) we find $\nu_{\text{SNrate, SFR}} = 0.1 \text{ yr}^{-1}$, less than half the rate required to power the [Fe II] emission.

We therefore rule out star formation as the excitation mechanism for the [Fe II], and instead argue that the emission is driven by a jet-ISM interaction. As illustrated in Fig. 2.10, the bubble drives fast shocks into the ISM, destroying molecular gas. The shocked gas is accelerated outwards by the forward shock and also by the jet streams, creating an expanding bubble illuminated in [Fe II].

2.5.3 The origin of the H₂ emission

Large masses of warm H₂ seem to be common in the hosts of nearby radio galaxies, suggesting a link between the H₂ emission and radio activity (e.g., Nesvadba et al. 2010; Ogle et al. 2010). As discussed in Section 2.4.2, we detect ro-vibrational H₂ emission in the circumnuclear disc $\approx 2 \text{ kpc}$ in diameter, which probes relatively hot ($\sim 10^3 \text{ K}$) molecular gas. The line ratios show the warm H₂ is shock excited (Table 2.2 and Fig. 2.7).

In this section, we show that the $\sim 10^3 \text{ K}$ H₂ represents a relatively hot fraction of a much larger reservoir of H₂ heated by a jet-ISM interaction, the bulk of which is much cooler ($\sim 10^2 \text{ K}$). In our model, shown in Fig. 2.10, the jet-driven bubble drives fast shocks into the gas at small radii, causing [Fe II] emission, before decelerating as it drives shocks into the denser molecular gas in the disc. We also postulate that jet plasma percolating radially throughout the disc also accelerates clouds to the observed systemic blueshift of $\approx 150 \text{ km s}^{-1}$ in the warmer H₂ component (Fig. 2.3c).

Excitation mechanism

The ro-vibrational-emitting H₂ probed by our observations is very warm (Fig. 2.6), and cools rapidly. This phase is therefore very short-lived, and accordingly only represents a very small fraction of the total H₂ mass (Table 2.3). Willett et al. (2010) report a much larger ($\sim 10^6 M_{\odot}$) reservoir of cooler H₂, at a temperature $\sim 300 \text{ K}$. We wish to determine whether this cooler component represents gas in the circumnuclear disc that has been processed by the jets and since cooled; to do this we use mid-IR diagnostics to reveal the excitation mechanism of the cooler H₂ component.

Using the combined luminosity of the H₂ 0–0 S(0,1,2,3) lines (Willett et al. 2010) we place a lower limit on the ratio $L(\text{H}_2)/L(\text{PAH } 7.7 \mu\text{m}) \geq 0.1$, where we calculate the luminosity of the PAH feature at $7.7 \mu\text{m}$ using that of the $11.3 \mu\text{m}$ and assuming $L(\text{PAH } 6.2 \mu\text{m})/L(\text{PAH } 7.7 \mu\text{m}) = 0.26$, which holds for the sample of H₂-luminous radio galaxies of Ogle et al. (2010); this gives $L(\text{PAH}, 7.7) = 1.55 \times 10^{42} \text{ erg s}^{-1}$. The criterion of Ogle et al. (2010) ($L(\text{H}_2)/L(\text{PAH } 7.7 \mu\text{m}) > 0.04$) strongly suggests the H₂ is shock heated.

We also use the diagnostic diagram of Nesvadba et al. (2010, their fig. 6), which separates star formation from other mechanisms as the source of H₂ heating using the luminosity ratios of the summed H₂ 0–0 S(0)–S(3) lines to the ¹²CO(1–0) and to the PAH feature at $7.7 \mu\text{m}$. Whilst the CO emission traces cold molecular gas from which stars form, PAH features trace UV photons excited by star formation; hence these ratios can be used to indicate the contribution of star formation in photon-dominated regions (PDRs) to the H₂ heating. To calculate the CO(1-0) luminosity,

we convert the I_{CO} given by Ocaña Flaquer et al. (2010) into a luminosity using eqn. 3 of Solomon et al. (1997), yielding $L(\text{CO}) = 3.56 \times 10^{38} \text{ erg s}^{-1}$. We find $L(\text{H}_2)/L(\text{PAH}, 7.7) \geq 0.148$ and $L(\text{H}_2)/L(\text{CO}) \geq 6.43 \times 10^2$, placing 4C 31.04 well outside the regions covered by PDR models, showing that the $\sim 300 \text{ K H}_2$ component is not predominantly heated by UV photons, leaving shocks, cosmic rays and X-ray heating as plausible mechanisms.

Based on our above arguments, both the $\sim 100 \text{ K}$ and $\sim 10^3 \text{ K H}_2$ is heated by a mechanism other than star formation. We argue that the $\sim 10^3 \text{ K}$ and $\sim 100 \text{ K H}_2$ are physically associated; in this case the strong shock signature we observe in the former (Fig. 2.7) shows that the warm H_2 is shock excited.

What is driving the shocks?

We now show that the observed H_2 luminosity cannot be produced by shocks driven by gas accreting on to the disc. The energy dissipated by gas accreting on to the disc at a rate \dot{M} from $r = \infty$ to $r = r_0$ is given by

$$L_{\text{disc}} = \left[\frac{1}{2} v_c(r_0)^2 + \Phi(r_0) \right] \dot{M} \quad (2.8)$$

where $\Phi(r)$ is the galactic potential and $v_c(r)$ is the velocity of a circular orbit at radius r . We assume that the jet-driven bubble disrupts the H_2 disc at smaller radii, hence we use $r_0 = 175 \text{ pc}$, the approximate extent of the [Fe II] emission.

To obtain $\Phi(r)$ and $v_c(r)$, we fit a simple $1/n$ Sérsic profile to the K band continuum and use the analytical expressions given by Terzić & Graham (2005). To check the validity of our M_* estimate, we compare the circular velocity predicted by the model with that of the warm H_2 in the circumnuclear disc from our NIFS observations. We find that a lower stellar mass $\log M_* = 10.9$ is better able to reproduce the observed v_c at 1 kpc than our estimate based on 2MASS K_s band photometry ($\log M_* = 11.4$; see Section 2.2.1). However, we find that this correction only changes the resulting accretion disc luminosity to within an order of magnitude; hence, for simplicity, we use the stellar mass predicted by the 2MASS K_s band magnitude.

If we assume a steady state accretion model, that is \dot{M} is equal to the accretion rate onto the black hole, and that 10 per cent of the rest-mass energy of the accreted material per unit time is emitted in the form of the radio jets, i.e., $L_{\text{BH}} = 0.1 \dot{M} c^2 = 2.94 \times 10^{44} \text{ erg s}^{-1}$, then the accretion rate $\dot{M} \approx 0.05 M_{\odot} \text{ yr}^{-1}$. Using Eqn. 2.8, we estimate an accretion disc luminosity $L_{\text{disc}} \sim 10^{40} \text{ erg s}^{-1}$, an order of magnitude lower than the observed H_2 0–0 luminosity $L_{\text{H}_2} \geq 2.3 \times 10^{41} \text{ erg s}^{-1}$, enabling us to rule out accretion as the mechanism heating the H_2 . Meanwhile, the H_2 luminosity represents ~ 0.1 per cent of the estimated jet flux (Section 2.5.1), so that there is ample jet power to drive the H_2 luminosity via radiative shocks. We therefore conclude that the shocks are being driven by the jets, a scenario which also explains the sharp peak in the H_2 flux in the vicinity of the nucleus (Fig. 2.3b).

Explaining the peculiar blueshift in the H_2

Shocks induced by a jet-ISM interaction out to kpc-scale radii in the circumnuclear disc could explain the peculiar systemic blueshift of $\approx 150 \text{ km s}^{-1}$ we observe in the

H₂ (Fig. 2.3c) relative to the redshift $z = 0.0602$ of Ga07.

Previous observations have revealed cold gas components with remarkably similar blueshifts: Ga07 detected an unresolved HCO⁺ component in absorption over the nucleus with a systemic blueshift of $\approx 150 \text{ km s}^{-1}$, whilst Struve & Conway (2012) found that the centre of the integrated H I absorption profile is centred on a similar blueshifted systemic velocity. The absorption profile also has a blue wing (their fig. 7) extending to $\sim 200 \text{ km s}^{-1}$. Prominent blue wings in the H I absorption profiles of powerful radio galaxies are a signature of fast neutral outflows (Morganti et al. 2005); we speculate that the blue wing in the profile of 4C 31.04 indicates that the jets are accelerating neutral gas out of the nucleus, albeit to much lower velocities than are observed in these more extended radio galaxies.

It is possible that the redshift is in fact lower than the estimate of Ga07, and that the H₂ rotation curve is centred on the systemic velocity of the galaxy. Ga07 calculated the redshift of 4C 31.04 by assuming that the HCO⁺ emission components to the North and South of the nucleus represented gas rotating in the disc, and that the mean velocity of the two components corresponds to the galaxy's systemic velocity. Struve & Conway (2012) argue that this assumption may be flawed if gas in the disc is dynamically unsettled. Correcting the redshift to remove the blueshift in the $\sim 10^3 \text{ K}$ H₂, H I and HCO⁺ absorption yields $z = 0.0597 \pm 0.001$. Whilst this is consistent with the redshift from optical spectroscopy ($z = 0.060 \pm 0.001$, Marcha et al. (1996)), it would mean the [Fe II] emission is in fact redshifted by $\approx 150 \text{ km s}^{-1}$, which would be difficult to explain under our interpretation that it traces a jet-driven bubble.

An alternate explanation is that the blueshifted warm and cold molecular phases trace clouds of gas being radially accelerated in circumnuclear disc by jet plasma. As mentioned earlier, hydrodynamical simulations by Mukherjee et al. (2018b) of jets evolving in galaxies with clumpy gas discs have shown that the expanding bubble driven by the jets drives subrelativistic radial flows into the disc plane. These flows drive turbulence and shocks into the gas, and introduce significant non-circular motions. In addition to the observed blueshifted gas, radial flows of jet plasma may be able to explain the reported unrelaxed dynamics in the gas disc (Pe01; Ga07), which has previously been attributed to gas settling on to the disc in the process of accretion. We note that $\sim 100 \text{ pc}$ -scale equatorial outflows have been recorded in other radio galaxies, such as NGC 5929 (Riffel et al. 2015) and NGC 1386 (Lena et al. 2015). These outflows have tentatively been attributed to torus outflows or accretion disc winds; it is unclear whether this mechanism could drive the relatively low-velocity blueshifted gas we observe in 4C 31.04.

We now calculate the kinetic energy associated with the observed blueshift in the H₂ to show that it is plausible that it is driven by the jets. Assuming that both the $\sim 100 \text{ K}$ and $\sim 10^3 \text{ K}$ H₂ are accelerated to the observed blueshifted velocity, the cooler component ($4.7 \pm 1.3 \times 10^6 M_{\odot}$, Willett et al. 2010) will dominate the kinetic energy. If the blueshifted clouds have a velocity 150 km s^{-1} , then the associated kinetic energy is $\approx 1.1 \times 10^{54} \text{ erg}$. Assuming the gas is being pushed radially outwards at a constant velocity, the time taken for material to reach the farthest extent of the warm H₂ disc $\approx 1 \text{ kpc}$ from the nucleus is $\tau = 6.5 \times 10^6 \text{ yr}$. Assuming the jet has been accelerating this gas over this time period, this yields an energy injection rate $\sim 10^{41} \text{ erg s}^{-1}$, approximately 0.1 per cent of the jet power we estimated in Section 2.5.1, showing that it is indeed plausible.

In light of these arguments, we tentatively agree with the redshift quoted by Ga07, and speculate that the blueshifted H_2 , H I and HCO^+ traces gas clouds being radially accelerated in the disc plane by the jet plasma. Confirmation of this scenario will require further observations, e.g., high-resolution optical spectroscopy to measure the galaxy’s redshift using stellar absorption features.

How far does the jet plasma extend?

In the previous sections we have shown that both the $[\text{Fe II}]$ and H_2 emission are caused by a jet-ISM interaction. However, the radio lobes extend ≈ 60 pc from the nucleus, whereas we detect $[\text{Fe II}]$ over a region ≈ 3 times larger, and warm H_2 out to \sim kpc radii—how could this emission possibly arise from a jet-ISM interaction?

Hydrodynamical simulations of jets propagating into clumpy discs (Mukherjee et al. 2018b) show that the brightest regions of jet plasma may become temporarily frustrated by dense clouds in the disc, slowing its propagation. This effect becomes more pronounced when the jets are inclined with respect to the disc normal, as it increases the effective path length over which the jets interact with the dense ISM. Meanwhile, the expanding bubble can advance rapidly once it escapes the dense ISM in the disc plane, allowing the bubble radius to grow several times larger than the radio lobes.

Our observations show the jets in 4C 31.04 are likely to be inclined $\sim 10^\circ - 20^\circ$ to the normal of the circumnuclear disc. This geometry is supported by the inclination of $\sim 60^\circ$ we measure from the warm H_2 and by the jets being at an angle of $\lesssim 15^\circ$ with respect to the sky, with the Western lobe nearest (Giovannini et al. 2001). Moreover, the kinematics of the $[\text{Fe II}]$ emission line (Fig. 2.2c) shows material being accelerated off the disc plane such that the Western lobe is pointing towards us.

In order to illustrate the role that a dense and clumpy disc can play in determining the outcome of a jet-ISM interaction, we show midplane density and temperature slices from a hydrodynamical simulation in which the jets are inclined 20° to the disc normal in Fig. 2.8. In Fig. 2.8a, the brightest parts of the jet plasma (magenta contours), particularly in the positive Z -direction, have become halted a short distance from the nucleus. Meanwhile, lower surface brightness plasma (black contours) propagates along channels in the clumpy ISM and fills the much larger bubble, which crucially may go undetected in high-resolution VLBI observations despite interacting strongly with the surrounding ISM. In Figs. 2.9a and 2.9b we show corresponding synthetic 1 GHz surface brightness maps with high and low dynamic ranges respectively, where we define the dynamic range as the maximum measured flux divided by the minimum flux level that can be detected. Comparing the two illustrates the importance of a high dynamic range in revealing the low surface brightness plasma that traces the true extent of the jet-driven bubble. We note that Fig. 2.9b is missing only ≈ 1 per cent of the total flux recovered in Fig. 2.9a. This illustrates that VLBI observations with flux completeness measurements in excess of 99 per cent can miss jet plasma that may still be interacting strongly with the surrounding ISM.

Multiple flux completeness measurements of VLBI observations of 4C 31.04 indeed indicates that some large-scale structure exists at lower surface brightnesses than have been observed. Cotton et al. (1995) find that 98 per cent and 76 per cent

of the flux density of 4C 31.04 measured with the VLA is recovered in VLBI observations at 1.7 and 8.4 GHz respectively. Gi03 find that approximately 90 per cent of the flux measured with single-dish observations is recovered with VLBI at 5 GHz. Altschuler et al. (1995) recover 80 per cent of the total flux density at 92 cm. We note that the 5 GHz VLBI image of Gi03 has a dynamic range of ~ 100 ; this, combined with the $\sim 75 - 95$ per cent flux completeness of GHz-range VLBI observations, suggests that 4C 31.04 may indeed harbour low surface brightness radio emission out to the radii at which we observe shocked gas, resolving the inconsistency between the extent of the shocked gas and the radio lobes.

2.5.4 Age of the radio source

We cannot estimate the true age of the radio jets in 4C 31.04 with existing VLBI observations as they resolve out low surface brightness radio emission that fills a much larger bubble revealed by our NIFS observations. Moreover, because the rate at which synchrotron-emitting electrons lose energy E is proportional to E^2 , high-frequency, high surface-brightness radio emission only probes the youngest synchrotron electrons; parts, or even most, of the emission from the jet plasma may be missed by GHz-frequency observations with a small dynamic range. We instead use the jet flux and our NIFS observations to estimate the true age of the radio jets.

We model the radio lobes as bubbles expanding adiabatically into a uniform ISM using the model of Bicknell & Begelman (1996). We assume that the bubbles are expanding out of the disc plane into the ambient hot ISM with pressure $P/k \sim 10^6 \text{ K cm}^{-3}$ typical in the interiors of local elliptical galaxies (Werner et al. 2012) and $T_a \sim 10^7 \text{ K}$, $n_a = P/kT_a \approx 0.1 \text{ cm}^{-3}$. The age of the bubble is given by

$$t_b = \left(\frac{384\pi}{125} \right)^{1/3} \rho_a^{1/3} F_{\text{jet}}^{-1/3} R_b^{5/3} \quad (2.9)$$

where R_b is the radius of the bubble and F_{jet} is the total jet flux in erg s^{-1} .

We calculate a lower limit for the age of the radio source by assuming that the jet plasma has only reached the extent of the [Fe II] emission, ignoring the extended H_2 emission. In this case, we set $R_b \approx 175 \text{ pc}$ and find $t_b \approx 17 \text{ kyr}$, more than 3 times older than the age estimated using synchrotron spectral decay (4000–5000 yr, Gi03).

In Section 2.5.3, we estimated an upper limit for the jet age $6.5 \times 10^6 \text{ yr}$ by calculating the time taken for material to reach the farthest extent of the warm H_2 disc, and is an upper limit as the gas may have decelerated along its trajectory.

Although these age estimates are very crude, together they suggest that the previous age estimates based on VLBI imaging alone may not represent the true age of the source. Our results demonstrate the importance of optical or near-IR tracers of jet-ISM interaction in estimating the true extent of the jet plasma, particularly when existing radio observations have a low dynamic range or are not sensitive to the angular scales associated with the diffuse plasma filling the jet-driven bubbles.

2.5.5 Density distribution of the clumpy ISM

Free-free absorption (FFA) by clumpy gas ionized by the radio jets is a feasible cause of the spectral turnover in GPS and CSS sources (Bicknell et al. 2018). Here,

we use the peak in the radio spectrum of 4C 31.04 to infer the parameters of the density distribution of the ionized, free-free absorbing ISM, in order to inform future hydrodynamical simulations. We use a simple analytical model to calculate the specific intensity of synchrotron-emitting plasma embedded in a clumpy free-free absorbing medium.

We assume the density n of the ionized medium follows a log normal distribution, which is appropriate for a turbulent medium (e.g., Federrath & Klessen 2012). The log normal distribution has the probability distribution function (PDF)

$$P(n) = \frac{1}{\sqrt{2\pi}s} \exp \left[-\frac{(\ln n - m)^2}{2s^2} \right] \quad (2.10)$$

which is a Gaussian in $\ln n$, where m is the mean log density and s is the width of the distribution in log density. (e.g., SB07). The parameters s and m can be related to the expected value $E(n)$ of the density, i.e. the mean density μ , $E(n^2)$, and the variance σ^2 of the density distribution using the relations

$$\mu = E(n) = e^{m+\frac{1}{2}s^2} \quad (2.11)$$

$$E(n^2) = e^{2(m+s^2)} \quad (2.12)$$

$$\sigma^2 = \mu^2 (e^{s^2} - 1). \quad (2.13)$$

We assume that the only ions contributing to FFA are H^+ , He^+ and He^{++} . For a species i with charge Ze the linear absorption coefficient at a frequency ν is

$$\alpha_{\nu,i}(Z) = \sqrt{\frac{32\pi}{27}} c^2 r_0^3 \left(\frac{kT}{m_e c^2} \right)^{-3/2} n_e n_i(Z) Z^2 g_\nu(T, Z) \nu^{-2} \quad (2.14)$$

where $n_i(Z)$ and n_e are the species and electron number densities respectively, T is temperature and $g(T, Z)$ is the Gaunt factor. For clarity, we write

$$\alpha_{\nu,i}(Z) = n^2 K T^{-3/2} \chi_{\nu,i}(Z) \nu^{-2} \quad (2.15)$$

where K is a collection of constants and

$$\chi_{\nu,i}(Z) = \frac{n_e n_i(Z)}{n} Z^2 g_\nu(T, Z). \quad (2.16)$$

If the absorption coefficients α_ν are constant along the line of sight, then the expected FFA optical depth is given by

$$\tau_\nu = E(n^2) K T^{-3/2} \left[\sum_i \sum_Z \chi_{\nu,i}(Z) \right] \nu^{-2} L \quad (2.17)$$

where $E(n^2)$ is the expected value of n^2 given the density PDF, and L is the depth of the absorbing screen. We assume that the 100 pc-scale jets ionize clouds of material on the inner edge of the circumnuclear disc, which then free-free absorb radio emission from the jet plasma. This is consistent with the high-velocity H I clouds and regions of free-free absorbed 1.4 GHz continuum emission detected in front of

Table 2.5: Parameters used in determining the parameters of the log-normal density distribution. Output parameters are denoted with daggers (\dagger).

Parameter	Symbol	Value
Peak frequency	ν_{peak}	400 MHz
Depth of absorbing slab	L	100 pc
Temperature	T	10059 K
Mean molecular mass	μ'	0.66504
Electron fractional abundance	n_e/n	0.47175
H ⁺ fractional abundance	n_{H^+}/n	0.41932
He ⁺ fractional abundance	n_{He^+}/n	0.024458
He ⁺⁺ fractional abundance	$n_{\text{He}^{++}}/n$	0.013770
Velocity dispersion	σ_v	350 km s ⁻¹
Turbulent forcing parameter	b	0.4
Ratio of thermal to magnetic pressure	β	1 (equipartition)
Expected value of $n^{2\dagger}$	$E(n^2)$	$1.89 \times 10^4 \text{ cm}^{-6}$
Mean density [†]	μ	15.5 cm^{-3}
Density variance [†]	σ^2	$1.86 \times 10^4 \text{ cm}^{-6}$

both lobes (Conway 1996). Hence we take $L = 100$ pc.

The parameter s in the log-normal distribution can be related to the properties of the ISM using

$$s^2 = \ln \left(1 + b^2 \mathcal{M}^2 \frac{\beta}{\beta + 1} \right) \quad (2.18)$$

which applies when the magnetic field strength $B \propto \rho^{1/2}$ (Federrath & Klessen 2012). Here, b is the turbulent forcing parameter, β is the ratio of thermal to magnetic pressure and $\mathcal{M} = \sigma_v/c_s$ is the Mach number where σ_v is the velocity dispersion and $c_s = \sqrt{kT/\mu' \text{amu}}$ is the sound speed. We assume the velocity dispersion of the absorbing medium is that of the [Fe II] emission, approximately 350 km s⁻¹.

We calculate μ and σ^2 as follows, using the input parameters shown in Table 2.5. First, we use a MAPPINGS V (Sutherland et al. 2018) model grid with non-equilibrium cooling and solar abundances to compute the fractional abundances of electrons, H⁺, He⁺ and He⁺⁺ at a temperature $T \approx 10^4$ K. For each species, we use these values to calculate $\chi_{\nu,i}(Z)$ using Eqn. 2.16. Then, by setting $\tau_\nu = 1$ at the spectral peak (400 MHz) in Eqn. 2.17, we solve for $E(n^2)$. We then find s using Eqn. 2.18, which in turn allows us to find m using Eqn. 2.12. Finally, we solve for μ and σ using Eqns. 2.11 and 2.13, yielding $\mu = 15.5 \text{ cm}^{-3}$ and $\sigma^2 = 1.86 \times 10^4 \text{ cm}^{-6}$.

2.6 Conclusion

We have reported H and K band Gemini/NIFS observations of the Compact Steep Spectrum source 4C 31.04, a young AGN with jets interacting strongly with a clumpy ISM. The host of 4C 31.04 is a $z = 0.0602$ elliptical galaxy that harbours $\sim 10^9 M_\odot$ of gas in a circumnuclear disc ≈ 2 kpc in diameter.

In the central few 100 pc, we detect [Fe II] emission that has a radial velocity field consistent with an expanding bubble driven by the jets. We rule out SNe explosions

as the cause of the [Fe II] emission; moreover, the kinematics of the line trace an expanding bubble, implying the emission is a result of a jet-ISM interaction.

We also detect ro-vibrational H₂ emission that traces $\sim 10^4 M_{\odot}$ of very warm ($\sim 10^3$ K) H₂. This warm molecular phase traces rapidly cooling gas in the innermost \sim kpc of the circumnuclear disc, and represents a small fraction of a much larger ($\sim 10^6 M_{\odot}$) reservoir of warm ($\sim 10^2$ K) H₂. Near- and mid-IR line ratios indicate both H₂ components are excited by shocks. We show that shocks driven by accretion of gas on to the kpc-scale circumnuclear disc is unable to reproduce the observed H₂ luminosity, and conclude that the shocks must be driven by jet plasma percolating to kpc radii through channels in the clumpy disc. The $\sim 10^3$ K H₂ emission shows a systemic blueshift of $\approx 150 \text{ km s}^{-1}$ relative to the most widely accepted redshift of Ga07. We speculate that the blueshift is caused by jet plasma radially accelerating clouds in the disc plane to kpc radii. Previous observations of 4C 31.04 have revealed spatially-unresolved HCO⁺ and H I in absorption at similarly blueshifted velocities, which may represent cooler gas entrained in the same low-speed outflow. The blueshift could also be explained if the redshift of the galaxy is in fact lower than currently believed, although this would impart a significant redshift to our [Fe II] observations which would be difficult to explain.

Our observations demonstrate that 4C 31.04 is currently in the ‘flood-and-channel’ phase of evolution that has been predicted by hydrodynamical simulations (e.g., Mukherjee et al. 2016; Sutherland & Bicknell 2007), in which streams of jet plasma follow paths of least resistance through the ISM and form an energy-driven bubble. The bubble pushes a forward shock into the ambient ISM, giving rise to the [Fe II] emission. Jet plasma also percolates into the circumnuclear disc, shocking and radially accelerating gas clouds, giving rise to the H₂ emission.

The extent of the shocked gas in our NIFS observations is much larger than the radio lobes resolved in VLBI imaging, suggesting the presence of low surface brightness radio plasma that has not been previously observed. This is consistent with multi-frequency VLBI observations of 4C 31.04 with < 100 per cent flux completeness. In simulations of jets propagating through clumpy discs, the brightest regions of plasma are temporarily halted by dense clumps, whilst the lower density plasma channels can continue to expand freely out of disc plane, enabling the bubble to grow much larger than the jets resolved by low-dynamic range VLBI observations.

We estimated the jet flux using VLBI observations and use the observed bubble radius to constrain the ‘true’ age of the radio jets. We find the jet age $\gtrsim 17$ kyr, much older than previous literature estimates derived from the lobe expansion rate and using synchrotron spectral decay (Giroletti et al. 2003).

Finally, we calculated the parameters of the density distribution of the ISM from the peak of the radio spectrum using a FFA model. These parameters together with our estimates of the jet flux will be used to inform future hydrodynamical simulations tailored to 4C 31.04.

Our observations of 4C 31.04 demonstrate that optical and near-IR studies of radio galaxies can be crucial in determining the true extent of the radio plasma, particularly in the early stages of evolution in which low surface brightness radio plasma may be resolved out by VLBI observations.

Acknowledgements

Based on observations obtained at the Gemini Observatory (processed using the GEMINI IRAF package), which is operated by the Association of Universities for Research in Astronomy, Inc., under a cooperative agreement with the NSF on behalf of the Gemini partnership: the National Science Foundation (United States), the National Research Council (Canada), CONICYT (Chile), Ministerio de Ciencia, Tecnología e Innovación Productiva (Argentina), and Ministério da Ciência, Tecnologia e Inovação (Brazil).

Based on observations made with the NASA/ESA *Hubble Space Telescope*, and obtained from the Hubble Legacy Archive, which is a collaboration between the Space Telescope Science Institute (STScI/NASA), the Space Telescope European Coordinating Facility (ST-ECF/ESA) and the Canadian Astronomy Data Centre (CADC/NRC/CSA).

This research has made use of the NASA/IPAC Extragalactic Database (NED), which is operated by the Jet Propulsion Laboratory, California Institute of Technology, under contract with the National Aeronautics and Space Administration.

This publication makes use of data products from the Wide-field Infrared Survey Explorer, which is a joint project of the University of California, Los Angeles, and the Jet Propulsion Laboratory/California Institute of Technology, funded by the National Aeronautics and Space Administration.

This work was supported by computational resources provided by the through the National Computational Infrastructure (NCI) facility under the National Computational and ANU Merit Allocation Schemes.

The authors also wish to recognize and acknowledge the very significant cultural role and reverence that the summit of Maunakea has always had within the indigenous Hawaiian community.

The authors thank the reviewer for their insightful comments, and Matthew Colless and Alice Quillen for helpful discussions.

3

Searching for signs of jet-driven feedback in the radio galaxy UGC 05771

The truth isn't easily pinned to a page. In the bathtub of history the truth is harder to hold than the soap and much more difficult to find.

Terry Pratchett

This chapter presents the content of the article *Searching for signs of jet-driven negative feedback in the nearby radio galaxy UGC 05771* (Zovaro et al. 2019b) as published in The Monthly Notices of the Royal Astronomical Society. The paper is reproduced here in full with minor formatting changes to make it consistent with the rest of the work in this thesis.

Abstract

Hydrodynamical simulations predict that the jets of young radio sources can inhibit star formation in their host galaxies by injecting heat and turbulence into the interstellar medium (ISM). To investigate jet-ISM interactions in a galaxy with a young radio source, we have carried out a multi-wavelength study of the $z = 0.025$ Compact Steep Spectrum radio source hosted by the early-type galaxy UGC 05771. Using Keck/OSIRIS observations, we detected H_2 1–0S(1) and [Fe II] emission at radii of 100s of pc, which traces shocked molecular and ionised gas being accelerated outwards by the jets to low velocities, creating a ‘stalling wind’. At kpc radii, we detected shocked ionised gas using observations from the CALIFA survey, covering an area much larger than the pc-scale radio source. We found that existing interferometric radio observations fail to recover a large fraction of the source’s total flux, indicating the likely existence of jet plasma on kpc scales, which is consistent with the extent of shocked gas in the host galaxy. To investigate the star formation

efficiency in UGC 05771, we obtained IRAM CO observations to analyse the molecular gas properties. We found that UGC 05771 sits below the Kennicutt-Schmidt relation, although we were unable to definitively conclude if direct interactions from the jets are inhibiting star formation. This result shows that jets may be important in regulating star formation in the host galaxies of compact radio sources.

3.1 Introduction

Feedback processes driven by active galactic nuclei (AGN) are now known to be pivotal in shaping the properties of galaxies in the modern Universe. For example, powerful quasar winds have been invoked to explain the observed galaxy luminosity function (Croton et al. 2006) and to establish correlations between properties of the stellar bulge and the mass of the central black hole (Silk & Rees 1998). Powerful, relativistic jets from radio galaxies in clusters have long been thought to prevent catastrophic cooling of the intracluster medium, reproducing observed star formation rates (SFRs) (Fabian 2012; McNamara & Nulsen 2012). In recent decades, numerous observational and theoretical studies have also shown that jets can both enhance (‘positive feedback’) and inhibit (‘negative feedback’) star formation in their host galaxies, carrying implications for the importance of radio activity in the context of galaxy evolution.

Hydrodynamical simulations suggest that jets have the potential to regulate star formation in the host galaxy, either by removing gas from the host galaxy altogether, or by heating it and thus preventing it from forming stars. When nascent jets emerge from the nucleus and propagate into the inhomogeneous interstellar medium (ISM) of their host galaxy, the jets become deflected and split as they encounter dense clumps, injecting their energy isotropically and forming a bubble that drives a shock into the ISM (Sutherland & Bicknell 2007; Wagner et al. 2016). While powerful jets may be able to expel gas from the host galaxy entirely, less powerful jets can create a ‘galactic fountain’, in which gas falls back towards the nucleus after being accelerated outward (Mukherjee et al. 2016), inducing turbulence into the ISM. Jets that are unable to drill efficiently through the ISM may also become temporarily trapped, injecting energy into the ISM over long periods of time.

Jet-induced negative feedback has now been observed in a number of radio galaxies. Many radio galaxies exhibit powerful outflows in the ionised, atomic and molecular phases (e.g., Nesvadba et al. 2006, 2010; Morganti et al. 2013; Tadhunter et al. 2014). Warm molecular gas, traced by ro-vibrational lines of H_2 , is also found in about 20–30 per cent of all massive radio galaxies, where jet-induced shocks are the most likely heating mechanism (Ogle et al. 2010; Willett et al. 2010; O’Dea 2016). The fact that ro-vibrational H_2 emission is so common in these galaxies, which are generally neither gas-rich nor very actively star forming (e.g., Ocaña Flaquer et al. 2010), has previously been interpreted as evidence that jets are able to continuously inject energy into the ISM over long periods of time (e.g., Nesvadba et al. 2010). Although some of these H_2 -luminous radio galaxies exhibit moderate rates of star formation, others have very low SFRs despite having large reservoirs of molecular gas (Nesvadba et al. 2010, 2011; Guillard et al. 2015), indicating that the jets are inducing negative feedback in their host galaxies.

Gigahertz Peak Spectrum (GPS) and Compact Steep Spectrum (CSS) sources are key in studying jet-induced feedback taking place within the host galaxy. They

are compact ($\lesssim 20$ kpc) radio galaxies characterised by a convex radio spectrum, peaking at GHz frequencies in GPS sources and at frequencies of a few 100 MHz in CSS sources, with both exhibiting a steep power-law spectrum to either side of the peak (O’Dea 1998). A larger fraction of GPS and CSS sources are asymmetric than more extended radio sources (Oriente 2016), suggesting that the jets are interacting strongly with an inhomogeneous ISM. They are also believed to represent AGN with young jets; age estimates based on the expansion rate of the radio lobes (e.g., de Vries et al. 2009; Giroletti et al. 2003) and based on the curvature of the radio spectrum at high frequencies (Murgia 2003) are typically within the range $10^2 - 10^5$ yr. Simulations show that jets couple most strongly to the ISM during the earliest phases of jet evolution, when the jet plasma is still confined to the host galaxy’s ISM (Sutherland & Bicknell 2007; Mukherjee et al. 2016; Wagner et al. 2016). Observations of GPS and CSS sources have confirmed the ability of compact jets to kinematically disrupt the ISM, leaving signatures such as line ratios consistent with shocks, broad line widths and outflows of a few 1000 km s^{-1} in some sources (Holt et al. 2008). Therefore, GPS and CSS sources are the ideal targets for observing jet-driven feedback processes which may have a significant impact upon the host galaxy’s evolution.

A recent study by Zovaro et al. (2019a) of the nearby CSS source 4C 31.04 demonstrated that compact jets have the potential to effect feedback processes far beyond the apparent extent of the radio source. The authors found evidence of low-surface brightness jet plasma driving shocks and turbulence into the gas of the host galaxy on kpc scales, while the apparent extent of the radio jets is < 100 pc.

To establish whether the phenomenon of low-surface brightness radio plasma is common in compact radio sources, and whether it plays an important role in jet-driven feedback, we build upon the work of Zovaro et al. (2019a) by studying the radio source associated with the galaxy UGC 05771. It is a CSS source with a spectral peak at 150 MHz, believed to be approximately 9 pc in size (de Vries et al. 2009), and therefore a very young radio source. To search for shock-heated ionised and molecular gas within a few 100 pc of the nucleus, both important tracers of jet-ISM interactions, we obtained high-resolution, adaptive optics (AO)-assisted near-IR integral field spectrograph observations using OSIRIS on the Keck I telescope. We complemented this data with optical integral field spectroscopy from the CALIFA survey, which has a much larger field of view, enabling us to search for signatures of jet-ISM interaction on kpc scales using the optical emission line gas. To determine if the jets are inducing negative feedback in UGC 05771, we also obtained CO data from the IRAM 30 m telescope, allowing us to investigate the star formation efficiency of the host galaxy.

In Section 3.2, we summarise the properties of UGC 05771 and its radio source. In Section 3.3 we discuss our OSIRIS observations, data reduction and analysis; in Section 3.4 we discuss the CALIFA data and our analysis; and in Section 3.5 we discuss our IRAM observations, data reduction and analysis. We present our interpretation of our findings in Section 3.6 before summarising in Section 3.7. For the remainder of this paper, we assume a cosmology with $H_0 = 70 \text{ km s}^{-1} \text{ Mpc}^{-1}$, $\Omega_M = 0.3$, and $\Omega_\Lambda = 0.7$, and use the fundamental plane-derived angular diameter distance and luminosity distance estimates of Saulder et al. (2016) (Table 3.1).

Table 3.1: Properties of UGC 05771. ^aluminosity-weighted stellar velocity dispersion within the effective radius. ^busing the $M_{\text{BH}} - \sigma_*$ relation of Gültekin et al. (2009). ^cfrom a Sérsic profile fit to the V band continuum.

Property	Value	Reference
z	0.02469 ± 0.00017	Falco et al. (1999)
D_L	95.6524 Mpc	Saulder et al. (2016)
D_A	91.5876 Mpc	Saulder et al. (2016)
Angular scale	$0.444 \text{ kpc arcsec}^{-1}$	Saulder et al. (2016)
$\log[M_*/M_\odot]$	11.27 ± 0.10	Sánchez et al. (2016a)
σ_*	$226 \pm 3 \text{ km s}^{-1}$	Oh et al. (2011)
σ_e	$223 \pm 3 \text{ km s}^{-1}$	This work ^a
$\log[M_{\text{BH}}/M_\odot]$	$8.54 \pm_{0.03}^{0.23}$	This work ^b
n	1.25	This work ^c
R_e	3.0 kpc	This work ^c

3.2 Host galaxy and radio source properties

UGC 05771 is an early-type galaxy (ETG) with stellar mass $M_* = 10^{11.27 \pm 0.10} M_\odot$, and is the most massive galaxy in a three-member group, with the stellar mass of the other two galaxies $\sim 10^{10} M_\odot$ (Saulder et al. 2016). We summarise its properties in Table 3.1.

UGC 05771 hosts a low-power CSS source with $P_{5.0\text{GHz}} = 10^{22.96} \text{ W Hz}^{-1}$ (Snellen et al. 2004). Fig. 3.1 shows the radio spectrum obtained from the integrated fluxes from the 6C 151 MHz, Texas 365 MHz, Bologna 408 MHz, Greenbank 1.4 GHz, NVSS, Becker & White 4.85 GHz, and 87GB catalogues. We also show integrated fluxes given by Snellen et al. (2004) from Jansky Very Large Array (VLA) (in BC configuration), Effelsberg observations and integrated fluxes provided by de Vries et al. (2009) using European Very Long Baseline Interferometry (VLBI) Network (EVN) and Global VLBI observations, and Very Long Baseline Array (VLBA) observations provided by Cheng & An (2018). These interferometric observations recover only $\sim 20 - 30$ per cent of the flux measured using single-dish observations at similar frequencies; excluding the EVN and EVN/VLBI fluxes, the spectrum is well-described by a power law at high frequencies with a spectral index $\alpha = 0.62^*$ (Snellen et al. 2004). The spectrum flattens and turns over at approximately 150 MHz.

To constrain the jet power we used the empirical correlation between radio luminosity $L_{151\text{MHz}}$ at 151 MHz and jet power L_{jet} of Ineson et al. (2017):

$$L_{\text{jet}} = 5 \times 10^{39} \left(\frac{L_{151\text{MHz}}}{10^{28} \text{ W Hz}^{-1} \text{ Sr}^{-1}} \right)^{0.89 \pm 0.09} \text{ erg s}^{-1} \quad (3.1)$$

Although the correlation between jet power and radio luminosity is believed to be fairly tight for extended radio sources, Ineson et al. (2017) warn that the correlation may not hold for compact radio sources, in which the radio luminosity is expected to increase over time due to the accumulation of radiative plasma. With this caveat in mind, using the 151 MHz flux $F_{151\text{MHz}} = 0.230 \text{ Jy}$ from the 6C survey, we estimate a jet power $L_{\text{jet}} \geq 4.2 \times 10^{41} \text{ erg s}^{-1}$.

*We define the spectral index α such that $S \propto \nu^{-\alpha}$.

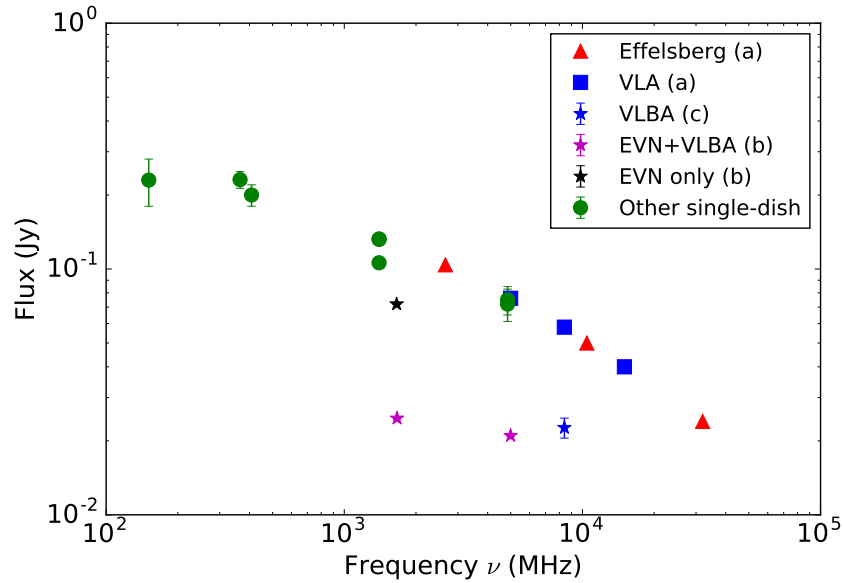


Figure 3.1: Radio spectrum of UGC 05771. References: (a) Snellen et al. (2004); (b) de Vries et al. (2009); other single dish fluxes are the integrated fluxes from the 6C 151 MHz, Texas 365 MHz, Bologna 408 MHz, Greenbank 1.4 GHz, NVSS, Becker & White 4.85 GHz, and 87GB catalogues.

VLBI observations at 1.665 GHz (EVN and VLBA) and 4.993 GHz (EVN only), taken in 2004, reveal a symmetric core-jet structure 9 pc across with a position angle of approximately 120° (de Vries et al. (2009), Figs. A1a and A1b). Interestingly, VLBA observations taken in 2011 at 8.4 GHz (Fig. A1c) reveal a single-sided core-jet morphology, with a bright hotspot 18.3 pc from the core to the South-East (Cheng & An 2018), and show no hints of emission along the jet axis. Although these inconsistencies are curious, they are only relevant to the parsec-scale structure of the source, which is well below the resolution limit of the observations discussed in this paper. Hence, determining the cause of these discrepancies is beyond the scope of this paper; none the less, we discuss these inconsistencies in Appendix A.

3.3 OSIRIS observations

3.3.1 Observations

We observed UGC 05771 using the OH-Suppressing Infra-Red Imaging Spectrograph (OSIRIS) (Larkin et al. 2006) on the 10 m Keck I telescope on Mauna Kea in Hawai‘i. OSIRIS is a lenslet-array integral field spectrograph operating over the wavelength range 1 – 2.4 μm . The instrument has a configurable plate scale (0.020", 0.035", 0.050" or 0.100" per spaxel) and a wide selection of both broad- and narrow-band filters, which determine the field-of-view. OSIRIS is fed by the Keck AO System (Wizinowich et al. 2006; van Dam et al. 2006), which can be used in laser guide star (LGS) or natural guide star mode, to provide near-diffraction limited angular resolution.

We used OSIRIS and the Keck AO system in LGS mode with a position angle of 0° on February 12, 2018 during program Z260. We observed with the *H* and *K* narrow-band Hn4 (1652–1737 nm), Kn3 (2121–2229 nm) and Kn4 (2208–2320 nm) filters in the 0.05" setting, providing fields of view of approximately $2.1'' \times 3.2''$,

2.4" \times 3.2" and 2.1" \times 3.2" respectively. The median spectral resolutions in the K and H bands are approximately 3900 and 2800 respectively. We used 600 s exposure times for both source and sky frames, integrating on-source for a total of 40, 60, and 40 minutes in the Hn4, Kn3 and Kn4 bands respectively. The HIPPARCOS stars HIP41798, HIP55182 and HIP53735, observed before and after UGC 05771, were used as telluric and flux standards.

3.3.2 Data reduction

We reduced our observations using the OSIRIS DATA REDUCTION PIPELINE (ODRP)[†], a software package for IDL, as follows.

We mean-combined our dark frames to create a master dark, which we subtracted from all science and sky frames. To associate each spectra on the detector with its corresponding lenslet, we ran the ‘extract spectra’ module, using the appropriate *rectification matrix* for the plate scale and filter, which provides the point spread function (PSF) for each lenslet as a function of wavelength. We then resampled the spectra to a linear wavelength grid, and assembled them into a data cube, before removing sky lines using the scaled sky subtraction method of Davies (2007). Next, we extracted 1D spectra of our telluric and flux standard stars and removed H I absorption features. We divided this 1D spectrum by a blackbody corresponding to the star’s effective temperature, which we estimated using its spectral class, and normalised it to a value of 1 at the filter’s effective wavelength. Lastly, we removed telluric absorption features from our object exposures by dividing the data cubes by the resulting 1D spectrum of the telluric standard.

Due to telescope pointing errors, the spatial shifts between individual exposures were not integer multiples of the spaxel size, meaning we could not use the in-built mosaicing function of the ODRP to combine our exposures. We instead created the mosaics as follows. For each data cube, we generated a continuum image by summing the data cube along the wavelength axis. We then calculated the spatial offsets for each data cube by cross-correlating the continuum images. To shift each data cube by the required amount, we used a 3rd-order spline function to shift and interpolate each wavelength slice of the data cube. We then median combined the shifted data cubes. The associated variance of each pixel in the final data cube was calculated as the variance of the pixels contributing to the pixel value.

To flux calibrate our science exposures, we generated a 1D spectrum of the flux standard in the same fashion as for the telluric standard, and multiplied it by the normalised blackbody to restore its original spectral shape, before removing telluric absorption lines by dividing the spectrum by the 1D spectrum of the telluric standard. Then, we determined the median number of counts n per second in the telluric-corrected spectrum of the flux standard in a small window around the effective wavelengths of the 2MASS K_s band (for our Kn3 and Kn4 band observations) and H band (for our Hn4 band observations). We created a conversion factor T by dividing the expected F_λ for the flux standard, estimated using its 2MASS magnitude, by n . Lastly, we multiplied our data cubes by T to convert them from units of counts s⁻¹ to erg s⁻¹ cm⁻² Å⁻¹.

We used a Median Absolute Deviation (MAD) smoothing algorithm to smooth the mosaicked data cubes and to remove artefacts. For each pixel, we computed

[†]Available <https://github.com/Keck-DataReductionPipelines/OsirisDRP>.

the median and standard deviation of the surrounding 8 pixels, and rejected those pixels with absolute value greater than 3 standard deviations from the median. We iterated until no more pixels were rejected. The value of the central pixel was then replaced by the mean of the remaining pixels, and the variance of the central pixel was replaced by the mean of the variance of the remaining pixels.

MAD smoothing degrades the intrinsic spatial resolution of our data σ by an amount σ_{MAD} such that the effective Gaussian sigma σ' of the PSF is increased to

$$\sigma' = \sqrt{\sigma_{\text{MAD}}^2 + \sigma^2} \quad (3.2)$$

where we measured σ by fitting a 2D Gaussian to our unsmoothed standard star exposures. We found the PSF of our observations to be slightly asymmetric, with $\sigma \approx 0.034'' \times 0.057''$ in the Kn3 and Kn4 bands and $\sigma \approx 0.027'' \times 0.041''$ in the Hn4 band. We measured $\sigma_{\text{MAD}} \approx 0.0459''$ by applying the MAD smoothing algorithm to 2D Gaussian profiles with known widths.

3.3.3 Emission line fitting

We used MPFIT (Markwardt 2009), a PYTHON implementation of the Levenberg-Marquardt algorithm (Moré 1978) developed by M. Rivers[‡], to simultaneously fit single-component Gaussian profiles to emission lines and a linear component to fit to the continuum, leaving the slope and the intercept as free parameters. We discard fits with reduced- $\chi^2 > 2$ and signal-to-noise (S/N) < 3 . We have corrected our line widths for instrumental resolution by subtracting the width of the line spread function in quadrature from the width of the fitted Gaussian, where we estimated the width of the line spread function by fitting a Gaussian to sky lines close in wavelength to the relevant emission line.

To calculate integrated line fluxes, we summed the fluxes in each spaxel. Due to poor S/N in the H₂1–0 S(0) line, we measured the total flux by fitting a Gaussian to the co-added spectrum within the central 200 pc, corresponding to the area in which we detect H₂1–0 S(1).

To calculate upper limits for the fluxes of emission lines not detected using our χ^2 and S/N criteria, we used the following method. In each spaxel, we calculated the standard deviation σ of the continuum in a window centred on the emission line. We assumed the non-detected emission line in that spaxel was a Gaussian with amplitude 3σ . For the Bry line, we used the width of the H α line measured using the CALIFA data (Section 3.4), and for non-detected H₂ lines, we used the width of the H₂ 1–0S(1) line. To estimate an upper limit for the total emission line flux, we assumed the lines are detected in every spaxel in which we detect the H₂ 1–0S(1) emission line.

3.3.4 Results

Fig. 3.2 shows the integrated spectra of our OSIRIS data cubes within 200 pc of the nucleus in the Kn3 and Hn4 bands. In the Kn3 and Kn4 bands, we detected ro-vibrational H₂ 1–0 emission lines which trace warm molecular gas, and in the Hn4 band we detected the [Fe II] $a^4D_{7/2} - a^4F_{9/2}$ line (rest-frame wavelength

[‡]Available <http://cars9.uchicago.edu/software/python/mpfit.html>.

Table 3.2: Total emission line fluxes and upper limits measured from the CALIFA data (top half of the table) and our OSIRIS observations (bottom half). For emission lines in the CALIFA and OSIRIS data, we measured the flux by simultaneously fitting Gaussian profiles to all lines in the integrated spectrum extracted from spaxels within 10 kpc and 200 pc of the nucleus respectively. Upper limits were estimated using the method detailed in Section 3.3.3. Emission lines in the CALIFA data have been corrected for extinction (Section 3.4.3).

Emission line	Flux (10^{-14} erg s $^{-1}$ cm $^{-2}$)
[O II] $\lambda\lambda$ 3726,3729	7.56 ± 0.12
H β	2.18 ± 0.05
[O III] $\lambda\lambda$ 4959,5007	4.35 ± 0.05
[N II] $\lambda\lambda$ 6548,6583	7.12 ± 0.04
H α	5.64 ± 0.03
[S II] λ 6716	4.10 ± 0.03
[S II] λ 6731	2.25 ± 0.03
H $_2$ 1–0 S(1)	1.85 ± 0.04
H $_2$ 1–0 S(0)	0.40 ± 0.05
H $_2$ 2–1 S(1)	≤ 1
Br γ	≤ 0.3
[Fe II]	1.09 ± 0.05

1.644 μ m) which traces the warm ionised medium. Table 3.2 lists the fluxes of the detected emission lines.

H $_2$ emission

Fig. 3.3 shows the Kn3 band continuum and the H $_2$ 1–0 S(1) emission line flux (rest-frame wavelength 2.122 μ m), radial velocity and velocity dispersion.

Ro-vibrational emission arises from several processes: hydrogen molecules can be collisionally excited by shocks, or radiatively excited by UV radiation from young stars or AGN. The H $_2$ 1–0 S(1)/Br γ ratio can be used to distinguish between shock and UV excitation. In Fig. 3.4 we show the H $_2$ 1–0 S(1)/Br γ ratio in each spaxel, where we have used upper limits for the Br γ flux in each spaxel estimated using the method described in Section 3.3.3. The ratio far exceeds the values of 0.1–1.5 typical of regions dominated by UV excitation, strongly suggesting that the H $_2$ is shock heated (Puxley et al. 1990). The fact that [Fe II] emission, a tracer of shocked gas, is present in the same region, further supports our hypothesis that the H $_2$ is shock-heated.

In Fig. 3.5 we show an excitation diagram, in which the strengths of the different H $_2$ emission lines are used to estimate the relative populations of H $_2$ molecules in different rotational (J) and vibrational (ν) energy levels. Using the emission line flux $I_{\text{obs}}(u, l)$ corresponding to a transition between an upper u and lower l energy level, we plot the column density of H $_2$ molecules in the upper level, $N_{\text{obs}}(\nu_u, J_u)$, normalised by the statistical weight g_{J_u} , from the expression of Rosenberg et al. (2013):

$$\frac{N_{\text{obs}}(\nu_u, J_u)}{g_{J_u}} = \frac{4\pi\lambda_{u,l}}{hc} \frac{I_{\text{obs}}(u, l)}{A(u, l)}, \quad (3.3)$$

where $\lambda_{u,l}$ is the rest-frame wavelength of the transition and $A_{u,l}$ is the spontaneous

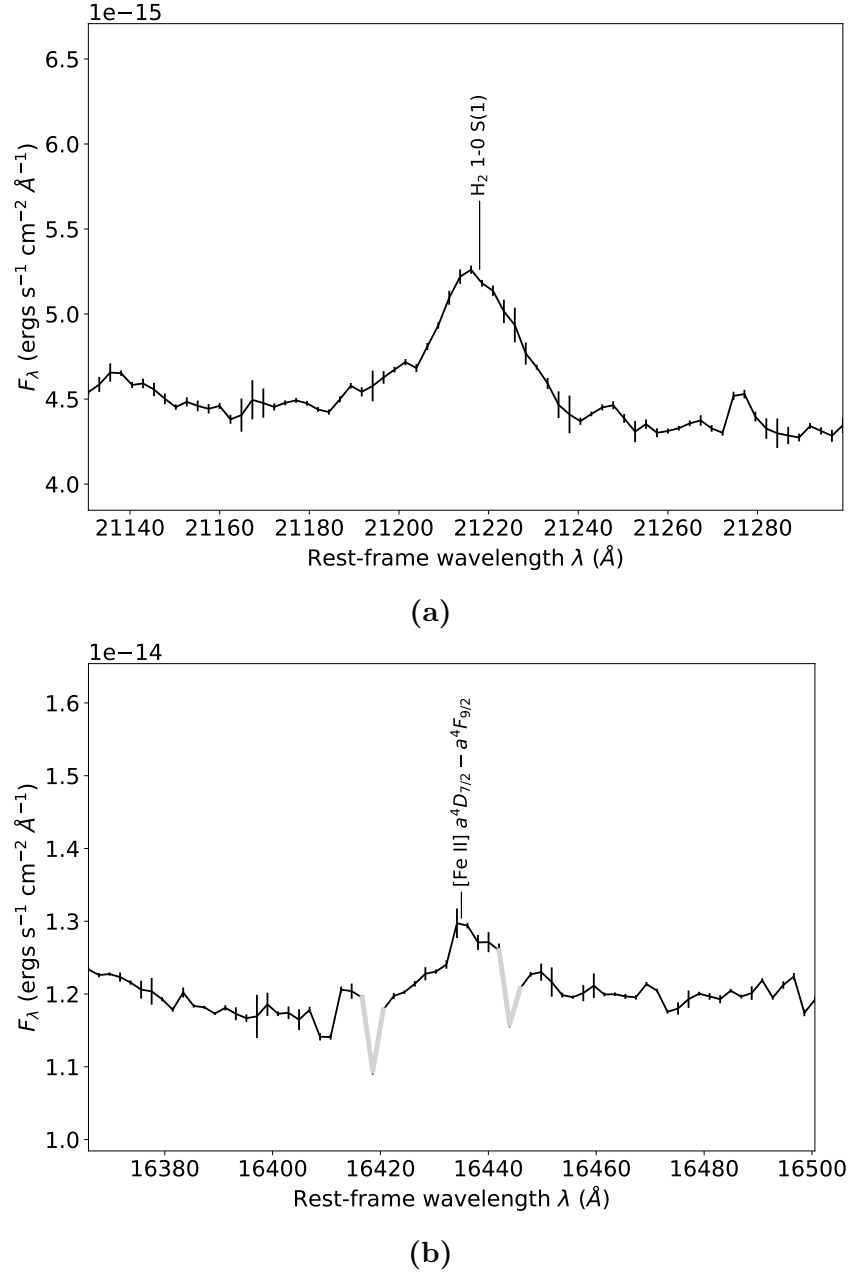


Figure 3.2: Integrated spectra extracted from the OSIRIS data cubes from spaxels within 200 pc of the nucleus in the Kn3 (a) and Hn4 (b) bands with 1σ error bars shown. Spectral regions dominated by sky emission have been indicated in grey.

emission coefficient, here obtained from Wolniewicz et al. (1998).

We estimated the gas temperature by plotting $N(\nu_u, J_u)/g_{J_u}$ as a function of transition energy. In local thermodynamic equilibrium (LTE), the points will fall on a straight line in $\log N(\nu_u, J_u)/g_{J_u}$, where the slope of the line indicates the temperature. As we only have detections for two emission lines and an upper limit for a third, we cannot confirm whether the gas is in LTE. None the less, a linear fit to our data yields $T \approx 5000$ K.

We estimated the mass of warm H_2 from the flux of the H_2 1–0 S(1) emission line

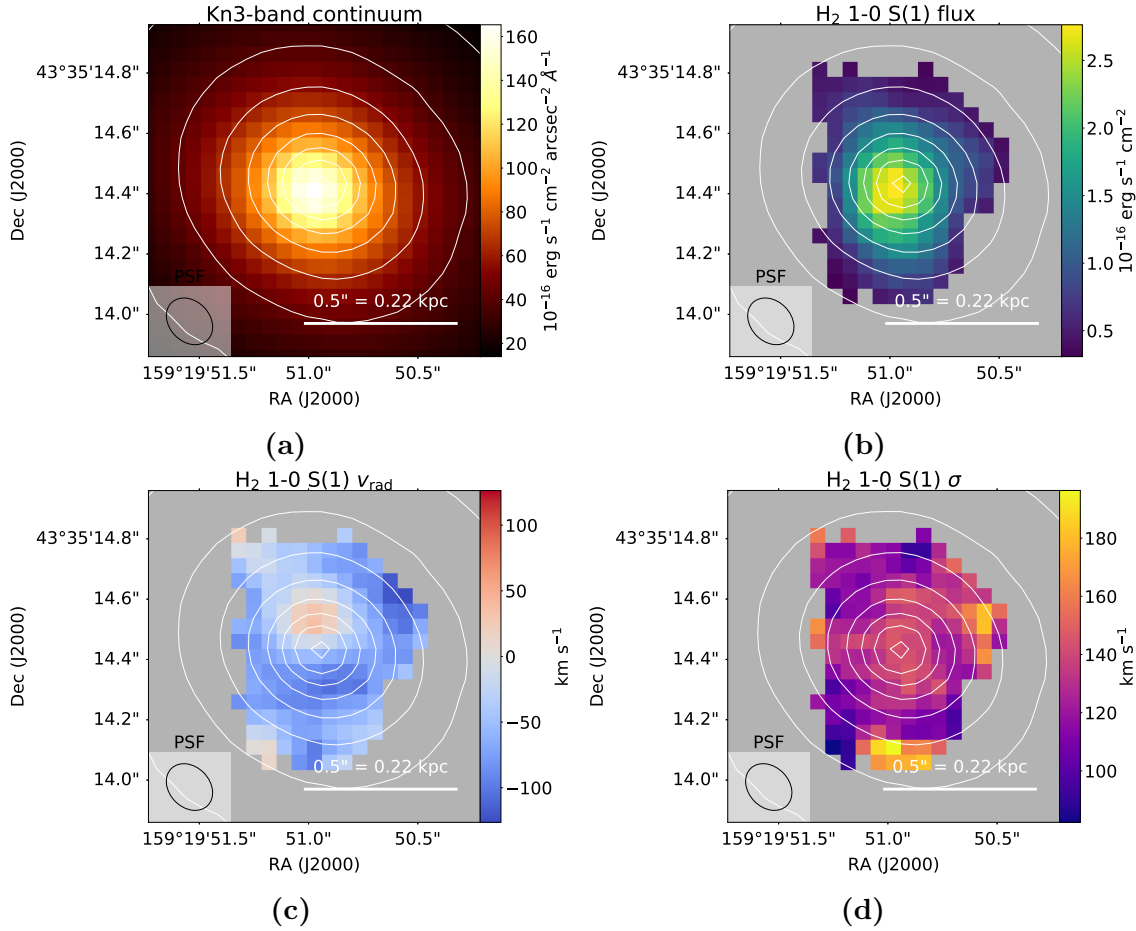


Figure 3.3: (a) The Kn3 band continuum, and (b) the integrated flux, (c) radial velocity (relative to rest frame wavelength) and (d) velocity dispersion of the H_2 1–0 S(1) emission line. The Kn3 band continuum is indicated in contours, and the full width at half-maximum (FWHM) of the PSF (taking into account the effects of MAD smoothing) is indicated in all figures.

$F_{1-0\text{S}(1)}$ using

$$M_{\text{H}_2}(T) = \frac{2m_p F_{1-0\text{S}(1)} 4\pi D_L^2}{f_{\nu=1, J=3}(T) A_{1-0\text{S}(1)} h\nu} \quad (3.4)$$

where $A_{1-0\text{S}(1)} = 3.47 \times 10^{-7} \text{ s}^{-1}$ is the spontaneous emission coefficient (Turner et al. 1977), $f_{\nu=1, J=3}(T)$ is the number fraction of H_2 molecules in the $\nu = 1$ vibrational state and $J = 3$ rotational state at temperature T , and h and c are the Planck constant and the speed of light respectively. In LTE, the number fraction of molecules in a rovibrational state with energy E_j and degeneracy g_j is described by the Boltzmann distribution

$$f_j(T) = \frac{g_j e^{-E_j/kT}}{Z_{\text{vr}}(T)} \quad (3.5)$$

where k is the Boltzmann constant and $Z_{\text{vr}}(T) = \sum_i g_i e^{-E_i/kT}$ is the partition function, which we computed using the molecular data of Dabrowski (1984). At a temperature of 5000 K, consistent with our excitation diagram (Fig. 3.5), $f_{\nu=1, J=3}(T) = 0.0210$. Using this value in Eqn. 3.4 yields $M_{\text{H}_2}(5000 \text{ K}) = 4400 \pm 70 M_\odot$.

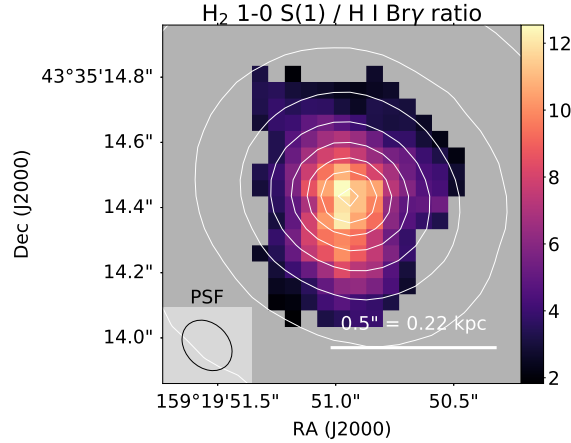


Figure 3.4: A map showing the H_2 1–0 S(1)/Br γ ratio in each spaxel. The large values of this ratio suggest shocks are the excitation mechanism. The Kn3 band continuum is indicated in contours, and the FWHM of the PSF (taking into account the effects of MAD smoothing) is indicated.

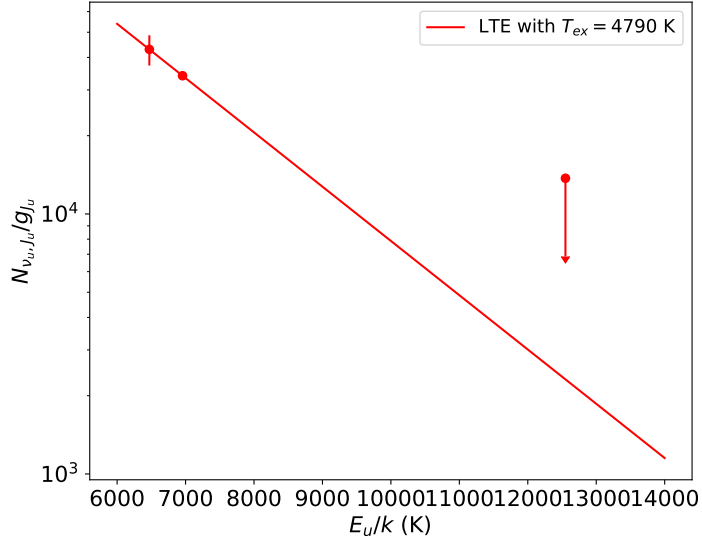


Figure 3.5: Excitation diagram, where we indicate the line of best fit.

[Fe II] emission

Fig. 3.6 shows the Hn4 band continuum and the $[\text{Fe II}]_{1.644 \mu\text{m}}$ emission line flux, radial velocity and velocity dispersion.

[Fe II] emission occurs when dust grains are destroyed by fast shocks, releasing iron atoms into the ISM which are then singly ionised by the ambient radiation field. Supernovae (SNe) explosions and AGN jets or disc winds can drive shocks into the ISM, causing [Fe II] emission.

To rule out SNe explosions, we estimated the star formation rate required to produce the observed [Fe II] luminosity in UGC 05771, using the same approach as in Zovaro et al. (2019a). First, we calculated the SNe rate $\nu_{\text{SN}, [\text{Fe II}]}$ from the $[\text{Fe II}]_{1.26 \mu\text{m}}$ luminosity using the empirical relation for SB galaxies derived by Rosenberg et al. (2012)

$$\log \left(\frac{\nu_{\text{SN}, [\text{Fe II}]}}{\text{yr}^{-1}} \right) = (1.01 \pm 0.2) \log \left(\frac{L([\text{Fe II}]_{1.26 \mu\text{m}})}{\text{erg s}^{-1}} \right) - (41.17 \pm 0.9) \quad (3.6)$$

where we assumed an intrinsic ratio $[\text{Fe II}] \ 1.26/1.64 \mu\text{m} = 1.36$, which yielded $\nu_{\text{SN}, [\text{Fe II}]} = 0.28 \text{ yr}^{-1}$.

We then estimated the SNe rate from the SFR of UGC 05771, $\nu_{\text{SN}, \text{SFR}}$ using a solar metallicity STARBURST99 (Leitherer et al. 1999) model with a continuous star formation law and a Salpeter initial mass function (IMF), where we estimated the SNe rate by scaling the SFR of the model to match the estimated $\text{H}\alpha$ -based SFR (Section 3.4.3). For ages $> 1 \text{ Gyr}$, consistent with the stellar age of the galaxy ($\sim 10 \text{ Gyr}$; Sánchez et al. 2016a), this gives $\nu_{\text{SN}, \text{SFR}} \approx 0.01 \text{ yr}^{-1}$, an order of magnitude too small to cause the $[\text{Fe II}]$ emission. Therefore, we conclude that SNe explosions are not the primary cause of the $[\text{Fe II}]$ emission.

3.4 CALIFA observations

3.4.1 Observations and data reduction using Pipe3D

UGC 05771 was observed using the Potsdam Multi Aperture Spectrograph (PMAS) instrument (Roth et al. 2005) on the 3.5 m telescope at the Calar Alto observatory as a part of the Calar Alto Legacy Integral Field Area (CALIFA) survey of $0.005 <$

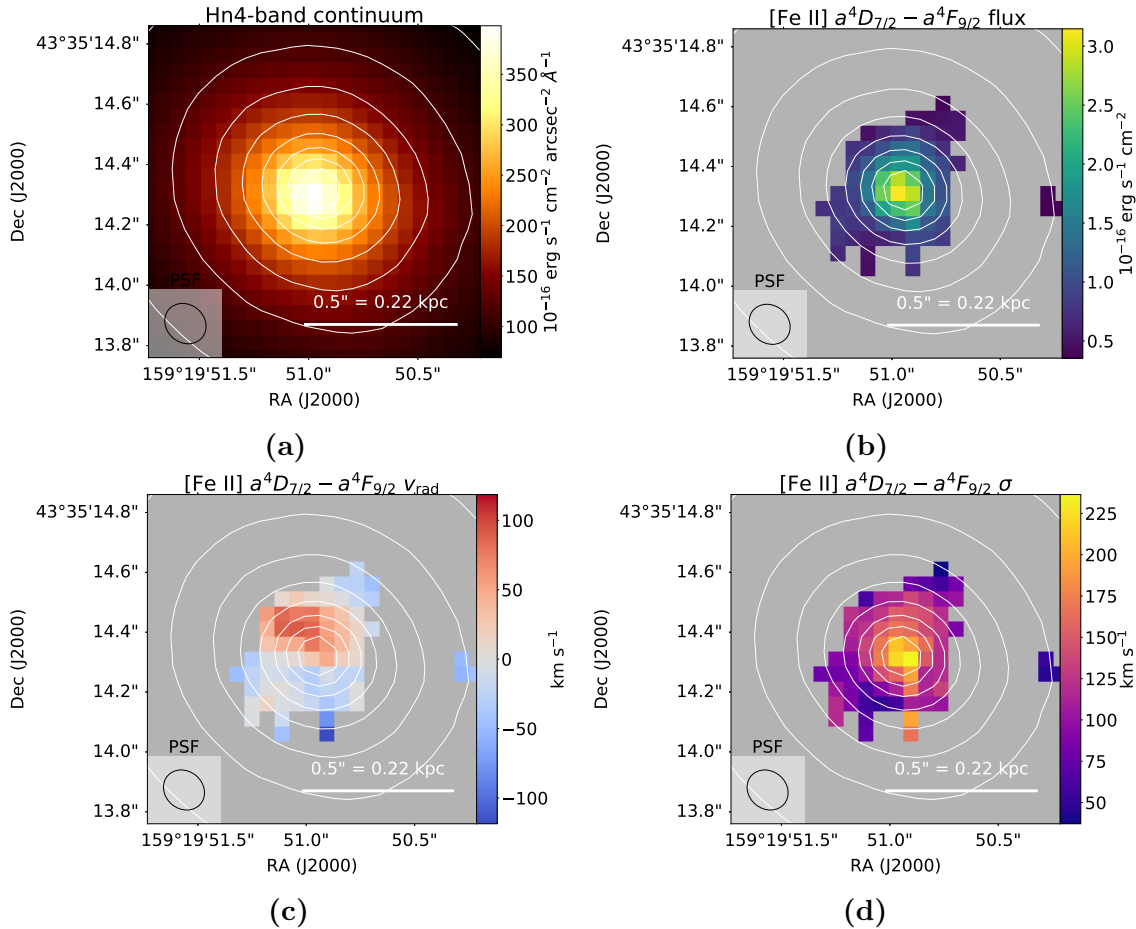


Figure 3.6: (a) The Hn4 band continuum and (b) the integrated flux, (c) radial velocity (relative to rest frame wavelength) and (d) velocity dispersion of the $[\text{Fe II}]$ emission line. The Hn4 band continuum is indicated in contours, and the FWHM of the PSF (taking into account the effects of MAD smoothing) is indicated in all figures.

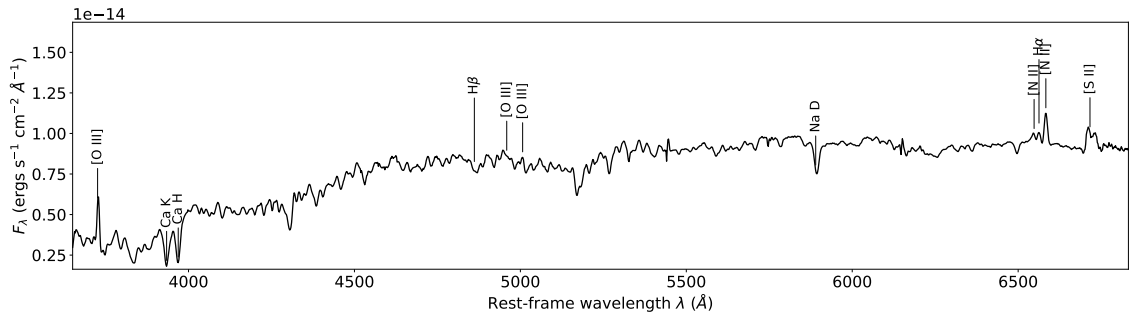


Figure 3.7: Integrated spectrum extracted from the CALIFA data cube from spaxels within 5 kpc of the nucleus.

$z < 0.03$ galaxies (Sánchez et al. 2012; Walcher et al. 2014; Sánchez et al. 2016a). PMAS is a fibre-bundle spectrograph that produces a hexagonal data cube with 2.5'' spatial resolution (FWHM) over a 74'' \times 64'' field of view. Each galaxy in the survey was observed in both high ($R \sim 1650$) and low spectral resolution ($R \sim 850$) modes of PMAS, covering wavelength ranges of 3700 to 4800 Å and 3749 to 7500 Å respectively. The spectral resolution of the high- and low-resolution modes corresponds to velocity dispersions of approximately $100 \text{ km s}^{-1} < \sigma < 200 \text{ km s}^{-1}$ and $60 \text{ km s}^{-1} < \sigma < 80 \text{ km s}^{-1}$ respectively. We show the spectrum extracted from the ‘combined’ data cube, which merges the high- and low-resolution spectra into a single data cube, from spaxels within 5 kpc of the nucleus in Fig. 3.7.

We used the data products produced by PIPE3D, a processing pipeline developed for integral field unit surveys (Sánchez et al. 2016a) developed by the CALIFA collaboration, to study the spatially resolved stellar population and ionised gas properties of UGC 05771. To elevate the S/N to a level sufficient for analysis of the stellar continuum, PIPE3D spatially bins the data cube, before fitting spectral templates to the spectra to provide quantities including the kinematics, metallicity and ages of the stellar population. The stellar continuum fit to each spaxel is then subtracted from the data cube, yielding an emission line-only data cube, to enable analysis of the emission line spectra.

3.4.2 Stellar properties

The best-fit stellar population of UGC 05771 produced by PIPE3D is predominantly old, with a star formation history well-approximated by an instantaneous burst ~ 10 Gyr ago. Fig. 3.8 shows the V band continuum reconstructed using the data cube, the stellar radial velocity and velocity dispersion.

We estimated the black hole mass using the $M_{\text{BH}} - \sigma_*$ relation of Gültekin et al. (2009), given by

$$\log_{10} \left[\frac{M_{\text{BH}}}{M_{\odot}} \right] = (8.23 \pm 0.08) + (3.96 \pm 0.42) \log_{10} \left[\frac{\sigma_e}{200 \text{ km s}^{-1}} \right] \quad (3.7)$$

where σ_e is the luminosity-weighted stellar velocity dispersion within the effective radius R_e . We calculated σ_e from the average flux intensity I_i and stellar velocity

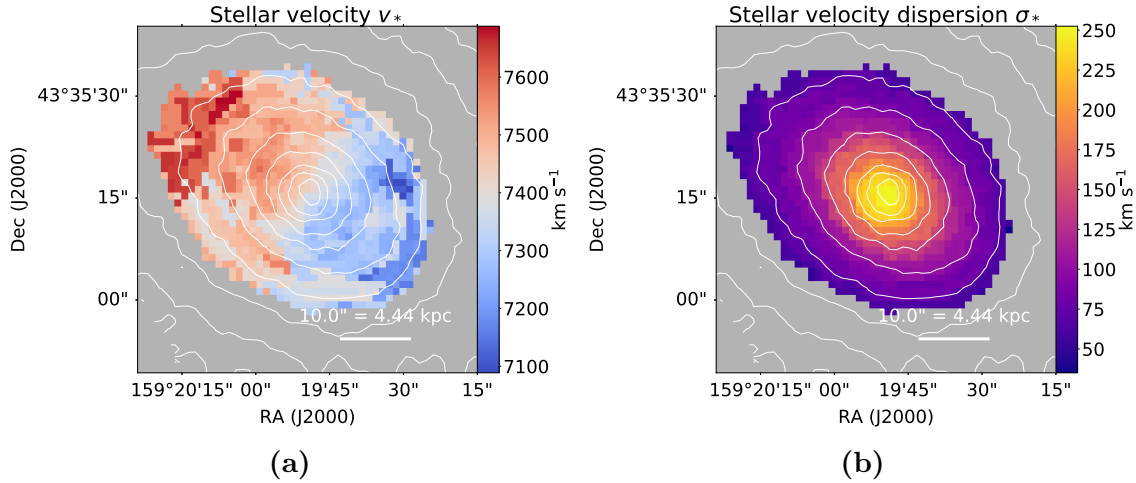


Figure 3.8: (a) The stellar radial velocity, relative to systemic, and (b) velocity dispersion (Gaussian σ). The contours indicate the logarithmically-scaled V band continuum.

dispersion $\sigma_{*,i}$ in each spaxel i using

$$\sigma_e = \frac{\sum_i I_i \sigma_{*,i}}{\sum_i \sigma_{*,i}}. \quad (3.8)$$

We calculated σ_e within $1 R_e$, which we estimated by fitting a Sérsic profile to the V band continuum image constructed from the data cube, which yields $\sigma_{*,i} = 226 \pm 3 \text{ km s}^{-1}$. Using this value, we estimated $\log_{10} M_{\text{BH}} = 8.54 \pm_{0.03}^{0.23} \log M_{\odot}$.

3.4.3 Emission line analysis

We performed our own Gaussian emission line fits to the emission line-only data cube using the method detailed in Section 3.3.3. We simultaneously fitted the emission lines [O II] $\lambda\lambda$ 3726,3729, H β , [O III] $\lambda\lambda$ 4959,5007, [N II] $\lambda\lambda$ 6548,6583, H α , [S II] λ 6716 and [S II] λ 6731, where we constrained each line to have the same kinematics, and we fixed the relative fluxes of the lines in the [N II] and [O III] doublets to their expected values of 1:3.06 and 1:2.94 respectively. Due to the low spectral resolution of PMAS at the wavelengths of most emission lines, we only fitted a single kinematic component to each line.

We show the total extinction-corrected emission line fluxes in Table 3.2, where we have summed fluxes from spaxels with fits that have $S/N > 3$ and reduced- $\chi^2 < 2$. The ionised gas kinematics are shown in Fig. 3.9, where we present the H α flux, radial velocity and velocity dispersion.

Reddening

To correct our emission line fluxes for extinction, we used the reddening curve of Fitzpatrick & Massa (2007) with $R_V = 3.1$, assuming that the ratio of the intrinsic line fluxes $I(\text{H}\alpha)/I(\text{H}\beta) = 2.85$ corresponding to Case B recombination. We calculated the total extinction in the V band, A_V , in each spaxel in which the line ratio had a $S/N > 3$ (Fig. 3.10). There were a number of spaxels in which the ratio of the observed fluxes $F(\text{H}\alpha)/F(\text{H}\beta) < 2.85$, corresponding to values of $A_V < 0$;

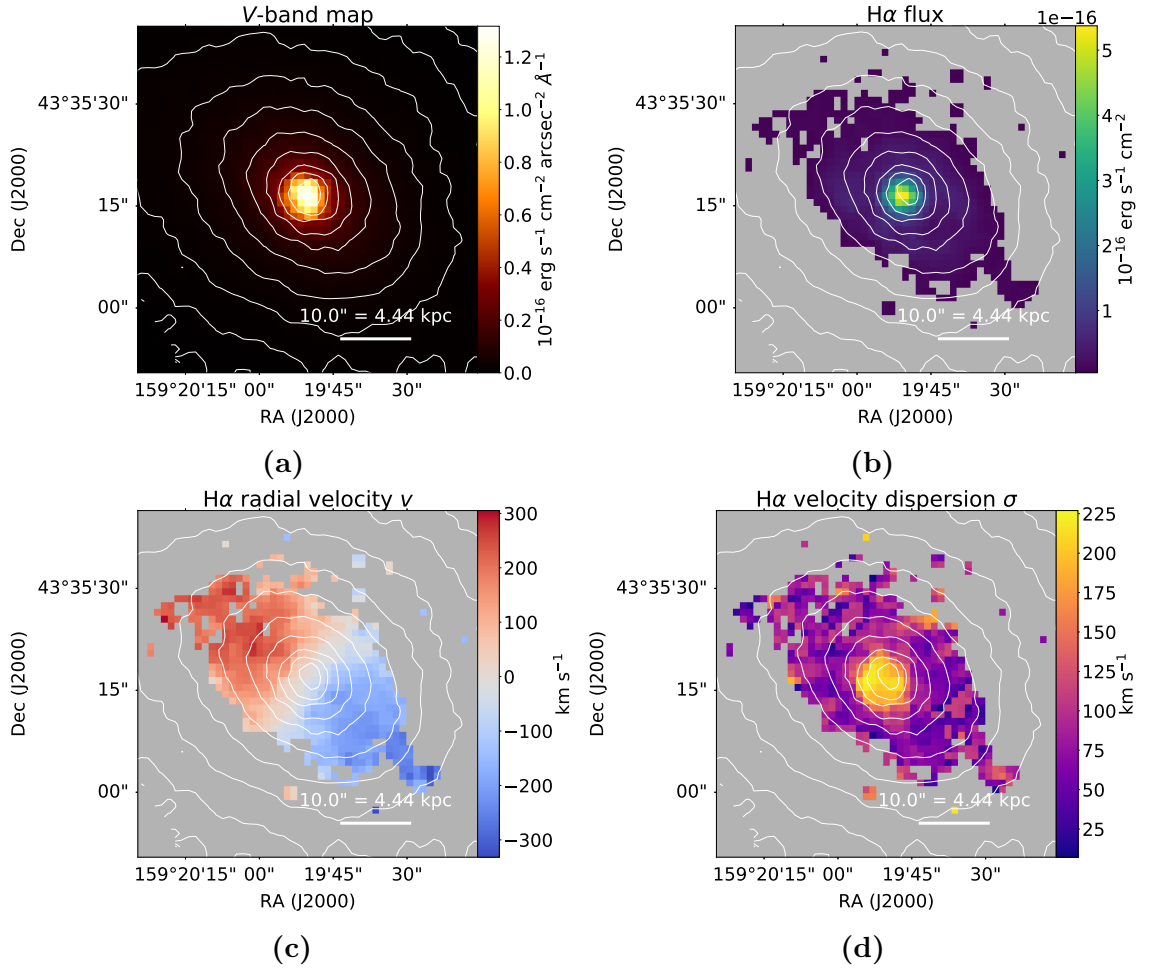


Figure 3.9: (a) V band continuum; (b) H α emission line flux, (c) radial velocity (relative to systemic) and (d) velocity dispersion (Gaussian σ), corrected for the instrumental dispersion. Contours show the logarithmically-scaled V band continuum.

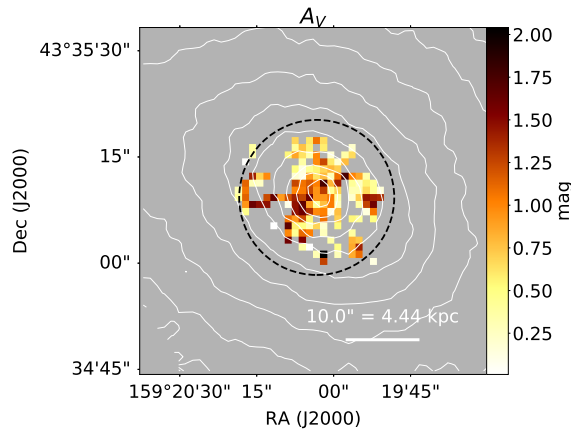


Figure 3.10: Total extinction in the V band A_V . The contours indicate the logarithmically-scaled V band continuum, and the dashed circle shows the FWHM of the IRAM 30 m telescope beam at the observed frequency of the CO(1-0) line (Section 3.5).

these non-physical line ratios are most likely due to systematic errors in fitting the underlying stellar continuum.

To estimate the mean A_V , we calculated the average of the H α /H β ratios in each

spaxel in which the ratio has $S/N > 3$ and $F(H\alpha)/F(H\beta) > 2.85$, which yielded $A_V = 0.831 \pm 0.014$.

In spaxels where the $H\beta$ $S/N < 3$ but $H\alpha$ is still detected, we estimated upper limits for the $H\beta$ flux using the method detailed in Section 3.3.3, which provided a lower limit for A_V . In spaxels closer to the nucleus, $A_V \gtrsim 0.5$; at larger radii, where the $H\alpha$ surface brightness drops off, we cannot provide any meaningful constraint on A_V . Therefore, without any further information, we assumed $A_V = 0.831 \pm 0.014$ across the whole galaxy, and have used this value to correct for extinction in the line fluxes given in Table 3.2.

We also used A_V to estimate the hydrogen column density N_H using the relation of Güver & Özel (2009). In the spaxels over which we could measure A_V , the mean column density $N_H = (1.84 \pm 0.03) \times 10^{21} \text{ cm}^{-2}$. We estimated the total hydrogen mass from the column densities in each spaxel i using $M_H = \sum_i \mu m_H N_{H,i} A_i \geq (4.7 \pm 0.2) \times 10^8 M_\odot$ where $\mu = 1.37$ is the mean molecular mass, m_H is the mass of the hydrogen atom and A_i is the area of each spaxel in cm^2 . This gave a mean molecular gas mass surface density $\Sigma_{\text{gas}} = 10.0 \pm 0.5 M_\odot \text{ pc}^{-2}$ which is consistent with our estimate based on our CO observations ($\Sigma_{\text{gas}} = 15 \pm 5 M_\odot \text{ pc}^{-2}$; Section 3.5).

Excitation mechanism

To investigate the excitation source of the ionised gas, we constructed optical diagnostic diagrams (ODDs) (Baldwin et al. 1981; Veilleux & Osterbrock 1987; Kewley et al. 2001; Kauffmann et al. 2003; Kewley et al. 2006). In an ODD, the ratios of certain pairs of emission line fluxes are plotted against one another to distinguish between excitation due to shocks, photoionisation from stellar radiation fields and harder radiation fields from AGN.

In Fig. 3.11a, we show the spaxel-by-spaxel ODDs for UGC 05771, where each spaxel is colour-coded by its projected distance from the nucleus in the plane of the sky. We used the line fluxes and velocity dispersion from our Gaussian fit, only including spaxels in which the S/N of all lines exceeds 3, except for the $[O\text{I}]\lambda 6300$ line for which we used the flux from the Monte Carlo-method fit provided by PIPE3D (Sánchez et al. 2016a, §3.6) because the S/N in this line was too low to be fit using our own method. In all 3 ODDs, most spaxels lie above the maximum $[O\text{III}]/H\beta$ ratio that can arise from star formation alone at a given $[N\text{II}]/H\alpha$ ratio (the solid curve) of Kewley et al. (2001).

Despite their diagnostic power, line ratios alone cannot be used to distinguish between photoionisation and shock excitation for spaxels with low-ionization nuclear emission line region (LINER)-like emission, which otherwise occupy overlapping regions to the right of all 3 ODDs. For this reason, in Fig. 3.11b we show the same ODDs with the spaxels colour coded by the $H\alpha$ velocity dispersion, which reveals that the spaxels with the largest $[N\text{II}]/H\alpha$ ratios are also those with the highest velocity dispersion, indicating shocks dominate the line emission.

Although we cannot rule out shocks as the excitation mechanism for the line emission in the outer regions of the galaxy, the lower velocity dispersion in these regions is consistent with line emission powered by a diffuse ionisation field, probably from evolved stars (Singh et al. 2013; Belfiore et al. 2016). This is consistent with the ~ 10 Gyr old stellar population of UGC 05771, in which post-AGB stars, hot and evolved stars that emit a hard ionising spectrum, are expected to dominate

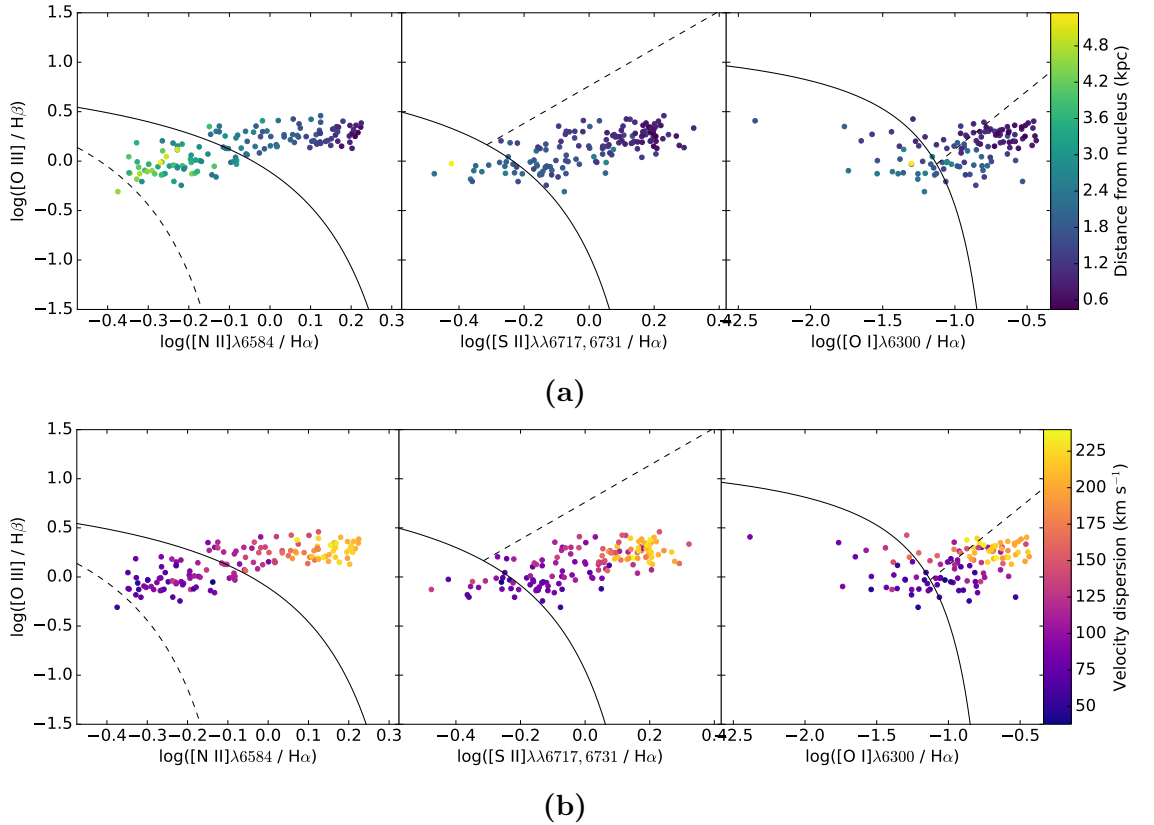


Figure 3.11: Optical diagnostic diagrams for spaxels in UGC 05771 (Baldwin et al. 1981; Veilleux & Osterbrock 1987) with points coloured by (a) their distance from the nucleus (assumed to coincide with the peak in the V band continuum) and (b) by the $H\alpha$ velocity dispersion. The solid lines represent the maximum $[O\text{ III}]/H\beta$ ratio that can arise from star formation alone, derived from photoionisation models (Kewley et al. 2001). In the left panels, the dashed line is the equivalent empirical relation of Kauffmann et al. (2003) which separates star-forming galaxies and AGN hosts. In the middle and right panels, the dashed lines separate Seyfert-like (above) and LINER-like ratios (below the line) (Kewley et al. 2006).

the ionisation field, contaminating SFR estimates based on the $H\alpha$ flux and FUV magnitude. We discuss the implications of this in the following section.

Star formation rate estimate

Using the total extinction-corrected $H\alpha$ flux and the calibration of Calzetti (2013) derived from stellar population modelling using a Kroupa IMF, we estimated the global $\text{SFR}(H\alpha) = 0.2795 \pm 0.0011 M_{\odot} \text{ yr}^{-1}$. However, we are confident this is an upper limit due to contamination from other sources of $H\alpha$ emission. Inspection of Fig. 3.9b reveals that the $H\alpha$ emission peaks sharply within a few kpc of the nucleus, which is also where we observe very strong shock signatures (Fig. 3.11). Therefore a substantial portion of the total $H\alpha$ flux is due to shocks.

To obtain a more strict upper limit to the SFR, we used the ODDs shown in Fig. 3.11. Although many spaxels lie in the LINER region of the ODD, a significant number of spaxels occupy the intermediate region (between the dashed and solid curves in the left panels of Figs. 3.11a and 3.11b), in which the line ratios indicate that both star formation and shocks and/or radiation from post-AGB stars contribute to the line emission. To obtain a better upper limit for the SFR, we only

included the $H\alpha$ flux from spaxels that lie in the intermediate and star-forming regions. Unfortunately, there are many spaxels that we could not show on the ODDs due to poor S/N in $[O\text{ III}]$ and $H\beta$. However, these spaxels are predominantly at large radii, where the surface brightness is low, and inspection of 3.11a shows that there are very few spaxels at radii $\gtrsim 2$ kpc that lie in the LINER region. Hence, we assumed that all spaxels at large radii with unknown line ratios lie in the intermediate or star-forming regions of the ODD. Summing the $H\alpha$ fluxes from all spaxels in the intermediate or star-forming regions yields $\text{SFR}(H\alpha) = 0.1046 \pm 0.0007 M_{\odot} \text{ yr}^{-1}$. We stress that this again represents an upper limit, as the majority of these spaxels lie in the intermediate region, implying contributions from sources other than star formation.

To determine whether there is any significant star formation obscured by extinction, we also estimated the SFR using far-IR fluxes from the *Infrared Astronomical Satellite* (*IRAS*, Neugebauer et al. 1984). Because UGC 05771 was not detected by *IRAS*, we instead used the *IRAS* Scan Processing and Integration tool[§] to estimate upper limits from the total integrated flux density within $\pm 2.5'$ of UGC 05771. Using the $60 \mu\text{m}$ flux density upper limit of $f_{\nu}(60 \mu\text{m}) = 0.12 \text{ Jy}$ and the total IR (TIR) bolometric correction $L_{\text{TIR}} = 1.7L_{60 \mu\text{m}}$ of Rowan-Robinson et al. (1997) and the TIR SFR calibration of Kennicutt (1998), we obtained $\text{SFR}(\text{TIR}) < 0.5 M_{\odot} \text{ yr}^{-1}$. Given that the FIR fluxes may also be contaminated by the AGN, this confirms that there is unlikely to be a significant amount of obscured star formation, which is expected given the modest A_V we estimate from our $H\alpha$ and $H\beta$ fluxes.

We also estimated the SFR using the *Galaxy Evolution Explorer* far-UV magnitude. After correcting for reddening, and using the UV SFR law of Salim et al. (2007), we found $\text{SFR}(\text{UV}) = 0.94 \pm 0.12 M_{\odot} \text{ yr}^{-1}$, much larger than that based on the $H\alpha$ and far-IR fluxes. However, the UV flux is likely to be strongly contaminated by emission from old stars; as discussed above, LINER-like emission line ratios suggest that post-AGB stars most likely dominate the UV radiation field in the outer regions of the galaxy. Hence, $\text{SFR}(\text{UV})$ represents a strict upper limit.

Therefore, because $\text{SFR}(\text{TIR})$, $\text{SFR}(\text{UV})$ and $\text{SFR}(H\alpha)$ represent strict upper limits, we conclude that the true SFR in UGC 05771 is most likely lower than $\text{SFR}(H\alpha) = 0.1046 \pm 0.0007 M_{\odot} \text{ yr}^{-1}$. We use this latter estimate of the SFR to investigate the star formation efficiency in UGC 05771 in Section 3.7.

Ionised gas kinematics

Fig. 3.9 shows the $H\alpha$ flux, radial velocity and velocity dispersion. Upon first inspection, there are no obvious signs of disrupted kinematics in the $H\alpha$ radial velocity. This is perhaps to be expected, given the low radio luminosity of the source, which is several orders of magnitude lower than those of the sample of GPS and CSS sources of Holt et al. (2008) in which outflows of up to a few 1000 km s^{-1} are observed.

None the less, to determine whether there are any significant non-circular motions in the ionised gas, we fitted a disc model to the radial velocity data using MPFIT. We first fitted a Sérsic profile to the galaxy's light profile along its semi-major axis in the V band continuum (Fig. 3.9a); we show the Sérsic parameters in Table 3.1. We then used the analytical expressions of Terzić & Graham (2005) for the circular

[§]Available <https://irsa.ipac.caltech.edu/applications/Scanpi/>.

velocity in a Sérsic potential, which also requires the total galaxy mass; we used the mass estimated by Sánchez et al. (2016a) (Table 3.1). We fitted the circular velocity profile to our data, allowing the systemic velocity, inclination and position angle to vary. We constrained the kinematic centre of the disc to coincide with the peak in the V band continuum.

Fig. 3.12 shows our model fit and residuals to the radial velocity of the $H\alpha$ disc. The reduced- $\chi^2 > 10$, indicating a poor fit for our rather simplistic disc model. To ensure that any disturbed kinematics in the central region were not biasing the fit, we re-ran our fit with the central 2 kpc masked. The best-fit parameters were almost identical in both cases, indicating that the kinematics in the nuclear region were not significantly biasing the fit. The residual reveals a counter-rotating structure in the nucleus and a velocity gradient on larger scales in the disc. Although counter-rotating cores are not uncommon in ETGs (e.g., Bender 1988), this may also indicate that our simple disc model is a poor fit to the data.

The $H\alpha$ velocity dispersion (Fig. 3.9d) is clearly elevated within 2 kpc of the nucleus, reaching values $\sigma \gtrsim 225 \text{ km s}^{-1}$, whereas the velocity dispersion in most parts of the disc does not exceed 100 km s^{-1} .

To determine whether the enhanced central velocity dispersion could be due to beam smearing, we used our best-fit disc model to obtain line-of-sight (LOS) velocities, which we then used to create synthetic emission lines in each spaxel of a data cube. We modelled each emission line with an intrinsic Gaussian σ of 75 km/s , to match the observed velocity dispersion in the outer regions of the gas disc, plus the instrumental resolution of PMAS. We spatially smoothed the cube to match the $2.5''$ seeing of the CALIFA data, and then spatially binned the cube to match the spaxel size. Finally we added Gaussian noise to replicate the S/N in the CALIFA data. By measuring the velocity dispersion in each spaxel using our emission line fitting routine, we found that beam smearing was unable to reproduce the observed line widths in the central 2 kpc[¶]. We hence rule out beam smearing as the sole cause of the elevated velocity dispersion in this region.

An alternative scenario to explain the high velocity dispersions and shock-like line ratios in the inner parts of the disk of UGC 05771 could be accretion of gas from the surroundings of the galaxy. In principle, such an accretion event could also have triggered the nuclear activity. UGC 05771 resides in a group environment with two massive galaxies within a few 100 kpc. Hence, a recent encounter or minor merger would not be implausible, although we do not see any evidence for that, e.g., in the stellar morphology of UGC 05771. Moreover, mass accretion rates required to fuel nuclear radio activity are very low, of order $10^{-3} M_{\odot} \text{ yr}^{-1}$ or less (e.g., Merloni et al. 2003), so that a specific triggering event may not be necessary. We also do not see any signatures of infalling neutral gas, such as interstellar NaD absorption line components, and the rotation of the gas disk is overall very regular (Fig. 3.9c); this is inconsistent with a recent merger event that would have been strong enough to stir up large parts of the gas in the nuclear regions.

An exception might be the small region within 2 kpc of the nucleus where we find non-circular motions, which could originate from a counter-rotating core, if this feature is not due to an interaction with extended jet plasma. However, for accreted gas to become bound to the disc, it cannot have a velocity much larger than the circular velocity of the disc, which is approximately 100 km s^{-1} within the

[¶]See Appendix B for more details.

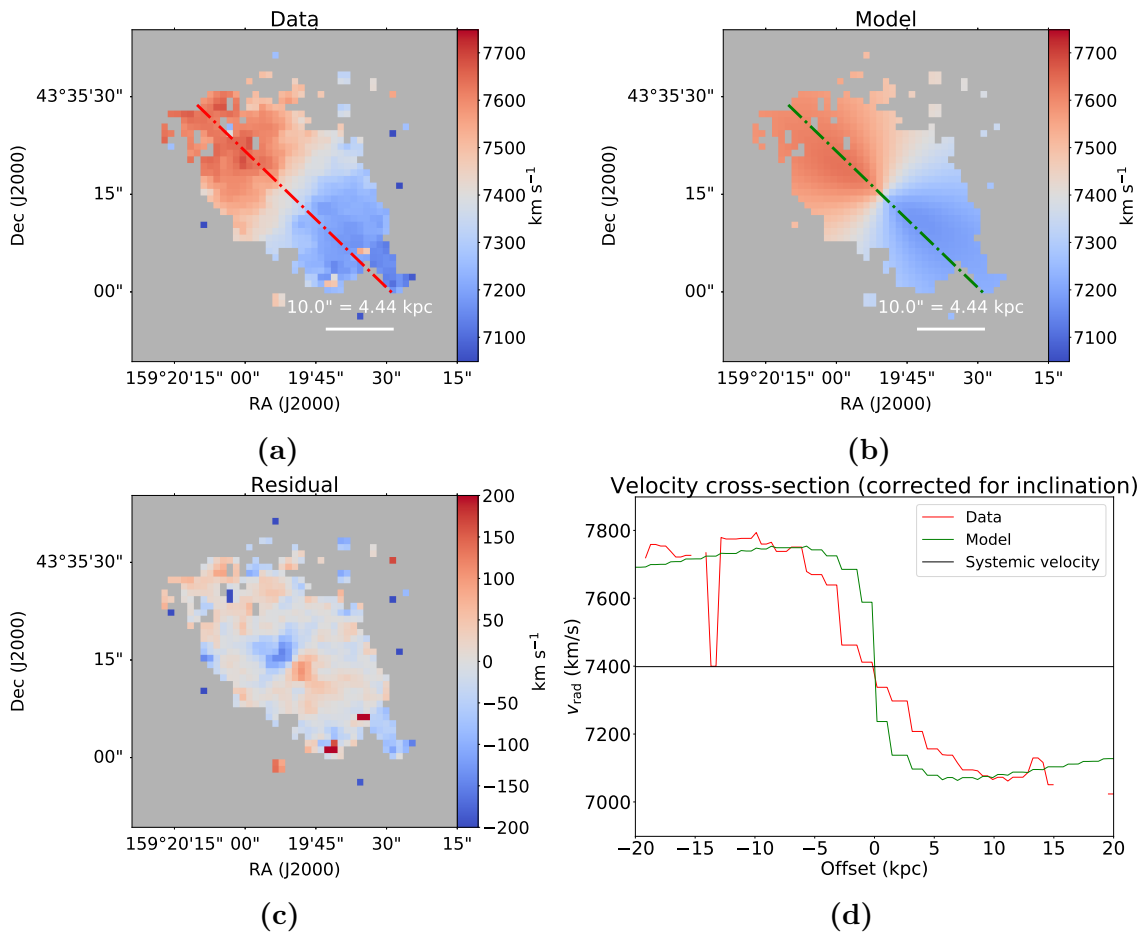


Figure 3.12: (a) H α radial velocity from the Gaussian fit, (b) Sérsic disc model fit, (c) velocity residuals, and (d) a plot showing the radial velocity along the dashed green and red lines in Figs. (a) and (b), corrected for inclination. In Fig. (c), subtracting the model fit reveals a counter-rotating structure in the central region of the galaxy. The velocities in Figs. (a) and (b) are given with respect to the local standard of rest.

inner kpc (Fig. 3.12d). Basic energy conservation arguments would therefore make it unlikely that such gas can cause the observed velocity dispersions of 225 km s^{-1} , which are much greater, even when neglecting that much of the kinetic energy of the gas is being radiated away by line emission from shocked gas. We therefore do not consider accretion a strong alternative explanation, although detailed, high-resolution hydrodynamical simulations of rapid gas accretion events would be very useful to explore this alternative further.

3.5 IRAM observations

3.5.1 Observations

We obtained CO(1–0) and CO(2–1) spectra of UGC 05771 with the Institut de Radio Astronomie Millimétrique (IRAM) 30 m telescope through the IRAM Director’s Discretionary Program D06-18 on February 25th, 2019. The source was observed with the Eight MIXer Receiver (EMIR), a wide-band heterodyne receiver, as part of the heterodyne pool. Both lines were observed together in dual-band mode with the FTS200 and The Wideband Line Multiple Autocorrelator (WILMA) backends.

They were placed in the UI sideband, with a tuning frequency corresponding to the expected observed frequencies ν_{obs} of the lines at $z = 0.02469$, 112.494 GHz and 224.983 GHz for CO(1–0) and CO(2–1) respectively. The IRAM beam FWHM is 21.8" at 114 GHz and 10.6" at 228 GHz.

We used Wobbler switching throws of 60", which is larger than the size of CO line emission in UGC 05771. The telescope was focused at the beginning of the observations on the bright quasar 1226+023, and then refocused every 3–4 hr. Another quasar, 0923+392, which is near the source, was used to reposition the telescope on the sky every 2–3 hr. Individual scans were 30 s long, and we obtained a calibration after sequences of 12 scans, i.e., every 6 minutes. The precipitable water vapour during observations varied between 1.5 and 5 mm. The total time on-source was 14580 s.

3.5.2 Data reduction

The data were calibrated at the telescope, and reduced with the CLASS package of the IRAM GILDAS software (Gildas Team 2013). All scans were examined by eye, and first-order polynomials were used to correct the baselines, after masking the spectral range covered by the line. We then averaged the individual scans, combining both horizontal and vertical polarizations. We used the antennae efficiencies given on the EMIR website of 5.9 Jy K^{-1} for the 3 mm, and 7.5 Jy K^{-1} for the 1.3 mm data to translate the measured brightness temperatures into flux density units, i.e., Jy. The lines are detected with both backends. We used WILMA to extract the scientific results, because it has a spectral resolution better suited to measurements of extragalactic emission lines, and more stable baselines. The resulting root-mean-square (rms) noise is 5.3 mJy and 7.5 mJy for CO(1–0) and CO(2–1), respectively, for a spectral channel width of 5 km s^{-1} at 112.5 GHz.

3.5.3 Results

We show the CO(1–0) and CO(2–1) spectra of UGC 05771 in Fig. 3.13, and the details of our observations and the fitted Gaussian profiles in Table 3.3. Both lines were clearly detected at the expected redshifts.

The CO(1–0) line shows a possible double-peaked profile, with a total line width of $\text{FWHM} = 476 \pm 23 \text{ km s}^{-1}$. The CO(2–1) line is somewhat broader, with $\text{FWHM} = 562 \pm 26 \text{ km s}^{-1}$, and appears to have a more complex line profile, although this may be due to the lower S/N and more irregular baselines at 1.3 mm. The CO(1–0) and CO(2–1) lines are centred around velocities of $49 \pm 13 \text{ km s}^{-1}$ and $22 \pm 11 \text{ km s}^{-1}$ respectively, relative to the systemic redshift of UGC 05771. The broad widths of the CO line profiles are consistent with the radial velocities observed in the ionised gas disc ($v_{\text{rad}} \approx 200 \text{ km s}^{-1}$, Fig. 3.9c) suggesting the broad line widths are dominated by rotation, although additional broadening due to turbulence may be present. The line fluxes are $8.6 \pm 0.4 \text{ Jy km s}^{-1}$ and $11.9 \pm 0.5 \text{ Jy km s}^{-1}$ for CO(1–0) and CO(2–1) respectively. The line ratio $\text{CO}(2-1)/\text{CO}(1-0) = 2.5$ is consistent with those in the sample of powerful radio galaxies with CO observations by Ocaña Flaquer et al. (2010), although this ratio may be affected by the different beam sizes of the 30-m telescope at 3 mm and 1.3 mm, which would have an effect if the CO reservoir is more extended than the 10" beam at 1.3 mm.

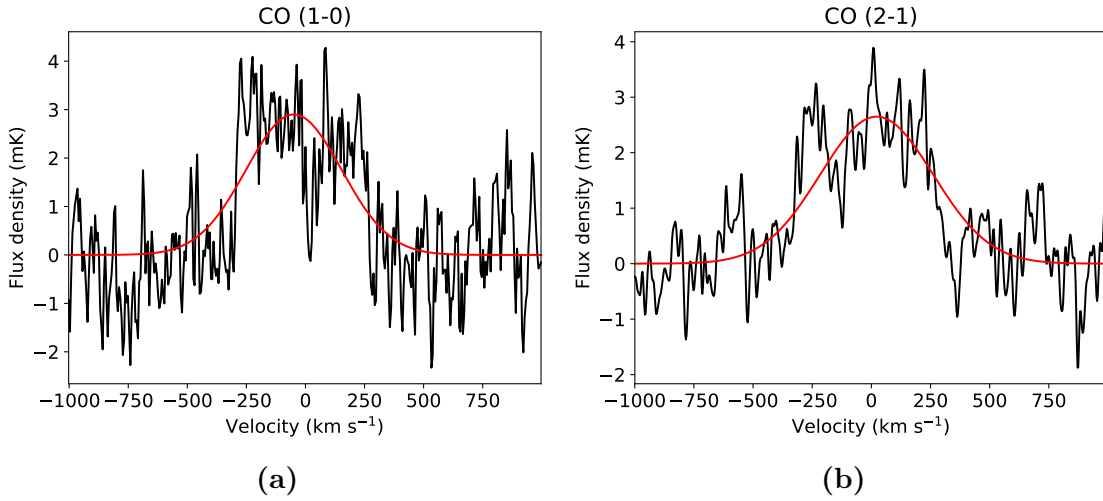


Figure 3.13: (a) CO(1–0) and (b) CO(2–1) line profiles of UGC05771. Red lines show the best Gaussian fit to each line.

Table 3.3: Observational results for CO: Rest-frame and observed frequency, velocity offset to $z = 0.02469$, FWHM line width, peak brightness temperature, and integrated line flux.

Property	CO(1–0)	CO(2–1)
ν_0 (GHz)	115.271	230.538
ν_{obs} (GHz)	112.4755 ± 0.0013	224.9662 ± 0.0009
Δv (km s $^{-1}$)	-49.4 ± 4.7	22.4 ± 11.5
FWHM (km s $^{-1}$)	476 ± 23	562 ± 26
T_{pk} (mK)	2.9 ± 0.1	2.65 ± 0.1
flux I_{CO} (Jy km s $^{-1}$)	8.6 ± 0.4	11.9 ± 0.5

Although both the CO(1–0) and CO(2–1) line profiles are complex, we could not justify the use of a more complex model than a simple Gaussian profile due to the poor S/N. To check the validity of this approach, we also estimated the integrated flux by summing the spectra between ± 500 km s $^{-1}$; for both the CO(1–0) and (2–1) lines, this method produced values within the 1σ errors of the fluxes from the Gaussian fit.

To estimate the molecular gas mass from the integrated CO(1–0) line flux I_{CO} , we first estimated the total CO line luminosity L'_{CO} using eqn. 3 of Solomon et al. (1997),

$$L'_{\text{CO}} = 3.25 \times 10^7 I_{\text{CO}} [\nu_0(1+z)]^{-2} D_L^2 (1+z)^{-3} \quad (3.9)$$

where L'_{CO} has units K km s $^{-1}$ pc 2 , the luminosity distance D_L is given in Mpc, the rest-frame emission line frequency ν_0 is given in GHz and I_{CO} is given in Jy km s $^{-1}$. As is standard for nearby ETGs, we used a Milky Way conversion factor between CO luminosity and H $_2$ gas mass, corresponding to $\alpha_{\text{CO}} = 4.6 M_{\odot} / [\text{K km s}^{-1} \text{pc}^2]$, which gives a molecular gas mass $M_{\text{H}_2, \text{CO}} = (1.1 \pm 0.4) \times 10^9 M_{\odot}$.

Surface density of dense gas

Resolved CO observations suggest that CO emission traces dust in ETGs (Alatalo et al. 2013). Hence, because our CO observations are not spatially resolved, we

estimated the dense gas mass surface density Σ_{gas} using the extinction as a proxy for the distribution of dense gas. At the frequency of the observed CO(1–0) transition, the FWHM of the IRAM beam is $\text{FWHM} = (2460/\nu_{\text{obs}}[\text{GHz}])'' = 21.9''$, slightly smaller than the size of the ionised gas disc. As shown in Fig. 3.10, the IRAM beam covers roughly the same area over which we are able to measure A_V ; over this region, A_V varies from 0 – 2 magnitudes and has a clumpy distribution, showing no clear trends with radius. Hence it is reasonable for us to assume that the CO emission is uniformly distributed across the IRAM beam, which gives $\Sigma_{\text{gas}} = 15 \pm 5 M_{\odot} \text{pc}^{-2}$, consistent with our A_V -based estimate ($\Sigma_{\text{gas}} = 10.0 \pm 0.5 M_{\odot} \text{pc}^{-2}$). We use this gas mass surface density estimate in Section 3.6.3 to investigate whether the jets are inducing negative feedback in UGC 05771.

3.6 Discussion

In this section, we present our interpretation of our OSIRIS, CALIFA and IRAM results. First, we argue that the shocked near-IR and optical line emission is due to jet-ISM interactions, and therefore that the radio source is much more extended than its apparent size in existing VLBI observations. We then use our CO observations and SFR estimates to determine whether the extended jet plasma is inhibiting star formation in UGC 05771. Finally, we constrain the properties of the density distribution of the ISM in UGC 05771 and estimate the age of the radio source.

3.6.1 Evidence for jet-ISM interaction in UGC 05771

Using our OSIRIS data (Section 3.3), we detected shocked molecular and ionised gas at radii of ≈ 200 pc, whereas the CALIFA data (Section 3.4) revealed shocked ionised gas at radii of ≈ 1 kpc. Here, we argue that both the optical and near-IR line emission is caused by the radio jets.

In Section 3.3.4, we showed that SNe explosions are unable to reproduce the observed [Fe II] line luminosity. Meanwhile, the [Fe II], H_2 and $\text{H}\alpha$ luminosities represent a few per cent of the estimated jet power ($4.2 \times 10^{41} \text{erg s}^{-1}$), meaning it is energetically plausible for the jets to power the line emission via radiative shocks. The [Fe II] exhibits a sharp velocity gradient of $\approx 200 \text{km s}^{-1}$ and has broad line widths of up to 230km s^{-1} (Fig. 3.6), indicating this gas is being excited by an energetic process. The radial velocities expected due to galactic rotation at these radii are insufficient to explain the velocity gradient in the [Fe II]. Meanwhile, there is no coherent rotation in the warm H_2 , with most of the line emission being blueshifted (Fig. 3.3), suggesting this material is being ejected from the nucleus. The radial velocities of both the [Fe II] and the H_2 are too small for the gas to escape the host galaxy’s potential, with $v_{\text{esc}} \approx 900 \text{km s}^{-1}$ at comparable radii. We therefore conclude that both the H_2 and the [Fe II] emission probe gas being accelerated out of the nucleus by the jets, entrained in a ‘stalling wind’ that will not escape the host galaxy. Similar phenomena have previously been observed in NGC 1266 (e.g., Alatalo et al. 2015) and in 3C 326 N (Nesvadba et al. 2010, 2011), in which only a fraction of the emission-line molecular gas accelerated by the jets exceeds the escape velocity of the host galaxy.

In our CALIFA data we detected a kpc-scale region of shocked gas with an elevated velocity dispersion in the vicinity of the nucleus. We have shown that beam

smearing is unable to reproduce the observed velocity dispersion (Section 3.4.3), and that the line ratios in this region are consistent with shocks (Fig. 3.11b). We also demonstrated that it is highly unlikely that UGC 05771 is accreting enough material to drive these shocks, given the relatively ordered kinematics in the ionised gas disc, and the lack of any signatures of infalling gas (Section 3.4.3). Hence, we conclude that kpc-scale jet plasma must be responsible for this line emission.

However, the apparent size of the radio source is 9 pc (e.g., Fig. A1a). This is inconsistent with our hypotheses that the jets power the H_2 and $[\text{Fe II}]$ emission, which extend ≈ 200 pc from the nucleus, and the $\text{H}\alpha$ emission, which extends ≈ 1 kpc from the nucleus. We address this in the following section.

3.6.2 How extended is the radio source?

The turnover frequency of GPS and CSS sources is strongly anticorrelated with the radio size of the source (O’Dea & Baum 1997). In Fig. 3.14, we show this correlation for the sample of GPS and CSS sources compiled by Jeyakumar (2016). We also indicate UGC 05771 on the plot (red star), using the linear size from the VLBI observations (de Vries et al. 2009, Figs. A1a and A1b). UGC 05771 is offset from the correlation by nearly two orders of magnitude, indicating it is possible that the radio source is in fact $\gtrsim 100$ times more extended than its size in existing VLBI observations.

If the jets are oriented at a small angle θ to the line of sight, the source will

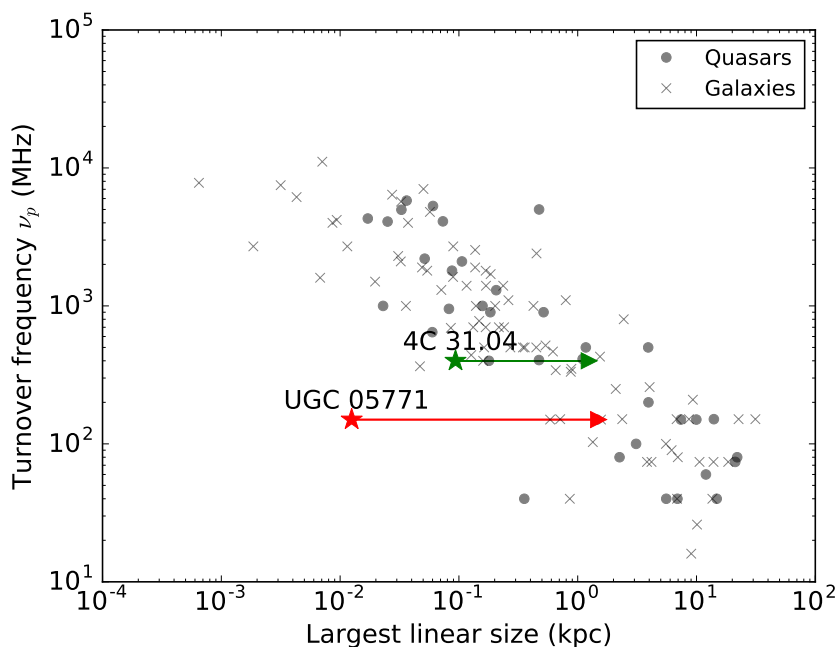


Figure 3.14: The peak frequency versus largest linear size for the catalogue of GPS and CSS sources compiled by Jeyakumar (2016), illustrating the strong anticorrelation between turnover frequency and linear size. The stars indicate the linear sizes, derived from VLBI observations, of 4C 31.04 (Zovaro et al. 2019a, green) and UGC 05771 (red) presented by Giroletti et al. (2003) and de Vries et al. (2009) respectively. Meanwhile, the arrows indicate the approximate extent of ro-vibrational H_2 emission in 4C 31.04 and optical emission line gas with line ratios consistent with shocks (Fig. 3.11b), which may trace extended, low surface brightness jet plasma that is resolved out in the VLBI images.

appear much more compact than it truly is. Such beamed sources generally exhibit high flux variability. However, Snellen et al. (2004) find that UGC 05771 does not have significant flux variability at 5 and 8.4 GHz. We therefore conclude that the compactness of the radio source is not an orientation effect. Why, then, does it appear to be so small?

The linear size of the radio source associated with UGC 05771 is based on the VLBI observations of de Vries et al. (2009) at 1.665 GHz. Referring to Fig. 3.1, these VLBI observations recover only 20 to 30 per cent of the unresolved single-dish fluxes at comparable frequencies. This implies that 70 – 80 per cent of the radio emission at these frequencies is emitted on scales larger than the spatial cutoff frequency of the VLBI observations.

The presence of bright, compact radio structures embedded in extended regions of low surface brightness radio emission is a key signature of jets in the ‘flood-and-channel phase’ of evolution (Sutherland & Bicknell 2007). In this phase, emergent jets split into multiple streams as they interact with a clumpy medium. Whilst the weaker streams percolate isotropically and form a bubble that drives a shock into the surrounding medium, the main jet stream emits brightly in the radio as it interacts with the ISM impeding its passage. Synthetic radio surface brightness images of these simulations (e.g., Fig. 2.9 of Zovaro et al. 2019a) show that the bubble can expand rapidly, enabling low-surface brightness plasma to be much more extended than the brightest radio structures. The low flux completeness of the pc-scale VLBI observations, coupled with the kpc-scale shocked gas, therefore suggests the jets in UGC 05771 are in the ‘flood-and-channel phase’, which we have previously observed in the CSS source 4C 31.04 (Zovaro et al. 2019a). The possible presence of a counter-rotating core (Fig. 3.12c) may additionally be a signature of jets interacting with a clumpy disc (Mukherjee et al. 2018b), a phenomenon also observed in IC 5063 (Morganti et al. 2015; Mukherjee et al. 2018a).

3.6.3 Are the jets inducing negative feedback in UGC 05771?

Even if the jets in UGC 05771 are not powerful enough to prevent star formation by ejecting gas from the host galaxy’s potential, our optical and near-IR observations indicate that there is kpc-scale jet plasma driving shocks and turbulence into the ISM. In this section, we use the Kennicutt-Schmidt (KS) relation (Kennicutt 1998) to determine whether the galaxy has a noticeable offset from that relation that could be attributed to the interactions with the radio jet.

Fig. 3.15 shows where UGC 05771 lies with respect to the KS relation (assuming a Salpeter IMF). To estimate Σ_{gas} in UGC 05771, we use our CO observations; for the SFR surface density Σ_{SFR} , we show our estimates computed using both the total H α flux (empty red triangle) and the H α flux only from spaxels with emission line ratios lying in the intermediate and star-forming regions of the ODDs (filled red triangle). We favour the latter value, as the first is contaminated by gas where shocks, AGN photoionisation and/or photoionisation from post-AGB stars dominates, as indicated by the line ratios.

For comparison, we also show galaxies from two different samples: 15 ETGs from Martig et al. (2013), which do not host AGN, but may show signatures of morphological quenching, and 16 bright, gas-rich radio galaxies (‘molecular hydrogen emission galaxies’ (MOHEGs)) from Lanz et al. (2016), which contain warm, shocked

molecular gas, presumably from interactions with the radio jet (Ogle et al. 2010; Nesvadba et al. 2010). The star-formation rates in these samples were derived from polycyclic aromatic hydrocarbon and far-infrared dust emission, respectively, which may imply small systematic uncertainties of-order 0.1 – 0.2 dex compared to UGC 05771.

We also show the original sample of spiral and starburst galaxies from Kennicutt (1998), where the SFRs have been estimated using H α and FIR fluxes respectively, both adjusted for a Salpeter IMF. Adopting the SFR(H α) estimate only using the intermediate and star-forming spaxels, UGC 05771 is shifted by a factor of 9 from the KS relationship of ordinary star-forming galaxies, corresponding to a shift of about 1σ , and in the regime covered by the samples of Martig et al. (2013) and Lanz et al. (2016). However, as discussed in Section 3.4.3, our Σ_{SFR} estimate should be interpreted as an upper limit due to contamination from shocks, AGN photoionisation and/or post-AGB stars. It is therefore feasible that UGC 05771 is even more strongly offset. Spatially resolved observations would be needed to see whether this offset of the global, source averaged gas and star-formation surface densities heralds a more pronounced, local decrease in star formation efficiency, or whether a slight global decrease is happening in UGC 05771. This would also help to distinguish whether such a decrease would be due to interactions with the radio jet, or other quenching mechanisms, e.g., morphological quenching. Regardless of the detailed mechanism in place, however, our results do show that UGC 05771 has a slightly lower star formation rate than would be expected from the KS relation at face value.

3.6.4 Constraining the parameters of the ISM density distribution

Free-free absorption (FFA) of synchrotron radiation by an inhomogeneous ionised medium enshrouding the jet plasma can replicate the characteristic spectrum of GPS and CSS sources (Bicknell et al. 2018). Under this paradigm, the frequency of the spectral peak is sensitive to the density probability distribution function (PDF) of the ISM. Here, we use the method of Zovaro et al. (2019a) to infer the properties of the density PDF in UGC 05771; for full details of the method, see Section 2.5.5.

We modelled the ISM as having a log-normal density distribution, which is appropriate for turbulent media (Nordlund & Padoan 1999; Federrath & Klessen 2012), and assumed the absorbing medium is a slab with depth $L = 2$ kpc, corresponding to the region of elevated velocity dispersion in the ionised gas (Fig. 3.9d). Eqn. 2.17 of Zovaro et al. (2019a) gives the free-free optical depth τ_ν as a function of ISM parameters shown in Table 3.4 and the expected value of n^2 in the slab $E(n^2)$. We estimated $E(n^2)$ by setting $\tau_\nu = 1$ at the spectral peak ν_p , and used eqns. 2.11, 2.12, 2.13 and 2.18 of Zovaro et al. (2019a) to estimate the mean density \bar{n} and the standard deviation σ of the density PDF, shown in in Table 3.4. The low mean density ($\sim 1 \text{ cm}^{-3}$) is consistent with the low-frequency spectral turnover of UGC 05771, whereas the inferred high turbulent Mach number and the assumption of a log-normal distribution gives a large value for $E(n^2)$.

We then estimated the age of the radio source using the extent of the shocked gas, our new density estimate and the jet power. Assuming that the jet-driven bubble evolves adiabatically, the time taken t_b for the bubble to reach its current size R_b if inflated by a jet with power L_{jet} expanding into a uniform medium with

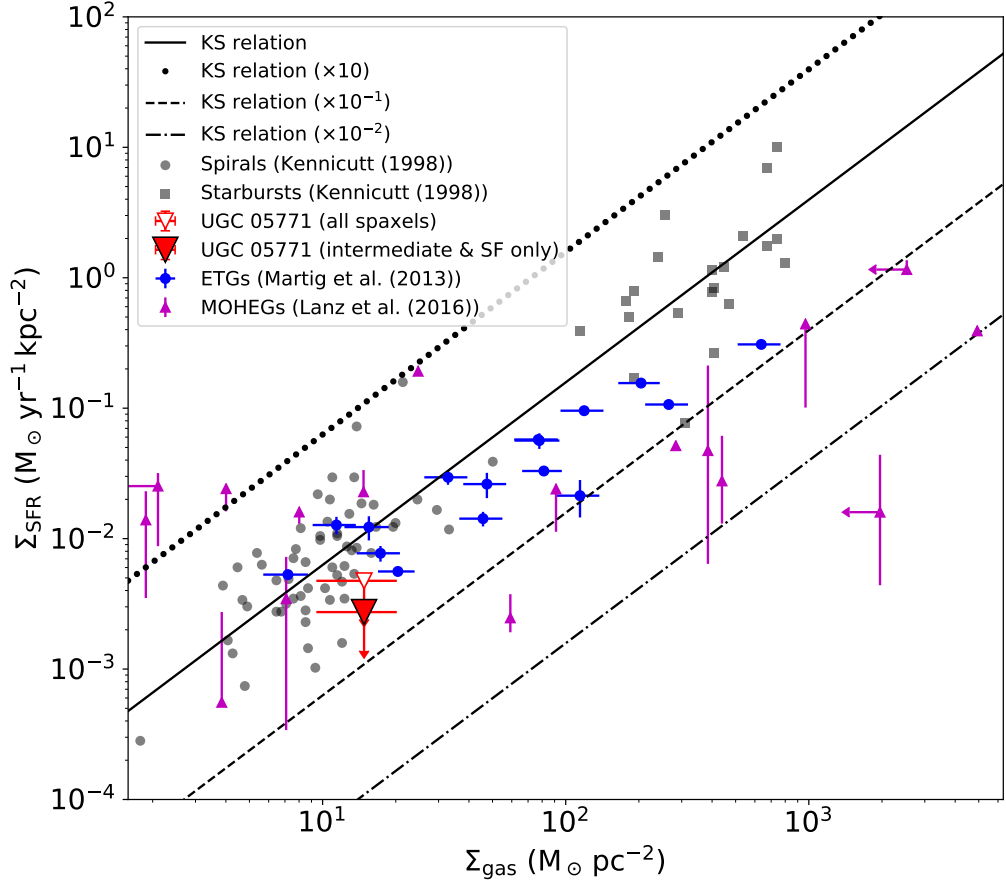


Figure 3.15: The Kennicutt-Schmidt (KS) relation. The black line represents the KS relation for a Salpeter IMF. We also show lines which display star forming efficiencies of $10\times$ (dotted line), $0.1\times$ (dashed line) and $0.01\times$ (dot-dashed line) that of the KS relation. We indicate UGC 05771 with 1σ error bars for Σ_{gas} and Σ_{SFR} , where we have adopted the $\text{H}\alpha$ -based SFR surface density computed using all spaxels within the IRAM beam (empty red triangle) and computed using only those spaxels with line ratios that lie in the intermediate or star-forming regions of the ODD shown in Fig. 3.11 (filled red triangle). The blue points are the sample of quiescent ETGs of Martig et al. (2013), where the SFRs have been estimated using the $8\ \mu\text{m}$ flux, and the magenta points are the sample of radio galaxies of Lanz et al. (2016). The grey circles and squares are the sample of spiral and starburst galaxies of Kennicutt (1998). The SFRs for all samples have been adjusted for a Salpeter IMF.

density ρ is given by (Bicknell & Begelman 1996)

$$t_b = \left(\frac{384\pi}{125} \right)^{1/3} \rho^{1/3} L_{\text{jet}}^{-1/3} R_b^{5/3} \quad (3.10)$$

where we adopted $R_b = 2\ \text{kpc}$ and a density $n = 1\ \text{cm}^{-3}$ consistent with our FFA model. This gives an age of approximately 19 Myr.

3.7 Conclusion

We have studied jet-ISM interactions in the low-power CSS source UGC 05771 in order to search for evidence that the jets are inhibiting star formation in the host galaxy.

Table 3.4: Parameters used in determining the parameters of the log-normal density distribution. Output parameters are denoted with daggers (\dagger). Fractional abundances were estimated using a MAPPINGS V (Sutherland et al. 2018) model grid with non-equilibrium cooling and solar abundances.

Parameter	Symbol	Value
Peak frequency	ν_p	150 MHz
Depth of absorbing slab	L	2 kpc
Temperature	T	10^4 K
Mean molecular mass	μ	0.66504
Electron fractional abundance	n_e/n	0.47175
H ⁺ fractional abundance	n_{H^+}/n	0.41932
He ⁺ fractional abundance	n_{He^+}/n	0.024458
He ⁺⁺ fractional abundance	$n_{\text{He}^{++}}/n$	0.013770
Line-of-sight velocity dispersion	σ_g	225 km s^{-1}
Sound speed	c_s	11.21 km s^{-1}
Turbulent Mach number	\mathcal{M}	34.75 km s^{-1}
Turbulent forcing parameter	b	0.4
Ratio of thermal to magnetic pressure	β	1 (equipartition)
Expected value of $n^{2\dagger}$	$E(n^2)$	116.7 cm^{-6}
Mean density [†]	\bar{n}	1.094 cm^{-3}
Density variance [†]	σ^2	115.5 cm^{-6}

We analysed the sub-kpc scale circumnuclear gas of the host galaxy to search for signatures of jet-ISM interactions using near-infrared integral field spectroscopy from OSIRIS.

We detected ro-vibrational H₂ emission in the central 200 pc of the host galaxy that probes shock-heated molecular gas at $T \approx 5000$ K. We also detected [Fe II]_{1.644 μm} emission in the same region with luminosity too high to be explained by SNe explosions, whereas the jet power is sufficient to power both the [Fe II] and H₂ luminosities, leaving shocks induced by the jets as the most likely cause. The kinematics of both the H₂ and [Fe II] emission lines imply that the jets are accelerating material out of the nucleus to velocities insufficient to expel the gas from the host galaxy potential, creating a ‘stalling wind’.

We analysed the properties of the kpc-scale optical emission line gas in the galaxy using optical integral field spectroscopy from the CALIFA survey. The host galaxy has a disc of ionised gas approximately 20 kpc in diameter. Line ratios, broad line widths and disturbed kinematics in the innermost 2 kpc cannot be explained by beam smearing or by accretion, indicating that the gas in this region is being shocked and disturbed by the jets. Further observations with higher spectral resolution are required to confirm the presence of multiple kinematic components in the emission lines that would arise from jet-ISM interactions.

Both the CALIFA and OSIRIS data show that the jets are interacting strongly with the ISM out to kpc radii, in apparent contradiction to the pc-scale structure revealed by VLBI imaging. We propose that UGC 05771 in fact hosts a kpc-scale radio source, and that the extended jet plasma is either resolved out by these observations or has too low a surface brightness to be detected, consistent with the

location of UGC 05771 on the peak frequency-size correlation.

To determine whether the jets are inhibiting star formation in UGC 05771, we obtained IRAM observations of CO(1–0) and CO(2–1), and found $M_{\text{gas}} = 1.1 \pm 0.4 \times 10^9 M_{\odot}$ and a mean surface density $\Sigma_{\text{gas}} = 15 \pm 5 M_{\odot} \text{ pc}^{-2}$. Although we found that it is possible that UGC 05771 is significantly offset from the KS relation, we were unable to confirm whether negative feedback is taking place due to systematic uncertainties in our H α -based SFR estimate due to contamination by shocks and evolved stars.

The fact that we have observed signatures of jet-ISM interactions out to kpc radii in both 4C 31.04 and UGC 05771 suggests that diffuse, low surface brightness radio plasma that is not visible in VLBI observations may be common in compact radio galaxies. Our observations have shown that this radio plasma interacts strongly with the ISM, heating and injecting turbulence, and potentially inhibiting star formation. This finding demonstrates that young radio sources with seemingly compact jets may have a substantial impact on the star formation of their host galaxy, having important implications for the role that jets play in galaxy evolution.

Acknowledgements

We would like to thank the anonymous reviewer for their insightful comments, and Anne Medling, Alec Thomson and Tiantian Yuan for helpful discussions.

This work is based on observations carried out under project number D06-18 with the IRAM NOEMA Interferometer [30 m telescope]. IRAM is supported by INSU/CNRS (France), MPG (Germany) and IGN (Spain). We would like to thank K. Schuster, the director of IRAM, for the generous attribution of Director’s Discretionary Time, and the staff and pool observers at the 30-m telescope, in particular C. Kramer and Wonju Kim, for the rapid scheduling and execution of our CO observations.

The data presented herein were obtained at the W. M. Keck Observatory, which is operated as a scientific partnership among the California Institute of Technology, the University of California and the National Aeronautics and Space Administration. The Observatory was made possible by the generous financial support of the W. M. Keck Foundation. Australian community access to the Keck Observatory was supported through the Australian Government’s National Collaborative Research Infrastructure Strategy, via the Department of Education and Training, and an Australian Government astronomy research infrastructure grant, via the Department of Industry and Science. We would like to thank the Keck support staff, in particular J. Lyke, for their help in obtaining our OSIRIS observations.

The authors recognize and acknowledge the very significant cultural role and reverence that the summit of Maunakea has always had within the indigenous Hawaiian community. We are most fortunate to have the opportunity to conduct observations from this mountain.

This study uses data provided by the Calar Alto Legacy Integral Field Area (CALIFA) survey (<http://califa.caha.es/>), based on observations collected at the Centro Astronómico Hispano Alemán (CAHA) at Calar Alto, operated jointly by the Max-Planck-Institut für Astronomie and the Instituto de Astrofísica de Andalucía (CSIC). We also thank Sebastian Sánchez for assistance with accessing CALIFA data products used in this work.

This study made use of data made available by the NASA/IPAC Extragalactic Database (NED), which is operated by the Jet Propulsion Laboratory, California Institute of Technology, under contract with the National Aeronautics and Space Administration.

This research made use of QFitsView^{||}, a software package for reducing astronomical data written by Thomas Ott, Scipy^{**} (Jones et al. 2001), and Astropy^{††} a community-developed core Python package for Astronomy (Astropy Collaboration et al. 2013, 2018).

^{||}<https://www.mpe.mpg.de/~ott/QFitsView/>

^{**}<http://www.scipy.org/>

^{††}<http://www.astropy.org>

4

Unravelling the enigmatic ISM conditions in Minkowski's Object

It is likely that unlikely things should happen.

Aristotle

This chapter presents the content of the article *Unravelling the enigmatic ISM conditions in Minkowski's Object* (Zovaro et al.), which is the late stages of preparation for submission to a peer-reviewed journal.

Abstract

Local examples of jet-induced star formation lend valuable insight into its significance in galaxy evolution and can provide important observational constraints for theoretical models of positive feedback. Using optical integral field spectroscopy, we present an analysis of the ISM conditions in Minkowski's Object ($z = 0.0189$), a peculiar star-forming dwarf galaxy located in the path of a radio jet from the galaxy NGC 541. Full spectral fitting with PPXF indicates that Minkowski's Object primarily consists of a young stellar population ~ 10 Myr old, confirming that the object formed during a recent jet interaction. Minkowski's Object exhibits line ratios largely consistent with star formation, although there is evidence for a low level ($\lesssim 15$ per cent) of contamination from a non-stellar ionising source. Strong-line diagnostics reveal a significant variation in the gas-phase metallicity within the object, with $\log(\text{O}/\text{H}) + 12$ varying by 0.5 dex, which cannot be explained by in-situ star formation, an enriched outflow from the jet, or enrichment of gas in the stellar bridge between NGC 541 and NGC 545/547. We hypothesise that Minkowski's Object either (a) was formed as a result of jet-induced star formation in pre-existing gas clumps in the stellar bridge, or (b) is a gas-rich dwarf galaxy that is experiencing

an elevation in its star formation rate due to a jet interaction, and will eventually redden and fade, becoming an ultra-diffuse galaxy as it is processed by the cluster.

4.1 Introduction

It has long been established that jets play a vital role in curbing star formation, by preventing cooling flows in cluster environments (McNamara & Nulsen 2012), by driving powerful outflows (Morganti et al. 2005; Holt et al. 2008; Schulz et al. 2018) and by rendering the interstellar medium (ISM) of their host galaxies turbulent (Nesvadba et al. 2010, 2011; Ogle et al. 2010). In comparison, the phenomenon of *positive feedback*, wherein jets enhance or trigger star formation, remains poorly understood, although it may make an important contribution to the star formation histories of galaxies across cosmic time (Silk 2005; Gaibler et al. 2012).

The observed alignment of jets with stellar components and enhanced emission from dense gas is strong evidence of positive feedback. Many radio galaxies at high redshifts exhibit extended stellar continua that are aligned with the axis of the radio jet, referred to as the ‘alignment effect’ (Chambers et al. 1987; McCarthy et al. 1987; Best et al. 1996). Similar alignments have been observed in cluster environments at low redshift (McNamara & O’Connell 1993). More recent studies have also revealed alignment of molecular gas and radio jets in galaxies at high redshift (Klamer et al. 2004; Emonts et al. 2014). Hydrodynamical simulations have shown that shocks generated by the passage of a jet through an ionised medium may induce runaway cooling, leading to the formation of both atomic and molecular gas, which may collapse to form stars (Fragile et al. 2004, 2017). However, the detailed workings of positive feedback remain elusive, largely due to the dearth of local examples of jet-induced star formation, severely limiting our ability to study this complex phenomenon with sufficient angular resolution to compare observations to detailed hydrodynamical simulations.

Minkowski’s Object (Minkowski 1958, hereafter MO) is one of only three known examples of jet-induced star formation in the local Universe, the others being the string of OB associations in the jet of Centaurus A (Blanco et al. 1975) and a star-forming region in the jet of 3C 285 (Salomé et al. 2015). Located in the cluster Abell 194, MO is a star-forming dwarf galaxy located along the path of a jet from the nearby elliptical galaxy NGC 541. Due to its low redshift ($z = 0.0189$, Croft et al. 2006), MO presents a critical opportunity to study an object formed by positive feedback in high resolution.

Whilst past studies of MO have focused on broad-band photometry or slit spectroscopy, this work utilises integral field spectroscopy, enabling us to spatially resolve the ISM conditions in this object for the first time. In this paper, we present a study of the stellar and gas properties of MO using optical integral field spectroscopy. In Section 4.2, we summarise the properties of MO, and in Section 4.3 we give an overview of NGC 541 and the cluster environment of MO. We present our observations and data reduction in Section 4.4, before detailing the stellar population analysis in Section 4.5 and our analysis of the emission-line gas in Section 4.6. We then consider the possible causes of the observed metallicity variation in MO in Section 4.7, before discussing the origin of MO in Section 4.8 and summarising our findings in Section 4.9. For the remainder of this paper, we assume a cosmology with $H_0 = 70 \text{ km s}^{-1} \text{ Mpc}^{-1}$, $\Omega_M = 0.3$, and $\Omega_\Lambda = 0.7$.

4.2 Minkowski’s Object

MO ($z = 0.0189$, Croft et al. 2006) is a peculiar dwarf galaxy located in the cluster Abell 194, with properties summarised in Table 4.1. MO lies in the path of an FRI-type (Fanaroff & Riley 1974) jet from the elliptical galaxy NGC 541 ($z = 0.01809$, Smith et al. 2000) which lies 18 kpc to the South-West, as shown in Fig. 4.1.

As can be seen in Figs. 4.2 and 4.3, MO has an irregular and filamentary structure, with the brightest clumps forming a ‘bar’ approximately perpendicular to the jet axis. Croft et al. (2006) estimated MO to have a stellar mass $M_* = 1.9 \times 10^7 M_\odot$, with a broad-band spectral energy distribution (SED) consistent with a stellar population resulting from a single starburst 7.5 Myr ago with a secondary population of stars older than 1 Gyr.

MO is embedded in a cloud of neutral gas with an estimated mass $M_{\text{HI}} = 4.9 \times 10^8 M_\odot$ (Croft et al. 2006) which is located along the path of the jet, extending downstream of MO (see their fig. 3). Molecular gas has been detected in four distinct clumps with intervening diffuse emission (Lacy et al. 2017, their fig. 2) with a total mass $M_{\text{H}_2} = 3.0 \times 10^7 M_\odot$ assuming a standard Milky Way (MW) CO-to-H₂ conversion factor. Both the H I and molecular gas exhibit steep velocity gradients perpendicular to the jet axis, which Lacy et al. (2017) attribute to a jet interaction. The velocity dispersion of the CO ($\lesssim 10 \text{ km s}^{-1}$) is much lower than that of the H I in the same region (25 km s^{-1}); this may be caused by shocks generated by the jet passing through an inhomogeneous medium (Lacy et al. 2017).

Table 4.1: Properties of MO and NGC 541.

Property	Symbol	MO	NGC 541
Stellar mass	M_*	$1.9 \times 10^7 M_\odot^a$	$4.7 \times 10^{11} M_\odot^d$
H I mass	M_{HI}	$4.9 \times 10^8 M_\odot^a$	—
Molecular gas mass	M_{H_2}	$3.0 \times 10^7 M_\odot^b$	$1.7 \times 10^8 M_\odot^d$
Star formation rate	SFR	$\leq 0.272 \pm 0.017 M_\odot \text{ yr}^{-1c}$	$0.095 M_\odot \text{ yr}^{-1d}$
Specific star formation rate	sSFR	14.3 Gyr^{-1c}	0.0002 Gyr^{-1d}
Depletion time	t_{dep}	$1.8 \text{ Gyr}^{e,\S}$	$1.79 \text{ Gyr}^{d,\S\S}$

References: ^aCroft et al. (2006); ^bLacy et al. (2017); ^cThis work; ^dSalomé et al. (2015); ^eBased on H I mass; ^{§§}Based on H₂ mass.

4.3 Abell 194 and NGC 541

Abell 194 is a poor (Abell et al. 1989) and cold (Sakelliou et al. 2008) cluster with a linear morphology at $z = 0.018$ (Struble & Rood 1999). It hosts two powerful radio galaxies close to the cluster centre, NGC 541 and NGC 547, which is part of the interacting pair NGC 545/547 ($z = 0.01781$ and $z = 0.01852$ respectively; Smith et al. 2000). The Southern jet from NGC 547 is associated with an X-ray cavity (Bogdán et al. 2011). As shown in Fig. 4.1, NGC 541 and NGC 545/547 are separated by approximately 100 kpc in projection, and are connected by a faint stellar bridge, a remnant of a previous or ongoing interaction. Both radio galaxies host bent jets, which Sakelliou et al. (2008) attribute to the motion of the galaxies through the cluster. Abell 194 may be undergoing a significant merger event, in

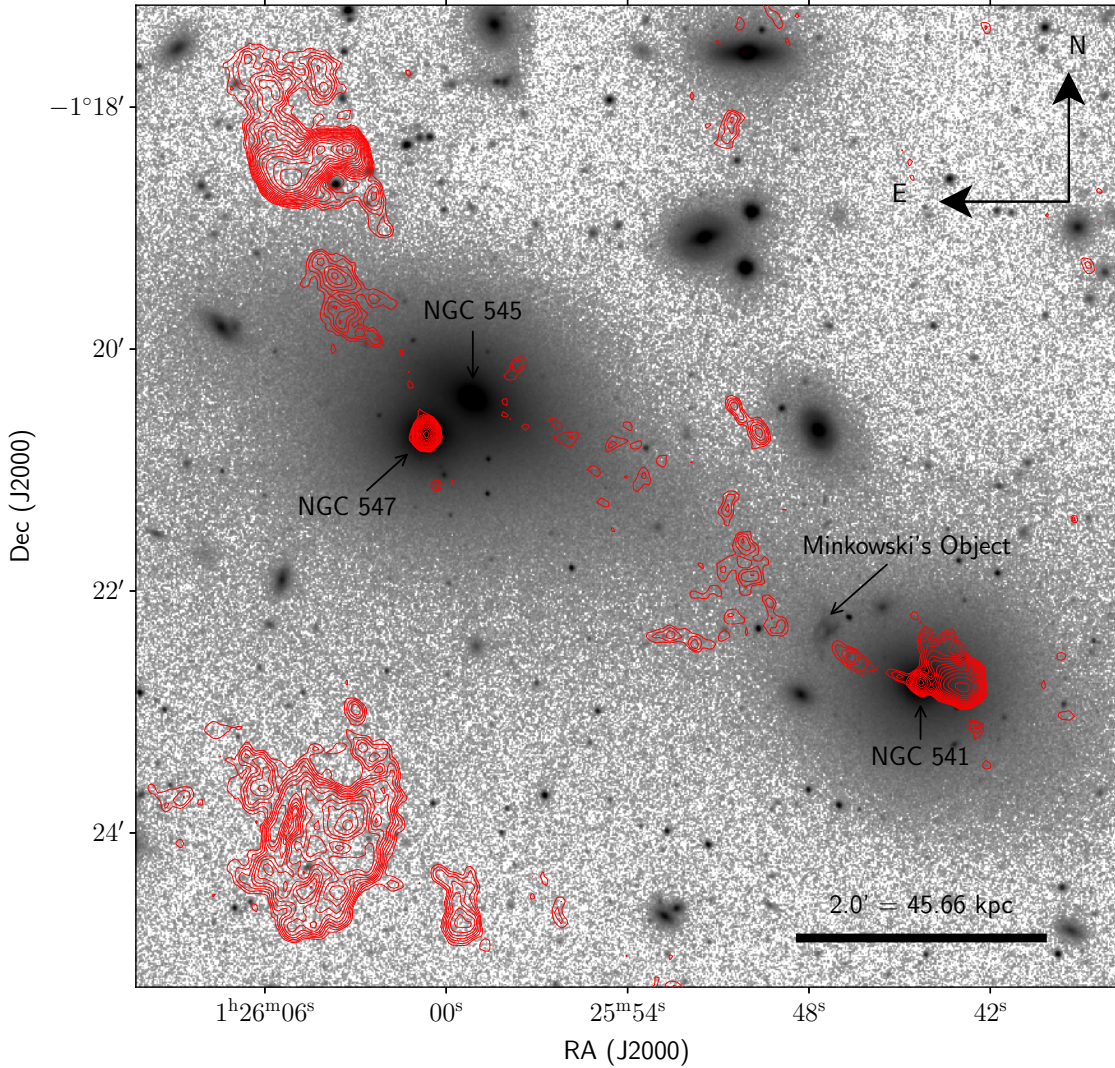


Figure 4.1: Sloan Digital Sky Survey (SDSS) *i* band image of Abell 194, showing the relative positions of NGC 541, NGC 545, NGC 547 and Minkowski's Object. The colour scale of the image has been adjusted to highlight the faint stellar bridge extending from NGC 541 to NGC 545/547. The red contours show the 1.4 GHz continuum flux from VLA/FIRST (Becker et al. 1995) indicating the radio jets from NGC 541 and NGC 547. The contours represent 30 logarithmically spaced intervals from 3σ Jy beam $^{-1}$ to 0.1 Jy beam $^{-1}$, where $\sigma = 1.4 \times 10^{-4}$ Jy beam $^{-1}$ is the measured rms noise in the image.

which both NGC 541 and NGC 545 are falling towards NGC 547 (Bogdán et al. 2011).

NGC 541 is a massive elliptical galaxy, and is the brightest cluster galaxy (BCG) in Abell 194. It is extremely gas-poor, with a gas fraction of 0.4 per cent and a star formation rate (SFR) of $0.095 M_{\odot} \text{ yr}^{-1}$ (Salomé et al. 2015). NGC 541 may harbour a disc or ring of molecular gas (Salomé et al. 2015), possibly a remnant of a previous interaction. The properties of NGC 541 are summarised in Table 4.1.

4.3.1 Properties of the radio jet

NGC 541 hosts an asymmetric FRI radio source with $P_{1.4 \text{ GHz}} = 5.9 \times 10^{23} \text{ W Hz}^{-1}$ (van Breugel et al. 1985) which can be seen in Figs. 4.2 and 4.3. The Eastern jet is

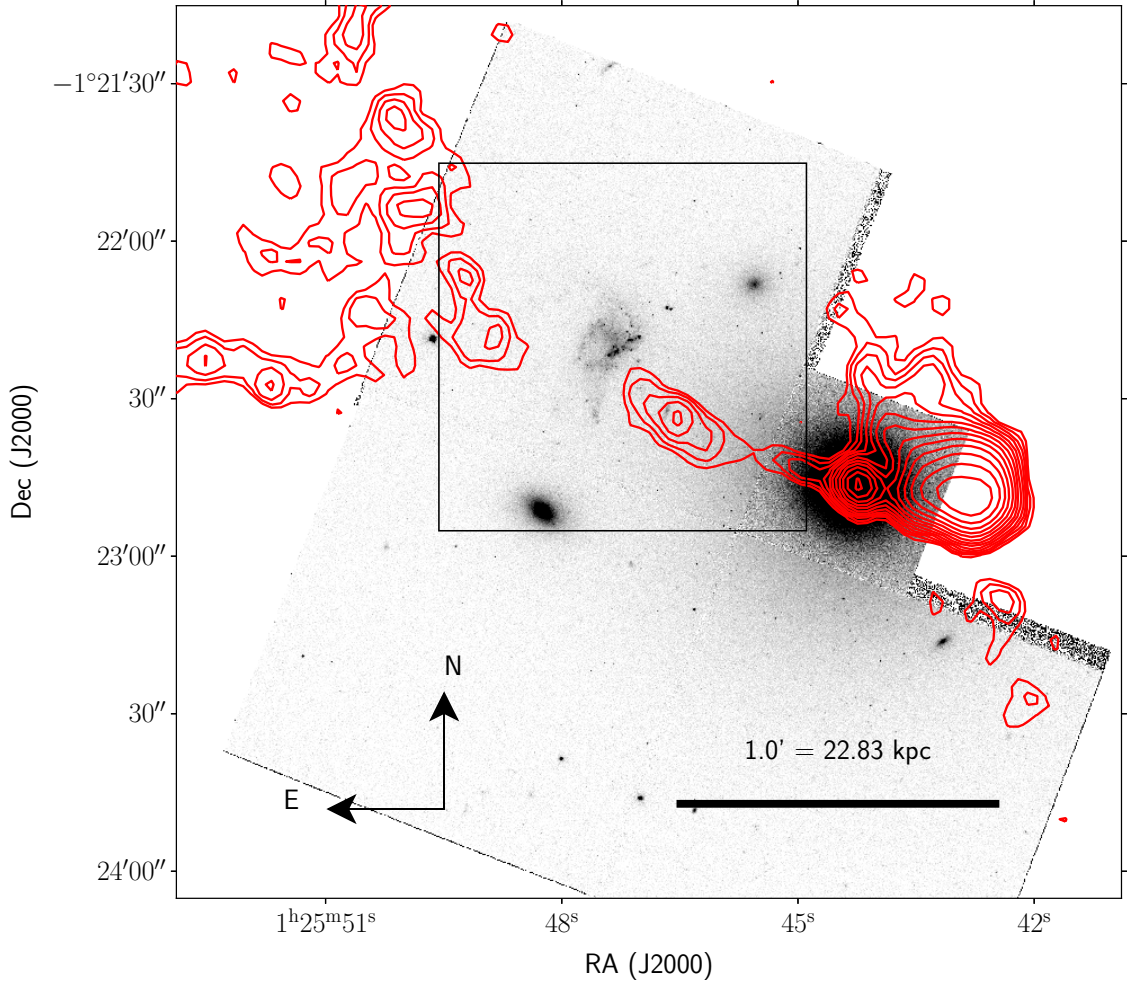


Figure 4.2: Archival *HST* WFPC2 F555W image of MO and NGC 541 (Verdoes Kleijn et al. 1999), overlaid with contours showing the 1.4 GHz continuum flux from VLA/FIRST indicating the path of the radio jet from NGC 541. The contours represent 20 logarithmically spaced intervals from 3σ Jy beam $^{-1}$ to 1×10^{-1} Jy beam $^{-1}$, where $\sigma = 1.4 \times 10^{-4}$ Jy beam $^{-1}$ is the measured rms noise in the image.

aligned with the stellar bridge, and gradually broadens along its path from the host galaxy until it interacts with MO, at which point it decollimates. The Western jet is less extended and is sharply bent a short distance from the nucleus.

Using the ALMA 106 GHz continuum image of Lacy et al. (2017), we used the minimum energy method, as detailed in Section 2.5.1 of Zovaro et al. (2019a), to estimate the power of the Eastern jet. The jet volume was approximated as a truncated cone, with length 21 kpc and end surface radii of 1.5 kpc and 6 kpc, and was assumed to have a constant flux density of $30 \mu\text{Jy beam}^{-1}$, with a spectral index $\alpha = 0.8^*$. A jet age of 10^7 yr was adopted, chosen to be consistent with the age of the stellar population of MO (Croft et al. 2006). Lower and upper Lorentz factors for the electrons were fixed to 10^2 and 10^5 respectively. These parameters yield a jet power of approximately 1.2×10^{43} erg s $^{-1}$.

*We define the spectral index α such that $S \propto \nu^{-\alpha}$.

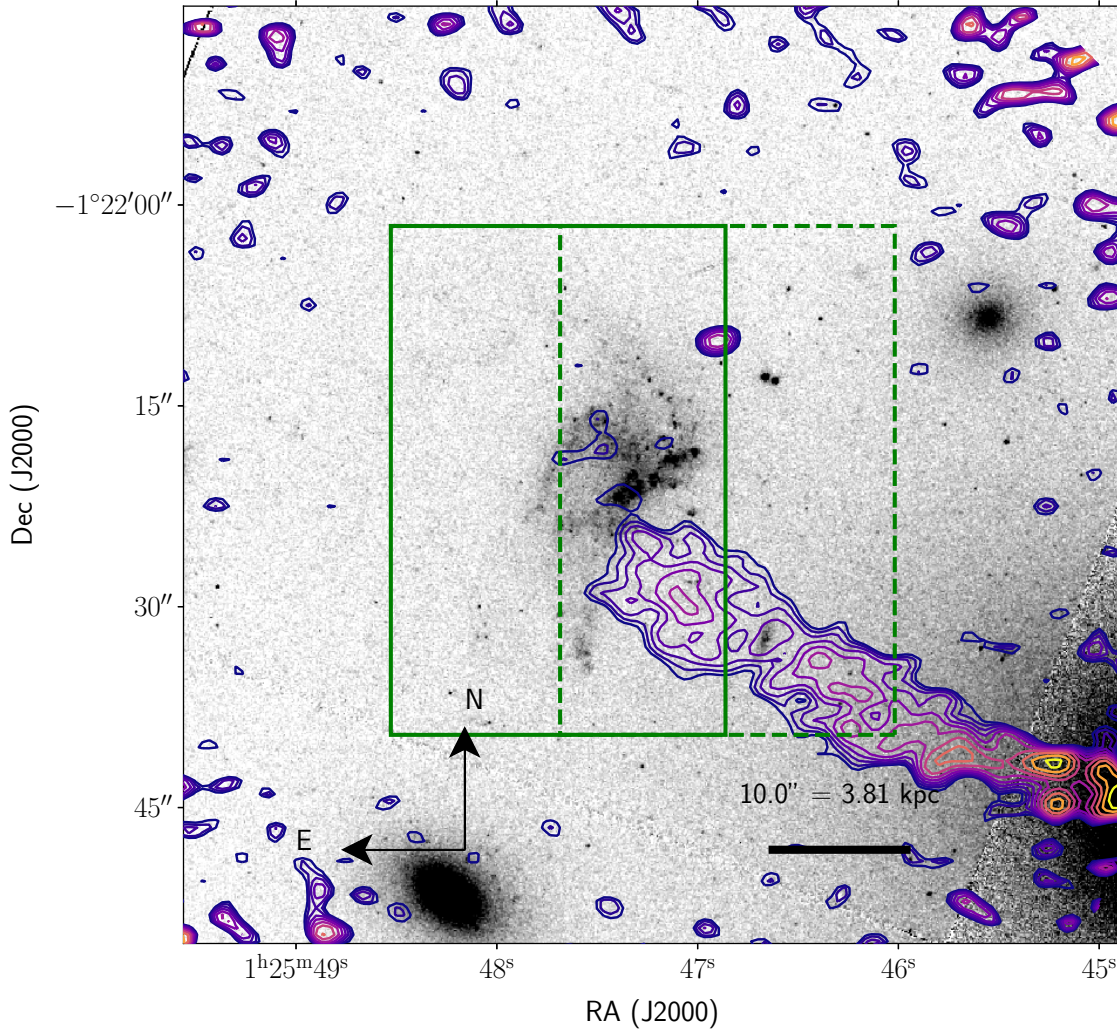


Figure 4.3: A magnified view of the region outlined by the black square in Fig. 4.2, overlaid with contours showing the ALMA 106 GHz continuum from the jet (Lacy et al. 2017). The contours represent 10 logarithmically spaced intervals from 3σ Jy beam^{-1} to 1.6×10^{-4} Jy beam^{-1} , where $\sigma = 9.2 \times 10^{-6}$ Jy beam^{-1} is the measured rms noise in the image. The green solid and dashed boxes indicate the two base pointings of our WiFeS integral field spectroscopy observations.

4.4 Observations and data reduction

We observed MO with the Wide-Field Spectrograph (WiFeS; Dopita et al. 2007, 2010) on the Australian National University 2.3 m telescope at Siding Spring Observatory, NSW, Australia. WiFeS is an image slicer integral field spectrograph comprising 25 $1''$ -width slices with $0.5''$ sampling along the image, binned to $1''$ to better match the seeing, providing $1'' \times 1''$ spaxels over a $25'' \times 38''$ field-of-view.

MO was observed on the 29th of November and 1st of December 2016 (PI Banfield, proposal ID 4160092) using the low-resolution B3000 ($3200 \text{ \AA} - 5000 \text{ \AA}$, $R \sim 3000$, $\Delta v \approx 100 \text{ km s}^{-1}$) and the high-resolution R7000 ($5290 \text{ \AA} - 7060 \text{ \AA}$, $R \sim 7000$, $\Delta v \approx 40 \text{ km s}^{-1}$) gratings with the RT560 beam splitter, using 1200 s exposures. Due to the large angular extent of MO, the observations were dithered in an E-W direction using an offset of $12''$, as shown in Fig. 4.3. The total effective exposure time was 9600 s. The stars HD26169, HD16031, HD44007 and HD9051 were used as flux and telluric standards (Bessell 1999).

4.4.1 Data reduction

The observations were reduced in the standard way using PYWIFES, the data reduction pipeline for WiFeS (Childress et al. 2014). Cu-Ar and Ne-Ar arc lamp exposures were used to derive the wavelength solution, and exposures of the coronagraphic wire mask were used to calibrate the spatial alignment of the slits. Quartz lamp and twilight flat exposures were used to correct for wavelength and spatial variations in the instrument response respectively. Exposures of standard stars were used to correct for telluric absorption and for flux calibration. Two data cubes were generated for each exposure, corresponding to the blue (B3000) and red (R7000) arms of the spectrograph respectively.

The data cubes were aligned using a cross-correlation technique before performing the sky subtraction, correcting for flux scaling factors in each data cube and finally combining the individual frames into a mosaic, as follows.

Sky subtraction

To maximise time on-source, we did not take sky frames in our observations. We instead used regions within the WiFeS field-of-view with no source signal to estimate and subtract the sky background, using the following method.

For each exposure, we extracted a rectangular ‘sky region’ expected to contain no source signal. For each spaxel in the sky region, we fitted Gaussian profiles to a subset of the brightest sky lines. We selected one spaxel as a reference, and calculated the multiplicative scaling factors required to adjust the intensity of each sky line to match that of those in the reference spaxel. We then computed the sigma-clipped mean of these scaling values, and multiplied the spectrum in the spaxel by this amount. This process ensures the intensity of the sky lines is relatively uniform across all spaxels in the sky region. We then created a master sky spectrum by taking the sigma-clipped mean of each spaxel in the sky region in every wavelength slice. Then, for every spaxel in the data cube, we fitted Gaussian profiles to a selection of bright sky lines and calculated the scaling factor required for the intensity of the sky lines to match those in the reference spaxel using the same method as before. We then scaled the master sky spectrum and subtracted it from each spaxel.

Flux scaling and mosaicing

The range of airmasses and seeing conditions of our observations resulted in subtle multiplicative offsets in the fluxes between different exposures. We used the following process to adjust the flux levels in each data cube prior to combining.

For simplicity, consider a series of images A_i of the same object. The optimal scaling factors α_i for each image will be those such that after the scaling is applied, the relative differences between all image pairs i, j is minimised; that is, we aim to find the α_i that minimise the objective function

$$\Delta = \sum_{i \neq j} \delta_{i,j}(\alpha_i, \alpha_j)^2, \quad (4.1)$$

where $\delta_{i,j}$ is the mean of the difference between the two images over all N pixels k ,

weighted by the error in the difference:

$$\delta_{i,j}(\alpha_i, \alpha_j) = \frac{1}{N} \sum_k \frac{\alpha_i A_{i,k} - \alpha_j A_{j,k}}{\sqrt{\alpha_i^2 \sigma_{A_{i,k}}^2 + \alpha_j^2 \sigma_{A_{j,k}}^2}}, \quad (4.2)$$

where $\sigma_{A_{i,k}}^2$ is the variance of image $A_{i,j}$ in pixel k .

In our case, we needed to perform this optimisation on 3-dimensional data cubes. To accomplish this, we summed over all wavelength slices within a range encompassing a strong emission line ($\text{H}\alpha$ for our R7000 exposures, and $[\text{O III}]\lambda 5007$ in our B3000 exposures), in addition to summing over all spatial pixels k . We also substituted the mean for a sigma-clipped mean in Eqn. 4.2 to prevent artefacts such as cosmic rays and bad pixels affecting the result.

We used MPFIT (Markwardt 2009), a PYTHON implementation of the Levenberg-Marquardt algorithm (Moré 1978) developed by M. Rivers[†] to solve for the α_i that minimise Eqn. 4.1. After calculating the scaling factors, we discarded cubes with scaling factors greater than ≈ 1.3 , as these cubes tended to contribute more noise than signal to the final mosaic. We then scaled the remaining cubes appropriately, and created a mosaic by taking the sigma-clipped median of each spatial and wavelength pixel from the shifted data cubes. We estimated 1σ errors for each pixel value in the final mosaic by calculating the standard deviation of the pixels in the individual cubes used in creating the mosaic. Fig. 4.4 shows 1D spectra extracted from the resulting mosaicked data cubes.

Finally, the data cubes were corrected for Galactic extinction using the extinction map of Schlafly & Finkbeiner (2011) which gives $A_V = 0.1198$. To apply the correction to our WiFeS data we used reddening curve of Fitzpatrick & Massa (2007) with $R_V = 3.1$. Fig. 4.4 shows 1D spectra extracted from the resulting data cubes.

[†]Available <http://cars9.uchicago.edu/software/python/mpfit.html>.

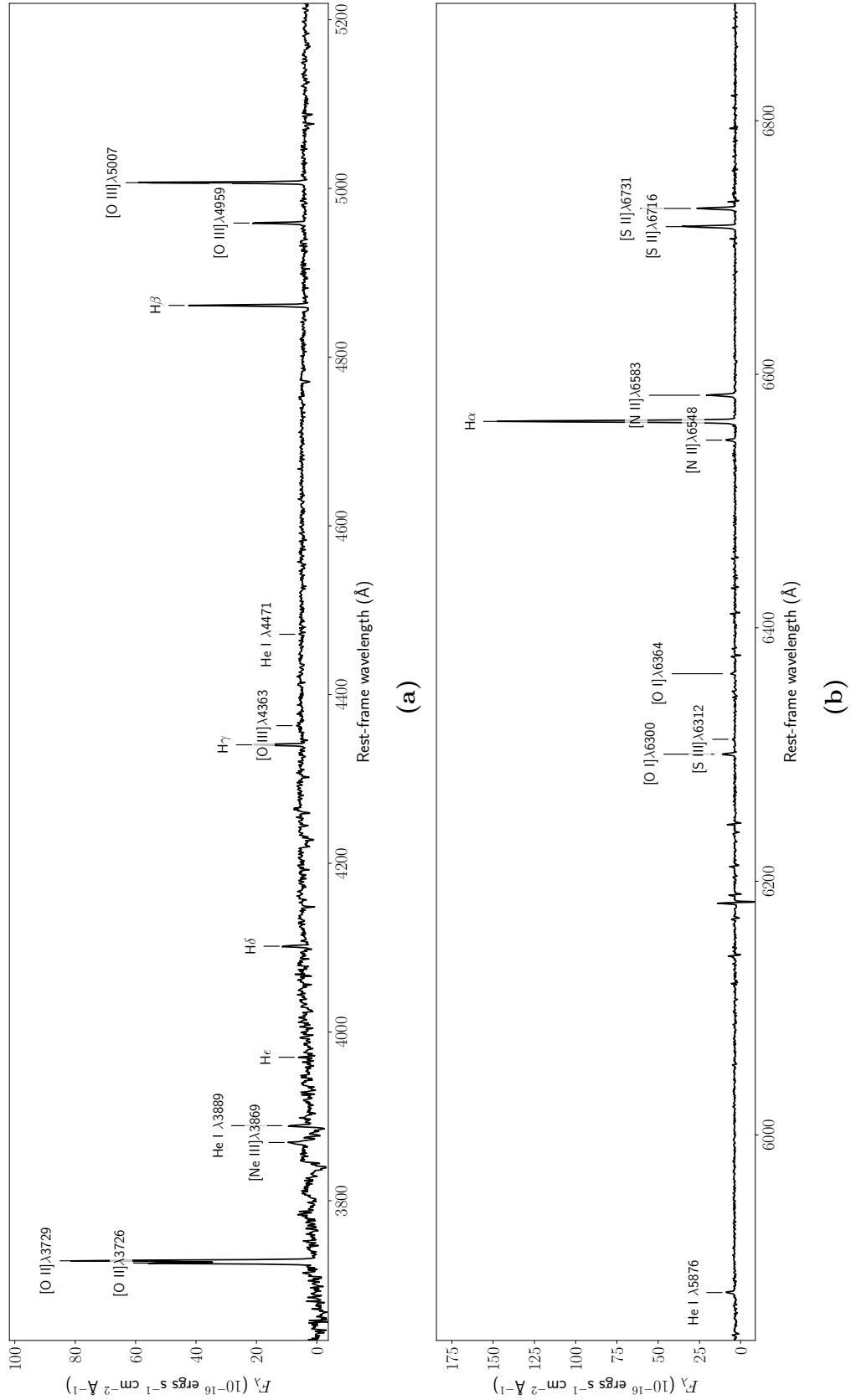


Figure 4.4: Integrated spectra extracted from spaxels in the WIFeS B3000 (a) and R7000 (b) data cubes in which the H α line has S/N > 3 and a flux greater than $10 \times 10^{-16} \text{ erg s}^{-1} \text{ cm}^{-2}$.

4.5 Stellar population analysis

We used the PYTHON implementation of Penalized Pixel Fitting (PPXF)[‡] (Cappellari & Emsellem 2004; Cappellari 2017) to analyse the stellar population by fitting combinations of simple stellar population (SSP) templates to the stellar continuum. This is a refinement of the work of Croft et al. (2006), who carried out a similar analysis using broad-band photometry.

PPXF uses a χ^2 -minimisation routine to determine best-fit parameters such as the kinematics (including the systemic velocity, line-of-sight velocity dispersion, and higher-order Gauss-Hermite coefficients), the weights for each stellar template, and emission lines. Additive polynomials can be included in the fit to correct for template mismatch, whilst multiplicative polynomials can be used to correct for spectral calibration errors. PPXF can also be used to estimate the gas reddening from the strengths of the Balmer emission lines.

A key feature of PPXF is *regularisation*. Recovery of the star formation history from the stellar continuum is an ill-conditioned inverse problem: typically, there are many combinations of the input templates that will reproduce the observed continuum within the provided errors. Regularisation is implemented in PPXF by including an additional term in the objective function that effectively penalises high-frequency fluctuations in the template parameter space (i.e., age and metallicity), biasing the best fit template weights towards the *smoothest* solution that is consistent with the data.

Due to the predominantly young stellar population of MO (Croft et al. 2006), we used the SSP models of González Delgado et al. (2005) which have a fine age resolution at young stellar ages, with a resolution of 1 Myr for ages up to 10 Myr, 5 Myr for ages from 10 Myr to 100 Myr and 100 Myr from 100 Myr to 1 Gyr. The SSP templates were generated using both the Geneva and the Padova isochrones with a Salpeter IMF, spanning an age range 1 Myr to 10 Gyr divided into 46 bins with five metallicities for the Geneva isochrones ($0.05Z_{\odot}$, $0.2Z_{\odot}$, $0.4Z_{\odot}$, $1Z_{\odot}$ and $2Z_{\odot}$), and three for the Padova isochrones ($0.2Z_{\odot}$, $0.4Z_{\odot}$ and $0.95Z_{\odot}$).

Because MO is thought to have a low gas-phase metallicity (Croft et al. 2006; Lacy et al. 2017), we used the Geneva isochrones for which the stellar templates extend to lower metallicities than the Padova isochrones. Although the Geneva isochrones do not include stellar evolution along the red giant branch, we do not believe this to be of critical importance due to the predominantly young stellar population of MO. We confirmed that this did not bias our results by repeating our analysis using the Padova isochrones, which yielded very similar results (see Appendix C).

As can be seen in Fig. 4.4, there are very few stellar absorption features in the R7000 wavelength range; hence we only analysed our B3000 data with PPXF. Due to the low continuum surface brightness of MO, our data cubes lacked the signal-to-noise (S/N) to recover ages and metallicities in each spaxel. Because MO has a young stellar population it is reasonable to assume that the majority of stars are located in the regions with bright emission line flux. We therefore created an integrated spectrum by summing the spaxels in which the $H\alpha$ flux exceeded $1.5 \times 10^{-15} \text{ erg s}^{-1} \text{ cm}^{-2}$. This flux limit was chosen as the resulting region is similar to the 8" aperture used by Croft et al. (2006) in their SSP analysis using SED fitting,

[‡]Available <https://www-astro.physics.ox.ac.uk/~mxc/software/#ppxf>.

enabling a direct comparison of our analysis to their results. The median S/N in the resulting spectrum was approximately 7.5 per spectral pixel.

To obtain the best-fit age and metallicity, the stellar continuum and the emission lines were fitted simultaneously, adopting independent velocity components for each, where emission lines were fit using Gaussian profiles. A 4th-order multiplicative polynomial was included in the fit to compensate for extinction and calibration errors, and regularisation was used to bias the best-fit template weights towards the smoothest solution consistent with the data. The regularisation parameter `regul` was determined using the standard method (e.g., Boardman et al. 2017). We performed a fit firstly with `regul` = 0, and secondly where the noise on the input spectrum was multiplied by the reduced- χ^2 of the first fit. `regul` was gradually increased until the difference in the reduced- χ^2 for the regularised and non-regularised fits $\Delta\chi^2 \simeq \sqrt{2N}$, where $\Delta\chi^2 = N(\chi^2/\text{DOF} - 1)$, and N is the number of data points in the input spectrum and DOF is the number of degrees-of-freedom.

Figs. 4.5 and 4.6 show the best-fit spectrum and template weights respectively. There are two clear stellar populations in MO, with approximate ages of 4 – 5 Myr and 1 Gyr. The younger population is directly associated with MO, whereas the older population may represent stars associated with the stellar bridge, or with the object itself. These results are consistent with the broad-band SED analysis of Croft et al. (2006), who found the best-fit stellar population is dominated by a component approximately 7.5 Myr old, with up to 20 per cent of the light attributed to a component at 1 Gyr.

Simultaneously constraining both the age and metallicity of the stellar population is challenging due to the lack of strong metal absorption features in the stellar continuum. We therefore repeated our analysis using templates with fixed metallicities, yielding similar results, as detailed in Appendix C.

To further check whether MO is dominated by a young stellar population, we individually fitted each SSP template in age and metallicity (for both the Padova and Geneva isochrones), including Gaussian emission lines and a multiplicative polynomial to correct for calibration errors, and calculated the resulting reduced- χ^2 . For all template metallicities, the minimum reduced- χ^2 occurs at ages $\lesssim 15$ Myr, with the χ^2 gradually increasing with template age. Thus we conclude the stellar population in MO is indeed young.

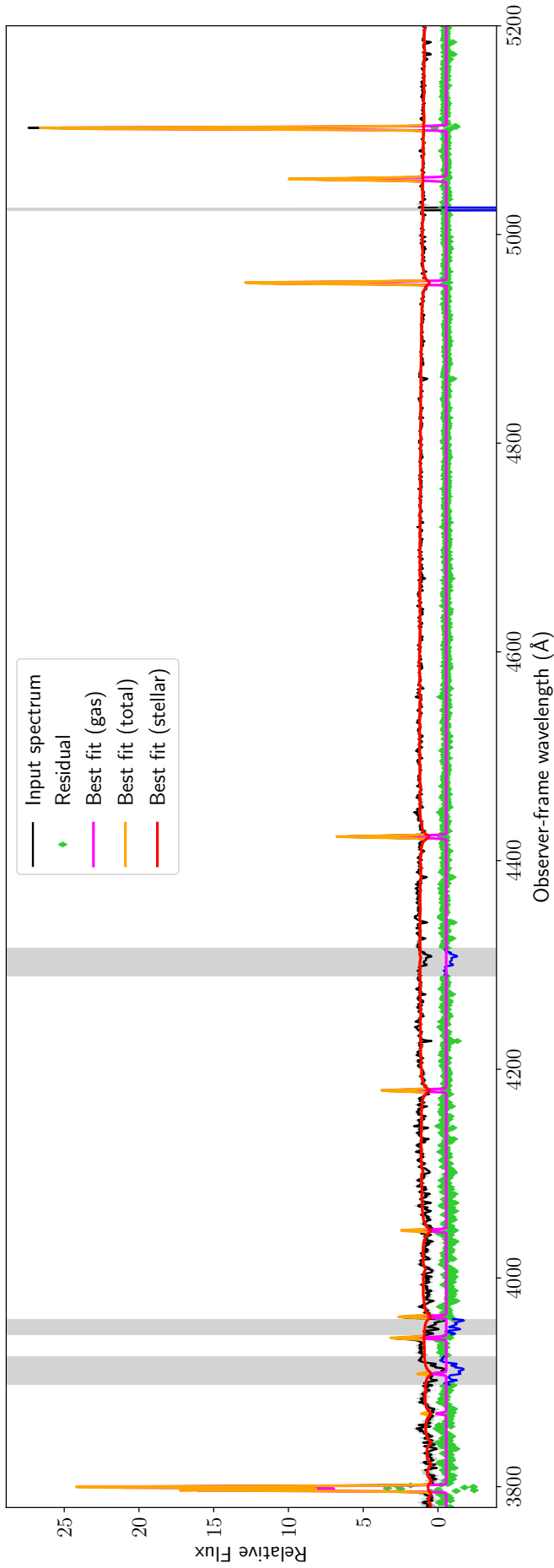


Figure 4.5: The integrated spectrum (corrected for Galactic extinction), overlaid with the best-fit spectrum with the stellar and emission line components shown separately. 1σ errors are indicated in grey, and the green dots indicate the residual to the fit. The grey shaded regions indicate spectral windows dominated by residuals from the sky subtraction, and were not included in the fit.

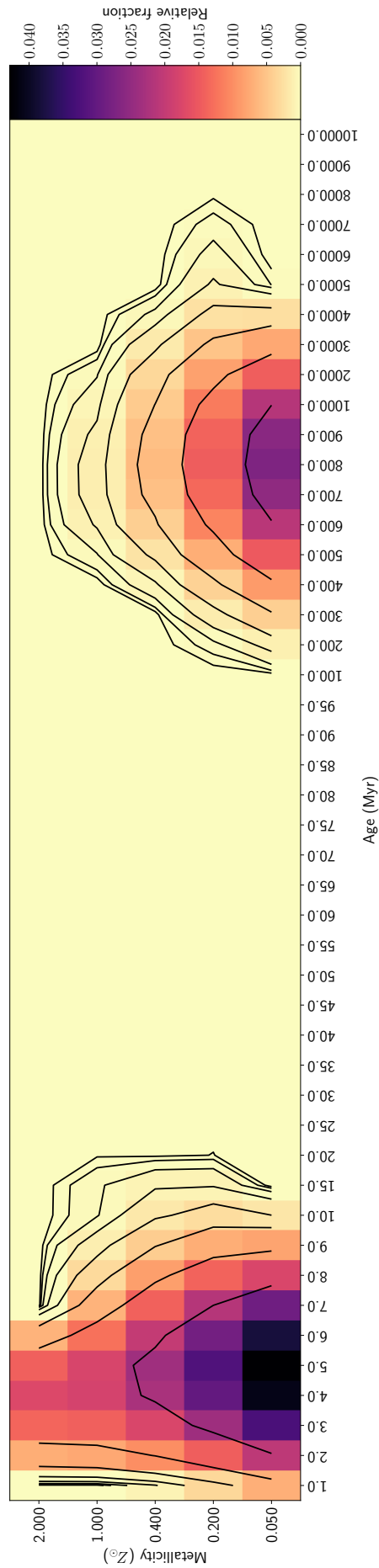


Figure 4.6: 2D histogram of the best-fit age and metallicity of the stellar population, where the contours correspond to logarithmically spaced intervals from 10^{-4} to 10^{-1} .

4.6 Emission line gas

4.6.1 Emission line fitting

We used MPFIT to estimate line fluxes in each spaxel by simultaneously fitting a single Gaussian profile to each emission line and a linear component to fit the continuum. All emission lines included in the fit were constrained to have the same systemic velocity and velocity dispersion.

Due to the lack of prominent stellar absorption features and the high equivalent widths of the Balmer emission lines compared to the corresponding stellar absorption features (see Fig. 4.4), and because we lacked the S/N to fit the stellar continuum in each spaxel, we did not subtract the stellar continuum from spaxels before fitting emission lines. To check whether this would effect our emission line fluxes, we used the equivalent width (EW) of the H β line (approximately 7.6 Å), estimated from our PPXF fit, to estimate the stellar absorption flux in each spaxel by measuring the continuum flux in two windows adjacent to the H β line. In most spaxels, the stellar absorption is less than 10 per cent of the measured H β emission line flux. To investigate the effect on the H α absorption, we used a solar-metallicity STARBURST99 model (Leitherer et al. 1999) with an instantaneous burst star formation history and a Salpeter IMF to estimate the H α EW because it was not measured in our PPXF analysis. At an age of 10^7 yr the H α EW ≈ 16 Å. Using the same method as for H β , we again found the stellar absorption accounts for less than 10 per cent of the measured H α emission line flux in most spaxels, confirming that this has a minimal effect on our reported emission line fluxes.

We kept fits with a reduced- $\chi^2 < 2$ and S/N > 3 . In all quoted linewidths, the instrumental resolution was accounted for by subtracting the width of the line spread function (LSF) in quadrature from the width of the fitted Gaussian, where the width of the LSF was estimated by fitting Gaussian profiles to sky lines.

Integrated line fluxes for emission lines in MO are shown in Table 4.2, which were estimated by summing the fluxes in each spaxel, except for very faint lines, such as He I $\lambda 3889$, for which fluxes were estimated by fitting a single Gaussian profile to the integrated spectrum.

4.6.2 Kinematics and morphology

Fig. 4.7 shows maps of the H α flux, radial velocity and velocity dispersion. The radial velocities increase from South to North, which is consistent with those of the CO and H I (Lacy et al. 2017). The velocity dispersion is low, with values around 15 km s^{-1} in most parts of the object, peaking in the West with $\sigma \approx 30 \text{ km s}^{-1}$.

4.6.3 Reddening

After correcting for foreground extinction, we used the H α and H β fluxes to estimate the extinction. The A_V in each spaxel is shown in the upper panel of Fig. 4.8, where we have used the reddening curve of Fitzpatrick & Massa (2007) with $R_V = 3.1$. Only spaxels in which the S/N in the H α /H β ratio exceeds 3 are shown. The mean $A_V = 0.17 \pm 0.04$, which is slightly higher than the value of Croft et al. (2006), who reported negligible reddening within MO. However, our spatially resolved extinction map reveals significantly higher values of A_V in several clumpy regions to the

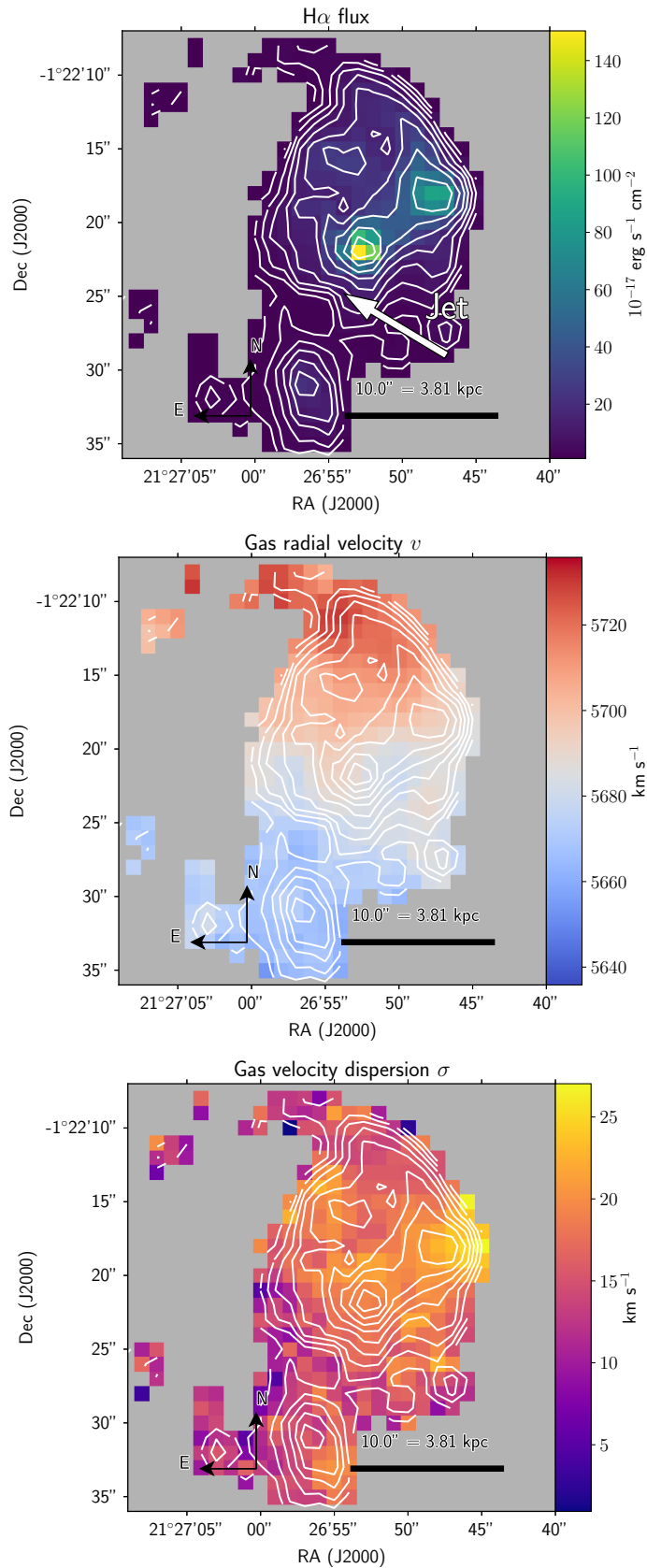


Figure 4.7: Top: H α flux, where the approximate direction of the radio jet is shown; middle: radial velocity (with respect to the local standard of rest); bottom: velocity dispersion (corrected for instrumental broadening) from our Gaussian line fit. The white contours indicate the H α flux on a log scale.

Table 4.2: Total emission line fluxes.

Emission line	Flux (10^{-15} erg s $^{-1}$ cm $^{-2}$)
[O II] λ 3726	15.1 ± 0.3
[O II] λ 3729	24.0 ± 0.4
H β	17.3 ± 0.2
[O III] $\lambda\lambda$ 4959, 5007	64.8 ± 0.6
[Ne II] λ 3869 [†]	1.7 ± 0.3
He I λ 3889 [†]	2.1 ± 0.3
H ϵ [†]	1.3 ± 0.3
H δ [†]	2.5 ± 0.2
H γ [†]	5.3 ± 0.2
[O I] λ 6300	0.86 ± 0.03
H α	47.9 ± 0.1
[N II] λ 6548, 6583	5.60 ± 0.06
[S II] λ 6716	8.87 ± 0.07
[S II] λ 6731	5.79 ± 0.06
He I λ 5876 [†]	1.13 ± 0.05
[O I] λ 6364 [†]	0.39 ± 0.05

[†]Flux estimated by fitting a single Gaussian profile to the integrated spectrum.

East, although as discussed in Section 4.6.5, this may be a result of an intrinsically enhanced Balmer decrement due to X-ray photoionisation.

Because the S/N was insufficient to measure A_V in all spaxels in which line emission was detected, we repeated the above process after spatially binning the data cube by a factor of three; the resulting extinction map is shown in the lower panel of Fig. 4.8. Emission line fluxes were corrected for intrinsic reddening by applying the A_V estimated in the corresponding spaxel in the binned data cube; in those spaxels in which A_V could not be measured or $A_V < 0$, no extinction correction was applied.

4.6.4 Electron density

To estimate the electron density in each spaxel, we used the ratio R of the emission lines in the [S II] $\lambda\lambda$ 6716, 6731 doublet and eqn. 3 of Proxauf et al. (2014), only including spaxels in which the S/N of R exceeded 3. We detected no significant variation in R across the object, with the mean $R = 1.474 \pm 0.015$, placing MO on the cusp of the low-density limit ($n_e \lesssim 10$ cm $^{-3}$), which is consistent with the findings of Croft et al. (2006).

4.6.5 Excitation mechanism

To determine the excitation mechanism of the emission line gas, we use optical diagnostic diagrams (ODDs; Baldwin et al. 1981; Veilleux & Osterbrock 1987; Kewley et al. 2001; Kauffmann et al. 2003; Kewley et al. 2006), in which the [O III] λ 5007/H β ratio is plotted as a function of the [N II] λ 6583/H α , [S II] $\lambda\lambda$ 6716, 6731/H α and

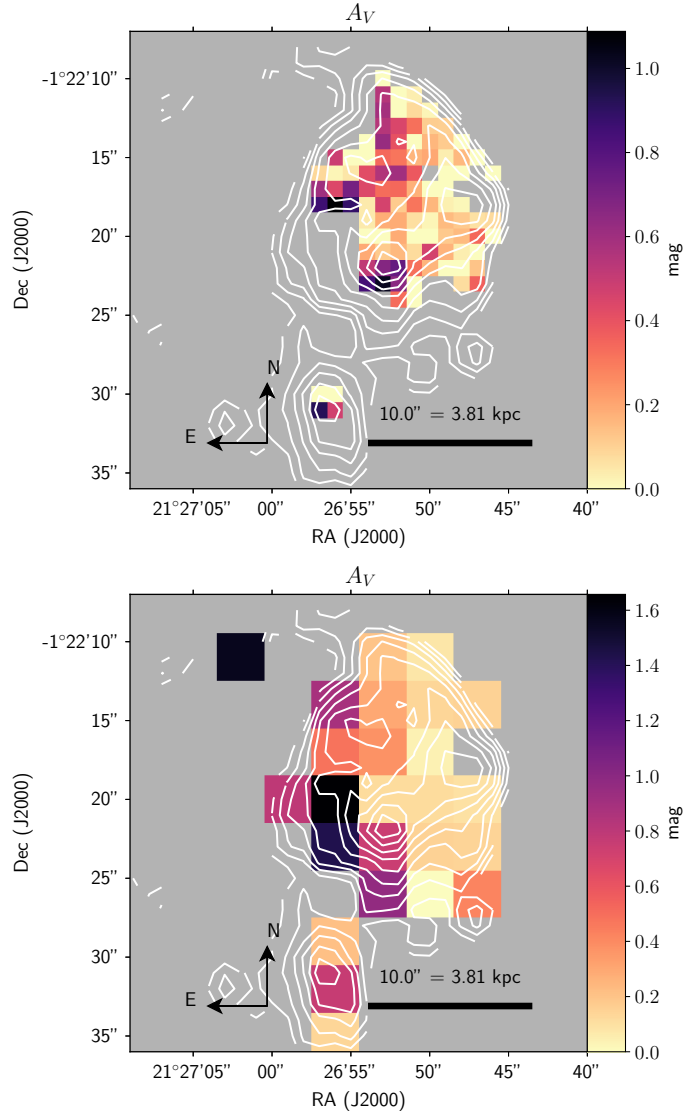


Figure 4.8: The A_V estimated in each spaxel using the extinction curve of Fitzpatrick & Massa (2007) with $R_V = 3.1$ in the spaxels of the unbinned data cube (top) and spatially binned data cube (bottom). Spaxels with $A_V < 0$ but with values within 1σ of zero are indicated as having $A_V = 0$. Spaxels with $A_V < 0$ by an amount greater than 1σ from zero are not shown. The white contours indicate the $H\alpha$ flux on a log scale.

$[O\text{I}]\lambda 6300/H\alpha$ ratios. ODDs for each spaxel in MO are shown in Fig. 4.9.

There is a broad spread in the $[S\text{II}]/H\alpha$ and $[O\text{I}]/H\alpha$ ratios within the object, which is likely due to an intrinsic metallicity variation within the object. Indeed, inspection of the middle panel of Fig. 4.9 shows that the metallicity calculated using the N2O2 diagnostic of Kewley et al. (2019a) increases smoothly as a function of the $[N\text{II}]/H\alpha$, $[S\text{II}]/H\alpha$ and $[O\text{I}]/H\alpha$ ratios, following a trajectory very similar to the metallicity sequence observed in SDSS galaxies (e.g., Kewley et al. 2006).

Although most spaxels lie beneath the line of maximal star formation, there are some spaxels that lie beyond this line, indicating a contribution from ionising sources other than star formation.

In Fig. 4.10 we present additional line ratio diagrams, where we include the sample of ‘typical’ H II regions in nearby spiral galaxies from van Zee et al. (1998). Grids from Kewley et al. (2019b) representing MAPPINGS V (Sutherland et al. 2018) H II

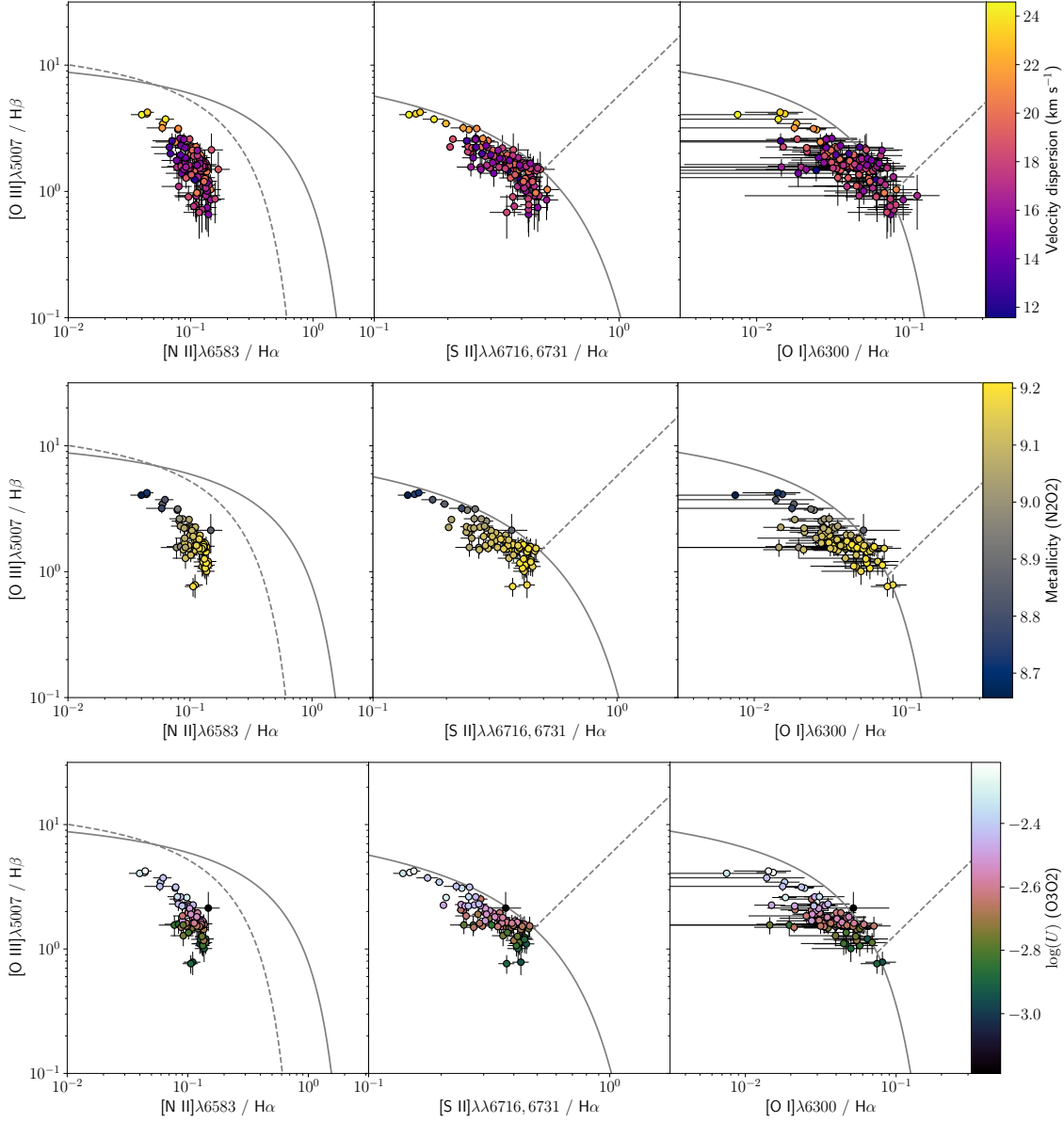


Figure 4.9: ODDs of MO, where each point represents an individual spaxel with 1σ error bars. The spaxels are colour coded by velocity dispersion (top), metallicity (middle) and ionisation parameter (bottom). The metallicity and ionisation parameter have been estimated using the N2O2 and O3O2 diagnostics respectively (see Fig. 4.15); in the top panel, spaxels with $S/N > 3$ in the $H\alpha$, $H\beta$, $[O\text{ III}]$, $[N\text{ II}]$ and $[S\text{ II}]$ lines are shown. In the middle and bottom panels, only spaxels with $S/N > 3$ in all lines used in the N2O2 and O3O2 diagnostics are shown. The solid grey lines represent the maximum $[O\text{ III}]/H\beta$ ratio that can arise from star formation alone, derived from photoionisation models (Kewley et al. 2001). In the left panels, the dashed line is the equivalent empirical relation of Kauffmann et al. (2003) which separates star-forming galaxies and AGN hosts. In the middle and right panels, the dashed lines of Kewley et al. (2006) separate Seyfert-like (above) and LINER-like ratios (below the line).

region plane-parallel models with $\log(P/k) = 5.0$, varying in ionisation parameter and metallicity, are shown for comparison. Although the spaxels in MO are similar to the H II regions in the R23 ($([\text{O III}]\lambda\lambda 3726, 3729 + [\text{O III}]\lambda\lambda 4959, 5007)/\text{H}\beta$) vs. N2O2 ($([\text{N II}]\lambda\lambda 6548, 6583)/[\text{O II}]\lambda\lambda 3726, 3729$) and O3O2 ($([\text{O III}]\lambda\lambda 4959, 5007)/[\text{O II}]\lambda\lambda 3726, 3729$) vs. N2O2 plots, many spaxels have S2 ($([\text{S II}]\lambda\lambda 6716, 6731)/\text{H}\alpha$) ratios much higher than both the H II regions and MAPPINGS models, suggesting the presence of secondary excitation mechanisms.

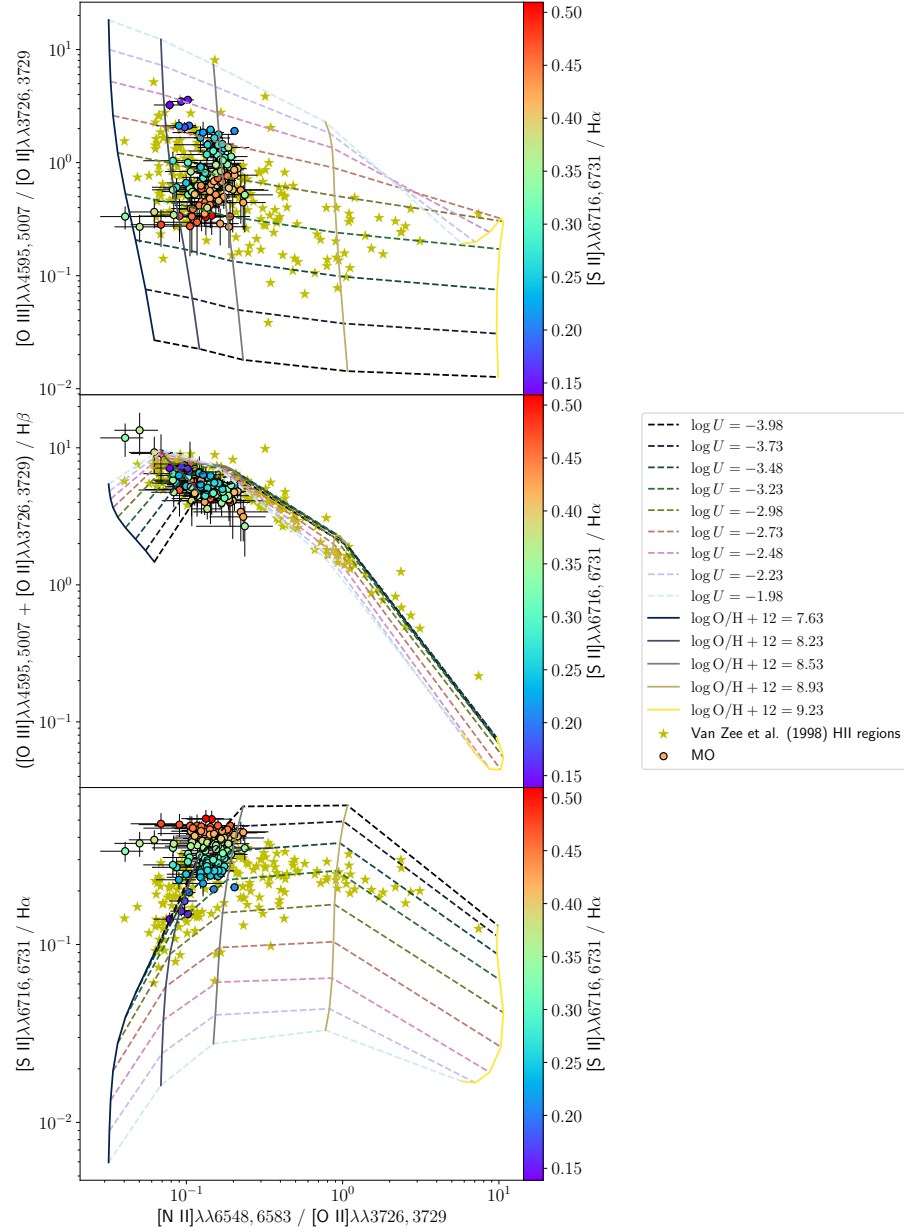


Figure 4.10: O3O2 (top), R23 (middle) and S2 (bottom) ratios as a function of the N2O2 ratio for spaxels in MO (circles with 1σ errors, coloured by S2 ratio) and for the van Zee et al. (1998) H II regions (gold stars). The grids indicate line ratios from MAPPINGS H II region models, varying in metallicity (solid lines) and ionisation parameter (dashed lines). Only spaxels with $S/N > 3$ in the $\text{H}\alpha$, $\text{H}\beta$, $[\text{O III}]$, $[\text{N II}]$ and $[\text{S II}]$ lines are shown.

As an additional check for whether the line ratios in MO are consistent with star formation alone, we used NEBULABAYES (Thomas et al. 2018), a PYTHON package that uses a Bayesian method to estimate ISM conditions from observed emission

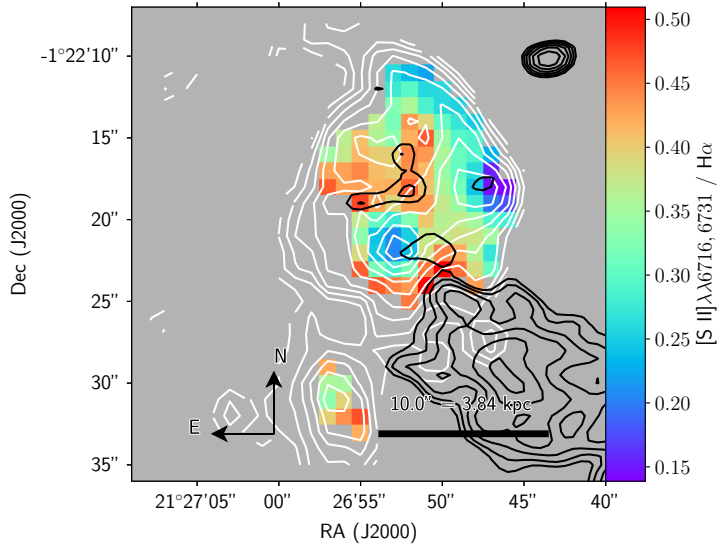


Figure 4.11: The S2 ratio in each spaxel. The white contours indicate the H α flux on a log scale, and the black contours show the ALMA 106 GHz continuum from the jet (Lacy et al. 2017). The contours represent 10 logarithmically spaced intervals from 3σ Jy beam $^{-1}$ to 1.6×10^{-4} Jy beam $^{-1}$, where $\sigma = 9.2 \times 10^{-6}$ Jy beam $^{-1}$ is the measured rms noise in the image.

line fluxes using input model grids. NEBULABAYES was used with the same H II region model grid generated using MAPPINGS, however with $\log(P/k)$ varying from $\log(P/k) = 4.0$ to $\log(P/k) = 9.0$. In most spaxels, the best fit model had a very poor reduced- χ^2 and $\log(P/k) \approx 6.5$. Such a high pressure is inconsistent with both the estimated conditions within the jet plasma in MO ($P/k \approx 1.2 \times 10^5$ K cm $^{-3}$, van Breugel et al. 1985), and with the low electron density predicted by the [S II] ratio ($n \lesssim 10$ cm $^{-3}$, Section 4.6.4). Using NEBULABAYES with a log-normal prior on the ISM pressure centred on $\log(P/k) \leq 5.0$ yielded similarly poor reduced- χ^2 values in most spaxels, providing further evidence for excitation mechanisms other than star formation.

In the following sections, we investigate shock excitation, diffuse ionised gas (DIG) and X-ray photoionisation from the nucleus of NGC 541 as possible ionising sources in MO.

Shock excitation

Given that the jet appears to be passing through the centre of MO (Fig. 4.3), shocks are likely to be present. In Appendix D, we estimate the shock velocities induced by a typical transonic FR I-type jet interacting with an H I cloud to be ≤ 20 km s $^{-1}$. This is consistent with the observed H I velocity dispersion (Lacy et al. 2017). Such slow shocks would not produce any detectable optical line emission; however, faster shocks may be present due to its inhomogeneous morphology.

To determine whether shocks could cause the enhanced [S II] and [O I] emission, in Figs. 4.12a and 4.12b we show ODDs overlaid with the slow and fast shock models of Dopita & Sutherland (2017) and Allen et al. (2008) respectively. The slow shock models are shown for shock speeds $v_s = 70 - 170$ km s $^{-1}$ and pre-shock densities $n = 1 - 10000$ cm $^{-3}$. In these models, the shock propagates into a solar metallicity nebula with a fixed magnetic parameter of $B/\sqrt{n} = 3.23$ μ G cm $^{3/2}$, corresponding to equipartition. The fast shock models are shown for shock speeds $v_s = 100 -$

500 km s⁻¹ and magnetic field strengths $B = 0 - 10 \mu\text{G}$. These models correspond to a solar metallicity nebula with a pre-shock density $n = 1 \text{ cm}^{-3}$, and include line emission from both the post-shock gas and the photoionised precursor.

Although the Dopita & Sutherland (2017) models appear to overlap with the data in the ODDs, slow shocks with pre-shock densities of $n = 1 - 10 \text{ cm}^{-3}$ models (consistent with the observed electron density estimated in Section 4.6.4) would tend to reduce the [S II] and [O I] whilst enhancing the [N II], contrary to our observations. Furthermore, as shown in Fig. 4.13, whilst the [N II]/[S II] ratio is consistent with shock speeds of $v_s \approx 55 \text{ km s}^{-1}$ and a pre-shock density of $n = 1 \text{ cm}^{-3}$, shocks of this speed do not generate any measurable [O III] emission. Rather, the measured [O III]/H β ratios are consistent with $v_s \gtrsim 70 \text{ km s}^{-1}$; shocks of this speed over-predict the observed [N II]/[S II] ratios by a factor $\approx 2 - 3$. Similarly, none of the fast shock models of Allen et al. (2008) would produce the enhanced [S II]/H α and [O I]/H α line ratios whilst keeping the [N II]/H α within the range of observed values.

Although simultaneously low [N II]/H α and high [O III]/H β could theoretically arise from a mixture of shock speeds resulting from the shock passing through an inhomogeneous medium, any significant contribution from shocks sufficiently fast to cause detectable [O III] would produce much higher line widths than observed ($\sigma \gtrsim 30 \text{ km s}^{-1}$; see Fig 4.7).

We therefore conclude that shocks are highly unlikely to be the primary cause of the enhanced [S II]/H α and [O I]/H α ratios. However, we cannot rule out the presence of shocks that are too slow to contribute to the optical line emission. Further observations in the near-IR may reveal ro-vibrational H₂ emission, which traces shocks too slow to dissociate molecular gas (e.g., Flower & Pineau Des Forêts 2010; Zovaro et al. 2019a,b).

Diffuse Ionised Gas

We now investigate whether the line ratios in MO are consistent with contamination from diffuse ionised gas (DIG), the low-density ionised medium outside H II regions that is photoionised by escaped radiation from nearby star-forming regions. DIG is characterised by strong emission in low-ionisation species such as [O I], [N II] and [S II], and weak emission in high-ionisation species such as [O III] (e.g., Rand 1998; Haffner et al. 2009).

The diffuse structure of MO implies that DIG is highly likely to contribute to the line emission, particularly in the inter-filament regions. Indeed, as shown in Fig. 4.11, the spaxels with the highest [S II]/H α ratios are located in the regions in between the brightest star-forming regions of MO, as expected of DIG.

In Fig. 4.14 we present a ODD diagram overlaid with the DIG photoionisation models of Mathis (1986), where the [O I] λ 6300/H α ratio has been replaced by the [O II] λ 3726/H β ratio because [O I] λ 6300 is not included in the models. The DIG models are parametrised by the temperature T_* of the central O-type star in the model H II region, and the parameter q , which is a proxy for the ionisation parameter; $q \approx 1$ in regular H II regions, whereas for the models used here, $-6 \leq q \leq -2$. The spaxels with line ratios most similar to the DIG models tend to have low H α surface brightnesses and lie outside the main star-forming regions round the outskirts of the object, or in between the filaments (see Fig. 4.7), as expected for DIG. However, the models are unable to explain the enhancement in the [S II] relative to the [N II] and

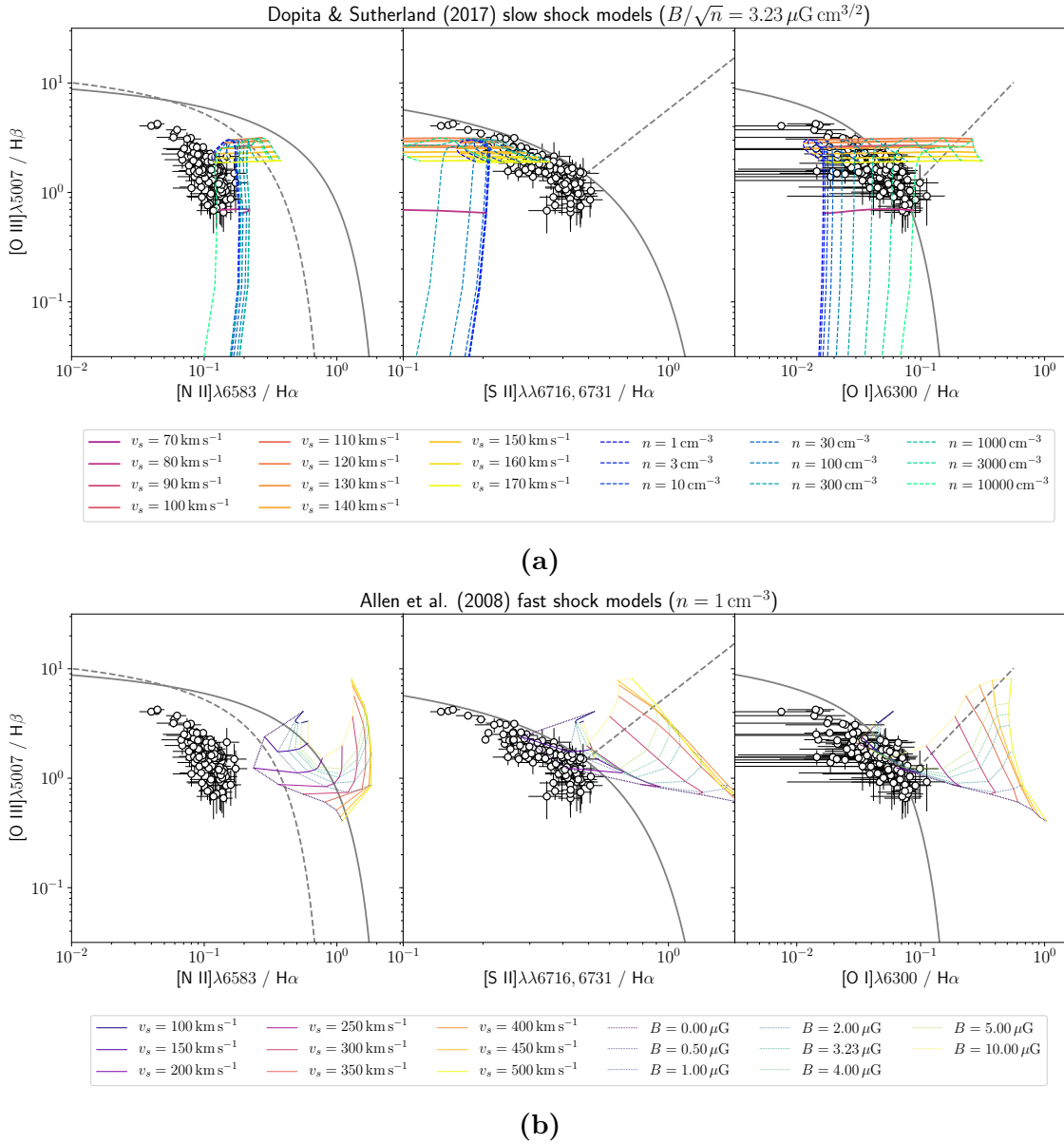


Figure 4.12: ODDs overlaid with (a) the slow shock models of Dopita & Sutherland (2017) and (b) the fast shock models of Allen et al. (2008). White circles correspond to individual spaxels in MO with 1σ error bars. The grey solid and dashed lines are as in Fig. 4.9. Only spaxels with $S/N > 3$ in the $\text{H}\alpha$, $\text{H}\beta$, $[\text{O III}]$, $[\text{N II}]$ and $[\text{S II}]$ lines are shown.

$[\text{O II}]$. We therefore rule out DIG as the main contributor to the unusual line ratios in MO.

X-ray photoionisation

We now consider whether X-ray photoionisation from the nucleus of NGC 541 can explain the observed line ratios. X-ray photons produced via inverse Compton scattering in the corona of the AGN have a long mean-free-path length in the ISM, resulting in a very hard radiation field in the outskirts of the nebula that creates an extended, weakly ionised transition region (Dopita & Sutherland 2003). Although this region has a low ionisation parameter, inner-shell photoionisations from X-ray photons create high-energy electrons that trigger cascades of collisional excitations,

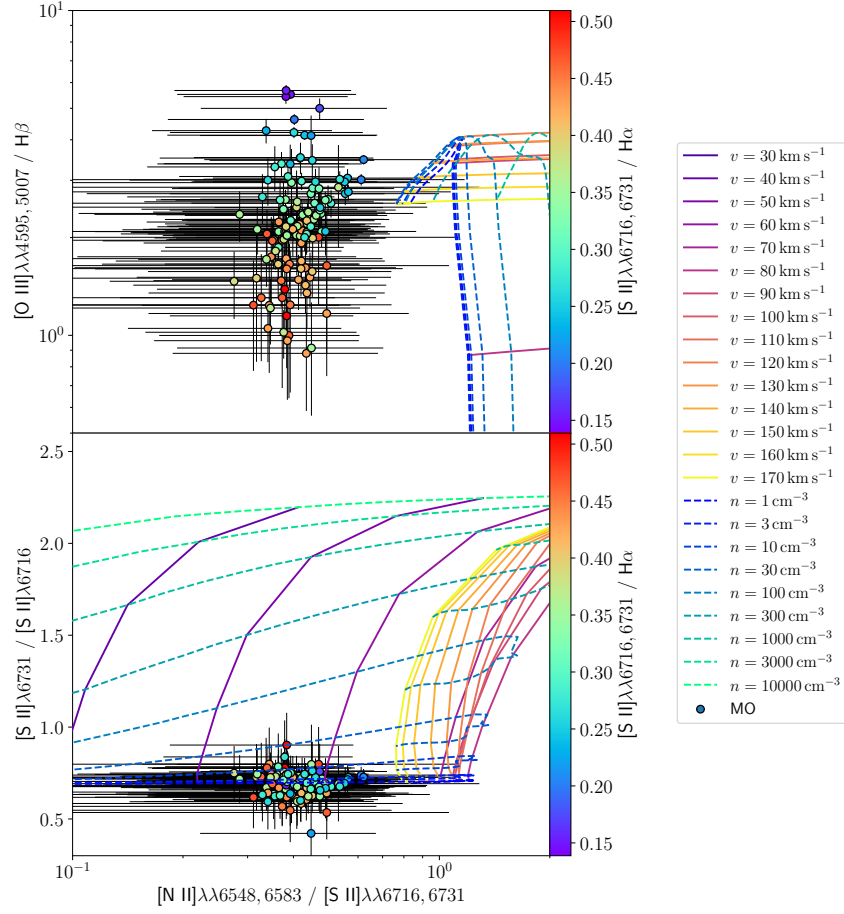


Figure 4.13: $[O III]\lambda\lambda 4959, 5007/H\beta$ (top) and $[S II]\lambda 6731/[S II]\lambda 6716$ (bottom) ratios as a function of $[N II]\lambda\lambda 6548, 6583/[S II]\lambda\lambda 6716, 6731$ for spaxels in MO (circles with 1σ error bars, coloured by S2 ratio). The grids indicate line ratios from the slow shock models of Dopita & Sutherland (2017), varying in shock speed (solid lines) and pre-shock density (dashed lines). Only spaxels with $S/N > 3$ in the $H\alpha$, $H\beta$, $[O III]$, $[N II]$ and $[S II]$ lines are shown.

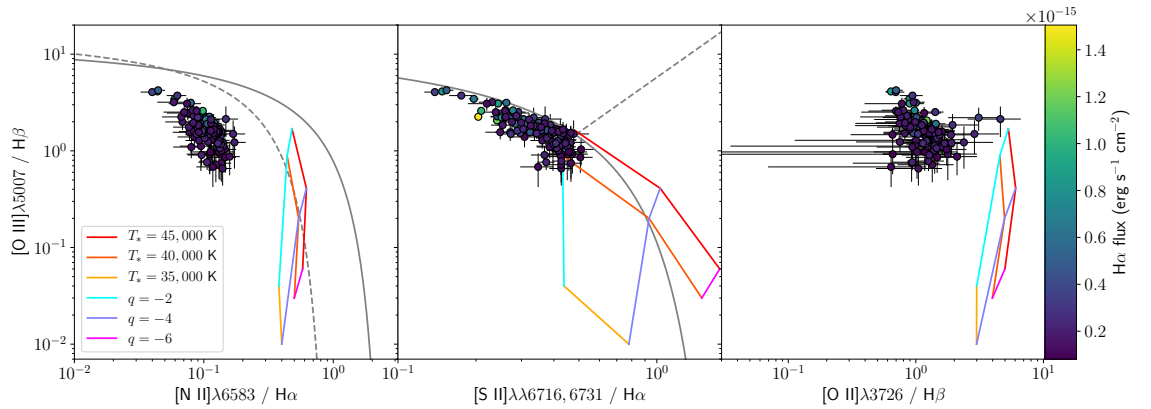


Figure 4.14: $[O III]\lambda 5007/H\beta$ ratio as a function of the $[N II]\lambda 6583/H\alpha$, $[S II]\lambda\lambda 6716, 6731/H\alpha$ and $[O II]\lambda 3726/H\beta$ ratios in each spaxel in MO (circles with 1σ error bars, coloured by the $H\alpha$ flux). The grids indicate the DIG photoionisation models of Mathis (1986) for different combinations of the parameter q (a proxy for the ionisation parameter) and the temperature of the ionising star T_* . The grey solid and dashed lines are as in Fig. 4.9. Only spaxels with $S/N > 3$ in the $H\alpha$, $H\beta$, $[O III]$, $[N II]$ and $[S II]$ lines are shown.

leading to enhanced forbidden line emission in species with ionisation potentials lower than that of H I. In particular, [S II] and [O I] are enhanced, whereas [N II] and [O III] are relatively weak, as is the case in MO.

Due to enhanced collisional excitation, X-ray photoionisation results in a Balmer decrement larger than the case B recombination value of 2.85 (Dopita & Sutherland 2003). Therefore, if X-ray photoionisation from the AGN of NGC 541 is the dominant secondary excitation mechanism, the A_V , which was estimated assuming the case B recombination Balmer decrement, will be correlated with the S2 ratio, which is indeed observed (see Figs. 4.8 and 4.11).

Due to its significant distance from the AGN, existing AGN photoionisation models, which generally simulate nebulae close to the AGN in the host galaxy, cannot be applied to MO. A program such as MAPPINGS (Sutherland et al. 2018) can be used to simulate a photoionised nebula placed at an arbitrary distance from the AGN, where the AGN SED can be simulated using existing models (e.g., those of Jin et al. 2012). However, such models require numerous parameters to constrain the properties of the nebula and AGN SED, many of which cannot be reliably estimated from existing observations of MO and NGC 541. For example, in MO, the [S II] ratio only provides an upper limit to the ISM density ($n \lesssim 10 \text{ cm}^{-3}$; see Section 4.6.4). Meanwhile, the AGN SED is controlled by the Eddington ratio, the presence of a soft X-ray excess, the radius of the hot corona, and other parameters that cannot be estimated from existing observations of NGC 541. In particular, the jet axis of NGC 541 suggests that the accretion disc's axis of rotation is transverse to the line-of-sight, obscuring our view of the accretion disc, thereby meaning we cannot directly measure the X-ray properties of the AGN. This is apparent from the measured X-ray luminosity of NGC 541 ($L_X = 10^{40.83} \text{ erg s}^{-1}$, Hudaverdi et al. 2006), which is consistent with a combination of low-mass X-ray binaries and hot ISM alone (Matsushita 2001). Hence, determining whether AGN photoionisation can reproduce the observed line ratios in MO requires a detailed exploration of the model parameter space, which will be the subject of future work.

In conclusion, star formation most likely dominates the line emission in MO, but the enhanced [S II]/H α and [O I]/H α ratios indicate the presence of other additional ionising sources. Neither shock nor DIG models can simultaneously produce the enhanced [S II]/H α and [O I]/H α ratios whilst keeping the [N II]/H α ratios within the range of observed values. X-ray photoionisation from the AGN of NGC 541 may contribute, but further modelling is required to confirm this. Given the unusual location and structure of MO, it is possible that the observed line ratios may be a result of gas photoionised by a combination of star formation, AGN and DIG, which is then shocked by the passage of the jet. Modelling such a complex system is beyond the scope of this paper; additional observations will be required to constrain the free parameters in such a model.

The presence of both an intrinsic metallicity variation, and possible ionisation from a range of sources other than star formation, makes MO too complex for us to quantify the contribution of shocks, DIG or AGN photoionisation to the line emission using a simple 'mixing' analysis (e.g., Davies et al. 2017). However, Kewley & Ellison (2008) found that only an AGN photoionisation contribution greater than 15 per cent can produce line ratios lying above the maximum starburst line of Kewley et al. (2001) in all three ODDs shown in Fig. 4.9. Since the harder radiation fields

of AGN have a similar effect on the line ratios as shocks and DIG, and because there are very few spaxels with line ratios above the maximum starburst line by greater than 1σ , we therefore place an upper limit of 15 per cent on the contribution of non-stellar ionisation sources in MO.

4.6.6 Star formation rate

We calculated the global SFR using the same calibration used by Croft et al. (2006) ($\text{SFR}(\text{H}\alpha) = (7.0 - 7.9) \times 10^{-42} L(\text{H}\alpha)$), which has a systematic uncertainty of approximately 30 per cent due to uncertainty in the shape of the IMF at the high-mass end. Using the total H α flux in each spaxel gives $\text{SFR} \leq 0.272 \pm 0.017 M_{\odot} \text{yr}^{-1}$. Adopting the total H I mass $M_{\text{HI}} = 4.9 \times 10^8 M_{\odot}$ (Croft et al. 2006), this corresponds to a depletion time of $t_{\text{dep}} \geq 1.8 \text{Gyr}$. As discussed in Section 4.6.5, the H α emission is contaminated by processes other than star formation; this SFR should therefore be treated as an upper limit.

Our SFR estimate and total H α flux ($(4.27 \pm 0.02) \times 10^{-14} \text{erg s}^{-1} \text{cm}^{-2}$) are approximately half that of Croft et al. (2006) ($0.5 M_{\odot} \text{yr}^{-1}$ and $8.6 \times 10^{-14} \text{erg s}^{-1} \text{cm}^{-2}$ respectively). The reason for this discrepancy is unclear. Our flux estimate is closer to that of van Breugel et al. (1985), who reported a combined H α + [N II] flux of $3.2 \times 10^{-14} \text{erg s}^{-1} \text{cm}^{-2}$.

Lacy et al. (2017) claimed that the recent type-II supernova (SN) explosion 2010ib (Cenko et al. 2010; Gal-Yam et al. 2010) is evidence that MO may have a top-heavy IMF due to the improbability of observing a SN explosion in an object with such a low SFR. However, the best-fit star formation history (SFH) from our PPF analysis (Section 4.5) indicates that the majority of the stellar mass formed during a period of $\sim 1 - 2 \text{Myr}$ approximately 10^7yr ago, during which the SFR would have been much greater than the present-day value. Modelling MO as a solar metallicity $10^7 M_{\odot}$ SSP with an instantaneous burst SFH and a Salpeter IMF using STARBURST99 (Leitherer et al. 1999), the expected SN rate at 10^7yr is approximately 0.03yr^{-1} , corresponding to one SN explosion every $\sim 30 \text{yr}$. Therefore, SN explosion 2010ib is consistent with MO having a conventional IMF.

4.6.7 Metallicity and ionisation parameter

We followed the iterative method of Kewley & Dopita (2002) to simultaneously estimate the gas-phase oxygen abundance $\log(\text{O}/\text{H}) + 12$ (henceforth referred to as metallicity) and dimensionless ionisation parameter $\log(\mathcal{U})$ in each spaxel using the theoretical diagnostics provided by Kewley et al. (2019a) assuming a constant pressure $\log(P/k) = 5.0$, which is appropriate for typical H II regions.

Strong-line abundance and ionisation parameter diagnostics are derived from models of standard H II regions, and may yield spurious results if the line emission is contaminated by processes other than star formation. As discussed in Section 4.6.5, we estimate the contribution to the line emission from sources other than star formation to be less than 15 per cent. At this level, Kewley & Ellison (2008) found that the N2O2 ($[\text{N II}]\lambda\lambda 6548, 6583 / [\text{O II}]\lambda\lambda 3726, 3729$) metallicity diagnostic is robust to contamination from AGN photoionisation. We expect the harder radiation fields from shocks and DIG to have a similar effect on the $[\text{N II}]/[\text{O II}]$ ratio. If this is the case, then the N2O2 diagnostic can be used reliably in MO; however, we note

that our metallicity estimates are uncertain because we are unable to quantify the amount of contamination from sources other than star formation.

The metallicity and ionisation parameter were only estimated in spaxels in which each line used in the diagnostic had $S/N > 3$. The bottom panel of Fig. 4.15 shows $\log(\mathcal{U})$ estimated using the O3O2 ($[\text{O III}]\lambda\lambda 4959, 5007/[\text{O II}]\lambda\lambda 3726, 3729$) diagnostic of Kewley et al. (2019a). The typical uncertainty in each spaxel is 0.02 dex. In most parts of the object $\log(\mathcal{U}) \approx -3.0$, which is consistent with the finding of Croft et al. (2006); however, $\log(\mathcal{U}) \approx -2.0$ in some regions, exceeding the values found in typical H II regions.

The top panel of Fig. 4.15 shows the metallicity estimated using the N2O2 metallicity diagnostic. The typical uncertainty in each spaxel is 0.01 dex. There is significant variation in the metallicity across the object, with the lowest-metallicity regions lying near the Eastern and Western edges of the object, and $\log(\text{O}/\text{H})+12$ increasing by up to 0.5 dex in the centre. Metallicity estimates using other diagnostics including the N2 ($[\text{N II}]\lambda 6583/\text{H}\alpha$), O2S2 ($[\text{O II}]\lambda\lambda 3726, 3729/[\text{S II}]\lambda\lambda 6716, 6731$), O3N2 ($([\text{O III}]\lambda 5007/\text{H}\beta)/([\text{N II}]\lambda 6583/\text{H}\alpha)$) and R23 ($([\text{O II}]\lambda\lambda 3726, 3729 + [\text{O III}]\lambda\lambda 4959, 5007)/\text{H}\beta$) are presented in Appendix E, revealing similar metallicity trends.

As noted previously, contamination from sources other than star formation may bias our metallicity estimates. As shown in Fig. 4.9, the N2O2 metallicity is strongly correlated with the S2 ratio. Comparison of Fig. 4.11 and Fig. 4.15 also shows that the higher-metallicity and higher-S2 regions are located away from the main star-forming regions, and would therefore have line ratios more strongly contaminated by processes other than star formation. It is therefore possible that the metallicity is being over-estimated in these regions.

4.7 Possible explanations for the metallicity variation

In this section, we explore several scenarios that could produce the large metallicity variation observed within MO.

4.7.1 Enrichment from star formation

Star formation proceeding from SE-NW could potentially cause the metallicity variation, as regions with more recent star formation would have had less time to enrich the ISM with metals via supernova explosions and stellar winds. Although we were unable to spatially resolve MO in our PPXF analysis (Section 4.5), the global best-fit stellar population is dominated by a young population $\lesssim 10$ Myr old, with a spread of only 1 – 2 Myr (Fig. 4.6).

To determine whether an age spread of a few Myr in the stellar population could explain the observed metallicity variation, we used an SSP model to estimate the oxygen yield per stellar mass for stars of a given age and metallicity. The SSP model considers enrichment contributions from various channels. Yields from type II supernovae (including a prescription for Ibc; Kobayashi 2004) are calculated as a function of age and metallicity, where the age determines the main-sequence turn off mass using the metallicity-dependent lifetimes of Kodama & Arimoto (1997). A metallicity-dependent hypernova (HN) fraction is also included, with a greater

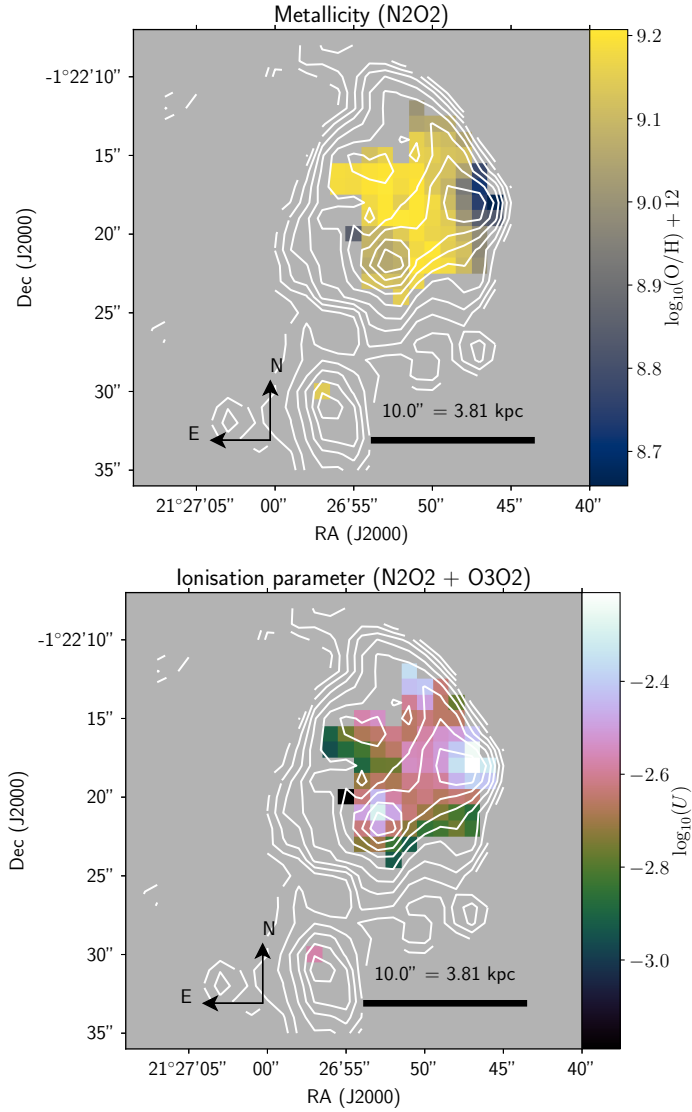


Figure 4.15: Gas-phase metallicity of MO (top) calculated using the N2O2 diagnostic of Kewley et al. (2019a) and the dimensionless ionisation parameter (bottom) calculated using the O3O2 diagnostic of Kewley et al. (2019a). The white contours show the H α flux on a log scale.

contribution from HN at low metallicity (Kobayashi & Nakasato 2011). Winds from asymptotic giant branch stars further contribute (Kobayashi et al. 2011). Type Ia supernovae are included in the model (Kobayashi & Nomoto 2009), but do not contribute on the short timescales considered here. We assume a Kroupa (2001) IMF (slope $\alpha = 1.3$) in the range $0.01 - 120 M_{\odot}$, with an upper mass limit for core-collapse supernovae of $50 M_{\odot}$.

As shown in Fig. 4.16, for stellar metallicities $\geq 0.1 Z_{\odot}$ (consistent with the gas-phase metallicity), the oxygen yield increases by only a factor of 2 over a period of 5 Myr, insufficient to explain the metallicity enhancement of 0.5 dex in the centre of the object. Stellar enrichment alone is therefore unable to explain the metallicity variation.

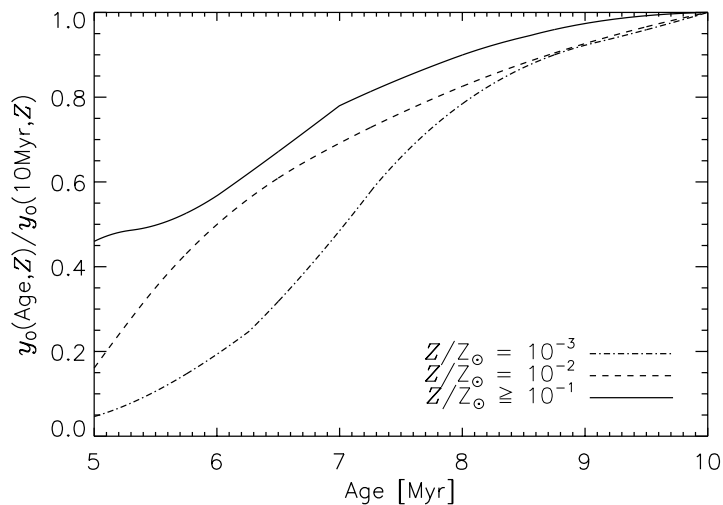


Figure 4.16: Oxygen yield per stellar mass (normalised to the yield at 10 Myr) as a function of stellar age, estimated using the chemical enrichment model described in Section 4.7.1. The solid, dashed and dash-dotted lines show yields for stellar metallicities of 10^{-3} , 10^{-2} and $\geq 10^{-1} Z_{\odot}$ respectively.

4.7.2 An enriched jet-driven outflow from NGC 541

A metallicity variation in MO could have arisen if some of the gas from which it formed originated in a jet-driven outflow from NGC 541. X-ray studies of clusters have revealed metallicity enhancements of up to 0.2 dex occurring along the path of jets from BCGs (Kirkpatrick et al. 2009, 2011), indicating that jets can transport enriched material up to several 100 kpc from the host. Hence it is plausible for enriched gas to be found along the jet of NGC 541. However, it is highly unlikely that any metal-enriched gas from NGC 541 would become bound to MO given its very low stellar mass ($\sim 10^7 M_{\odot}$). We therefore rule out this scenario.

4.7.3 Pre-existing enriched gas in the stellar bridge

MO may have formed from dense clumps of gas residing in the stellar bridge connecting NGC 541 and NGC 545/547, as we discuss further in Section 4.8. This gas will have been stripped from the interacting galaxies, and would therefore be enriched relative to the ICM. Moreover, the recent type Ia supernova explosion 2018ctv (Chen et al. 2018; Moral-Pombo et al. 2018; Panizo-Espinar et al. 2018) in the stellar bridge indicates ongoing stellar enrichment in the ICM of Abell 194.

To check whether this is plausible, we compared the gas-phase metallicities in MO and in NGC 541. Hamer et al. (2016) observed NGC 541 with VLT/VIMOS and obtained spatially resolved emission line fluxes, which we used to estimate the gas-phase metallicity. In Table 4.3, we show the metallicity computed from the line fluxes reported in their appendix F integrated over the entire extent of the galaxy ('total'), in the nucleus ('central') and the fluxes calculated as the difference between these two estimates ('extended'). Due to the limited number of emission lines in the wavelength range of their observations, we used the N2 diagnostic, adopting a fiducial $\log(\mathcal{U}) = -3.0$, appropriate for normal H II regions. The metallicity in the outer regions of NGC 541 ($\log(\text{O}/\text{H}) + 12 \approx 8.8$) is approximately 0.2 dex higher

than that observed in MO using the same diagnostic (see Appendix E), meaning that the ISM in NGC 541 is sufficiently enriched to explain the high observed metallicities in MO. However, this scenario cannot explain the metallicity variation of 0.5 within the object. Moreover, the N2 diagnostic is subject to contamination by the AGN; further observations of NGC 541 are therefore required to observe emission lines enabling us to apply a metallicity diagnostic more robust to AGN contamination, such as N2O2.

Table 4.3: Gas-phase metallicity in different regions of NGC 541 estimated using VLT/VIMOS emission line fluxes from Hamer et al. (2016), where we have used the N2 diagnostic of Kewley et al. (2019a) assuming $\log(U) = -3.0$.

Region	$\log(\text{O}/\text{H}) + 12$
Total	8.9682
Central	9.2353
Extended	8.7814

Having ruled out star formation, an enriched jet-driven outflow and enrichment of gas in the stellar bridge as the cause of the metallicity variation, its origin is uncertain, although we note that the magnitude of the variation may be over-estimated due to contamination from sources other than star formation.

4.8 On the formation of Minkowski's Object

Here, we discuss possible scenarios for the formation of MO.

Croft et al. (2006) suggest that MO formed from the hot, tenuous ICM that underwent runaway cooling due to shocks induced by the passage of the jet. However, simulations by Fragile et al. (2004) suggest that MO would have required a pre-collision cloud density of approximately 10 cm^{-3} to form via a jet interaction. This density is substantially higher than estimated ICM densities in local clusters ($\sim 10^{-3} - 10^{-2} \text{ cm}^{-3}$; e.g., Mohr et al. 1999); it therefore appears unlikely that MO formed directly from the ICM. MO may instead have formed from pre-existing dense clouds in the path of the jet. As shown in Fig. 4.1, Abell 194 harbours a stellar bridge connecting NGC 541 and NGC 545/547, which is aligned with the jet from NGC 541 in projection. The stellar bridge may contain H I stripped from the interacting galaxies, akin to the intra-group H I observed in groups such as Stephan's Quintet (Sulentic et al. 2001). MO is indeed associated with a large H I cloud with mass $4.9 \times 10^8 M_{\odot}$; such pre-existing H I may have been sufficiently dense for jet-induced star formation to occur.

One of the only other known examples of jet-induced star formation, the string of OB associations in the Northern jet of Centaurus A, is believed to have formed due to a jet interaction with an H I cloud that drifted into the jet's path. Crucially, this cloud has been detected *outside* the jet's path, and appears to be part of a larger ring of H I clouds that may have formed during a past merger event (Schiminovich et al. 1994; Oosterloo & Morganti 2005), indicating that this gas existed prior to the jet interaction. In contrast, all of the H I associated with MO is spatially coincident with the jet; Croft et al. (2006) claim this is evidence that the jet triggered the formation of the cloud. However, Croft et al. (2006) remark that additional H I could exist

at velocities outside the low bandwidth (500 km s^{-1}) of their observations, and that the H I cloud may be part of a larger pre-existing H I complex.

We note that although both systems have a similar total molecular gas mass ($1.4 \times 10^7 M_{\odot}$ in the Cen A filaments, Charmandaris et al. (2000); $3 \times 10^7 M_{\odot}$ in MO, Lacy et al. (2017)), the Cen A filaments have a total SFR = $4 \times 10^{-3} M_{\odot} \text{ yr}^{-1}$ (Salomé et al. 2016), 10 times lower than that of MO even if only 10 per cent of the H α emission in MO is attributed to star formation. It is unclear why the star-formation efficiency should differ so drastically between the two objects.

A second possibility is that MO formed from pre-existing filaments in the ICM. H α -emitting filaments are regularly observed in cool-core clusters, and may trace cooling gas flowing into the BCG (e.g., Heckman et al. 1989). Many filaments exhibit line emission with LINER-like line ratios, attributed to in-situ star formation and shocks (e.g., McDonald et al. 2012). Jet-induced shocks could lead to enhanced star formation in these filaments. However, it seems unlikely that Abell 194 would harbour such filaments, because it lacks the localised, enhanced X-ray emission associated with cooling gas (Nikogosyan et al. 1999; Sakelliou et al. 2008). Moreover, these filaments generally exhibit $\log([\text{N II}]\lambda 6583/\text{H}\alpha) \sim -0.5 - 0.5$, much higher than observed in MO ($\log([\text{N II}]\lambda 6583/\text{H}\alpha) \sim -1$), in addition to much broader line widths ($\sim 100 \text{ km s}^{-1}$; e.g., Heckman et al. 1989; Sabra et al. 2000; Farage et al. 2010; McDonald et al. 2012; Hamer et al. 2015). We therefore conclude that it is unlikely for MO to have formed from such filaments.

The final scenario we consider is that MO is a gas-rich dwarf galaxy that is currently falling into Abell 194, and has a temporarily elevated SFR due to the jet interaction. In recent years, a population of isolated H I-rich ultra-diffuse dwarf galaxies (HUDs) have been discovered, characterised by blue colours, extended ($\sim 10 - 30 \text{ kpc}$) clumpy morphologies and high gas fractions, with $M_{\text{HI}} \sim 10^8 - 10^9 M_{\odot}$ and $M_{*} \sim 10^7 - 10^8 M_{\odot}$ (Leisman et al. 2017), similar to MO. However, with a surface brightness $\mu_g = 21.8 \text{ mag arcsec}^{-2}$, MO is much brighter than most HUDs, which by definition have $\mu_g \geq 24 \text{ mag arcsec}^{-2}$. If MO truly originated from a HUD, its current surface brightness may be temporarily elevated due to jet-induced star formation.

Under this formation scenario, we may speculate on the fate of MO. As they fall into clusters, gas-rich dwarfs are predicted to rapidly lose their gas due to ram-pressure stripping or tidal interactions, eventually transforming into ultra-diffuse galaxies (Leisman et al. 2017; Román & Trujillo 2017): extended, low surface-brightness, quiescent galaxies which are numerous in local clusters (e.g., van Dokkum et al. 2015; Koda et al. 2015). To model the quenching of MO as it falls into Abell 194, we used a STARBURST99 (Leitherer et al. 1999) solar metallicity SSP model with a Salpeter IMF and an instantaneous SFH. Given the present-day V band surface brightness of $\mu_V = 22.7 \text{ mag arcsec}^{-2}$, we predict MO to fade to $\mu_V = 24.2 \text{ mag arcsec}^{-2}$ and $\mu_V = 25.7 \text{ mag arcsec}^{-2}$ in approximately 100 Myr and 1 Gyr respectively, firmly placing MO into the surface brightness regime of ultra-diffuse galaxies. The correspondingly low stellar mass surface densities suggests that MO will eventually become disrupted as it falls into the cluster.

If MO is truly a gas-rich dwarf that has wandered into the path of the jet, we may be observing it during a brief phase where it is bright enough to see in shallow observations. It is therefore possible that there are many objects similar to MO that have now faded, and that MO is perhaps not as unique as is currently believed.

Establishing whether MO resides in its own dark matter (DM) halo would enable us to distinguish between these different formation scenarios. If MO formed from the ICM, then it would not be associated with a DM halo, whereas ultra-diffuse galaxies are known to span a range of DM halo masses (Zaritsky 2017). Unfortunately, the irregular morphology of MO makes it difficult to measure its inclination using our WiFeS observations, meaning we cannot constrain the gravitational mass of MO from its rotation curve. Further observations and modelling of MO and Abell 194 will be required to distinguish between these different formation scenarios.

4.9 Conclusion

We conducted a study of Minkowski’s Object (MO), an peculiar star-forming dwarf galaxy located along the path of a jet from the nearby radio galaxy NGC 541, using optical integral field spectroscopy.

Analysis of the stellar continuum with PPAFF confirms that MO is dominated by a predominantly young stellar population ~ 10 Myr old, indicating that the bulk of its stellar mass formed during a recent jet interaction. A secondary population at ~ 1 Gyr is also present, and may represent stars in the stellar bridge between NGC 541 and NGC 545/547 or a pre-existing stellar population associated with MO.

In most parts of the object, the emission line ratios are consistent with star formation, although some regions exhibit enhanced $[\text{S II}]/\text{H}\alpha$ and $[\text{O I}]/\text{H}\alpha$ ratios suggesting the presence of non-stellar ionising sources. A complex combination of shock, DIG and X-ray photoionisation from the AGN of NGC 541 may explain the line ratios, although further modelling is required to determine whether this is plausible.

Strong-line metallicity diagnostics indicate a gas-phase metallicity that varies by 0.5 dex across the object, which cannot be explained by enrichment from in-situ star formation, enriched gas entrained in the jet from NGC 541, nor the presence of pre-existing enriched gas in the stellar bridge, although we note the magnitude of the variation may be over-estimated due to contamination from sources other than star formation.

We explored several formation scenarios for MO, and concluded that it formed from either (a) pre-existing H I clouds in the stellar bridge between NGC 541 and NGC 545/547 that were stripped from these galaxies during an interaction or (b) a gas-rich dwarf galaxy that wandered into the path of the jet. Further observations and modelling may enable us to distinguish between these two scenarios.

Acknowledgements

The authors would like to thank Julie Banfield for leading the initial observing programme, Adam D. Thomas for providing assistance with NEBULABAYES, and Chiaki Kobayashi for assistance with the SSP chemical enrichment modelling.

This research has made use of the NASA/IPAC Extragalactic Database, which is funded by the National Aeronautics and Space Administration and operated by the California Institute of Technology.

This research made use of QFitsView[§], a software package for reducing astronomical data written by Thomas Ott, Scipy[¶] (Jones et al. 2001), and Astropy,^{||} a community-developed core Python package for Astronomy (Astropy Collaboration et al. 2013, 2018).

Model generated with SED@.0 code** with the following inputs: IMF from Salpeter (1955) in the mass range $0.1 - 120 M_{\odot}$; High Resolution library from Martins et al. (2004); González Delgado et al. (2005) based on atmosphere models from PHOENIX (Hauschildt & Baron 1999; Allard et al. 2001), ATLAS9 (Kurucz 1991) computed with SPECTRUM (Gray & Corbally 1994), ATLAS9 library computed with SYNSPEC (Hubeny & Lanz 2011), and TLUSTY (Lanz & Hubeny 2003). Geneva isochrones computed with the isochrone program presented in Meynet (1995) and following the prescriptions quoted in Cerviño et al. (2001) from the evolutionary tracks from Schaller et al. (1992) at $Z = 0.001/Z = 0.020$; Charbonnel et al. (1993) at $Z = 0.004$; Schaerer et al. (1993b) at $Z = 0.008$ and Schaerer et al. (1993a) at $Z = 0.040$. Padova isochrones presented in Girardi et al. (2002)^{††} based on the (solar scaled mixture) tracks from Girardi et al. (2000); Bertelli et al. (1994) that includes overshooting and a simple synthetic evolution of TP-AGB Girardi & Bertelli (1998).

Parts of this research were supported by the Australian Research Council Centre of Excellence for All Sky Astrophysics in 3 Dimensions (ASTRO 3D), through project number CE170100013. L. J. K. gratefully acknowledges the support of an ARC Laureate Fellowship (FL150100113).

[§]<https://www.mpe.mpg.de/~ott/QFitsView/>

[¶]<http://www.scipy.org/>

^{||}<http://www.astropy.org>

**SED@ is a synthesis code included in the *Legacy Tool project* of the *Violent Star Formation Network*; see SED@ *Reference Manual* at <http://www.iaa.es/~mcs/sed@> for more information.

^{††}Available at <http://pleiadi.pd.astro.it/>

5

Conclusions and summary

It doesn't stop being magic just because you know how it works.

Terry Pratchett

In this thesis, I have used IFS to study the impact that jets have upon their environment. In Chapters 2 and 3, I studied the effects that compact jets have upon their host galaxies, and in Chapter 4, I investigated the properties of an object formed via jet-induced star formation. Here, I summarise these chapters and discuss potential avenues for future research, before closing with some final remarks.

5.1 Jets blowing bubbles in the young radio galaxy 4C 31.04

In Chapter 2, I presented my study of 4C 31.04, a local galaxy hosting a CSS source. In this study, I used AO-assisted near-IR IFS from Gemini/NIFS to search for signatures of jet-ISM interactions on sub-kpc scales. The K band observations revealed shock-excited ro-vibrational H_2 emission tracing the inner kpc of the host galaxy's circumnuclear disc, whilst in the H band, I detected $[\text{Fe II}]$ emission tracing an expanding 'bubble' with a radius of approximately 200 pc. I demonstrated that neither star formation nor accretion are sufficient to power either the H_2 or the $[\text{Fe II}]$ line emission, leaving jet-induced shocks as the only plausible excitation mechanism. This appeared to contradict earlier VLBI observations of the source, which showed the jets to be approximately 100 pc in size.

Hydrodynamical simulations held the key to resolving this discrepancy. These simulations show that when young jets emerge from the nucleus, the brightest regions of jet plasma may become temporarily halted by dense clumps, whilst weaker tendrils of jet plasma can percolate through channels in the ISM. These tendrils form a quasi-spherical bubble, which drives a shock into the ISM as it expands (Sutherland &

Bicknell 2007; Wagner et al. 2016; Mukherjee et al. 2016). Crucially, this bubble is filled with low-surface brightness jet plasma that may not be detected in VLBI observations due to a lack of sensitivity to the relevant spatial scales, or simply due to insufficient flux sensitivity. Whilst only accounting for a small fraction of the total radio flux, my NIFS observations showed that the expanding bubble interacts strongly with the ISM, and is detectable in the form of emission lines from shocked gas.

This study demonstrated that IFS is a critical tool for studying jet-ISM interactions in galaxies hosting young radio AGN, in which VLBI observations may not reveal the true extent of the jet plasma.

5.2 Searching for signs of jet-driven feedback in the radio galaxy UGC 05771

In Chapter 3, I presented my second paper, in which I studied UGC 05771, the host galaxy of another local CSS source. Using AO-assisted near-IR IFS from Keck/OSIRIS, I detected shocked gas traced by ro-vibrational H_2 lines and [Fe II] emission, tracing a multi-phase ‘stalling wind’ extending several hundred pc from the nucleus. I paired my OSIRIS observations with IFS data from the CALIFA survey, which provided spatially resolved optical spectra on kpc scales. These data revealed a kpc-scale region of ionised gas surrounding the nucleus with LINER-like line ratios and line widths too broad to be explained by beam smearing, indicating shock excitation.

Using similar methods to those in Chapter 2, I demonstrated that the jets are the only plausible mechanism for driving the shocks causing both the near-IR and optical line emission. Again, I found that the extent of shocked gas was much larger than the size of the radio jets in existing VLBI imaging, suggesting the presence of a kpc-scale ‘bubble’ filled with low-surface brightness jet plasma.

I also obtained CO(1–0) and CO(2–1) observations from the IRAM 30 m telescope to investigate the molecular gas content of the host galaxy, in order to determine the jets’ impact on the star formation efficiency. By comparing the molecular gas mass surface density to the $\text{H}\alpha$ -derived star formation rate, I found that UGC 05771 sits below the Kennicutt-Schmidt relation, although further observations are required to better constrain the star formation rate, as the $\text{H}\alpha$ -based estimate is subject to contamination from shocks.

5.3 Unravelling the enigmatic ISM conditions in Minkowski’s Object

In Chapter 4, I presented a study of Minkowski’s Object (MO), a peculiar star-forming object believed to exhibit jet-induced star formation. Using deep optical IFS from the WiFeS instrument, I probed the star formation history and ISM conditions of this unique object.

Analysis of the stellar continuum indicated that MO is dominated by stars ~ 10 Myr old, consistent with results from previous photometry-based studies. This

confirms that the bulk of the galaxy’s stellar mass formed during a recent jet interaction.

I found that whilst the emission line ratios are consistent with star formation across most of the object, some regions exhibit high $[\text{S II}]/\text{H}\alpha$ and $[\text{O I}]/\text{H}\alpha$ ratios that cannot arise from star formation alone, although the level of contamination is estimated to be $\lesssim 15$ per cent. I concluded that a complex combination of excitation mechanisms may be present in the object, including star formation, shocks, DIG and X-ray photoionisation, although further modelling is required to confirm this.

Strong-line metallicity diagnostics revealed that MO has a gas-phase oxygen abundance that varies by up to 0.5 dex across the object. I considered several scenarios that could explain such a metallicity distribution, including stellar enrichment and the jet transporting enriched material from NGC 541. However, none of these scenarios were found to be plausible. The origin of the metallicity gradient therefore remains unknown.

I explored several formation scenarios for MO, and concluded that it formed from either (a) pre-existing H I clouds in the stellar bridge between NGC 541 and NGC 545/547 that were stripped from these galaxies during an interaction or (b) a gas-rich dwarf galaxy that wandered into the path of the jet. Further observations and modelling of Abell 194 may enable us to distinguish between these two scenarios.

5.4 Future work

The work presented in this thesis has opened several compelling avenues for future research, several of which are summarised here.

5.4.1 Jet-ISM interactions in large samples of compact radio galaxies

Although the research presented in Chapters 2 and 3 indicated that seemingly compact jets can drive shocks and turbulence into the ISM on kpc scales, the significance of this mode of feedback in the context of galaxy evolution remains unclear: in particular, very little is known about the long-lasting impact of compact jets upon the star formation histories of their host galaxies. However, because radio galaxies are relatively common at both low and high-redshift, this form of feedback may affect a significant fraction of galaxies in the Universe. By carrying out studies similar to those presented in this thesis, but on large samples of galaxies, we can quantitatively determine the effects that jets have upon the evolution of their host galaxies.

As I have shown in this thesis, IFS is an excellent tool that can be used to probe jet-driven feedback processes. Collectively targeting tens of thousands of nearby galaxies, recent optical IFS surveys such as MANGA (Bundy et al. 2015), SAMI (Bryant et al. 2015; Scott et al. 2018) and CALIFA (Sánchez et al. 2012, 2016b)—and upcoming surveys such as HECTOR (Bland-Hawthorn 2015)—represent a treasure-trove of data that can be used to conduct a survey of compact radio galaxies. This would, for the first time, enable us to carry out a statistical study of the impact that compact jets have on the evolution of their host galaxies. Although these surveys lack the angular resolution of the AO-assisted near-IR observations that have formed the basis of my studies into compact radio galaxies, I have demonstrated in my study

of UGC 05771 (Chapter 3) that IFS data with a much lower spatial resolution, such as that from the CALIFA survey, can be useful in detecting signatures of jet-ISM interactions on kpc scales.

Targeting compact radio galaxies selected from existing catalogues (e.g., de Vries et al. 2009; Jeyakumar 2016), the spatially resolved optical spectroscopy can be used to search for signatures of shocked gas on scales larger than the jet emission, which would indicate the presence of low-surface brightness jet plasma. This would enable us to determine how common this phenomenon is, in turn providing further verification for hydrodynamical simulations. State-of-the-art radio telescope facilities, such as The Australian Square Kilometre Array Pathfinder (ASKAP) and the Murchison Wide-field Array (MWA), will also provide the necessary sensitivity in terms of both angular scales and surface brightness to directly detect radio emission from these extended structures.

Studying a much larger sample size would also further our understanding of the effect that jets have on the star formation histories of their host galaxies. Analysis of the stellar population, following the method employed in Chapter 4 with a tool such as PPA, would reveal signatures of feedback such as quenching (e.g., as observed in the Shocked Post-starburst Galaxies (SPOGs) of Alatalo et al. 2016) or recent star-formation events. Comparison of these galaxies with a sample of non-AGN hosts, matched in properties such as morphology and stellar mass, would enable us to quantify the impacts of jet-driven feedback.

5.4.2 Sub-kpc scale jet-driven feedback at high redshift

Even with AO correction on 8–10 m telescopes, only in the most local radio galaxies are we able to study jet-ISM interaction on spatial scales comparable to the sub-arcsecond jet structures resolved by VLBI observations (e.g., the parsec-scale jets of UGC 05771; Figs. A1a, A1b and A1c). As a result, we are unable to resolve these processes in high-redshift targets, hampering our efforts to gauge the importance of jet-driven feedback in shaping the evolution of galaxies across cosmic time.

High-redshift studies of jet-driven feedback on sub-kpc scales will become possible with the advent of Extremely Large Telescope (ELT) facilities such as the Giant Magellan Telescope (GMT), the European Extremely Large Telescope (E-ELT) and the Thirty-Metre Telescope (TMT) equipped with AO-assisted integral field spectrographs such as the GMT Integral Field Spectrograph (GMTIFS, Sharp et al. 2018), ELT/HARMONI (Thatte et al. 2010) and TMT/IRIS (Larkin et al. 2010). For example, at the diffraction limit of the GMT at a wavelength of 2 μm , spatial scales of approximately 170 pc can be resolved in a $z = 1$ galaxy, whereas with an 8 m telescope, a similar resolution can only be achieved for a galaxy at $z = 0.16^*$.

Extending this work to targets at higher redshift will enable us to better understand the role of jets in shaping the properties of galaxies in the local Universe. With next-generation near-IR facilities such as GMT/GMTIFS, we will be able to study the rest-frame optical spectra of these much more distant radio galaxies with the necessary sensitivity and angular resolution to enable a direct comparison with local targets such as UGC 05771 and 4C 31.04. These facilities will also enable us to search for objects similar to MO at high redshift, which may be associated with the ‘alignment effect’ observed in high-redshift galaxies (e.g., Klammer et al. 2004);

* Assuming a cosmology with $H_0 = 70 \text{ km s}^{-1} \text{ Mpc}^{-1}$, $\Omega_M = 0.3$ and $\Omega_\Lambda = 0.7$

studying a larger sample of MO-like targets will shed light on the conditions required for the formation of these unusual systems.

As demonstrated in Chapters 2 and 3, jet interactions with molecular gas, traced by ro-vibrational H_2 emission, may play an important role in regulating star formation. However, observing these lines in galaxies at $z \gtrsim 0.1$ is challenging due to low atmospheric transmission beyond the K band (e.g., Smette et al. 2015). With its NIRSpec instrument (Bagnasco et al. 2007), the *James Webb Space Telescope* (*JWST*, Gardner et al. 2006) will provide $R \sim 1000 - 2700$ IFS in the $2 - 5 \mu\text{m}$ range, enabling these lines to be spatially resolved at sub-kpc scales in radio galaxies out to $z \sim 1.5$, albeit at a coarser spatial resolution than with near-IR IFUs on ELTs. Combined with rest-frame optical IFS from ground-based ELTs, rest-frame near-IR observations with *JWST* will help us better understand the impact of jets upon different ISM phases at high redshift.

Studying higher redshift targets will provide crucial validation of theoretical models of jet-driven feedback. Conditions in high-redshift radio galaxies are understood to be far more extreme than in their local counterparts, with higher gas densities and a more turbulent ISM (e.g., Wisnioski et al. 2015; Sanders et al. 2016). Studies of jet-ISM interactions in these sources are therefore critical for validating hydrodynamical simulations in these regions of the parameter space (e.g., Gaibler et al. 2012; Mukherjee et al. 2016) that cannot be probed in local radio galaxies.

5.4.3 Further investigation of the ISM conditions in Minkowski's Object

As discussed in Section 5.3, MO exhibits ISM conditions that indicate shocks, DIG and X-ray photoionisation may contribute to the excitation mechanism in the object.

Further IFS with an instrument such as FLAMES/GIRAFFE spectrograph with the ARGUS integral field unit on the Very Large Telescope (VLT) would enable us to confirm, or rule out, the presence of shocks. The much higher spectral resolution of FLAMES/GIRAFFE would enable multiple kinematic components in the optical emission-line gas to be distinguished, potentially allowing us to separate emission line components dominated by different excitation mechanisms.

As discussed in Chapter 4 the narrow widths of the emission lines and the fact that the jet is only weakly over-pressured with respect to its environment (Lacy et al. 2017) indicates that any shocks in MO are likely to be slow, and may therefore be only observable in the form of near-IR H_2 emission lines (e.g., Zovaro et al. 2019a,b). Near-IR IFS from an instrument such as Gemini/NIFS, Keck/OSIRIS or VLT/KMOS would reveal any such H_2 emission. These lines can also be used to infer the state of the molecular gas, in turn indicating whether these slow shocks have any impact on the star formation efficiency.

5.5 Summary and final remarks

In this thesis, I have demonstrated the power of spatially resolved spectroscopy to provide a detailed view into jet-driven feedback processes on sub-kpc scales.

By using IFS to study local radio galaxies in both the optical and near-IR, I have shown that very young jets can have a significant impact upon the ISM of

their host galaxy, with the potential to prevent star formation, thereby inducing negative feedback. I have also used optical IFS to probe the ISM conditions in Minkowski's Object, in doing so discovering unusual spectral signatures that may be associated with positive feedback.

There are still many unanswered questions: what long-lasting impacts—if any—do jets have upon their host galaxies? How do jet-driven feedback processes operate differently at high redshifts? Are objects such as Minkowski's Object more common in the high-redshift Universe? Upcoming surveys targeting thousands of galaxies, together with future ELT and space-based facilities, will enable us to answer these, and many more, questions about the impact that jets have upon their environment.

Despite the questions that remain, the work presented here represents a small—but significant—piece of the puzzle, paving our way towards a complete understanding of the complex processes shaping the galaxies in our Universe across cosmic time.

6

Appendix

Appendix

These appendices contain supplementary material to the work presented in Chapters 2, 3 and 4.

Appendix A was originally published as an appendix in Zovaro et al. (2019b), as presented in Chapter 3, and is reproduced here with minor formatting changes to make it consistent with the rest of the work in this thesis. Appendix B, also supplementary to the work presented in Chapter 3, is an extended discussion on beam smearing which did not appear in Zovaro et al. (2019b) as published; this content has been adapted from a response to reviewer comments received during peer-review.

Appendices C, D and E supplement the work presented in Chapter 4.

A UGC 05771: the morphology of the radio source

The radio source associated with UGC 05771 has a strikingly different morphology at 1.665 GHz (Fig. A1a), 4.993 GHz (Fig. A1b) and at 8.4 GHz (Fig. A1c). A South-West (SW) component at a projected distance of 18.3 pc is visible at 8.4 GHz; whilst there is faint contour to the SW at 4.993 GHz, it is absent at 1.665 GHz. In this section we address the apparent discrepancies between the three images.

The SW contour is offset by ≈ 16 mas (7.1 pc) between the 4.993 GHz and 8.4 GHz images. The observations are separated by 6.6 yr, corresponding to an apparent speed of $\approx 3.5c$, which would only be plausible if the source were strongly beamed. We rule this out due to the source's low flux variability (Snellen et al. 2004); therefore the SW contour in the 4.993 GHz image is probably an artefact.

Using the 8.4 GHz radio source count of Fomalont et al. (2002) we estimate the likelihood that the SW component is a background source to be vanishingly small, and therefore is most probably associated with UGC 05771. It is instead likely to be a site where jet plasma has interacted with a particularly dense cloud in the ISM,

re-accelerating electrons and creating a temporary hot spot.

The SW component may be absent from the 1.665 GHz and 4.993 GHz images due to beam smearing. If the integrated flux of a point source is lower than the rms noise per beam, the component will be indistinguishable from noise. The integrated flux of the SW component at 8.4 GHz is $S_{\text{int}}(8.4 \text{ GHz}) = 2.13 \text{ mJy}$ (Cheng & An 2018). Assuming the spectral index of the source $\alpha = 0.62$ (Snellen et al. 2004), then the integrated fluxes $S_{\text{int}}(5.0 \text{ GHz}) = 2.94 \text{ mJy}$ and $S_{\text{int}}(1.7 \text{ GHz}) = 5.74 \text{ mJy}$. The rms noise of the observations is $0.23 \text{ mJy beam}^{-1}$ and $0.10 \text{ mJy beam}^{-1}$ at 4.993 GHz and 1.665 GHz respectively, meaning that the SW component would be detected with a high S/N in either case; hence beam smearing cannot explain why the component is not visible.

We conclude that either (i) the SW component is strongly absorbed at these frequencies, either by synchrotron self-absorption or FFA, or (ii), there is structure at these lower frequencies that has been resolved out, which is consistent with the low flux completeness of these observations (≤ 30 per cent, see Fig. 3.1). For example, the jet structure visible at 1.7 GHz and 5 GHz is absent at 8.4 GHz. Using the flux along the jet axis from Fig. A1b and assuming $\alpha = 0.62$, the emission at 8.4 GHz should be $\approx 5 \text{ mJy}$, well above the rms noise (0.07 mJy), indicating that the jets have been resolved out in these observations. It is therefore plausible that the SW component has lower frequency counterparts that are not visible in these observations.

*The astrogeo database is maintained by Leonid Petrov, and is available at <http://astrogeo.org/>.

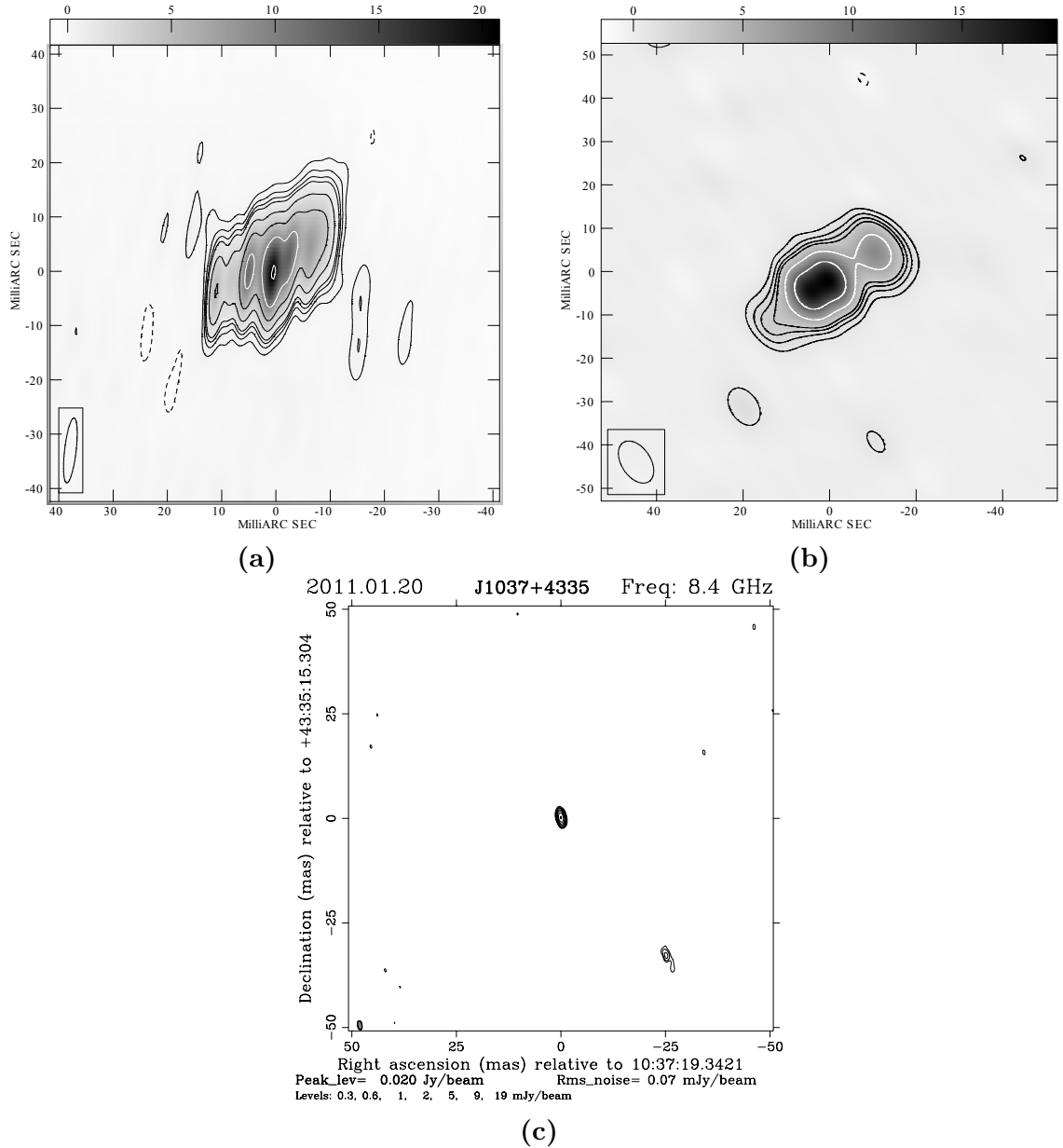


Figure A1: (a) and (b) show VLBI images of UGC 05771 at 1.665 GHz and 4.993 GHz respectively (de Vries et al. (2009), *A&A*, 498, 641, 2009, reproduced with permission © ESO). (c) shows the VLBI image at 8.4 GHz, obtained from the astrogeo database*. The root-mean-square (rms) sensitivities for these observations are 0.10, 0.23 and 0.09 mJy beam⁻¹ respectively.

B UGC 05771: ruling out beam smearing

To determine whether the enhanced H α velocity dispersion in the central 2 kpc of UGC 05771 could be a result of beam smearing, we created a synthetic data cube from a ‘toy model’ as follows. Using the best-fit Sérsic parameters for UGC 05771 (Table 3.1) and the best-fit PA and inclination for the ionised gas disc (Section 3.4.3), we used the expressions provided by Terzić & Graham (2005) to obtain the LOS velocity in the disc at a given radius. We then created a data cube from this model: for each spaxel, we created a spectrum comprising a H α emission line, modelled as a Gaussian profile, red/blueshifted by the appropriate amount, and with a relative intensity corresponding to the Sérsic profile at the given radius. We gave each emission line an intrinsic Gaussian $\sigma = 75 \text{ km s}^{-1}$ (to match the observed velocity dispersion in the outer regions of the gas disc (Fig. 3.9d), plus the instrumental resolution of PMAS, added in quadrature. We then spatially convolved the data cube to match the 2.5” seeing of the CALIFA data, before spatially binning the cube to match the 1” spaxel size of the CALIFA data. Finally, we added Gaussian noise so that the toy model data cube had comparable S/N to the CALIFA data. We then ran our line fitting routine on the resulting data cube; resulting plots are shown in Fig. B1.

As expected, beam smearing does artificially enhance the central velocity dispersion. However,

- The velocity dispersion in the toy model does not exceed approximately 160 km s^{-1} , whereas velocity dispersions of up to 225 km s^{-1} are observed in the region of enhanced velocity dispersion in the CALIFA data;
- The region of enhanced velocity dispersion in the toy model is not circular, but is elongated along the line where the disc has zero LOS velocity, whereas it is circular in the observations;
- The toy model velocity dispersion smoothly decreases moving away from the nucleus, whereas in the observations, the region of enhanced velocity dispersion ends relatively abruptly, over a distance of only 1-2 spaxels; and
- As shown in our optical diagnostic diagrams, the observed line ratios in this region are consistent with shocks, which cannot arise from beam smearing alone.

To see whether inaccuracies in our model parameters could be underestimating the effects of beam smearing in our toy model, we repeated the above using $n = 4$ as the Sérsic index (Fig. B2), and again with a much higher inclination (i.e. more edge-on, Fig. B3), both of which result in a much sharper gradient in the LOS velocity across the nucleus. In both cases, the central velocity dispersion can reach the observed values; however, in both cases, the region of enhanced velocity dispersion is elongated SE-NW, and has a smooth edge, both of which are not present in our observations. We hence conclude that beam smearing is not the sole cause of the enhanced velocity dispersion.

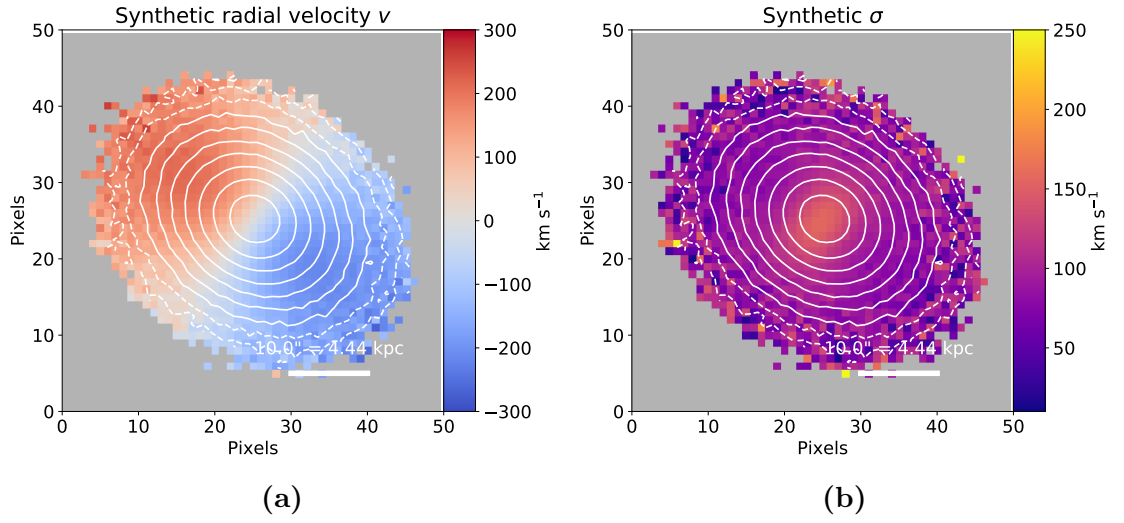


Figure B1: Radial velocity (a) and velocity dispersion (b) of our synthetic data cube of a thin disc in a Sérsic potential with $n = 1.28$ and $R_e = 3$ kpc with beam smearing.

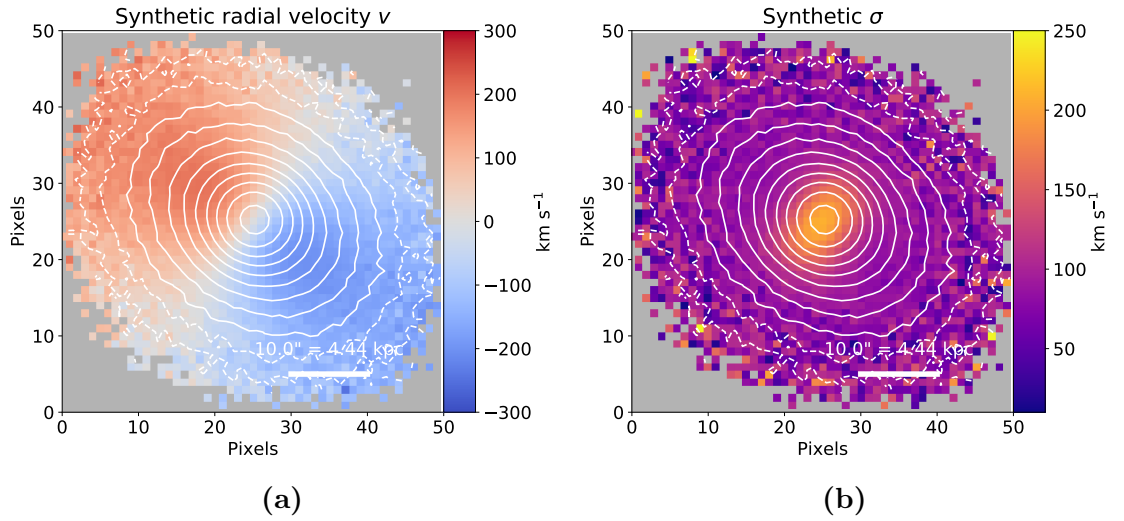


Figure B2: Same as Fig. B1 but with $n = 4$.

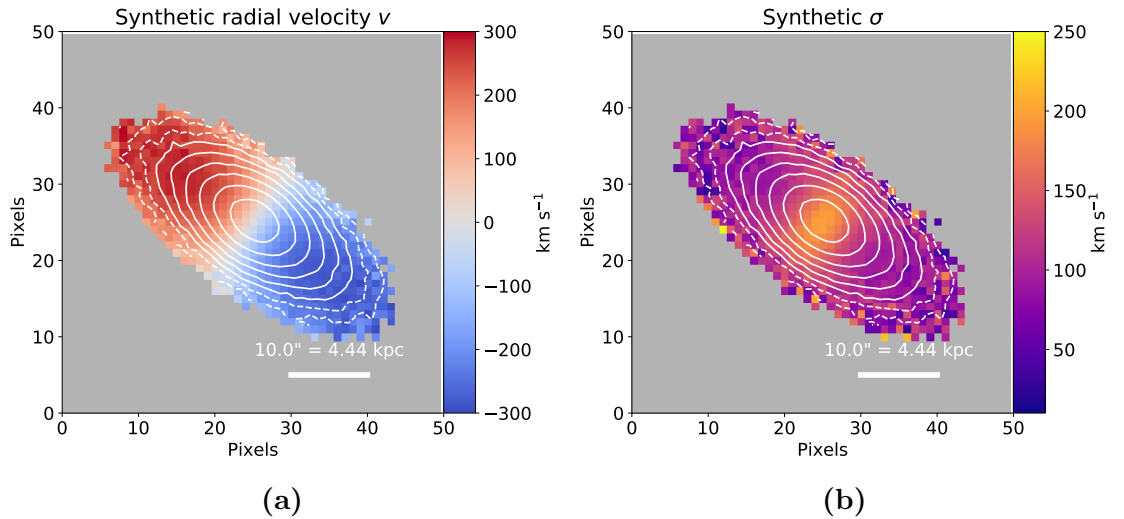


Figure B3: Same as Fig. B1 but at a higher inclination.

C Minkowski's Object: additional ppxf fits

In Fig. C1 we show the best-fit combination of stellar templates generated using PPXF with Padova isochrones, and the corresponding template weights in Fig. C2. The results are very similar to those obtained using the Geneva isochrones.

We also repeated our analysis using stellar templates with constant metallicity using both the Geneva and Padova isochrones. The best-fit SFHs, shown in Fig. C3, are similar regardless of the metallicity and isochrones used.

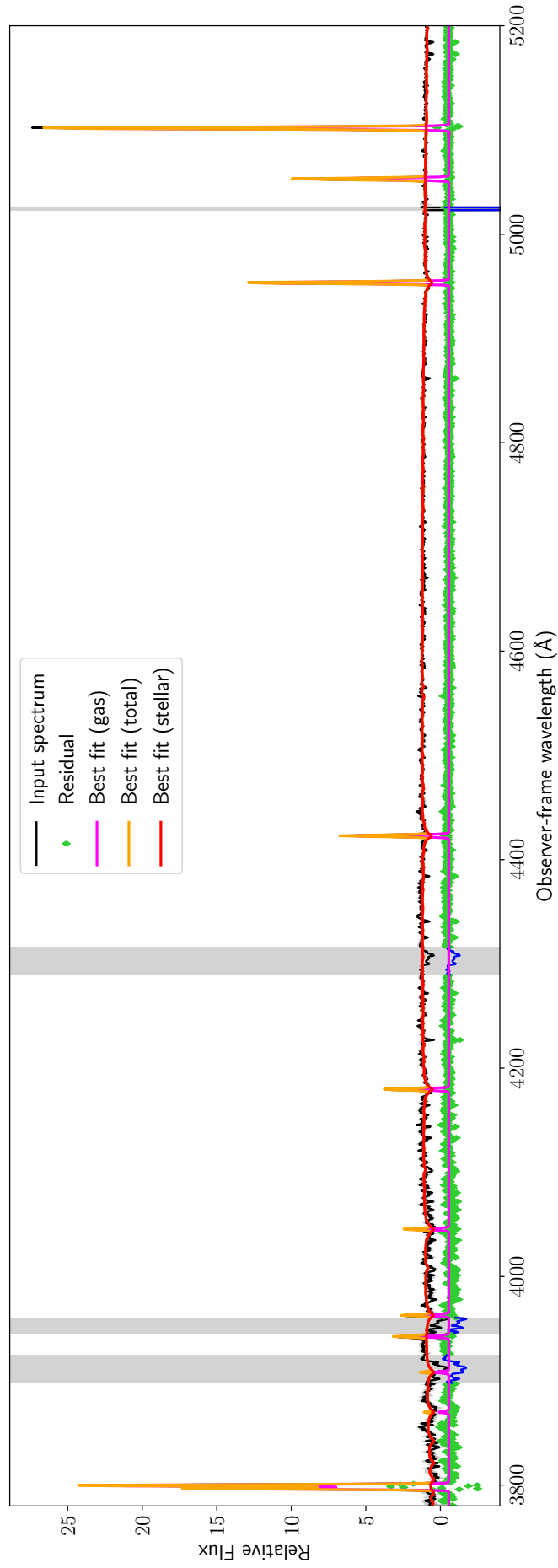


Figure C1: The integrated spectrum (corrected for Galactic extinction), overlaid with the best-fit spectrum (using the Padova isochrones) with the stellar and emission line components shown separately. 1σ errors are indicated in grey, and the green dots indicate the residual to the fit. The grey shaded regions indicate spectral windows dominated by residuals from the sky subtraction, and were not included in the fit.

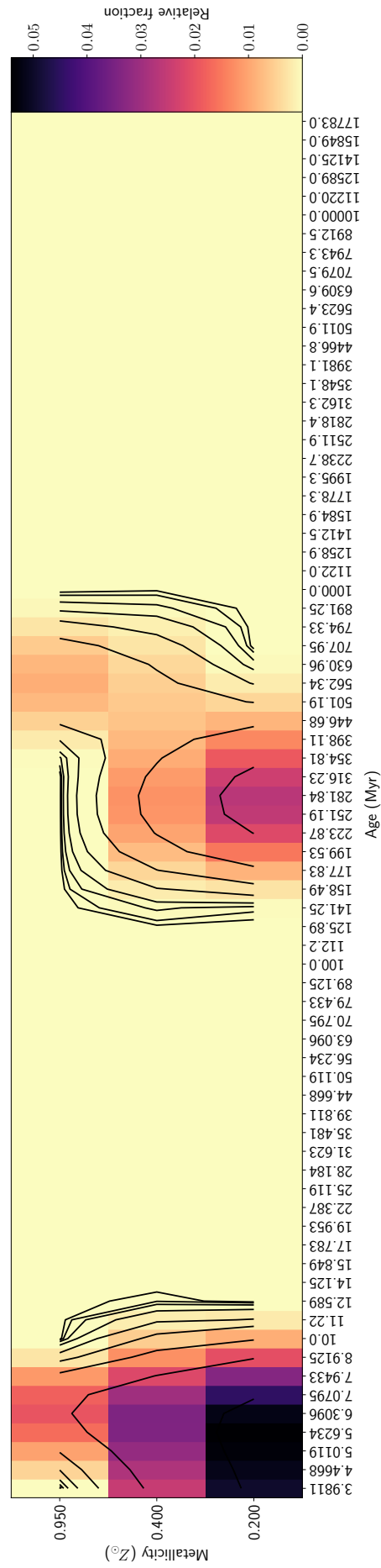


Figure C2: 2D histogram of the best-fit age and metallicity of the stellar population using the Padova isochrones, where the contours correspond to logarithmically spaced intervals from 10^{-4} to 10^{-1} .

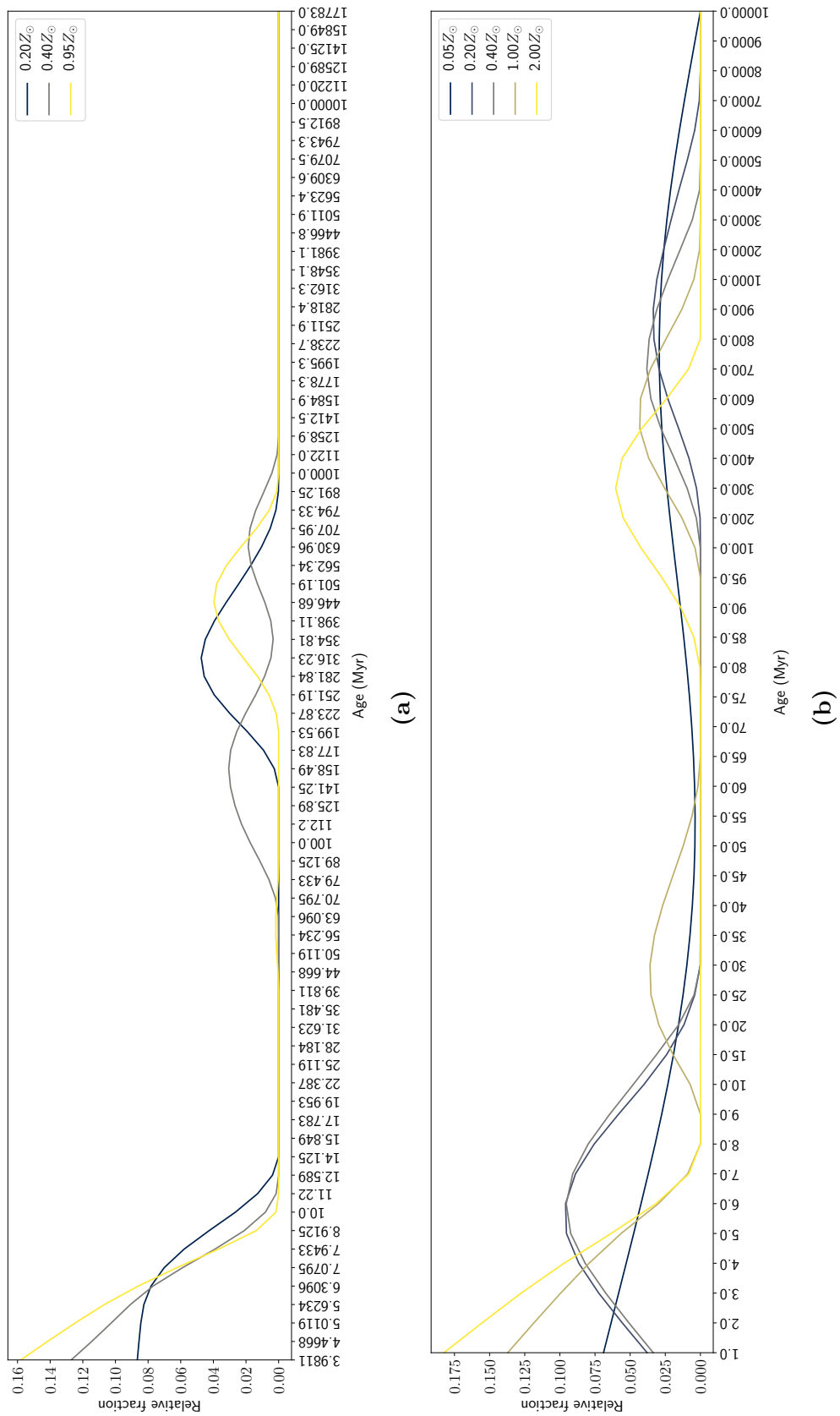


Figure C3: Best-fit SFHs generated using Geneva (a) and Padova (b) isochrones as a function of metallicity.

D Minkowski's Object: estimation of shock velocities

Because the jet impacting MO is an FRI jet, the usual approximations derived from a hypersonic or supersonic jet impacting a relatively dense medium (e.g. Blandford & Rees 1974) are not appropriate. In this appendix, we develop an estimate for the cloud shock velocity resulting from the impact of a transonic jet on a relatively dense cloud.

The dynamical setting, which is a classic shock tube configuration (see Landau & Lifshitz 1987, §100) is indicated in Figure D1. The jet pressure and density are p_1 and ρ_1 , and the cloud pressure and density are p_2 and ρ_2 . The shock pressure for both the jet terminus and the shocked cloud is p_3 , the shocked jet density is ρ_3 and the shocked cloud density is ρ'_3 . In the following we assume that, initially, both the cloud and jet are in pressure equilibrium with the ISM so that $p_1 \approx p_2$. The pressure difference $p_3 - p_1$ is denoted by Δp ; we cannot assume that $\Delta p \gg p_1$. The polytropic indices for jet and cloud are γ_1 and γ_2 respectively, and the velocities of the jet and cloud in the frame of the contact discontinuity are v_1 and v_2 , respectively.

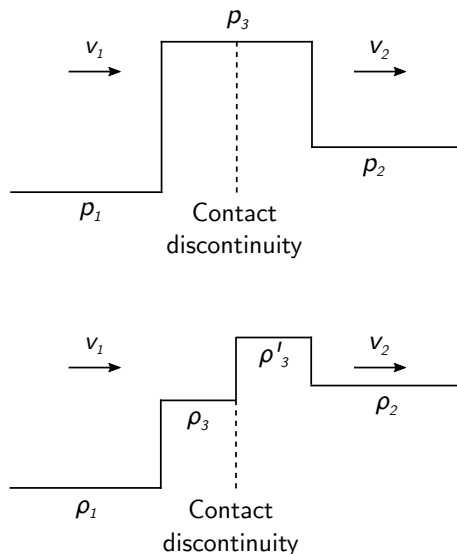


Figure D1: Configuration of pressure (top) and density (bottom) for a one-dimensional shock tube, following Landau & Lifshitz (1987). Region 1 corresponds to the jet and region 2 to the ISM impacted by the jet. In the calculations presented here, we assume that $p_1 = p_2$.

The frame-independent relative velocity between jet and cloud is

$$\Delta v = v_{\text{jet}} + v_{\text{infall}} \quad (\text{D1})$$

where v_{jet} and v_{infall} are respectively the jet velocity and infall velocity of MO in the frame of the radio galaxy NGC 541. For the shock tube analysis:

$$\Delta v = v_1 - v_2 \quad (\text{D2})$$

where v_1 and v_2 are respectively the jet velocity and cloud velocity in the frame of

the contact discontinuity separating the jet and cloud gas. We have:

$$\begin{aligned} \Delta v = v_1 - v_2 = & \left(\frac{2}{\rho_1}\right)^{1/2} \frac{p_3 - p_1}{[(\gamma_1 - 1)p_1 + (\gamma_1 + 1)p_3]^{1/2}} \\ & + \left(\frac{2}{\rho_2}\right)^{1/2} \frac{p_3 - p_2}{[(\gamma_2 - 1)p_2 + (\gamma_2 + 1)p_3]^{1/2}} \end{aligned} \quad (\text{D3})$$

Because the cloud density ρ_2 is much greater than the jet density ρ_1 , we neglect the second term in this expression and write:

$$\Delta v = \left(\frac{2}{\rho_1}\right)^{1/2} \frac{\Delta p}{[2\gamma_1 p_1 + (\gamma_1 + 1)\Delta p]^{1/2}} \quad (\text{D4})$$

Defining the Mach number, corresponding to Δv , by $M_1 = (\gamma_1 p_1 / \rho_1)^{-1/2} \Delta v$ the solution of Eqn. D4 for Δp is

$$\frac{\Delta p}{p_1} = \frac{\gamma_1(\gamma_1 + 1)}{2} M_1^2 f(M_1) \quad (\text{D5})$$

where

$$f(M_1) = \frac{1}{2} \left\{ 1 + \left[1 + \frac{16}{(\gamma_1 + 1)^2} M_1^{-2} \right]^{1/2} \right\} \quad (\text{D6})$$

$$\rightarrow 1 \quad \text{for } M_1 \gg 1 \quad (\text{D7})$$

It follows from the Rankine Hugoniot relations that the velocity of the shock propagating from region 3' to region 2 (i.e. the cloud shock) is given by:

$$v_{\text{sh,cl}}^2 = \frac{1}{2\rho_2} [(\gamma_2 - 1)p_2 + (\gamma_2 + 1)p_3] \quad (\text{D8})$$

and for $p_1 = p_2$

$$v_{\text{sh}}^2 = c_{\text{s},2}^2 \left[1 + \frac{(\gamma_2 + 1)}{2\gamma_2} \frac{\Delta p}{p_1} \right] \quad (\text{D9})$$

where $c_{\text{s},2}$ is the adiabatic sound speed in the cloud.

Using Eqn. D5 for Δp , we have for the velocity of the cloud shock

$$v_{\text{sh,cl}} = c_{\text{s},2} M_{\text{sh,cl}} \quad (\text{D10})$$

where the shock Mach number

$$M_{\text{sh,cl}} = \left[1 + \frac{\gamma_1(\gamma_1 + 1)(\gamma_2 + 1)}{4\gamma_2} M_1^2 f(M_1) \right]^{1/2} \quad (\text{D11})$$

and $f(M_1)$ is given by Eqn. D6 above. $M_{\text{sh,cl}}$ is always greater than unity, but ~ 1 , for low M_1 .

In terms of the temperature, T_2 , of the cloud, the shock velocity is

$$v_{\text{sh,cl}} = \left(\frac{kT_2}{\mu m} \right)^{1/2} M_{\text{sh,cl}} \quad (\text{D12})$$

$$\approx 15 \left(\frac{T_2}{10^4} \right)^{1/2} M_{\text{sh,cl}} \text{ km s}^{-1} \quad (\text{D13})$$

where $\mu \approx 0.62$ is the molecular weight and $m \approx 1.66 \times 10^{-24}$ g represents an atomic mass unit.

For jet Mach numbers = (1, 2, 3) the values of $M_{\text{sh,cl}} \approx (1.7, 2.6, 3.6)$. Hence, attributing the velocity dispersion in Minkowski's Object to a population of shocks, driven by a transonic ($M_1 \sim 1 - 2$) jet, it is apparent that a velocity dispersion $\leq 20 \text{ km s}^{-1}$ would arise for cloud temperatures $\sim 10^3 - 10^4$ K and a jet Mach number $\sim 1 - 2$.

The velocity dispersion resulting from such slow shocks are consistent with those measured in the H I cloud associated with MO (Lacy et al. 2017). Although they are also consistent with those observed in the ionised gas (see Fig. 4.7), we note that the resultant velocity dispersions are similar to those of H II regions where the line widths are driven by internal processes (e.g., Rozas et al. 2006). Hence we cannot attribute the observed line widths in our WiFeS observations to these shocks, although it does indicate that the jet does not significantly increase the turbulent velocities in the ionised gas.

E Minkowski's Object: additional metallicity diagnostics

The gas-phase metallicity and ionisation parameter estimated using the O2S2, R23 (Fig. E1), N2 and O3N2 (Fig. E2) metallicity diagnostics and the O3O2 ionisation parameter diagnostic of Kewley et al. (2019a).

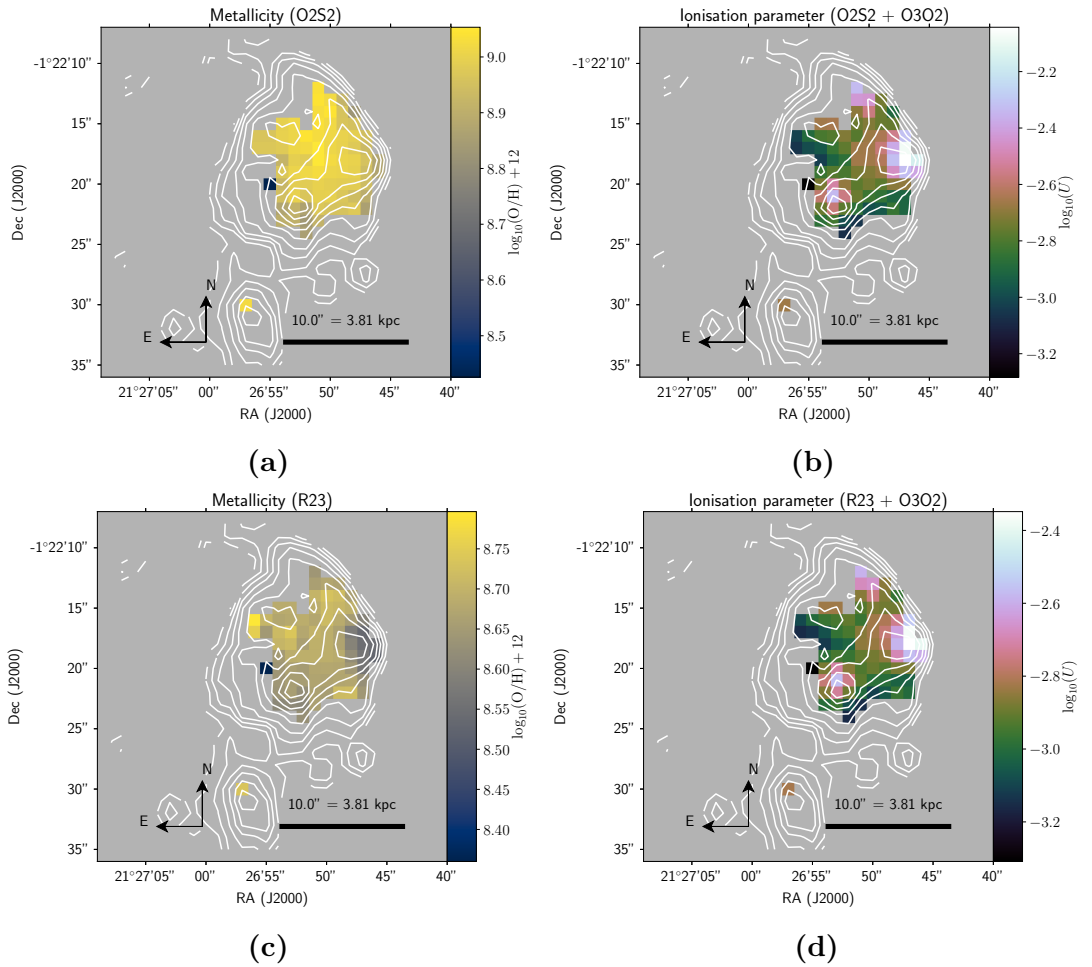


Figure E1: Gas-phase metallicity $\log(\text{O}/\text{H}) + 12$, calculated using (a) the O2S2 ($[\text{O II}]\lambda\lambda 3726, 3729/[\text{S II}]\lambda\lambda 6716, 6731$) and (c) R23 ($([\text{O II}]\lambda\lambda 3726, 3729 + [\text{O II}]\lambda\lambda 4959, 5007)/\text{H}\beta$). The dimensionless ionisation parameter $\log(U)$ corresponding to the different metallicity diagnostics used, calculated using the O3O2 diagnostic, is shown in (b) and (d). The white contours show the $\text{H}\alpha$ flux on a log scale.

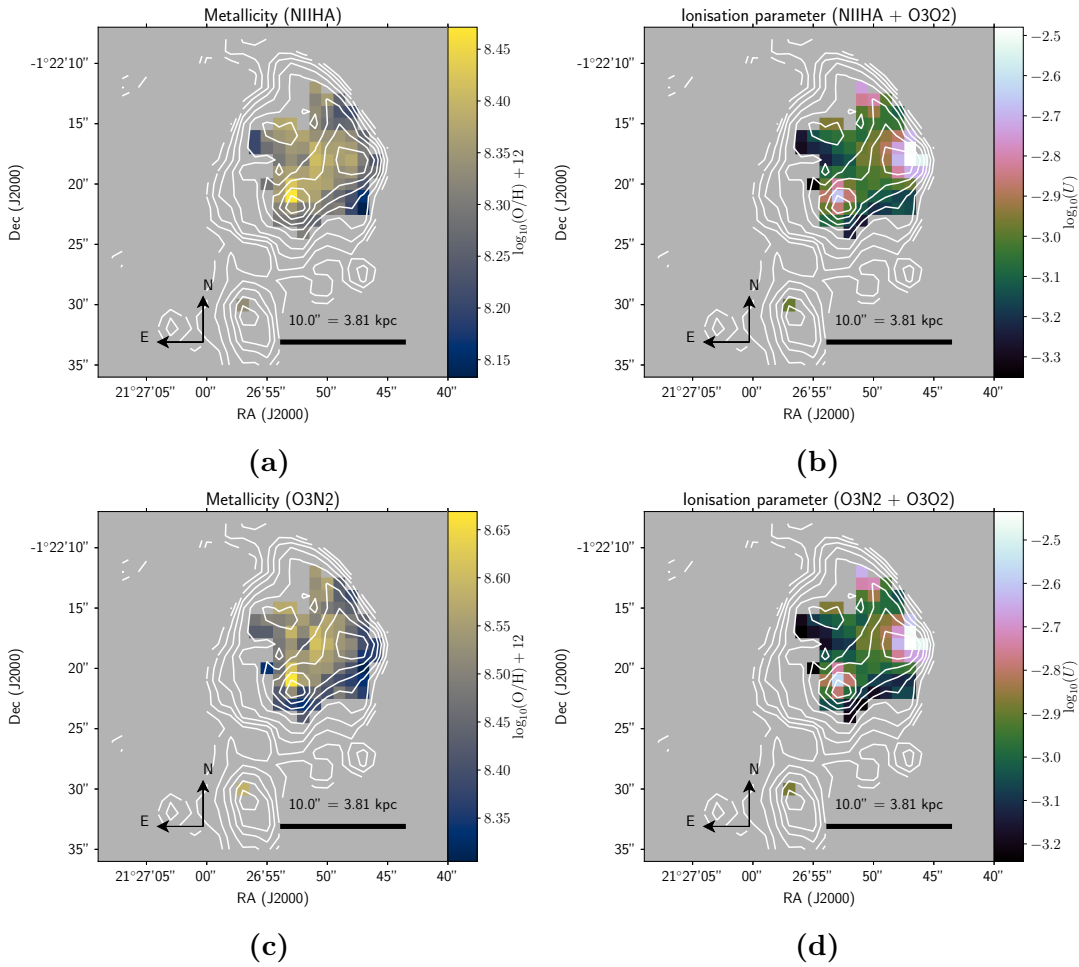


Figure E2: Gas-phase metallicity $\log(\text{O}/\text{H}) + 12$, calculated using (a) the N2 ($[\text{N II}]\lambda 6583/\text{H}\alpha$) and (b) O3N2 ($([\text{O III}]\lambda 5007/\text{H}\beta)/([\text{N II}]\lambda 6583/\text{H}\alpha)$) diagnostics. The dimensionless ionisation parameter $\log(U)$ corresponding to the different metallicity diagnostics used, calculated using the O3O2 diagnostic, is shown in (b) and (d). The white contours show the $\text{H}\alpha$ flux on a log scale.

Bibliography

- Abell G. O., Corwin Harold G. J., Olowin R. P., 1989, *ApJS*, 70, 1
- Alatalo K., et al., 2013, *MNRAS*, 432, 1796
- Alatalo K., et al., 2015, *ApJ*, 798, 31
- Alatalo K., et al., 2016, *ApJS*, 224, 38
- Allard F., Hauschildt P. H., Alexander D. R., Tamanai A., Schweitzer A., 2001, *ApJ*, 556, 357
- Allen M. G., Groves B. A., Dopita M. A., Sutherland R. S., Kewley L. J., 2008, *ApJS*, 178, 20
- Altschuler D. R., Gurvits L. I., Alef W., Dennison B., Graham D., Trotter A. S., Carson J. E., 1995, *A&AS*, 114, 197
- An T., Baan W. A., 2012, *ApJ*, 760, 77
- Astropy Collaboration et al., 2013, *A&A*, 558, A33
- Astropy Collaboration et al., 2018, *AJ*, 156, 123
- Baade W., Minkowski R., 1954, *ApJ*, 119, 206
- Bacon R., et al., 2001, *MNRAS*, 326, 23
- Bagnasco G., et al., 2007, in *Proc. SPIE*. p. 66920M, doi:10.1117/12.735602
- Baldwin J. A., Phillips M. M., Terlevich R., 1981, *PASP*, 93, 5
- Banfield J. K., et al., 2016, *MNRAS*, 460, 2376
- Becker R. H., White R. L., Helfand D. J., 1995, *ApJ*, 450, 559
- Belfiore F., et al., 2016, *MNRAS*, 461, 3111
- Bender R., 1988, *A&A*, 202, L5
- Bertelli G., Bressan A., Chiosi C., Fagotto F., Nasi E., 1994, *A&AS*, 106, 275
- Bessell M. S., 1999, *PASP*, 111, 1426
- Best P. N., Longair M. S., Rottgering H. J. A., 1996, *MNRAS*, 280, L9
- Bicknell G. V., 2002, *New A Rev.*, 46, 365
- Bicknell G. V., Begelman M. C., 1996, *ApJ*, 467, 597
- Bicknell G. V., Dopita M. A., O’Dea C. P. O., 1997, *ApJ*, 485, 112
- Bicknell G. V., Sutherland R. S., van Breugel W. J. M., Dopita M. A., Dey A., Miley G. K., 2000, *ApJ*, 540, 678
- Bicknell G. V., Mukherjee D., Wagner A. Y., Sutherland R. S., Nesvadba N. P. H., 2018, *MNRAS*, 475, 3493
- Blanco V. M., Graham J. A., Lasker B. M., Osmer P. S., 1975, *ApJ*, 198, L63
- Bland-Hawthorn J., 2015, in Ziegler B. L., Combes F., Dannerbauer H., Verdugo M., eds, *IAU Symposium Vol. 309, Galaxies in 3D across the Universe*. pp 21–28 (arXiv:1410.3838), doi:10.1017/S1743921314009247
- Blandford R. D., Rees M. J., 1974, *MNRAS*, 169, 395
- Blandford R., Meier D., Readhead A., 2019, *ARA&A*, 57, 467
- Boardman N. F., et al., 2017, *MNRAS*, 471, 4005
- Bogdán Á., et al., 2011, *ApJ*, 743, 59

- Bruzual G., Charlot S., 2003, MNRAS, 344, 1000
- Bryant J. J., et al., 2015, MNRAS, 447, 2857
- Bundy K., et al., 2015, ApJ, 798, 7
- Callingham J. R., et al., 2017, ApJ, 836, 174
- Calzetti D., 2013, Star Formation Rate Indicators. Cambridge University Press, Cambridge, UK, p. 419
- Cappellari M., 2017, MNRAS, 466, 798
- Cappellari M., Emsellem E., 2004, PASP, 116, 138
- Carvalho J. C., O’Dea C. P., 2002, ApJS, 141, 371
- Cenko S. B., Li W., Filippenko A. V., 2010, Central Bureau Electronic Telegrams, 2464
- Cerviño M., Gómez-Flechoso M. A., Castander F. J., Schaerer D., Mollá M., Knödseder J., Luridiana V., 2001, A&A, 376, 422
- Chambers K. C., Miley G. K., van Breugel W., 1987, Nature, 329, 604
- Charbonnel C., Meynet G., Maeder A., Schaller G., Schaerer D., 1993, A&AS, 101, 415
- Charmandaris V., Combes F., van der Hulst J. M., 2000, A&A, 356, L1
- Chen P., et al., 2018, The Astronomer’s Telegram, 11762
- Cheng X.-P., An T., 2018, ApJ, 863, 155
- Childress M. J., Vogt F. P. A., Nielsen J., Sharp R. G., 2014, Ap&SS, 349, 617
- Cluver M. E., Jarrett T. H., Dale D. A., Smith J. D. T., August T., Brown M. J. I., 2017, ApJ, 850, 68
- Collier J. D., et al., 2018, MNRAS, 477, 578
- Conway J. E., 1996, in Ekers R. D., Fanti C., Padrielli L., eds, IAU Symposium Vol. 175, Extragalactic Radio Sources. p. 92
- Cotton W. D., Feretti L., Giovannini G., Venturi T., Lara L., Marcaide J., Wehrle A. E., 1995, ApJ, 452, 605
- Crockett R. M., et al., 2012, MNRAS, 421, 1603
- Croft S., et al., 2006, ApJ, 647, 1040
- Croton D. J., et al., 2006, MNRAS, 365, 11
- Dabhade P., Gaikwad M., Bagchi J., Pandey-Pommier M., Sankhyayan S., Raychaudhury S., 2017, MNRAS, 469, 2886
- Dabrowski I., 1984, Canadian Journal of Physics, 62, 1639
- Dale D. A., Sheth K., Helou G., Regan M. W., Hüttemeister S., 2005, AJ, 129, 2197
- Davies R. I., 2007, MNRAS, 375, 1099
- Davies R. L., et al., 2017, MNRAS, 470, 4974
- Djorgovski S., Davis M., 1987, ApJ, 313, 59
- Dopita M. A., Sutherland R. S., 2003, Astrophysics of the diffuse universe. Springer-Verlag Berlin Heidelberg
- Dopita M. A., Sutherland R. S., 2017, ApJS, 229, 35
- Dopita M., Hart J., McGregor P., Oates P., Bloxham G., Jones D., 2007, Ap&SS, 310, 255
- Dopita M., et al., 2010, Ap&SS, 327, 245
- Emonts B. H. C., et al., 2014, MNRAS, 438, 2898
- Fabian A. C., 2012, ARA&A, 50, 455
- Falco E. E., et al., 1999, Publications of the Astronomical Society of the Pacific, 111, 438
- Fanaroff B. L., Riley J. M., 1974, MNRAS, 167, 31P

- Farage C. L., McGregor P. J., Dopita M. A., Bicknell G. V., 2010, *ApJ*, 724, 267
- Federrath C., 2015, *MNRAS*, 450, 4035
- Federrath C., Klessen R. S., 2012, *ApJ*, 761, 156
- Ferrarese L., Merritt D., 2000, *ApJ*, 539, L9
- Fitzpatrick E. L., Massa D., 2007, *ApJ*, 663, 320
- Flower D. R., Pineau Des Forêts G., 2010, *MNRAS*, 406, 1745
- Fomalont E. B., Kellermann K. I., Partridge R. B., Windhorst R. A., Richards E. A., 2002, *AJ*, 123, 2402
- Fragile P. C., Murray S. D., Anninos P., van Breugel W., 2004, *ApJ*, 604, 74
- Fragile P. C., Anninos P., Gustafson K., Murray S. D., 2005, *ApJ*, 619, 327
- Fragile P. C., Anninos P., Croft S., Lacy M., Witry J. W. L., 2017, *ApJ*, 850, 171
- Gaibler V., Khochfar S., Krause M., Silk J., 2012, *MNRAS*, 425, 438
- Gal-Yam A., et al., 2010, *Central Bureau Electronic Telegrams*, 2490
- García-Burillo S., Combes F., Neri R., Fuente A., Usero A., Leon S., Lim J., 2007, *A&A*, 468, L71
- Gardner J. P., et al., 2006, *Space Sci. Rev.*, 123, 485
- Gebhardt K., et al., 2000, *ApJ*, 539, L13
- Gildas Team 2013, *GILDAS: Grenoble Image and Line Data Analysis Software, Astrophysics Source Code Library (ascl:1305.010)*
- Giovannini G., Cotton W. D., Feretti L., Lara L., Venturi T., 2001, *ApJ*, 552, 508
- Girardi L., Bertelli G., 1998, *MNRAS*, 300, 533
- Girardi L., Bressan A., Bertelli G., Chiosi C., 2000, *A&AS*, 141, 371
- Girardi L., Bertelli G., Bressan A., Chiosi C., Groenewegen M. A. T., Marigo P., Salasnich B., Weiss A., 2002, *A&A*, 391, 195
- Giroletti M., Giovannini G., Taylor G. B., Conway J. E., Lara L., Venturi T., 2003, *A&A*, 399, 889
- Gonçalves A. C., Serote Roos M., 2004, *A&A*, 413, 97
- González Delgado R. M., Cerviño M., Martins L. P., Leitherer C., Hauschildt P. H., 2005, *MNRAS*, 357, 945
- Gray R. O., Corbally C. J., 1994, *AJ*, 107, 742
- Guillard P., Boulanger F., Lehnert M. D., Pineau des Forêts G., Combes F., Falgarone E., Bernard-Salas J., 2015, *A&A*, 574, A32
- Gültekin K., et al., 2009, *ApJ*, 698, 198
- Güver T., Özel F., 2009, *MNRAS*, 400, 2050
- Haffner L. M., et al., 2009, *Reviews of Modern Physics*, 81, 969
- Hamer S., Salomé P., Combes F., Salomé Q., 2015, *A&A*, 575, L3
- Hamer S. L., et al., 2016, *MNRAS*, 460, 1758
- Hart J., McGregor P. J., Bloxham G. J., 2003, in Iye M., Moorwood A. F. M., eds, Vol. 4841, *Instrument Design and Performance for Optical/Infrared Ground-based Telescopes*. SPIE, pp 319 – 329, doi:10.1117/12.459940, <https://doi.org/10.1117/12.459940>
- Hauschildt P. H., Baron E., 1999, *Journal of Computational and Applied Mathematics*, 109, 41
- Heckman T. M., Baum S. A., van Breugel W. J. M., McCarthy P., 1989, *ApJ*, 338, 48
- Holt J., Tadhunter C. N., Morganti R., 2008, *MNRAS*, 387, 639
- Hubeny I., Lanz T., 2011, *Synspec: General Spectrum Synthesis Program (ascl:1109.022)*

- Hudaverdi M., Kunieda H., Tanaka T., Haba Y., Furuzawa A., Tawara Y., Ercan E. N., 2006, PASJ, 58, 931
- Husemann B., et al., 2019, A&A, 627, A53
- Ineson J., Croston J. H., Hardcastle M. J., Mingo B., 2017, MNRAS, 467, 1586
- Jeyakumar S., 2016, MNRAS, 458, 3786
- Jin C., Ward M., Done C., Gelbord J., 2012, MNRAS, 420, 1825
- Jones E., Oliphant T., Peterson P., et al., 2001, SciPy: Open source scientific tools for Python, <http://www.scipy.org/>
- Kauffmann G., et al., 2003, MNRAS, 346, 1055
- Keim M. A., Callingham J. R., Röttgering H. J. A., 2019, A&A, 628, A56
- Kennicutt Jr. R. C., 1998, ApJ, 498, 541
- Kewley L. J., Dopita M. A., 2002, ApJS, 142, 35
- Kewley L. J., Ellison S. L., 2008, ApJ, 681, 1183
- Kewley L. J., Dopita M. A., Sutherland R. S., Heisler C. A., Trevena J., 2001, ApJ, 556, 121
- Kewley L. J., Groves B., Kauffmann G., Heckman T., 2006, MNRAS, 372, 961
- Kewley L. J., Nicholls D. C., Sutherland R. S., 2019a, ARA&A, 57, 511
- Kewley L. J., Nicholls D. C., Sutherland R., Rigby J. R., Acharya A., Dopita M. A., Bayliss M. B., 2019b, ApJ, 880, 16
- King A., Pounds K., 2015, ARA&A, 53, 115
- Kirkpatrick C. C., Gitti M., Cavagnolo K. W., McNamara B. R., David L. P., Nulsen P. E. J., Wise M. W., 2009, ApJ, 707, L69
- Kirkpatrick C. C., McNamara B. R., Cavagnolo K. W., 2011, ApJ, 731, L23
- Klamer I. J., Ekers R. D., Sadler E. M., Hunstead R. W., 2004, ApJ, 612, L97
- Kobayashi C., 2004, MNRAS, 347, 740
- Kobayashi C., Nakasato N., 2011, ApJ, 729, 16
- Kobayashi C., Nomoto K., 2009, ApJ, 707, 1466
- Kobayashi C., Karakas A. I., Umeda H., 2011, MNRAS, 414, 3231
- Koda J., Yagi M., Yamanoi H., Komiyama Y., 2015, ApJ, 807, L2
- Kodama T., Arimoto N., 1997, A&A, 320, 41
- Krause M., 2003, A&A, 398, 113
- Kroupa P., 2001, MNRAS, 322, 231
- Krumholz M. R., Dekel A., McKee C. F., 2012, ApJ, 745, 69
- Kurucz R. L., 1991, in Crivellari L., Hubeny I., Hummer D. G., eds, NATO Advanced Science Institutes (ASI) Series C Vol. 341, Stellar Atmospheres: Beyond Classical Models, Proceedings of the Advanced Research Workshop, Trieste, Italy. D. Reidel Publishing Co., Dordrecht, p. 441
- Lacy M., Croft S., Fragile C., Wood S., Nyland K., 2017, ApJ, 838, 146
- Landau L. D., Lifshitz E. M., 1987, Fluid Mechanics
- Lanz T., Hubeny I., 2003, ApJS, 146, 417
- Lanz L., Ogle P. M., Alatalo K., Appleton P. N., 2016, ApJ, 826, 29
- Larkin J., et al., 2006, in Society of Photo-Optical Instrumentation Engineers (SPIE) Conference Series. p. 62691A, doi:10.1117/12.672061
- Larkin J. E., et al., 2010, The infrared imaging spectrograph (IRIS) for TMT: instrument overview. p. 773529, doi:10.1117/12.856305
- Leisman L., et al., 2017, ApJ, 842, 133
- Leitherer C., et al., 1999, ApJS, 123, 3
- Lena D., et al., 2015, ApJ, 806, 84

- Li M. P., Shi Q. J., Li A., 2008, *MNRAS*, 391, L49
- MacDonald G. H., Kenderdine S., Neville A. C., 1968, *MNRAS*, 138, 259
- Maccagni F. M., Santoro F., Morganti R., Oosterloo T. A., Oonk J. B. R., Emonts B. H. C., 2016, *A&A*, 588, A46
- Marcha M. J. M., Browne I. W. A., Impey C. D., Smith P. S., 1996, *MNRAS*, 281, 425
- Markwardt C. B., 2009, in Bohlender D. A., Durand D., Dowler P., eds, *Astronomical Society of the Pacific Conference Series Vol. 411, Astronomical Data Analysis Software and Systems XVIII*. p. 251 ([arXiv:0902.2850](https://arxiv.org/abs/0902.2850))
- Martig M., et al., 2013, *MNRAS*, 432, 1914
- Martins L. P., Leitherer C., Cid Fernand es R., González Delgado R. M., Schmitt H. R., Storchi-Bergmann T., Heckman T., 2004, in Storchi-Bergmann T., Ho L. C., Schmitt H. R., eds, *IAU Symposium Vol. 222, The Interplay Among Black Holes, Stars and ISM in Galactic Nuclei*. pp 337–338, doi:10.1017/S1743921304002492
- Mathis J. S., 1986, *ApJ*, 301, 423
- Matsushita K., 2001, *ApJ*, 547, 693
- May D., Rodríguez-Ardila A., Prieto M. A., Fernández-Ontiveros J. A., Diaz Y., Mazzalay X., 2018, *MNRAS*, 481, L105
- McCarthy P. J., van Breugel W., Spinrad H., Djorgovski S., 1987, *ApJ*, 321, L29
- McDonald M., Veilleux S., Rupke D. S. N., 2012, *ApJ*, 746, 153
- McGregor P. J., et al., 2003, in Iye M., Moorwood A. F. M., eds, *Proc. SPIE Vol. 4841, Instrument Design and Performance for Optical/Infrared Ground-based Telescopes*. pp 1581–1591, doi:10.1117/12.459448
- McNamara B. R., Nulsen P. E. J., 2012, *New Journal of Physics*, 14, 055023
- McNamara B. R., O’Connell R. W., 1993, *AJ*, 105, 417
- Merloni A., Heinz S., di Matteo T., 2003, *MNRAS*, 345, 1057
- Meynet G., 1995, *A&A*, 298, 767
- Minkowski R., 1958, *PASP*, 70, 143
- Mohr J. J., Mathiesen B., Evrard A. E., 1999, *ApJ*, 517, 627
- Moral-Pombo D., et al., 2018, *The Astronomer’s Telegram*, 12313
- Moravec E., et al., 2019, *ApJ*, 871, 186
- Moré J. J., 1978, *The Levenberg-Marquardt algorithm: Implementation and theory*. Springer, Berlin, Heidelberg, pp 105–116, doi:10.1007/BFb0067700
- Morganti R., Tadhunter C. N., Oosterloo T. A., 2005, *A&A*, 444, L9
- Morganti R., Fogasy J., Paragi Z., Oosterloo T., Orienti M., 2013, *Science*, 341, 1082
- Morganti R., Oosterloo T., Oonk J. B. R., Frieswijk W., Tadhunter C., 2015, *A&A*, 580, A1
- Mukherjee D., Bicknell G. V., Sutherland R., Wagner A., 2016, *MNRAS*, 461, 967
- Mukherjee D., Wagner A. Y., Bicknell G. V., Morganti R., Oosterloo T., Nesvadba N., Sutherland R. S., 2018a, *MNRAS*, 476, 80
- Mukherjee D., Bicknell G. V., Wagner A. Y., Sutherland R. S., Silk J., 2018b, *MNRAS*, 479, 5544
- Murgia M., 2003, *PASA*, 20, 19
- Nesvadba N. P. H., Lehnert M. D., Eisenhauer F., Gilbert A., Tecza M., Abuter R., 2006, *ApJ*, 650, 693
- Nesvadba N. P. H., et al., 2010, *A&A*, 521, A65
- Nesvadba N. P. H., Boulanger F., Lehnert M. D., Guillard P., Salome P., 2011,

- A&A, 536, L5
- Neugebauer G., et al., 1984, *The Astrophysical Journal*, 278, L1
- Nikogossyan E., Durret F., Gerbal D., Magnard F., 1999, A&A, 349, 97
- Nordlund Å. K., Padoan P., 1999, in Franco J., Carraminana A., eds, *Interstellar Turbulence*. p. 218 (arXiv:astro-ph/9810074)
- O’Dea C. P., 1998, PASP, 110, 493
- O’Dea C. P., 2016, *Astronomische Nachrichten*, 337, 141
- O’Dea C. P., Baum S. A., 1997, AJ, 113, 148
- Ocaña Flaquer B., Leon S., Combes F., Lim J., 2010, A&A, 518, A9
- Ogle P., Boulanger F., Guillard P., Evans D. A., Antonucci R., Appleton P. N., Nesvadba N., Leipski C., 2010, ApJ, 724, 1193
- Oh K., Sarzi M., Schawinski K., Yi S. K., 2011, ApJS, 195, 13
- Oosterloo T. A., Morganti R., 2005, A&A, 429, 469
- Orienti M., 2016, *Astronomische Nachrichten*, 337, 9
- Panizo-Espinar G., et al., 2018, *The Astronomer’s Telegram*, 12315
- Perlman E. S., Stocke J. T., Conway J., Reynolds C., 2001, AJ, 122, 536
- Proxauf B., Öttl S., Kimeswenger S., 2014, A&A, 561, A10
- Puxley P. J., Hawarden T. G., Mountain C. M., 1990, ApJ, 364, 77
- Rand R. J., 1998, PASA, 15, 106
- Rich J. A., Kewley L. J., Dopita M. A., 2013, *WiFeS and GOALS: An IFS Study Of Shocks and More In Nearby U/LIRGS*. p. 231
- Riffel R. A., Vale T. B., Storchi-Bergmann T., McGregor P. J., 2014, MNRAS, 442, 656
- Riffel R. A., Storchi-Bergmann T., Riffel R., 2015, MNRAS, 451, 3587
- Robinson I., Schild A., Schucking E. L., 1965, in *Quasi-Stellar Sources and Gravitational Collapse*.
- Rodman P. E., et al., 2019, MNRAS, 482, 5625
- Román J., Trujillo I., 2017, MNRAS, 468, 4039
- Rosenberg M. J. F., van der Werf P. P., Israel F. P., 2012, A&A, 540, A116
- Rosenberg M. J. F., van der Werf P. P., Israel F. P., 2013, A&A, 550, A12
- Roth M. M., et al., 2005, PASP, 117, 620
- Rowan-Robinson M., et al., 1997, *Monthly Notices of the Royal Astronomical Society*, 289, 490
- Rozas M., Richer M. G., López J. A., Relaño M., Beckman J. E., 2006, A&A, 455, 539
- Rybicki G. B., Lightman A. P., 1979, *Radiative processes in astrophysics*. John Wiley & Sons, Inc.
- Sabra B. M., Shields J. C., Filippenko A. V., 2000, ApJ, 545, 157
- Sakelliou I., Hardcastle M. J., Jetha N. N., 2008, MNRAS, 384, 87
- Salim S., et al., 2007, ApJS, 173, 267
- Salim D. M., Federrath C., Kewley L. J., 2015, ApJ, 806, L36
- Salomé Q., Salomé P., Combes F., 2015, A&A, 574, A34
- Salomé Q., Salomé P., Combes F., Hamer S., Heywood I., 2016, A&A, 586, A45
- Salomé Q., Salomé P., Miville-Deschênes M.-A., Combes F., Hamer S., 2017, A&A, 608, A98
- Salpeter E. E., 1955, ApJ, 121, 161
- Sánchez S. F., et al., 2012, A&A, 538, A8
- Sánchez S. F., et al., 2016a, *Rev. Mexicana Astron. Astrofis.*, 52, 171

- Sánchez S. F., et al., 2016b, *A&A*, 594, A36
- Sanders R. L., et al., 2016, *ApJ*, 825, L23
- Santoro F., Oonk J. B. R., Morganti R., Oosterloo T. A., Tadhunter C., 2016, *A&A*, 590, A37
- Saulder C., van Kampen E., Chilingarian I. V., Mieske S., Zeilinger W. W., 2016, *A&A*, 596, A14
- Schaerer D., Meynet G., Maeder A., Schaller G., 1993a, *A&AS*, 98, 523
- Schaerer D., Charbonnel C., Meynet G., Maeder A., Schaller G., 1993b, *A&AS*, 102, 339
- Schaller G., Schaerer D., Meynet G., Maeder A., 1992, *A&AS*, 96, 269
- Scharwächter J., McGregor P. J., Dopita M. A., Beck T. L., 2013, *MNRAS*, 429, 2315
- Schimminovich D., van Gorkom J. H., van der Hulst J. M., Kasow S., 1994, *ApJ*, 423, L101
- Schlafly E. F., Finkbeiner D. P., 2011, *ApJ*, 737, 103
- Schmidt M., 1959, *ApJ*, 129, 243
- Schulz R., Morganti R., Nyland K., Paragi Z., Mahony E. K., Oosterloo T., 2018, *A&A*, 617, A38
- Scott N., et al., 2018, *MNRAS*, 481, 2299
- Serote Roos M., Gonçalves A. C., 2004, *A&A*, 413, 91
- Sharp R., et al., 2015, *MNRAS*, 446, 1551
- Sharp R., et al., 2018, in *Proc. SPIE*. p. 107021V, doi:10.1117/12.2313010
- Shulevski A., et al., 2019, *A&A*, 628, A69
- Silk J., 2005, *MNRAS*, 364, 1337
- Silk J., Rees M. J., 1998, *A&A*, 331, L1
- Singh R., et al., 2013, *A&A*, 558, A43
- Smette A., et al., 2015, *A&A*, 576, A77
- Smith R. J., Lucey J. R., Hudson M. J., Schlegel D. J., Davies R. L., 2000, *MNRAS*, 313, 469
- Snellen I. A. G., Mack K.-H., Schilizzi R. T., Tschager W., 2004, *MNRAS*, 348, 227
- Solomon P. M., Downes D., Radford S. J. E., Barrett J. W., 1997, *ApJ*, 478, 144
- Storchi-Bergmann T., Riffel R. A., Riffel R., Diniz M. R., Borges Vale T., McGregor P. J., 2012, *ApJ*, 755, 87
- Struble M. F., Rood H. J., 1999, *ApJS*, 125, 35
- Struve C., Conway J. E., 2012, *A&A*, 546, A22
- Sulentic J. W., Rosado M., Dultzin-Hacyan D., Verdes-Montenegro L., Trinchieri G., Xu C., Pietsch W., 2001, *AJ*, 122, 2993
- Sutherland R. S., Bicknell G. V., 2007, *ApJS*, 173, 37
- Sutherland R., Dopita M., Binette L., Groves B., 2018, *MAPPINGS V: Astrophysical plasma modeling code (ascl:1807.005)*
- Tadhunter C., Morganti R., Rose M., Oonk J. B. R., Oosterloo T., 2014, *Nature*, 511, 440
- Terzić B., Graham A. W., 2005, *MNRAS*, 362, 197
- Thatte N., et al., 2010, *HARMONI: a single-field wide-band integral-field spectrograph for the European ELT*. p. 77352I, doi:10.1117/12.857445
- Thomas A. D., Dopita M. A., Kewley L. J., Groves B. A., Sutherland R. S., Hopkins A. M., Blanc G. A., 2018, *ApJ*, 856, 89
- Tingay S. J., et al., 2015, *AJ*, 149, 74

- Tremaine S., et al., 2002, *ApJ*, 574, 740
- Turner J., Kirby-Docken K., Dalgarno A., 1977, *ApJS*, 35, 281
- Tzioumis A. K., et al., 2010, *AJ*, 140, 1506
- Veilleux S., Osterbrock D. E., 1987, *ApJS*, 63, 295
- Verdoes Kleijn G. A., Baum S. A., de Zeeuw P. T., O’Dea C. P., 1999, *AJ*, 118, 2592
- Wagner A. Y., Bicknell G. V., 2011, *ApJ*, 728, 29
- Wagner A. Y., Bicknell G. V., Umemura M., Sutherland R. S., Silk J., 2016, *Astronomische Nachrichten*, 337, 167
- Walcher C. J., et al., 2014, *A&A*, 569, A1
- Werner N., Allen S. W., Simionescu A., 2012, *MNRAS*, 425, 2731
- Willett K. W., Stocke J. T., Darling J., Perlman E. S., 2010, *ApJ*, 713, 1393
- Willis A. G., Strom R. G., Wilson A. S., 1974, *Nature*, 250, 625
- Wisnioski E., et al., 2015, *ApJ*, 799, 209
- Wizinowich P. L., et al., 2006, *PASP*, 118, 297
- Wolniewicz L., Simbotin I., Dalgarno A., 1998, *ApJS*, 115, 293
- Wright E. L., 2006, *PASP*, 118, 1711
- Zaritsky D., 2017, *MNRAS*, 464, L110
- Zovaro H. R. M., Sharp R., Nesvadba N. P. H., Bicknell G. V., Mukherjee D., Wagner A. e. Y., Groves B., Krishna S., 2019a, *MNRAS*, 484, 3393
- Zovaro H. R. M., Nesvadba N. P. H., Sharp R., Bicknell G. V., Groves B., Mukherjee D., Wagner A. Y., 2019b, *MNRAS*, 489, 4944
- Zubovas K., Bourne M. A., 2017, *MNRAS*, 468, 4956
- de Vries N., Snellen I. A. G., Schilizzi R. T., Mack K.-H., Kaiser C. R., 2009, *A&A*, 498, 641
- van Breugel W., Miley G., Heckman T., 1984, *AJ*, 89, 5
- van Breugel W., Filippenko A. V., Heckman T., Miley G., 1985, *ApJ*, 293, 83
- van Dam M. A., et al., 2006, *PASP*, 118, 310
- van Dokkum P. G., Abraham R., Merritt A., Zhang J., Geha M., Conroy C., 2015, *ApJ*, 798, L45
- van Zee L., Salzer J. J., Haynes M. P., O’Donoghue A. A., Balonek T. J., 1998, *AJ*, 116, 2805
- van den Bergh S., 1970, *Publications of the Astronomical Society of the Pacific*, 82, 1374
- JWST User Documentation 2016–, Baltimore, MD. Space Telescope Science Institute [accessd 18th November 2019], <https://jwst-docs.stsci.edu>